Modelling and Analysis of Wireless Power Transfer System for Electric Vehicle Charging

Brijesh Kumar Kushwaha

Modelling and Analysis of Wireless Power Transfer System for Electric Vehicle Charging

A

Thesis submitted

for the award of the degree of

Doctor of Philosophy

By

Brijesh Kumar Kushwaha

Department of Electronics and Electrical Engineering

Indian Institute of Technology Guwahati

Guwahati - 781 039, Assam, India

February 2020

Dedicated to
my maa

Certificate

This is to certify that the thesis entitled "**Modelling and Analysis of Wireless Power Transfer System for Electric Vehicle Charging**", submitted by **Brijesh Kumar Kushwaha** (126102029), a research scholar in the *Department of Electronics and Electrical Engineering, Indian Institute of Technology Guwahati*, for the award of the degree of **Doctor of Philosophy**, is a record of an original research work carried out by him under my supervision and guidance. The thesis has fulfilled all requirements as per the regulations of the institute and in my opinion has reached the standard needed for submission. The results embodied in this thesis have not been submitted to any other University or Institute for the award of any degree or diploma.

Date:

Place: Guwahati.

Prof. Praveen Kumar

Dept. of Electronics and Electrical Engg
Indian Institute of Technology Guwahati
Guwahati - 781 039, Assam, India.

Acknowledgements

First and foremost, I feel it as a great privilege in expressing my deepest and most sincere gratitude to my supervisor Prof. Praveen Kumar, for his excellent guidance throughout my study. His kindness, dedication, hard work and attention to detail have been a great inspiration to me. My heartfelt thanks to you for the unlimited support and patience shown to me. I have no doubts that finishing my degree in a proper and timely manner was impossible without his help, suggestions and advice.

I am also very thankful to my doctoral committee members Professor Ratnajit Bhattacharjee, Professor Sisir Kumar Nayak, and Dr. Sanjib Ganguly, for sparing their precious time to evaluate the progress of my work. I am also grateful to all the members of the research and technical staff of the department without whose help I could not have completed this thesis.

I would also like to thank the Head of the Department and the other faculty members for their kind help in carrying out this work. I express my thanks to seniors, Dr. Kannan T., Dr. Reena Joy, Dr. Ankit Dalal, and Umesh Chaudhary.

Thanks to all my friends, namely Rajendra Kumar, Upendra reddy, Kashyap Prabhakar, Krishna Pawan Inala, Ripudaman Singh, Prosenjit Mondal, Bikash Shah, Tarique. They all contributed directly or indirectly to this thesis. Thanks also go to all my friends at the Power and Control Laboratory. They have always been around to provide useful suggestions, companionship, and created a peaceful research environment. A special thanks to Gautam Rituraj for their cooperation.

I also express my deepest gratitude to my parents for their endless love and support throughout my studies. The opportunities that they have given me and their immense sacrifices are the reasons where I am and what I have accomplished. Especially my mothers blessings and best wishes are with me forever. I shall be in debt to their immense sacrifices for my success.

My other family members also played a significant role during my PhD., and they are my brothers Mr. Rajesh, Mr. Girijesh and, sister Ms. Sushma and my lovable Neha, Nidhi, and Raj. Finally, I am very grateful to my wife, who has been a constant source of inspiration during my PhD.

B. K. Kushwaha

Brijesh Kumar Kushwaha

Abstract

Wireless power transfer (WPT) technology offers better operational flexibility, safety, and durability in comparison to plug-in power transfer. Therefore, many applications, such as domestic appliances, rotating systems, mobile robots, and wearable devices, use WPT technology. In recent years, WPT systems are also used for charging the electric vehicle (EV) batteries. In the WPT system, power is transferred from source to load without any physical connection. Therefore, mutual inductance is an essential parameter in designing of WPT system. Generally, for calculating mutual inductance between the coils for the WPT system, the 3-D finite element analysis (FEA) is used because of its high accuracy. However, high mesh-density in the 3-D FEA model requires intensive computational power. The coil system with magnetic shields requires more numbers of mesh elements and results in substantial calculation time. The significant computational burden makes the design and optimization of the coil system a tedious process. Moreover, the designing of the WPT system involves numerous geometrical modifications in the 3-D FEA model. An analytical model is another approach to design the coil system, and this thesis deals with this issue.

This thesis begins with a review of various possible modelling technique for the coil system without the magnetic shield of the WPT system. A 3-D analytical model based on the harmonic modelling technique is developed to calculate air gap magnetic field distribution as well as mutual inductance between the coils. For the modelling, 3-D magnetic vector potential and magnetic scalar potential definitions in the Cartesian coordinate system is used. The current density distribution in the coil is modelled by four overlapping bars. Moreover, using the proposed analytical model, two new expressions are derived for faster calculation of the mutual inductance between the coils of the WPT system. The

proposed analytical model takes into account the variation of mutual inductance due to different misalignments for the air core transmitter and receiver coil system. All possible misalignments that can occur during the charging of EV are considered. The magnetic flux density distribution and mutual inductances are calculated with the analytical, and they are validated with finite element analysis and experimental results.

The harmonic model is further modified to include a magnetic shield below the primary coil. This model has the flexibility to change the width and permeability of shielding material. The magnetic flux density distribution and mutual inductance between the coils, obtained from the analytical model, FEM, and experiment results, which are in close agreement. The proposed analytical model considers the length of the magnetic shield is infinite, which is impractical. In practice, the magnetic shielding of finite permeability and finite dimensions is used with the primary and secondary coils. In this context, a 3-D analytical model that considers the magnetic shields of finite permeability and finite dimension is developed. This 3-D model is developed by the superposition of two 2-D analytical models. These 2-D models are developed based on the subdomain technique. Since 2-D models are invariant in their third direction (i.e., in the *y*-direction for *xz*-plane and the *x*-direction for *yz*-plane), a correction factor is introduced for 2-D subdomain models to make it variant in their third directions. The results obtained from the subdomain model are compared with FEM and experimental results, which are found in good agreement.

The change in the mutual inductance impacts the power transfer capability and the efficiency of the entire system. A steady-state model of series-parallel (SP) compensated WPT system is developed to analyse the impact of change in the electrical parameter due to misalignments. Effect of harmonics is considered in the steady-state model to get an accurate result. Magnetic model is coupled with the steady-state model to calculate the variation in electrical parameters during misalignments. The coupled model gives a comprehensive mathematical model for a WPT system for the charging of EV batteries. The mutual inductance calculated from the analytical model for different coil systems is used

as direct input for the steady-state model. The proposed model can be used for analysing the component stress of the SP compensated WPT system for different misalignments, which helps in the initial design process of such a WPT system.

Overall, this thesis presents a comprehensive analytical model for research and design of the wireless power transfer system.

Contents

List of Figures **xix**

List of Tables **xxvii**

List of Acronyms **xxix**

List of Symbols **xxxi**

1 Introduction **1**

1.1 Introduction 2

1.2 Literature Review 3

1.2.1 Numerical Method 4

1.2.1.1 Finite Difference Method (FDM) 4

1.2.1.2 Finite Element Analysis (FEA) 5

1.2.1.3 The Moment Method (MoM) 6

1.2.2 Analytical Method 6

1.2.2.1 Biot Savert Law 6

1.2.2.2 Magnetic Equivalent Circuit (MEC) 7

1.2.2.3 Harmonic Method (HM) 7

1.3 Research Motivation 8

1.4 Aim of the thesis 9

1.5 Thesis Contribution 10

1.6 Thesis Overview 11

2 3-D Analytical Model for Computation of Mutual Inductance for Different Misalignment in Wireless Power Transfer System **15**

2.1 Introduction 16

2.2 Analytical Model . . . 18
2.2.1 System Description and Assumptions . . . 19
2.2.2 Solution of the magnetic vector potential and scalar potential . . . 20
2.2.2.1 Magnetic vector potential in coil . . . 21
2.2.2.2 Solution of magnetic scalar potential in air medium . . . 24
2.2.3 Modelling of the current density distribution . . . 25
2.2.4 Boundary conditions . . . 28
2.3 Possible Misalignments . . . 30
2.4 Mutual Inductance Calculation . . . 31
2.5 Verification of Analytical Model . . . 33
2.5.1 FEA Simulation . . . 34
2.5.2 Experimental Set-up . . . 34
2.5.3 Magnetic Field Distribution in the Air Gap . . . 36
2.5.4 Mutual Inductance . . . 36
2.6 Summary . . . 40

3 3-D Analytical Model for Computation of Mutual Inductance for Different Misalignment with Shielding in WPT System 43

3.1 Introduction . . . 44
3.2 Analytical modelling . . . 45
3.2.1 Coil System Overview . . . 45
3.2.2 Magnetic Field Description . . . 47
3.2.2.1 Region IV . . . 48
3.2.2.2 Region I, II, III, and V . . . 49
3.2.3 Boundary Conditions . . . 50
3.3 Possible Misalignments . . . 52
3.4 Verification of Analytical Model . . . 54
3.4.1 FEA Simulation . . . 54
3.4.2 Experimental Set-up . . . 54

3.4.3 Magnetic Field Distribution in the Air Gap . . . 55
3.4.4 Mutual Inductance . . . 57
3.4.5 Comparison with method given in [1] . . . 61
3.5 Summary . . . 62

4 A Subdomain Analytical Model of Coil System with Magnetic Shields of Finite Dimensions and Finite Permeability for WPT systems 65

4.1 Introduction . . . 66
4.2 2-D Subdomain Model for the Coil System . . . 67
4.2.1 System Overview . . . 68
4.2.2 Magnetic Field Description . . . 71
4.2.3 Magnetic Vector Potentials . . . 72
4.2.3.1 Regions II_b, IV_b, IV_d, and VI_b . . . 72
4.2.3.2 Regions III and V . . . 73
4.2.3.3 Regions II_a, II_c, IV_a, IV_c, IV_e, VI_a, and VI_c . . . 73
4.2.3.4 Regions I and VII . . . 74
4.2.4 Boundary Conditions . . . 74
4.2.5 2-D Subdomain Model Verification . . . 80
4.3 Superposition of Two 2-D Subdomain Models . . . 83
4.4 Verification of Analytical Model . . . 88
4.4.1 Experimental Setup . . . 88
4.4.2 Results Description . . . 89
4.5 Summary . . . 90

5 Mathematical Model for Analysis of Series Parallel Compensated Wireless Power Transfer System for Different Misalignments 93

5.1 Introduction . . . 94
5.2 System Description and Mathematical Model . . . 95
5.2.1 System Description . . . 95
5.2.2 Steady-State Model . . . 95

5.2.2.1 Modelling of the Primary Side 97
5.2.2.2 Modelling of the Secondary Side 98
5.3 Experimental Setup Description 100
5.4 Results and Discussion 102
5.4.1 Results with Different Misalignments 103
5.4.2 Variation in electrical parameter for coil system having magnetic shields . . . 111
5.5 Summary 113
6 Conclusion and Future Works 115
6.1 Summary of the Work 116
6.2 Limitations of the Work 118
6.3 Scope for Future Research 119
A Calculation of Expression of Mutual Inductance 121
A.1 Calculation of Expression 122
B Magnetic Vector Potential of Different Regions 125
B.1 Applied Boundary Conditions Between Different Regions 126
B.2 Regions with Applied Boundary Conditions 132
B.3 Magnetic Vector Potential of Different Regions 132
B.3.1 General Solution of Magnetic Vector Potential 133
B.3.2 Derivation of magnetic vector potential according to imposed boundary conditions 134
Bibliography 143
List of Publications 151

List of Figures

1.1 Block diagram of inductively coupled WPT system. 3

1.2 Classification of available methods to model a coil system 4

1.3 Division of magnetic problem into grid points. 5

1.4 Division of magnetic problem into different mesh. 6

1.5 Geometric definition of a flux tube and its representation. 7

1.6 3D illustration of coil system without magnetic shield. 10

1.7 3D illustration of coil system having magnetic shield of finite permeability and infinite length. 10

1.8 3D illustration of coil system having magnetic shield of finite permeability and finite length. 11

2.1 Classification of available methods to model coil system shown in Fig. 2.2. 16

2.2 3D illustration of coil system with its regions. 19

2.3 Arrangement of coils 20

2.4 The actual coil and its approximation. 26

2.5 Current density distribution of J_x (a) along y-direction, (b) along x-direction, and (c) along x- and y-direction.. 27

2.6 xz face of rectangular coil 28

2.7 Schematic of studied variations (a) vertical variation (VV), (b) planar misalignment (PM), (c) angular misalignment (AM), (d) horizontal misalignment (HM), (e) planar with horizontal misalignment (PHM) and (f) angular with horizontal misalignment (AHM). 31

2.8 Flowchart presenting the steps involved in calculating the mutual inductance for different misalignments (as given in (2.44) and (2.45)). 32
2.9 3-D FEA model of rectangular coils. 34
2.10 Experimental set-up (a) hardware prototype, and (b) pick-up coil. 34
2.11 Distribution of (a) B_x and (b) B_z along x-direction at $y = 0$ and $z = 2$ cm. 37
2.12 Distribution of (a) B_y and (b) B_z along y-direction at $x = 0$ and $z = 2$ cm. 38
2.13 Mutual inductance variation in z-direction without shielding. 38
2.14 Mutual inductance variation for angular misalignment. 39
2.15 Mutual inductance variation for planar misalignment at $z = 10.25$ cm 39
2.16 Mutual inductance variation for horizontal misalignment at $z = 1.35$ cm. 39
2.17 Mutual inductance variation for both angular and horizontal misalignment. 40
2.18 Mutual inductance variation for both planar and horizontal misalignment. 40

3.1 3D illustration of contactless coils with its regions. 45
3.2 Schematic cross section of the coil system shown in Fig. 3.1 46
3.3 WPT system having (a) an actual coils, and (b) equivalent circuit model of contactless coils (where V_p is the high frequency AC source, I_p is the primary current, L_s and L_s are the self-inductances of primary and secondary side respectively, V_s is the open circuit voltage of secondary side, and M is the mutual inductance). 46
3.4 xz face of rectangular coil 50
3.5 Schematic of studied variations (a) vertical variation (VV), (b) planar misalignment, (c) angular misalignment, (d) horizontal misalignment, (e) planar with horizontal misalignment and (f) angular with horizontal misalignment. 53
3.6 Magnetic flux lines (a) without shielding and (b) with shielding. 55
3.7 3-D FEM model of rectangular coils. 55
3.8 Experimental set-up (a) hardware prototype, (b) pick-up coil and (c) magnetic shield. 56
3.9 Magnetic field distribution of B_z along x-direction at $y = 0$ and $z = 2$ cm (a) without shielding and (b) with shielding. 56

3.10 Magnetic field distribution of B_z along y-direction at $x = 0$ and $z = 2$ cm (a) without shielding (b) with shielding and. 56

3.11 Magnetic field distribution of B_x along x-direction at $y = 0$ and $z = 2$ cm (a) without shielding and (b) with shielding. 57

3.12 Magnetic field distribution of B_y along x-direction at $x = 0$ and $z = 2$ cm (a) without shielding and (b) with shielding. 57

3.13 Mutual inductance variation in z-direction (a) without shielding and (b) with shielding. 58

3.14 Mutual inductance variation for angular misalignment (a) without shielding and (b) with shielding. 58

3.15 Mutual inductance variation for planar misalignment at $z = 10.25$ cm (a) without shielding and (b) with shielding. 59

3.16 Mutual inductance variation for horizontal misalignment at $z = 1.35$ cm. (a) without shielding and (b) with shielding. 60

3.17 Mutual inductance variation for both angular and horizontal misalignment. (a) without shielding and (b) with shielding. 60

3.18 Mutual inductance variation for both planar and horizontal misalignment. (a) without shielding and (b) with shielding. 60

4.1 (a) 3-D illustration of the coil system (Shields 1 and 2 have finite dimensions and finite permeability). (b) An equivalent circuit model of the coil system (Here, V_p and I_p are the high-frequency voltage source and primary current, respectively. L_p and L_s are the self-inductances of the primary and secondary coils, and M is the mutual inductance between these coils. V_s is the open-circuit voltage of the secondary coil. The primary coil generates the high-frequency magnetic field through I_p, and the secondary coil receives these magnetic fields to generate the voltage V_s). 66

4.2 Steps involved in creating the 2-D subdomain model. 68

4.3 xz-face of the coil system. 69

4.4 Co-ordinate representation of different regions demonstrated in Fig. 4.3. 69
4.5 Illustration of the interface conditions by continuity of (a) magnetic field intensity and (b) magnetic vector potential at $z=z'$, and continuity of (c) magnetic field intensity and (d) magnetic vector potential at $x=x'$. 75
4.6 2-D flux distribution of the practical coil system in xz-plane (a) without shift and (b) with 40mm horizontal shift of the secondary coil arrangement. 81
4.7 Distribution of (a) B_x and (b) B_z along Path 1. 81
4.8 Distribution of (a) B_x and (b) B_z along Path 1 with 40mm horizontal shift of the secondary coil arrangement. 82
4.9 B_x distribution, along the x-direction, on the center of (a) Shield 1 and (b) Shield 2. . 82
4.10 B_x distribution, along the x-direction with 40mm horizontal shift of the secondary coil arrangement, on the center of (a) Shield 1 and (b) Shield 2. 83
4.11 Magnetic field density distribution of B_z on Path 1, obtained from 2-D subdomain model and 3-D FEA (a) without shift and (b) with 40 mm shift of the secondary coil arrangement. 83
4.12 3-D FEA model of coil system. 84
4.13 Distribution of B_z on Path 3 using (25) and 3-D FEA. 84
4.14 Top view of coil. 84
4.15 Result of G_{μ_r} at different μ_r. 86
4.16 Results of $f_{xz}(x, y, z)$ along (a) Path 2 and (b) Path 3. 86
4.17 Prediction of B_z distribution (on Path 2) for the considered coil system using (4.63) and 3-D FEA. 86
4.18 Prediction of B_z distribution (on Path 2) for the coil system whose dimension is half of the considered coil system using (4.63) and 3-D FEA. 86
4.19 Prediction of B_z distribution (on Path 2) for the coil system whose dimension is two times of the considered coil system using (4.63) and 3-D FEA. 87
4.20 Prediction of B_z distribution (on Path 2) for the square coil system whose length is x5-x2 using (4.63) and 3-D FEA. 87

4.21 Development of 3-D subdomain model form 2-D subdomain models. 87
4.22 (a) Experimental setup. (b) Pick-up coil. (c) Magnetic shield. 89
4.23 Distributions of B_x and B_z shown in (a) and (b), respectively, along Path 2. Distributions of B_x and B_z shown in (c) and (d), respectively, along Path 3. The coils are perfectly aligned at z_m = 13.89 mm. 90
4.24 Mutual inductance variation in the (a) *x*-direction , (b) *y*-direction, and (c) *z*-direction. 91

5.1 (a) Block diagram of the SP compensated WPT system for the coil system (b) without a magnetic shield, and (c) with magnetic shields. 96
5.2 Equivalent circuit model of the SP compensated WPT system. 96
5.3 Impedance of the SP compensated WPT system seen by the source. 96
5.4 Flowchart presenting procedure of proposed analytical model. 101
5.5 (a) Experimental setup and (b) Measurement connections of the electrical parameters with considered misalignments. 102
5.6 Waveforms at z = 20.15 mm for (a) primary voltage, (b) primary current, (c) load voltage, and (d) load current. 103
5.7 The variation in total impedance during (a) VV, (b) AM, (c) HM, (d) AHM (e) PHM. 104
5.8 (a)-(b) and (c)-(d) are the current and voltage variation w.r.t. VV and AM, respectively. 105
5.9 (a)-(b) and (c)-(d) are the current and voltage variation w.r.t. HM and AHM, respectively. 105
5.10 (a) Current and (b) voltage variation for PHM. 106
5.11 (a) Representation of VV, (b) primary power, (c) output power and, (d) compensated coil efficiency. 106
5.12 Variation in, (a) input reactive power and, (b) power factor for vertical variation. . . 107
5.13 At z = 108.40 mm (a) Representation of AM, (b) primary power, (c) output power and, (d) compensated coil efficiency. 108

5.14 Variation in, (a) primary reactive power and (b) power factor for angular misalignments. . . . 108
5.15 At z = 20.15 mm (a) Representation of HM, (b) primary power, (c) output power and, (d) compensated coil efficiency. . . . 109
5.16 Variation in (a) primary reactive power, (b) power factor for horizontal misalignments. 109
5.17 At an angle of 10.17° and z = 39.06 mm (a) Representation of AHM, (b) primary power, (c) output power and, (d) compensated coil efficiency. . . . 110
5.18 Variation in (a) input reactive power and (b) power factor for AHM variation. . . . 110
5.19 At an angle of 8° and z = 26.40 mm (a) Representation of PHM, (b) primary power, (c) output power and, (d) compensated coil efficiency. . . . 111
5.20 Variation in (a) primary reactive primary power and (b) power factor for PHM variation. . . . 111
5.21 Self-inductance variation w.r.t. VV and HM. . . . 112
5.22 Variation in electrical parameter w.r.t. VV. . . . 112
5.23 Variation in electrical parameter w.r.t. horizontal misalignments. . . . 113

A.1 Generalized coil position. . . . 122

B.1 Illustration of boundary condition at z=z_2. . . . 126
B.2 Illustration of boundary condition at z=z_3. . . . 126
B.3 Illustration of boundary condition at z=z_4. . . . 127
B.4 Illustration of boundary condition at z=z_5. . . . 128
B.5 Illustration of boundary condition at z=z_6. . . . 128
B.6 Illustration of boundary condition at z=z_7. . . . 129
B.7 Illustration of boundary condition at x=x_2. . . . 130
B.8 Illustration of boundary condition at x=x_3. . . . 130
B.9 Illustration of boundary condition at x=x_4. . . . 131
B.10 Illustration of boundary condition at x=x_5. . . . 132

B.11 Illustration of divided regions with applied boundary condition (a) case 1, (c) case 2, (d) case 3, (b) cse 4, and (e) case 5. 133

B.12 case 1 where Az is applied at all edge a region and principle of superposition. (a) (b) (c) (d) (e) 135

List of Tables

1.1 Comparison of Magnetic Field Modelling techniques 8

2.1 Parameters of the coil system and analytical model 23

2.2 Specification for FEA Simulation 34

3.1 Design parameters for WPT system 47

3.2 Comparison of the primary self-inductance (L_p) 61

3.3 Comparison of Angular, Planar, and Horizontal Misalignment Results with [1] 62

4.1 Parameters of the Coil System and Subdomain Model 70

5.1 Experimental parameters of the SP compensated WPT system 100

List of Acronyms

2-D	Two dimensional
3-D	Three dimensional
AM	Angular Misalignment
AHM	Angular with Horizontal Misalignment
EV	Electric vehicle
FEA	Finite element analysis
FDM	finite difference method
HM	Harmonic Method
MEC	Magnetic Equivalent Circuit
MoM	Method of moments
PM	Planar Misalignment
PHM	Planar with Horizontal Misalignment
SP	Series parallel
SS	Series-series
VV	Vertical Variation
WPT	Wireless power transfer

List of Symbols

$\mathbf{A}$	Magnetic vector potential
A_x	Magnetic vector potential in the x-direction
A_y	Magnetic vector potential in the y-direction
A_z	Magnetic vector potential in the z-direction
$\mathbf{B}$	Magnetic flux density
B_x	Magnetic flux density in the x-direction
B_y	Magnetic flux density in the y-direction
B_z	Magnetic flux density in the y-direction
$\mathbf{H}$	Magnetic field strength
H_x	Magnetic field strength
H_y	Magnetic field strength
H_z	Magnetic field strength
φ	Magnetic scalar potential
$\nabla\times$	Curl operator
∇	Gradient operator
$\times$	Cross product
μ_0	Magnetic permeability of vacuum
μ_r	Relative magnetic permeability
μ	Magnetic permeability of a material
x	The Cartesian x-direction
y	The Cartesian y-direction
z	The Cartesian z-direction

1

Introduction

Contents

1.1 Introduction 2
1.2 Literature Review 3
1.3 Research Motivation 8
1.4 Aim of the thesis 9
1.5 Thesis Contribution 10
1.6 Thesis Overview 11

1.1 Introduction

Wireless power transfer (WPT) system is widely used in many applications such as consumer electronics, medical devices, rotating systems, and DC microgrids due to the advantages of high convenience, safety, and high reliability [2–15]. In recent years, WPT systems are also being used for charging electric vehicle (EV) batteries [16–37].

In the WPT system, power is transferred by the magnetic field created by the primary coil (transmitter) and coupled to secondary coil (receiver) through the air medium. The transferred power and efficiency of the WPT system depend on the magnetic coupling between the coils [38–43]. The magnetic coupling depends on the flux linkage, and the alignment of the secondary coil [44, 45], which is determined with mutual inductance. Therefore, the mutual inductance becomes very sensitive to the relative position between the coils [46]. The change in the mutual inductance impacts the power transfer capability, and the efficiency of the entire system [47, 48]. Hence, for designing a WPT system for the EV charging, robust modelling of the coil system is required.

Moreover, in the WPT system with the air-core coils, large leakage flux results in reduced mutual coupling. Usually, the ferrite core (Magnetic shield) is used in both primary and secondary coils to increase the mutual coupling and minimize the exposure of the magnetic field with the other components installed nearby [49]. Hence, the primary and secondary coils with the ferrite core (coil system) are preferred. The focus of this thesis is on developing analytical models for different coil systems (with magnetic shield and without magnetic shield) of the WPT systems that can give understanding to the working of the system and are computationally less intensive.

The inductively coupled WPT system is typically used for EV charging. It consists of two subsystems, as shown in Fig. 1.1. One subsystem is under the ground, and it is used to transfer the power. It includes a power supply, H-bridge inverter, a primary capacitor bank, and the primary coil (transmitter). The other subsystem is underneath the vehicle, and it consists of a secondary coil (receiver), secondary capacitor bank, high-frequency ac-dc converter, and electric load (battery). The primary coil creates the high-frequency time-varying magnetic field from high-frequency ac current. This magnetic field links with the secondary coil and induces a voltage across that secondary coil.

H-bridge inverter is used to generate the high-frequency ac signal. A compensating capacitor is connected at the primary and secondary side, respectively, to reduce the VA rating of the wireless power transfer system. This capacitor can be connected either in series or parallel with the coils.

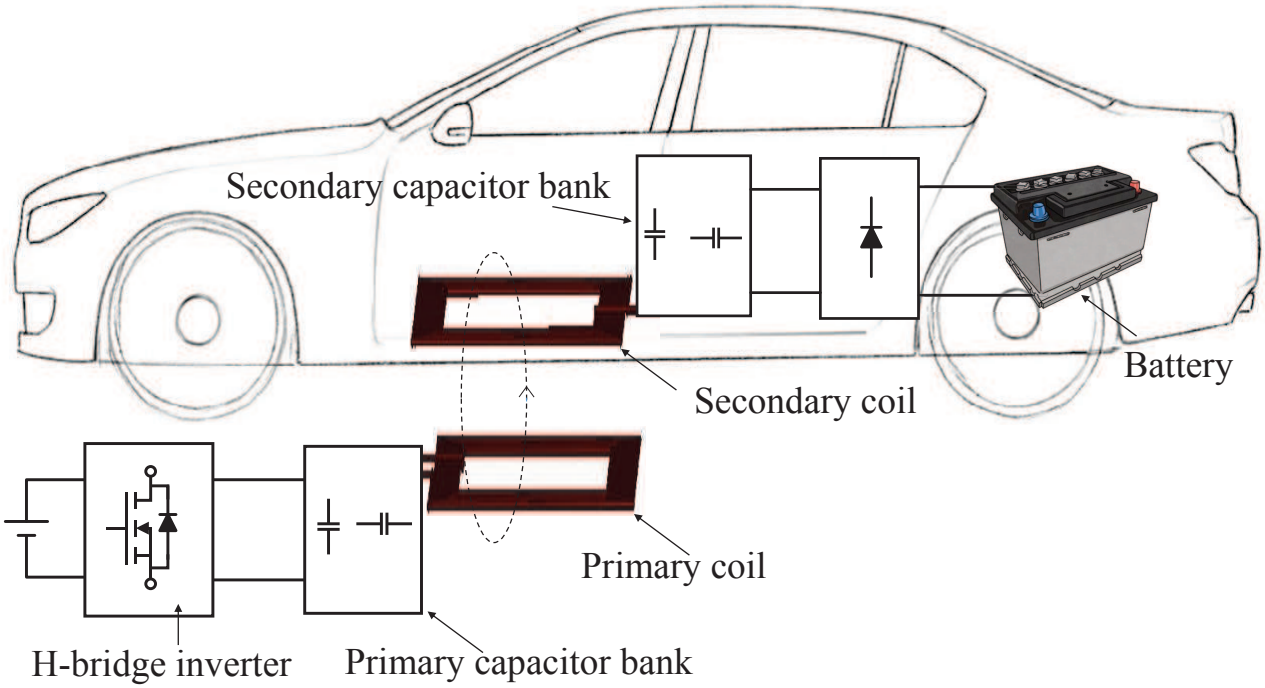

Figure 1.1: Block diagram of inductively coupled WPT system.

1.2 Literature Review

The WPT system is divided into two categories: near field and far-field technique. The far-field power technology includes microwave power transfer [50–52] or radio wave power transfer [53] and laser power transfer [54–56]. The far-field power transfer technology suffers from lower efficiency [57]. The other is near field transmission, which is further classified as inductive power transfer and capacitive power transfer.

In the capacitive power transfer system, power is transferred from source to electrical load through the electric field [58, 59]. Here, the transferred power depends on the value of the capacitance system. For higher output power, the capacitance value should be very high, which requires a large area of the capacitor plate. The requirement of the larger capacitor plate is undesirable for practical implementation. Moreover, the capacitance value is inversely proportional to the air-gap length [60]. Therefore,

the larger the capacitive power transfer is suitable for the minimal distance (less than 1 mm), whereas inductive power transfers are suitable for air gap distance between the coils greater than 1 mm [61]. Apart from this, for the same power level, inductive power transfer is safer as compared to capacitive power transfer [62]. Therefore inductive coupling is more widely used in the WPT system for EV charging.

Since, in the WPT systems, the power is transferred from the source to the electrical load via electromagnetic induction. Therefore, the accurate magnetic field modelling is an essential part of designing of WPT system. This section studies the available possible magnetic modelling method, which can be applied to the WPT system. The possible methods are shown in Fig. 1.2.

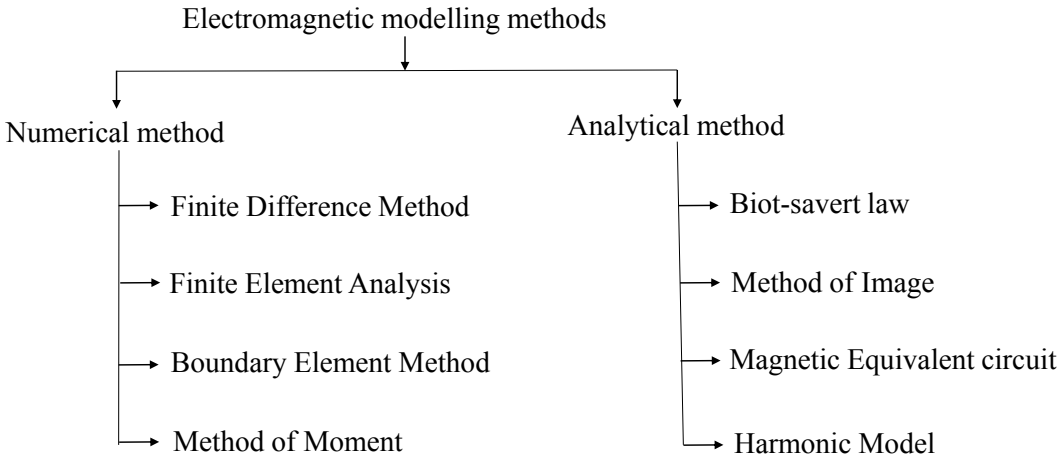

Figure 1.2: Classification of available methods to model a coil system

1.2.1 Numerical Method

The numerical methods are the most accurate methods to describes the magnetic field of considered magnetic domain. These methods discretize the geometry of the magnetic domain. The most promising used numerical methods include the finite difference method (FDM), finite element analysis(FEA), and method of moments (MoM).

1.2.1.1 Finite Difference Method (FDM)

The finite difference method is one of the oldest numerical methods used in solving the magnetic problem. In this modelling technique, the whole magnetic system is discretized into a grid of lines. The intersection of points called grid points of nodes, as shown in Fig. 1.3, then a set of linear

algebraic equations (difference equations) on grid points are obtained using differential equations [63]. The disadvantage of this method is that the regular grid does not confirm to have a grid point at the interface of different media. This can be overcome by using finer grid lines, but it requires greater computation time.

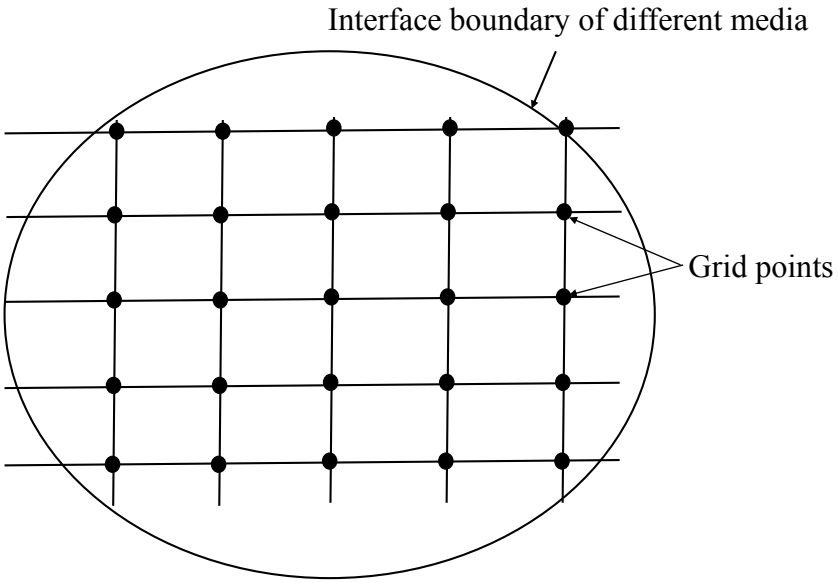

Figure 1.3: Division of magnetic problem into grid points.

1.2.1.2 Finite Element Analysis (FEA)

The 3-D finite element analysis is another numerical method, which is commonly used in modelling. Similar to the finite difference method, the finite element analysis is used to solve differential equations. In the finite difference method due to the constant grid point, it is not suitable for the magnetic problem, which has irregular boundary shaped boundaries [63]. The magnetic problem with such types of boundaries is easily solved using FEA [63]. This method discretizes the magnetic problem into the mesh elements, as shown in Fig. 1.4. The mesh elements are the generally triangular shape for the 2-D problem and a tetrahedral shape for a 3-D problem. The mesh should be such a size that magnetic field variation in mesh element can be assumed linear. Therefore, the accuracy of the obtained magnetic field depends on the size of the mesh. For more accuracy, the size of the mesh should be smaller, which results in a larger number of mesh elements in the magnetic problem. The computational time increases with the increase in the number of mesh element. Therefore to get accurate results, this method requires computational time. The FEA model of the magnetic problem with

a magnetic shield requires even more computational time due to its multiphysics structure. When the meshing is done at only the boundaries, it is called a boundary element method (BEM).

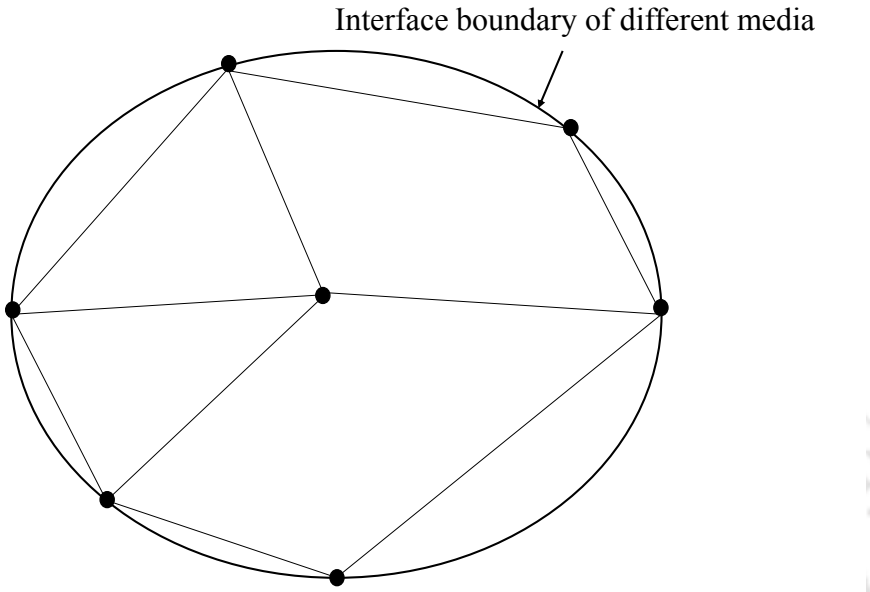

Figure 1.4: Division of magnetic problem into different mesh.

1.2.1.3 The Moment Method (MoM)

The FDM and FEA are used for solving the differential equation, whereas the moment method is used for solving integral equations. The method of the moment offers a progressively smaller computational domain, due to the use of integral formulation. This method has lesser computation time as compared to FEM or FDM. The major drawback of this technique is an increase in implementation complexity.

1.2.2 Analytical Method

Numerical methods do not offer an intuitive understanding of the effect of geometrical parameters on WPT system performance. Therefore, the numerical method is not suitable for the designing of the WPT system.

1.2.2.1 Biot Savert Law

The Biot Savert law is commonly used to calculate the magnetic field of a coil. The Biot Savert law is a specific solution of Greens function. The Biot Savert law is applicable when coils are surrounded by air. When the distance between the point of interest and coil is very large as compared to the thickness of turn, then the magnetic field at the point can be calculated by assuming turns of the coil

as current-carrying segments [60, 64, 65]. Then the magnetic field due to each segment is added to get the magnetic field due to coil. In case when the thickness of the turn is comparable to the point of interest, then the filament method is used. In the filament method, turns of coils are considered as an enclosed volume, which is divided into a finite number of filaments. The total current is equally distributed in each filament [60]. The biot Savert law is not applicable to the magnetic problem where high permeable material is present. For this situation, the method of the image is used [66]. But the magnetic problem which involves multiple boundaries the method of the image is not convenient [67].

1.2.2.2 Magnetic Equivalent Circuit (MEC)

The magnetic equivalent circuit is one of the widely used modelling methods to calculate magnetic field in the magnetic system [68]. In this method, the whole magnetic system is divided into small flux tubes, which forms a network of magnetic reluctance [69, 70]. The general definition of a flux tube is shown in Fig.1.5. The magnetic reluctance $\mathfrak{R}$ is given by-

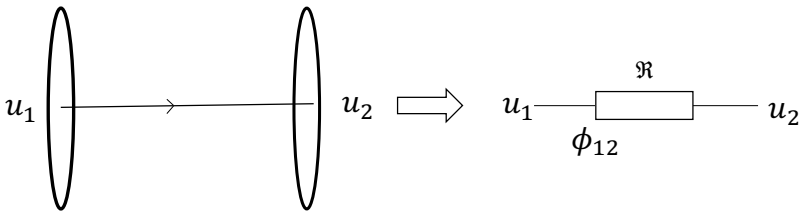

Figure 1.5: Geometric definition of a flux tube and its representation.

$$\mathfrak{R} = \frac{u_1 - u_2}{\phi_{12}} \tag{1.1}$$

where, $u_1 - u_2$ is the potential difference across the flux tube and ϕ_{12} is the magnetic flux flowing through flux tube. The network of magnetic reluctance is obtained in two ways either by meshing the system into small domains [70] or with the knowledge of the predefined path of the magnetic field [**?**]. With the meshing, no prior knowledge of magnetic flux is required, but it increases the computational effort, makes it less suitable for the design process. The magnetic equivalence of Kirchoff's current law or the equivalence of Kirchoff's voltage law is used to solve the obtained magnetic network [71].

1.2.2.3 Harmonic Method (HM)

For the modelling, a 3- D electromechanical system using the harmonic method needs periodicity in the two directions. The implementation of the harmonic method is suitable when all the divided re-

gion is equal-sized to the periodicity [72]. However, some researcher has modified harmonic method to include material smaller than the periodicity, called as mode-matching technique [72–76]. In the harmonic modelling method, the whole domain is divided into regions along the non-periodic direction based on their material property. Then Poisson's or Laplace equation using separation of the variable method is solved in each region. The solution of magnetic potential can be written as a Fourier series.

The features of various modelling techniques of the magnetic field are presented in 1.1

Table 1.1: Comparison of Magnetic Field Modelling techniques

Method	Characteristics
Finite Difference Method	Less suitable for curvillinear boundaries High computational time High accuracy
Finite Element Analysis	Suitable for curvillinear boundaries High computational time High accuracy
Moment Method	Suitable for curvillinear boundaries Less computational time compared to FDM an FEA High accuracy
Biot Savert Law	Straight forward procedure [77] Elliptical integrals should be solved for complicated geometries [78] Applicable to only coil system surrounded by air [60]
Method of the image	Suitable when finite permeable material present in the neighborhood of a coil [60] For multiple boundaries, infinite number of images need to be present [69]
Magnetic Equivalent Circuit	Suitable only for small air-gap with ferromagnetic structure around the coils Not suitable for coils surrounded by air [60] More computational time
Schwartz Christoffel Mapping	Limited to 2D problems [69] Considers infinite permeability of magnetic material More computational time
Harmonic Method	Able to model the coils surrounded by air Able to model the coils having magnetic shield nearby

1.3 Research Motivation

Accurate modelling is an integral part of designing the coil system of the WPT system. Generally, the 3-D finite element analysis (FEA) is used to design a coil system because of its high accuracy.

However, high mesh-density in the 3-D FEA model requires intensive computational power [79, 80]. This computational power increases further according to the increase in the dimensions of the coil system [80]. The iterative design process requires numerous modifications in the 3-D FEA model to achieve the desired coil system, which is a tedious process.

An analytical model is another approach to design the coil system. Here, any modifications in the design of the coil system can easily be incorporated for irrespective dimensions of the coil system without change in computational power. Moreover, the analytical model gives a better understanding of the fundamental physics of the coil system [81,82]. Hence, the analytical model is convenient in the initial designing and optimization of the coil system. Nevertheless, the analytical models are problem-specific and involve geometrical and physical assumptions that highly influence the calculated results [83].

1.4 Aim of the thesis

In literature, many analytical studies have been done to calculate the mutual inductance for the rectangular and square type geometry considering different misalignments [1, 84–87]. Though these studies have analyzed different misalignments of the coil, the magnetic shielding effect has not been included in the analysis. However, Some literature has presented an analytical model to calculate the mutual inductance and magnetic flux density distribution by considering a magnetic shield with a relative permeability of infinite value [77, 88, 89]. The analytical model with the assumption of infinite permeability does not give the effect of a finite permeable shield, which is practically used. Practically a magnetic shielding used in the WPT system has finite permeability and dimension.

By considering the contributions made in literature, the aim of this thesis to present an analytical model for the coil system having magnetic shields of finite permeability and dimension. The analytical model should be able to describe the magnetic field in the coil system accurately. Moreover, the proposed model should be able to model the various geometrical variation in the coil system having magnetic shields. The ability to adapt the change in geometrical parameters makes the analytical model suitable for designing of WPT system.

1.5 Thesis Contribution

This thesis presents an analytical model (Electromagnetic model) for the coil system having magnetic shields of finite permeability and dimension. For this, modelling of the coil system without shields is developed at first. In the next step, magnetic shielding of finite permeability and infinite length is included in the modelling. After this, the modelling for the coil system having the magnetic shield of finite permeability and finite dimension has been presented. The presented electromagnetic models accurately described the magnetic field for the coil system. Furthermore, to analyze the impact of change in mutual inductance of electrical parameters of the WPT system, a steady-state model also has been developed. The contributions of this thesis are:

- Detailed 3-D analytical models to predict magnetic field distribution in the air gap and mutual inductance between the coils for the coil system shown in Figs. 1.6- 4.1(a) have been developed. To develop the analytical model for the coil system shown in Figs. 1.6 and 1.7, the harmonic modelling technique is used. Whereas, for the coil system shown in Figs. 4.1(a), the sub-domain technique is used.

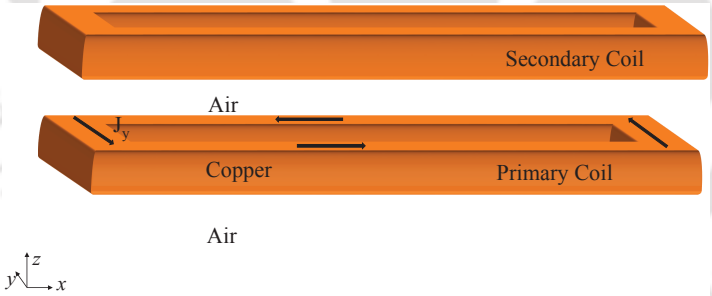

Figure 1.6: 3D illustration of coil system without magnetic shield.

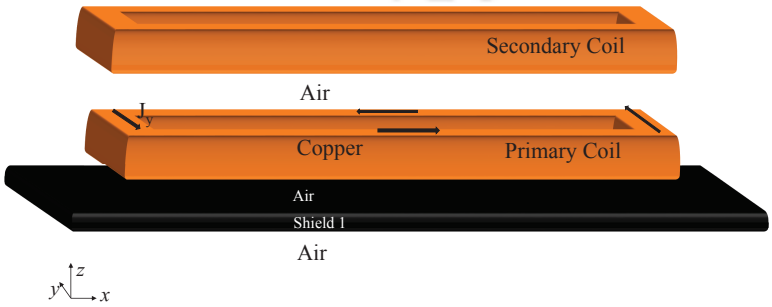

Figure 1.7: 3D illustration of coil system having magnetic shield of finite permeability and infinite length.

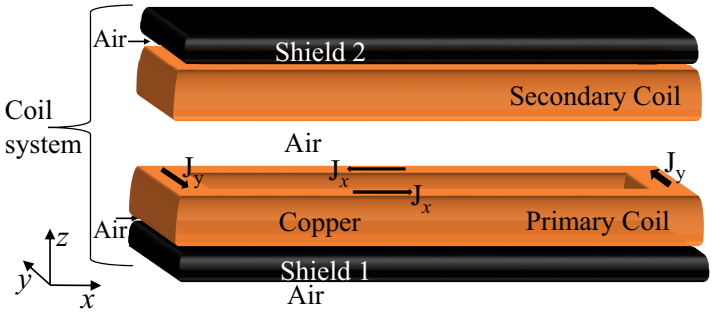

Figure 1.8: 3D illustration of coil system having magnetic shield of finite permeability and finite length.

- The 3-D FEA models for the coil system shown in Figs. 1.6- 4.1(a) is also developed, and the results of the FEA model and analytical model are compared.
- The variation in mutual inductance for the different misalignments are studied.
- Examines the variation in electrical parameter for Series-Parallel compensated WPT system during misalignments.
- The analytical results are verified with 3-D FEA model and measurement results.

1.6 Thesis Overview

The thesis contributions described above are presented in different chapters. A brief description of these chapters is as follows:

- **Chapter 1** gives a general introduction of the wireless power transfer system, advantages, and applications in different areas. The working principle of the WPT system has been discussed. It also describes the problem statement and the motivation behind the work.
- **Chapter 2** This presents a 3-D analytical model to describe the magnetic field distribution in the air gap between the coils for the WPT system. For the modelling 3-D magnetic vector potential and magnetic scalar potential have been defined. To include coil as a magnetic field source in the modelling it has been considered as four overlapping bars, and Fourier series is used to define the current density distribution in the coil. The developed analytical model is applied to calculate mutual inductance for different misalignments, which usually occurs during EVs battery charging. Moreover, two new expressions are derived for the calculation of

the mutual inductance between the coils for different misalignments, which makes the initial designing of the WPT system faster. The results of the 3-D analytical model are compared with the simulation and the measurement results, and a good agreement has been found.

- **Chapter 3** In the WPT system with air-core coils large leakage flux occurs, which is reduced with the inclusion of high permeable material (magnetic shield). Many researchers have modeled a magnetic shield with the assumption of infinite permeability. The analytical model with the assumption of infinite permeability does not give the effect of a finite permeable shield, which is practically used. To deal with this problem this chapter presents a 3-D analytical model using a harmonic modelling technique which includes a magnetic shield with finite permeability.This model has the flexibility to change the width and permeability of shielding material. A comparison in mutual inductance for coil system with shield and without shield also has been made. The results of the mutual inductance and magnetic field distribution obtained from analytical and finite element simulation modelling are compared with the experiment, and good agreement is found.

- **Chapter 4** The previous chapter presents an analytical model for the coil system having magnetic shielding of finite permeability, but the length of the magnetic shield assumed infinite. This chapter presents a 2-D analytical model using the subdomain technique to incorporate the finite dimension of the magnetic shields. This subdomain model incorporates magnetic shields of finite dimension and finite permeability. To get tangible results, a 3-D subdomain model is developed using the superposition of two 2-D subdomain models. These 2-D subdomain models are developed for *xz*- and *yz*-planes, which are invariant in their third direction (i.e., in the y-direction for *xz*-plane and the x-direction in *yz*-plane). In this context, a correction factor for 2-D subdomain model is introduced to make it variant in their third direction. The proposed 3-D subdomain model can incorporate any changes in the parameters of magnetic shielding such as length, width, and relative permeability. Moreover, with the proposed subdomain model, square and rectangular coil system of any dimensions can be designed and analyzed. The comparison in magnetic field distribution obtained from the 2-D subdomain model and 2-D FEA has been

made. The magnetic field distributions obtained from the 2-D subdomain model coincide with the magnetic field obtained from 2-D FEA, which confirms the accuracy of the 2-D subdomain model. Moreover, The mutual inductances obtained for the vertical and horizontal misalignments from the 3-D subdomain model are compared with those obtained from 3-D FEA and measurements. The obtained results are in close agreement, which confirms the accuracy of the 3-D subdomain model.

- **Chapter 5** The change in the mutual inductance between the coils impacts the power transfer capability and the efficiency of the entire WPT system. This chapter presents a steady-state model to investigate the variation in electrical parameters of the SP compensated WPT system during different misalignments. The mutual inductances calculated from the analytical model presented in chapter 2 and 4 are used as input to the steady-state model. In order to get an accurate result, the effect of the harmonics is considered in the steady-state model. This model can be used to analyze the component stress of SP compensated WPT system. The results of the steady-state model are verified experimentally. Thus, the proposed method can be adopted in the initial design process of SP compensated WPT system.

- **Chapter 6** presents the conclusive remark based on the work presented in the previous chapters. All the findings have been highlighted. Further, the future work for extending the research also has been outlined.

भारतीय प्रौद्योगिकी संस्थान गुवाहाटी
Indian Institute of Technology Guwahati

2

3-D Analytical Model for Computation of Mutual Inductance for Different Misalignment in Wireless Power Transfer System

Contents

2.1 Introduction 16
2.2 Analytical Model 18
2.3 Possible Misalignments 30
2.4 Mutual Inductance Calculation 31
2.5 Verification of Analytical Model 33
2.6 Summary 40

2.1 Introduction

In the WPT system, the transferred energy depends on the amount of magnetic flux linked to the secondary coil. Accurate knowledge about the magnetic field distribution of the coils is required to model the mutual flux. The possible modelling methods which can be used to calculate the magnetic field for the coil system shown in Fig. 2.2 are classified as numerical and analytical methods. Fig. 2.1 shows the classification of available modelling methods.

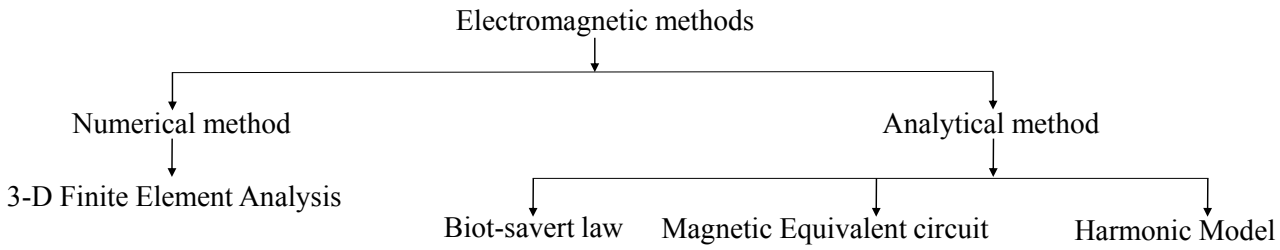

Figure 2.1: Classification of available methods to model coil system shown in Fig. 2.2.

The 3-D finite element analysis (FEA) is the most commonly used numerical method to design such a coil system because of its high accuracy. The method divides the coil system into mesh elements. The high mesh-density in the 3-D FEA model requires intensive computational power [79, 80, 90]. This computational power increases further according to the increase in the dimensions of the coil system [80]. To achieve the desired coil system, the iterative design process requires numerous modifications in the 3-D FEA model, which is a tedious process. Moreover, it unable to give an insight into the effect of geometrical parameters on WPT system performance.

The analytical model is another approach to design the coil system. Here, any modifications in the design of the coil system can be easily included irrespective of the dimensions of the coil system without change in computational power. Moreover, the analytical model gives a better understanding of the fundamental physics of the coil system [81, 82]. Hence, the analytical model is more convenient in the initial designing and optimization of the coil system. Nevertheless, the analytical models are problem-specific and involve geometrical and physical assumptions that highly influence the calculated results [83].

The Biot-Savart law is the is most commonly used analytical model to calculate the magnetic

field for the coil system shown in Fig. 2.2. It gives a direct solution of magnetic flux density. In this analytical modelling magnetic field at a point is calculated for to the current flowing in the finite length conductor. The turns of the coil are represented as current-carrying bars to model the coil system. The total magnetic field due to the coil can be calculated by superposition of magnetic flux obtained by each bar. The Biot-Savart law is applied only for the coil system where the magnetic shield is absent.

The Magnetic Equivalent Circuit (MEC) method uses Ampere's circuit law and Gauss' law for the calculation of magnetic field density in the coil system. The method is applicable for the coil system, having a very small air gap and should have ferromagnetic material around coils. Therefore, MEC is not suitable for the modelling shown in Fig. 2.2.

The harmonic model is another method to calculate magnetic field density for the coil system shown in Fig. 2.2. In the harmonic modelling method whole domain is divided into different regions based on their material property. The magnetostatic Maxwell ($\nabla \cdot \mathbf{B} = 0$ and $\nabla \times \mathbf{H} = \mathbf{J}$) equations are solved for each region. For the regions with current density, Poisson equation is used whereas for other regions Laplace equation is used [91]. The magnetic field in the region is obtained by solving passion or Laplace equation using separation of variables method, which gives the solution as a product of independent variables can be written as Fourier series [72]. The harmonic modelling method can calculate the magnetic field in the air medium as well as in a finite permeable magnetic material [60]. This model originates from the structures with periodic field distribution like motors. The same is extended to the single-coil systems with assuming that the period of the spatial distribution is large enough to neglect the electromagnetic influence of repeated structure on it [75, 91].

A comparison has been made between different available modelling methods relating to the ability to model the three-dimensional magnetic field of the coils, which can be surrounded by air or having magnetic materials nearby. It is found that the harmonic modelling method can model such a coil system, which includes a magnetic shield. Compare to the harmonics model; the Biot Savert's law can model the coils which are surrounded by air. The MEC modelling method is suitable only for that coil system which has a small air gap between the coils, as well as magnetic materials near the coils, which restrict the possibility to calculate the magnetic field for the coil system surrounded by

air. The FEA model can be used for modelling, but it requires high computation power due to the meshing of the 3D structure of the coil system. The computational power of FEA simulation varies with the dimension of the model. Therefore, FEA is not suited for parametric search compared to an analytical method. The harmonic modelling method is selected to model the coil system shown in Fig. 2.2 because of flexibility and geometrical options.

This chapter presents an analytical model using harmonic modelling method to calculate the magnetic field in the air gap for the coil system having two coils surrounded by the air. The calculated magnetic field is used to determine self-inductance and mutual inductance. These parameters are essential for the design of a wireless power transfer system. Moreover, two new expressions are derived for faster calculation of the mutual inductance between the coils of the WPT system. The proposed model takes into account the variation of mutual inductance due to different misalignments for the air core transmitter and receiver coil system. All possible misalignments that can occur during the charging of EV are considered.

The organization of this chapter is as follows: Section 2.2 presents the system description and the governing equations used to develop the analytical model with assumptions. Section 2.3 describes the possible misalignment between the coils during EV charging. Section 2.5 gives the detail description of the experimental setup and the comparison of the results obtained from the mathematical model, simulation, and experiment. Finally, Section 2.6 discusses the summary of this chapter.

2.2 Analytical Model

The harmonic modelling method is used for developing the 3-D analytical model for the coil system shown in Fig. 2.2. This section presents a detailed discussion about the analytical model in subsequent subsections. This section is organized as follows: Subsection 2.2.1 presents the description of the coil system, and assumption involves in the analytical modelling, then the coil system has been divided into different regions based on their material properties. Further, the differential equations for magnetic vector potential and scalar potential are solved for each region, given in Subsection 2.2.2. These potentials contain various unknown coefficients, which is calculated by applying the interface conditions at the boundaries of each region, presented in subsection 2.2.4.

2.2.1 System Description and Assumptions

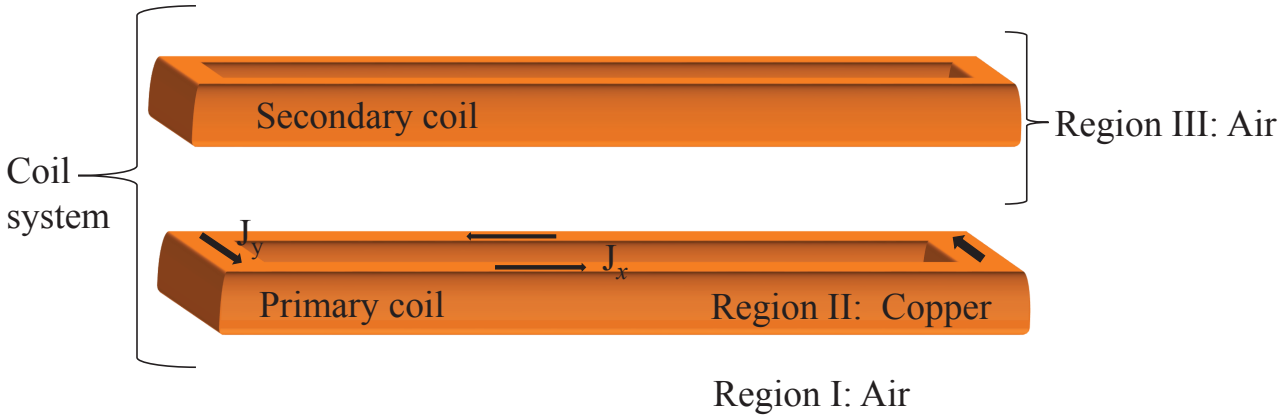

Figure 2.2: 3D illustration of coil system with its regions.

For calculating the magnetic field distribution, the 3-D analytical model for the coil system is derived. In the modelling, the coil system is divided into three different regions along the *z*-direction, as shown in Fig. 2.2. The areas below and above the primary coil is named as Region I and Region III, respectively. The primary coil, which is the current-carrying region, is denoted as Region II. Here, the mutual inductance is calculated using the open circuit method, that is no current flows through the secondary coil. Hence, the secondary coil is included in Region III. The parameters of the coil system necessary for the analytical model are listed in Table 2.1. These parameters have been chosen as an example to verify the analytical model; however, one can use this analytical model for different dimensions of the rectangular coils.

The modelling has been done in the 3-D Cartesian coordinate system. The magnetic field calculated from the proposed model considers the following assumptions:

- In the harmonic model, the solution of magnetic potentials is written as a Fourier series. Thus, to model a single coil using the Fourier series, a periodic structure in *x*- and *y*-direction with a period of τ_x and τ_y, respectively is assumed. However, the system has only one primary coil which is physically present and named as a working coil. The coils which are used to make the structure periodic are physically absent and are named as fictitious coil, as shown in Fig.2.3. The repetition of the fictitious coils is assumed large enough to ensure the interference of the magnetic field produced by the fictitious coil on the working coil is negligible.

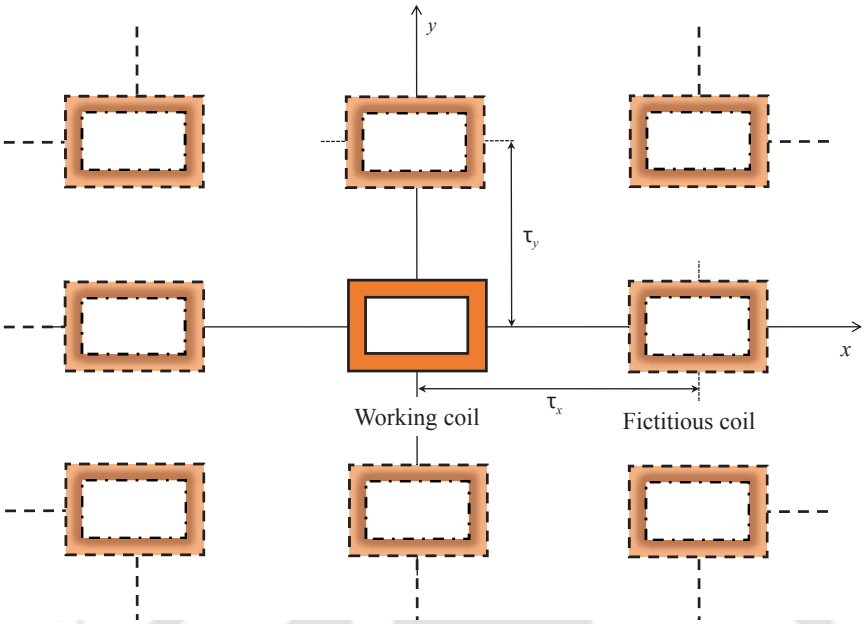

Figure 2.3: Arrangement of coils

- The quantities which are temperature-dependent such as resistance of the primary coil is neglected in magnetic modelling.
- The material properties of a medium are linear, homogeneous and isotropic.
- No current exists in the z - direction.

This subsection described the coil system with assigned regions and assumptions involved during the analytical modelling. After assigning different regions to the coil system, for calculating the magnetic field, either magnetic vector potential or scalar potential needs to be solved. The next subsection discusses magnetic vector potential, scalar potential, and its governing equations.

2.2.2 Solution of the magnetic vector potential and scalar potential

The coil system is divided into various regions to calculate magnetic field density using the proposed modelling method. The magnetic vector potential or scalar potential is used to calculate the magnetic field in each region. These potentials are described in the subsequent section. Sub-sub section 2.2.2.1 presents the solution of the magnetic vector potential, whereas magnetic scalar potential is explained in sub-sub section 2.2.2.2.

2.2.2.1 Magnetic vector potential in coil

The magnetostatic Maxwell equations are used for the derivation of the equations, which is given as-

$$\nabla \times \mathbf{H} = \mathbf{J}, \tag{2.1}$$

$$\nabla \cdot \mathbf{B} = 0, \tag{2.2}$$

where **H** is the magnetic field strength, **B** is the magnetic flux density, and **J** is the current density vector. Considering the vector calculus identity, the divergence of the curl of any vector field is always zero as

$$\nabla \cdot (\nabla \times \mathbf{G}) = 0, \tag{2.3}$$

where **G** is an arbitrary vector field. From Gauss law for magnetism (2.2) and vector identity (2.3), the magnetic field density can be written as the curl of vector potential [63], given as-

$$\mathbf{B} = \nabla \times \mathbf{A} \tag{2.4}$$

where **A** is the magnetic vector potential. The magnetic vector potential must satisfy the Coulomb Gauge condition, therefore

$$\nabla \cdot \mathbf{A} = 0 \tag{2.5}$$

The Magnetic flux density **B** and the magnetic field intensity **H** are related by (2.6)

$$\mathbf{B} = \mu_0 \mu_r \mathbf{H} \tag{2.6}$$

where μ_0 is the magnetic permeability of vacuum and μ_r relative magnetic permeability of the material. By using (2.1) and (2.6) the magnetic field density **B** can be written in terms of current density as

$$\nabla \times \mathbf{B} = \mu_0 \mu_r \mathbf{J} \tag{2.7}$$

substituting (2.4) into (2.7)

$$\nabla \times (\nabla \times \mathbf{A}) = \mu_0 \mu_r \mathbf{J}, \tag{2.8}$$

and using vector identity

$$\nabla(\nabla.\mathbf{A}) - \mathbf{A}(\nabla.\nabla) = \mu_0\mu_r\mathbf{J}, \tag{2.9}$$

substituting (2.5) in (2.9) reduces to

$$\nabla^2\mathbf{A} = -\mu_0\mu_r\mathbf{J}. \tag{2.10}$$

The (2.10) is known as the Poisson equation. The solution of the magnetic vector potential, which satisfies (2.10), gives valid magnetic field density in the considered domain.

This region represents the current-carrying primary coil. The direction of the magnetic vector potential is along the direction of current density. Here, the current density in the primary coil flow along x and y directions, represented as J_x and J_y, respectively shown in Fig 2.2, where the current density along the z- direction is assumed to be zero. The component form of (2.10) is given as

$$\nabla^2 A_x = -\mu_0\mu_r J_x \tag{2.11}$$

$$\nabla^2 A_y = -\mu_0\mu_r J_y \tag{2.12}$$

$$\nabla^2 A_z = 0. \tag{2.13}$$

where A_x, A_y, and A_z are the magnetic vector potentials in x-, y-, and z-directions. Here, due to the absence of the current in the z-direction, A_z is considered as zero [92]. The current densities $J_x(x, y)$ and $J_y(x, y)$ are discussed in detail in subsection 2.2.3. The differential form of (2.11)-(2.13) is given as

$$\frac{\partial^2 A_x}{\partial x^2} + \frac{\partial^2 A_x}{\partial y^2} + \frac{\partial^2 A_x}{\partial z^2} = -\mu_0\mu_r J_x \tag{2.14}$$

$$\frac{\partial^2 A_y}{\partial x^2} + \frac{\partial^2 A_y}{\partial y^2} + \frac{\partial^2 A_y}{\partial z^2} = -\mu_0\mu_r J_y \tag{2.15}$$

$$\frac{\partial^2 A_z}{\partial x^2} + \frac{\partial^2 A_z}{\partial y^2} + \frac{\partial^2 A_z}{\partial z^2} = 0 \tag{2.16}$$

After solving(2.14)-(2.16) using the separation of variables method, we get the magnetic vector

potential given by (2.17).

$$\begin{aligned} A_x &= -\sum_{n=1,3,5}^{N}\sum_{m=1,3,5}^{M}\left(c_{II_1}e^{k_z z}+d_{II_1}e^{-k_z z}\right)\cos(k_x x)\sin(k_y y)+\frac{\mu_0 J_x(x,y)}{k_z^2} \\ A_y &= \sum_{n=1,3,5}^{N}\sum_{m=1,3,5}^{M}\left(c_{II_2}e^{k_z z}+d_{II_2}e^{-k_z z}\right)\sin(k_x x)\cos(k_y y)+\frac{\mu_0 J_y(x,y)}{k_z^2} \\ A_z &= 0 \end{aligned} \tag{2.17}$$

The magnetic vector potential may also be used to calculate the magnetic field because of the validity of Gauss law magnetism (2.2) in the air medium. But the magnetic vector potential for representing a region of coil system (shown in Fig. 2.2) requires two components and, hence more unknown coefficients. These unknown coefficients need to be known to calculate the magnetic field, and they are obtained by solving the boundary condition. More unknown needs more boundary conditions which increase the complexity of the analytical model. The magnetic scalar potential can be an alternate way to calculate the magnetic field in the domain. The magnetic scalar potential and their governing equation are discussed in the next subsection.

Table 2.1: Parameters of the coil system and analytical model

Parameters	Definition	Value	Unit
a_{1p}	Inner distance of primary coil from centre in x-direction	66.3	mm
a_{2p}	Outer distance of primary coil from centre in x-direction	92.7	mm
b_{1p}	Inner distance of primary coil from centre in y-direction	42.8	mm
b_{2p}	Outer distance of primary coil from centre in y-direction	69.2	mm
a_{2s}	Inner distance of secondary coil from centre in x-direction	92.5	mm
b_{2s}	Outer distance of secondary coil from centre in y-direction	69.0	mm
w	Diameter of the primary and secondary coils	2.5	mm
τ_x	Coil pitch in x-direction	465	mm
τ_y	Coil pitch in y-direction	353.75	mm
J	Current density in the coil	0.713	A-mm^{-2}
N	Harmonics in x- direction	50	
M	Harmonics in y- direction	50	

2.2.2.2 Solution of magnetic scalar potential in air medium

For deriving the magnetic scalar potential from the magnetostatic equations, the current density is assumed to zero. Therefore, Ampere's law (2.1) can be written as

$$\nabla \times \mathbf{H} = 0. \tag{2.18}$$

The vector calculus identity, the curl of the gradient of the scalar field is zero, i.e

$$\nabla \times (\nabla \varphi) = 0, \tag{2.19}$$

where Ψ is a scalar potential. Therefore, the magnetic filed strength can be expressed as the gradient of a scalar potential, given as

$$\mathbf{H} = -\nabla \varphi. \tag{2.20}$$

Here, φ is a magnetic scalar potential. Besides satisfying (2.18) in the region where current is absent, The Gauss law for magnetism (2.2) should also be satisfied. By using (2.6), (2.2) can be written in terms of magnetic field intensity as

$$\nabla \cdot \mathbf{H} = 0. \tag{2.21}$$

With the help of (2.20), (2.21) can be written as

$$-\nabla \cdot (\nabla \varphi) = 0. \tag{2.22}$$

By using vector identity the magnetic scalar potential is given as

$$\nabla^2 \varphi = 0. \tag{2.23}$$

The (2.23) is known as the Laplace equation. The solution of the magnetic scalar potential, which satisfies (2.23), gives valid magnetic field density behaviour in the considered domain. However, this is all under the condition that no current density can exist in the considered region. Therefore, the magnetic scalar potential can be used for the formulation in the region where the current density is absent. Among all the divided regions of the coil system shown in Fig. 2.2, *I* and *III* are the regions

where the current density is absent. Therefore, magnetic scalar potential is used for the formulation in the region *I* and *III*. The Laplace equation for the region *I* and *III* are given in (2.24)-(2.25).

$$\nabla^2 \varphi_I = 0 \tag{2.24}$$

$$\nabla^2 \varphi_{III} = 0 \tag{2.25}$$

By solving (2.24) and (2.25) using separation of variables method, the expression of the magnetic scalar potential for these regions is expressed as

$$\varphi_I = \sum_{n=1,3,5}^{N} \sum_{m=1,3,5}^{M} c_I e^{k_z z} \cos(k_x x) \cos(k_y y) \tag{2.26}$$

$$\varphi_{III} = \sum_{n=1,3,5}^{N} \sum_{m=1,3,5}^{M} c_{III} e^{-k_z z} \cos(k_x x) \cos(k_y y) \tag{2.27}$$

$$k_x = \frac{n\pi}{\tau_x}, \quad k_y = \frac{m\pi}{\tau_y}, \quad \text{and} \quad k_z = \sqrt{\left(\frac{n\pi}{\tau_x}\right)^2 + \left(\frac{m\pi}{\tau_y}\right)^2} \tag{2.28}$$

where, k_x and k_y are the spatial frequencies in the x and y direction with period τ_x and τ_y respectively. The solution of the magnetic scalar potential for region I and III which satisfied the Laplace equation has been given in this subsubsection.

In this subsection, the solution of the magnetic vector potential and scalar potential for different regions derived from the magnetostatic Maxwell equations has been discussed. From (2.17), it can be seen that for the calculation of magnetic vector potential expression, current density distribution should be known. The next subsection gives a detailed description of the current density distribution in the primary coil.

2.2.3 Modelling of the current density distribution

At the four-round corner of the rectangular coil, as shown in Fig. 2.4, the *x* and *y*-components are related to each other, which restricts the application of separation of variables method. To consider the four round corners in the analytical model, the coil can be modeled with different configurations as (1) Non-overlapping bars, (2) Trapezoidal bars, and (3) overlapping bars [60]. Among these ar-

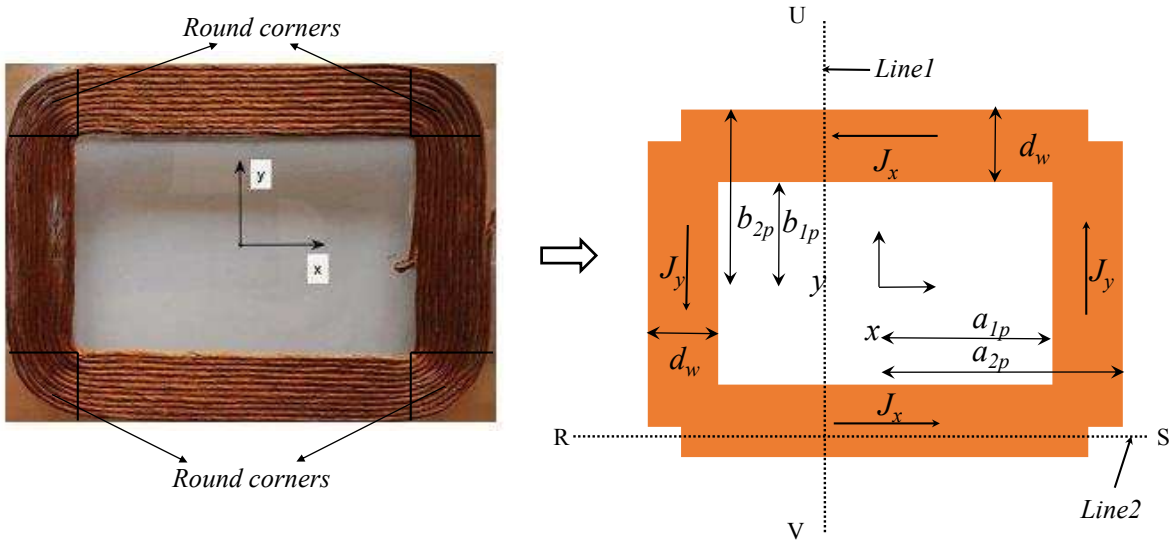

Figure 2.4: The actual coil and its approximation.

rangement, trapezoidal arrangement and overlapping arrangement give better results as compare to the non-overlapping bar, but the trapezoidal arrangement can only be applied with square coil [77]. The configuration of four overlapping bars can be used for the rectangular shape of the coil. Therefore, in the proposed analytical model, uses four overlapping bars in the modelling.

The rectangular coil, as shown in Fig. 2.4 can be considered as four-bar with four round corners. At the four-round corner, the *x* and *y*-components are related to each other, which restricts the application of separation of variables method. To consider the four round corners in the analytical model, the coil can be modeled with different configurations as (1) Non-overlapping bars, (2) Trapezoidal bars, and (3) overlapping bars [60]. Among these arrangements, trapezoidal arrangement and overlapping arrangement give better results as compare to the non-overlapping bar, but the trapezoidal arrangement can only be applied with square coil [77]. The configuration of four overlapping bars can be used for the rectangular shape of the coil. Therefore, the current density distribution in the primary coil is modeled by assuming four overlapping rectangular bars, as shown in Fig. 2.4 [77]. These bars have a finite length in the current direction. Here, to include the effect of the round corner on magnetic filed density, the coils are overlapped at the corners. The Fourier series is used to represent the current density distributions [77, 92].

The current density distribution of J_x on Line 1 (UV-Line), i.e along the *y*-direction, is shown in Fig. 2.5(a). Fig. 2.5(b) show the current density distribution of J_x on Line 2 (RS-Line), i.e along the

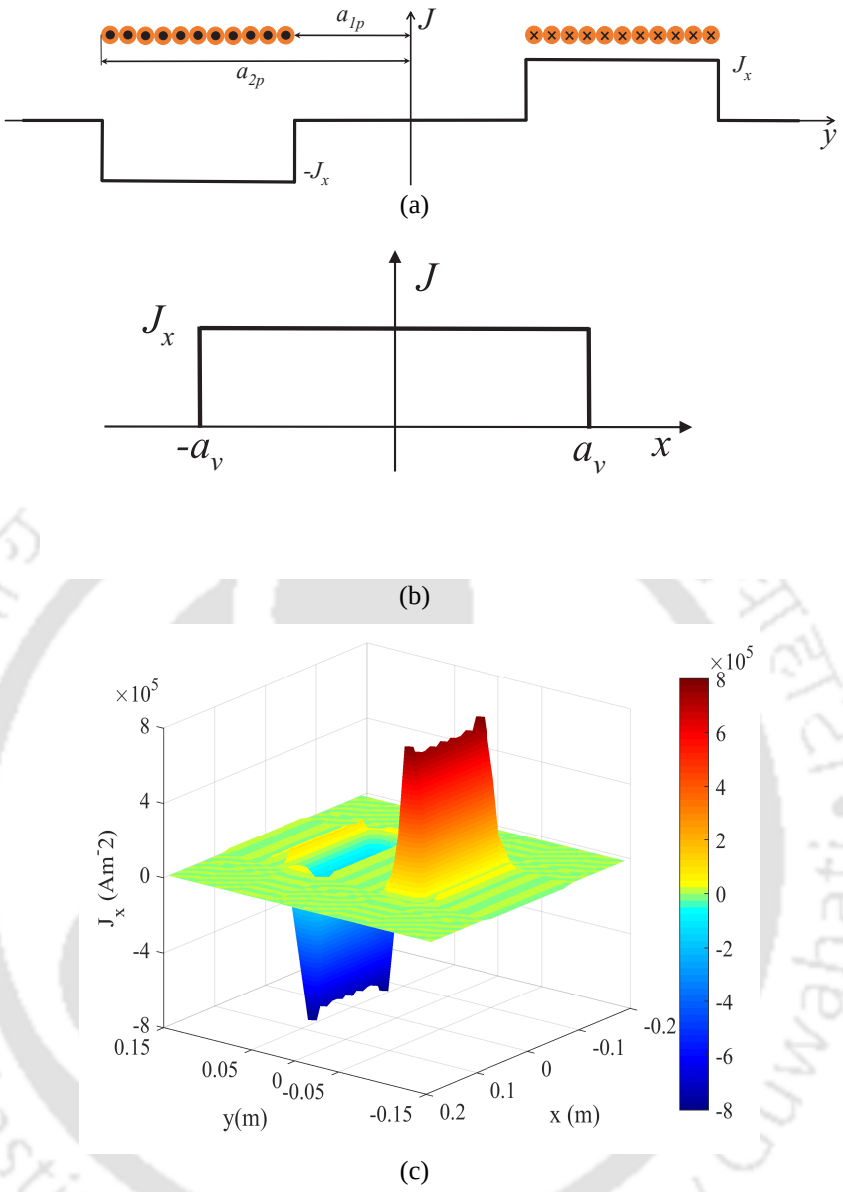

Figure 2.5: Current density distribution of J_x (a) along y-direction, (b) along x-direction, and (c) along x- and y-direction..

x-direction. The current density distributions $J_x(x, y)$ and $J_y(x, y)$ are expressed by (2.29) and (2.32), respectively [92, 93].

$$J_x(x,y) = \sum_{n=1,3,5}^{N} \sum_{m=1,3,5}^{M} j_1 \sin(k_y y) \cos(k_x x) \tag{2.29}$$

where

$$j_1 = \frac{16J(\cos(k_y b_{1p}) - \cos(k_y b_{2p}))\sin(k_x a_v)}{mn\pi^2} \tag{2.30}$$

$$a_v = \frac{a_{1p} + a_{2p}}{2}. \tag{2.31}$$

$$J_y(x,y) = \sum_{n=1,3,5}^{N} \sum_{m=1,3,5}^{M} j_2 \sin(k_x x)\cos(k_y y) \tag{2.32}$$

where

$$j_2 = \frac{16J(\cos(k_x a_{1p}) - \cos(k_x a_{2p}))\sin(k_y a_v)}{mn\pi^2} \tag{2.33}$$

$$b_v = \frac{b_{1p} + b_{2p}}{2}\,. \tag{2.34}$$

For the calculation of magnetic field density using (2.6), the coefficients of the potentials should be known for each region. These unknown coefficients are determined using the boundary conditions. The next subsection explains the applied boundary conditions.

2.2.4 Boundary conditions

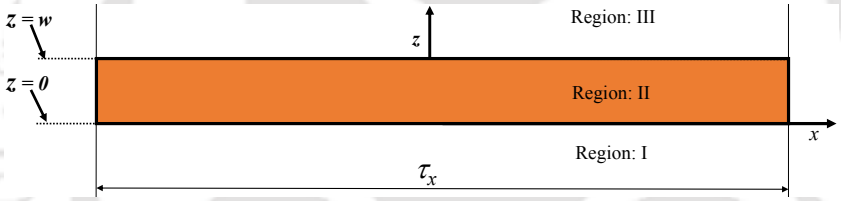

Figure 2.6: *xz* face of rectangular coil

The expression of coefficients in potentials should be known to calculate the magnetic field with the potentials. The potentials in (2.17), (2.26) and (2.27) contain six unknown coefficients c_I, c_{II_1}, d_{II_1}, c_{II_2}, d_{II_2}, and c_{III}. For calculating these unknowns coefficients, six equation is required, which is obtained by applying the boundary conditions at the boundaries in *z*- direction of each region. The boundary conditions are defined by the continuity of tangential magnetic field intensity (H_x and H_y) and normal component magnetic field density (B_z) at $z = 0$ and $z = w$, as shown in Fig. 2.6 and is

given as

$$\begin{aligned} H_{xI}(x,y,0) &= H_{xII}(x,y,0) \\ H_{yI}(x,y,0) &= H_{yII}(x,y,0) \\ B_{zI}(x,y,0) &= B_{zII}(x,y,0) \\ H_{xII}(x,y,w) &= H_{xIII}(x,y,w) \\ H_{yII}(x,y,w) &= H_{yIII}(x,y,w) \\ B_{zII}(x,y,w) &= B_{zIII}(x,y,w). \end{aligned} \tag{2.35}$$

With these boundary conditions a set of 6 simultaneous linear equations is obtained. These set of equations are solved to get the unknown coefficients. The obtained analytical expression of unknowns are given as-

$$c_I = \frac{0.5\left(J_x k_y + J_y k_x\right)\left(1 - e^{-k_z w}\right)}{k_z^3} \tag{2.36}$$

$$c_{II_1} = \frac{0.5 k_y \mu_0 \left(J_x k_y + J_y k_x\right) e^{-k_z w}}{k_z^4} \tag{2.37}$$

$$d_{II_1} = \frac{0.5 k_y \mu_0 \left(J_x k_y + J_y k_x\right)}{k_z^4} \tag{2.38}$$

$$c_{II_2} = \frac{0.5 k_x \mu_0 \left(J_x k_y + J_y k_x\right) e^{-k_z w}}{k_z^4} \tag{2.39}$$

$$d_{II_2} = \frac{0.5 k_x \mu_0 \left(J_x k_y + J_y k_x\right)}{k_z^4} \tag{2.40}$$

$$c_{III} = \frac{0.5\left(J_x k_y + J_y k_x\right)\left(e^{k_z w} - 1\right)}{k_z^3} \tag{2.41}$$

After determining the coefficients of magnetic potentials, the magnetic field in region III, where the secondary coil exists, can be calculated. The calculated magnetic field and alignments of the secondary coil with respect to the primary coil are required for calculating mutual inductance. The next section discusses the possible misalignments during EV charging.

2.3 Possible Misalignments

The analytical model presented in this chapter is used to calculate the mutual inductance, which depends upon the alignment of the secondary coil. Therefore, the following misalignments are considered.

(i) Vertical Variation (VV);

(ii) Planar Misalignment (PM);

(iii) Angular Misalignment (AM);

(iv) Horizontal Misalignment (HM);

(v) Planar with Horizontal Misalignment (PHM);

(vi) Angular with Horizontal Misalignment (AHM).

The vertical variation and planar misalignment are shown in Fig. 2.7(a) and 2.7(b). In both cases, the secondary coil plane is parallel to the primary coil plane. In the case of vertical variation, the secondary coil moves along z-axis whereas, in planar misalignment, secondary coil rotate around z-axis at fixed hight. Here, z-component of the magnetic field B_z constitutes in mutual inductance. When the plane of the secondary coil is tilted through y-axis, keeping the centre of secondary coil at fixed hight is considered as angular misalignment shown in Fig. 2.7(c), here B_x and B_z contribute to mutual inductance.

The other types of variations are possible when the secondary coil moves along the x-axis. In this type of misalignment, there is an offset of Δx in the x-direction, between the centre of the primary and secondary coil, as shown in Figs. 2.7(d)-2.7(f). When the secondary coil moves along the x-axis, having the plane parallel to the primary coil plane at a fixed height, is considered as horizontal misalignment, as shown in Fig. 2.7(d). Fig. 2.7(e) shows the situation, where the secondary coil moves along the x-direction with the rotated plane around the z-axis, is considered as planar with horizontal misalignment (PHM). Fig. 2.7(f) shows the arrangement, which is referred to as angular

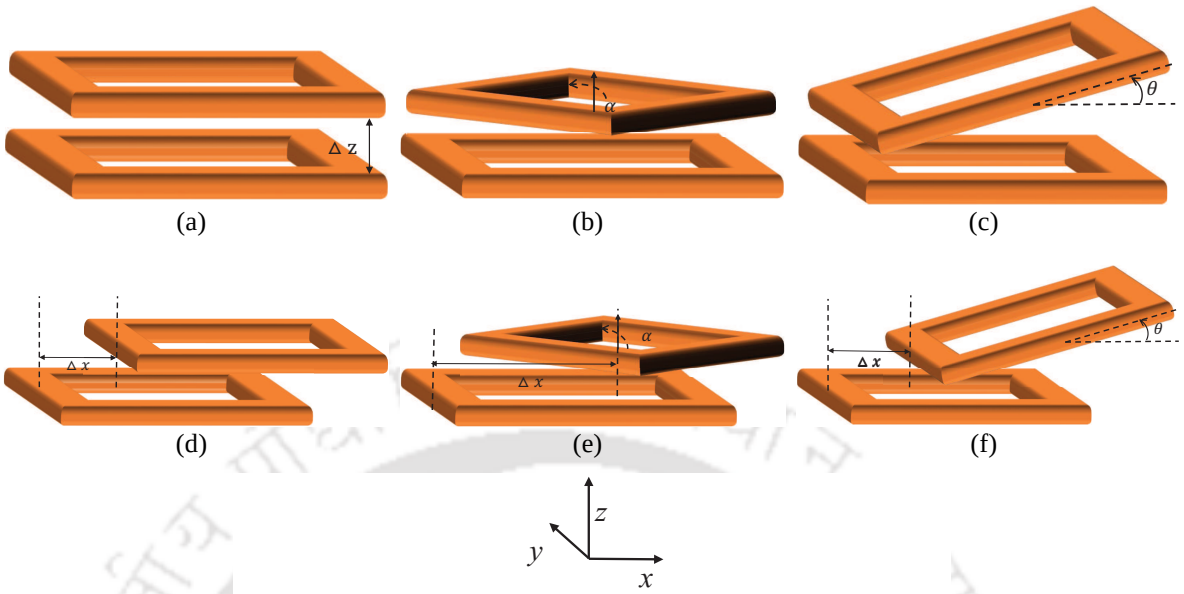

Figure 2.7: Schematic of studied variations (a) vertical variation (VV), (b) planar misalignment (PM), (c) angular misalignment (AM), (d) horizontal misalignment (HM), (e) planar with horizontal misalignment (PHM) and (f) angular with horizontal misalignment (AHM).

with horizontal misalignment (AHM). In this arrangement, the secondary coil moves along the *x*-direction with the tilted plane around the *y*-axis.

This section presented different types of misalignments that occur during EV charging. The next section discusses the calculation of mutual inductance using magnetic field density calculated from the proposed analytical model for the discussed misalignments.

2.4 Mutual Inductance Calculation

The magnetic field distribution using (2.6) can be used to calculate the mutual inductance. This mutual inductance is the direct input for the steady-state model of SP- compensated WPT system, which is given in Chapter 5. The mutual inductance is defined as the ratio of flux linkage to each turn of the secondary coil with current flowing through the primary coil, given as-

$$M(x,y,z) = \frac{\lambda_{12}}{I_p} \tag{2.42}$$

where $M(x,y,z)$ is the mutual inductance due to the variation of the secondary coil in *x*-, *y*-, and *z*-directions with respect to the primary coil, λ_{12} is flux linked to the secondary coil, I_P is the r.m.s. current in the primary coil. With respect to magnetic field density, the flux linkage to the secondary

coil can be written as-

$$\lambda_{12} = \oiint B_{III}.dA \tag{2.43}$$

B_{III} represents the magnetic field density of Region III.

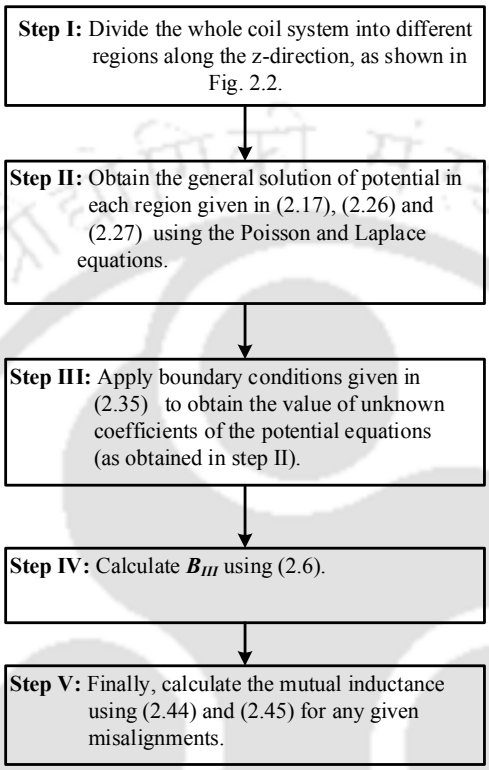

Figure 2.8: Flowchart presenting the steps involved in calculating the mutual inductance for different misalignments (as given in (2.44) and (2.45)).

After calculating B_{III} using (2.6), the final expressions of mutual inductance, calculated from (2.42), are given by (2.44) and (2.45). Here, expressions contain the misalignments parameters such as Δz, θ, Δx, and α, due to the dependency of surface integration limit on misalignment parameters (the detailed derivation is given in Appendix A). Equation (2.44) is valid for AM and AHM, whereas (2.45) is valid for PHM. However, for VV and HM, both (2.44) and (2.45) can be used to determine the mutual inductance by putting θ and α equal to zero.

$$M(x,y,z) = \sum_{n_s=1,2,3}^{N_S} \sum_{n=1,3,5}^{\infty} \sum_{m=1,3,5}^{\infty} k_1[0.5k_y{}^2 \sin 2\theta\,(p_1 \cos\gamma_1 - p_2 \cos\gamma_2) - k_x k_z\,(p_1 \sin\gamma_1 + p_2 \sin\gamma_2)\,] \tag{2.44}$$

$$
\begin{aligned}
M(x,y,z) \;=\; & \sum_{n_s=1,2,3}^{N_S} \sum_{n=1,3,5}^{\infty} \sum_{m=1,3,5}^{\infty} k_2[\Big(2k_xk_y\cos 2\alpha \\
& - \left(k_x^2 - k_y^2\right)\sin 2\alpha\Big)\sin\gamma_3\sin\gamma_4 + \Big(2k_xk_y\cos 2\alpha \\
& + \left(k_x^2 - k_y^2\right)\sin 2\alpha\Big)\sin\gamma_5\sin\gamma_6] \qquad (2.45)
\end{aligned}
$$

where the expressions of parameters k_1, k_2, p_1, p_2, γ_1, γ_2, γ_3, γ_4, γ_5, and γ_6 are given in (2.46). The misalignments parameters such as Δz, θ, Δx, and α are shown in Fig. 2.7.

$$
\begin{aligned}
k_1 &= \frac{-4\mu_0 c_{III} e^{-k_z((a_{2s}+n_s w)\sin\theta+\Delta z)}\sin\left(k_y\left(b_{2s}-n_s w\right)\right)}{I_{P1}\left(k_x^2 - k_y^2\cos 2\theta + k_z^2\right)} \\
k_2 &= \frac{c_{III}\mu_0 k_z e^{-k_z\Delta z}\cos\left(k_x\Delta x\right)}{I_{P1}\left(k_z^2\cos^2\alpha - k_y^2\right)\left(k_z^2\cos^2\alpha - k_x^2\right)} \\
p_1 &= e^{2k_z n_s w\sin\theta} \qquad (2.46) \\
p_2 &= e^{2k_z a_{2s}\sin\theta} \\
\gamma_1 &= -k_x[\left(n_s w - a_{2s}\right)\cos\theta + \Delta x] \\
\gamma_2 &= -k_x[\left(n_s w - a_{2s}\right)\cos\theta - \Delta x] \\
\gamma_3 &= -\left(k_y\sin\alpha - k_x\cos\alpha\right)\left(a_{2s} - n_s w\right) \\
\gamma_4 &= -\left(k_x\sin\alpha + k_y\cos\alpha\right)\left(n_s w - b_{2s}\right) \\
\gamma_5 &= -\left(k_y\sin\alpha + k_x\cos\alpha\right)\left(n_s w - a_{2s}\right) \\
\gamma_6 &= -\left(k_x\sin\alpha - k_y\cos\alpha\right)\left(b_{2s} - n_s w\right).
\end{aligned}
$$

This section explains the calculation of mutual inductance through magnetic field density obtained from the analytical model. The next section examines the accuracy of the calculated mutual inductance and magnetic field density.

2.5 Verification of Analytical Model

In this section, the verification of the proposed analytical model has been done by comparing the analytical results with 3-D FEA simulation and measurements. Subsection 2.5.1 presents a description of the developed 3D FEA model. Subsection 2.5.2 explains each component of the built hardware. The obtained magnetic field results from 3-D analytical and 3-D FEA with the measurements are

given subsection 2.5.3; finally, the verification of the mutual inductance for different misalignments has been discussed in subsection 2.5.4.

2.5.1 FEA Simulation

A 3-D FEA simulation has been done in ANSYS Maxwell 14.0.0 environment to validate the proposed model. The model is based on the parameters given in Table 2.1. The prepared 3-D FEA model of rectangular coils is shown in Fig. 2.9. The primary coil is made of four rectangular bars, as in the case of the analytical model, with the only difference of circular edge at the corners of the coil. The primary coil is excited with current density J, whereas no current density is given to secondary coil. The specification of the FEA simulation is given in Table 3.2.

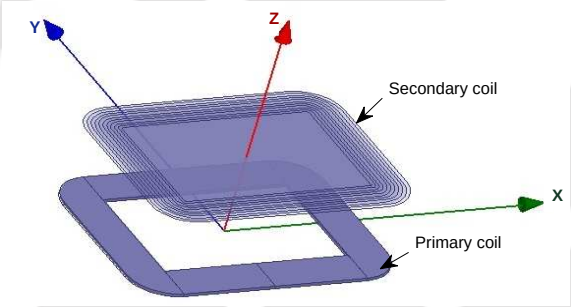

Figure 2.9: 3-D FEA model of rectangular coils.

Table 2.2: Specification for FEA Simulation

Number of mesh	58405
Type of mesh	Tetrahedral
Solver type	Magnetostatic

2.5.2 Experimental Set-up

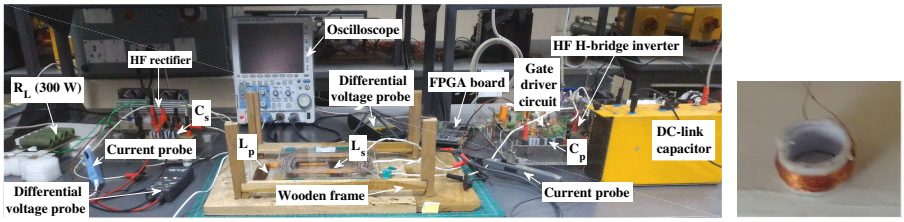

(a) (b)

Figure 2.10: Experimental set-up (a) hardware prototype, and (b) pick-up coil.

The set-up consists of a dc-ac power converter, two rectangular coils, and four pick-up coils. A square wave bipolar dc-ac power converter is used to generate the high-frequency current, which is fed to the primary coil. It generates a high-frequency voltage signal which switched from positive dc supply to negative supply voltage using four IRFP460 MOSFETs. Altera Cyclone II, an FPGA starter board, is used to generate the HF (100 kHz) gate pulse to drive the H-bridge inverter by using two numbers of the half-bridge gate driver IC IR2110. The FPGA starter board is isolated from a high power dc-ac converter by two optocouplers.

Two rectangular coils of eleven turns each are made using Litz wire of American wire gauge (AWG)#32 copper wire and glued on acrylic sheet. The coils are composed of 100 strands with 0.1 mm in diameter. The dimensions of the rectangular coil are given in Table 2.1.

To measure the magnetic flux density at different points in the air gap, four pick up coils of radius 2 mm, and 200 turns are used, shown in Fig. 2.10(b). This pick-up coil is made of (AWG)#40 copper wire. The magnetic field density is obtained by the open-circuit voltage at the pick- up coil. Based on the measured value magnetic field density is obtained by

$$B = \frac{\int_0^T V_{pick-up} dt}{\pi \cdot r_{pick-up}^2} \tag{2.47}$$

where $r_{pick-up}$ is the radius of the pick-up coil, T is the time period of the applied voltage to the primary coil, and $V_{pick-up}$ is the voltage of the pick-up coil. In (2.47), B can be B_x , B_y and B_z depending upon the orientation of the pick-up coil. When the direction of area vector of pick- up coil is along x, y, and z-axis, (2.47) gives B_x , B_y and B_z, respectively.

The mutual inductance between the coils is measured with Hewlett Packard 4263B LCR meter. The inductance of the in-phase and out-phase connected primary and secondary coil is measured to calculate the mutual inductance between the coils. After calculating the in-phase and out-phase inductance, these two connection gives the following inductances-

$$L_{in} = L_p + L_s + 2 \cdot M$$

$$L_{out} = L_p + L_s - 2 \cdot M$$

where L_p and L_s are the self inductances of the primary and the secondary coil respectively. With the measurement of L_{in} and L_{out}, the mutual inductance between the coils is calculated by (2.48)

$$M = \frac{L_{in} - L_{out}}{4}. \tag{2.48}$$

Here, the component of built experiment set-up and method to measure the mutual inductance has been discussed. The next sub-section compares the magnetic field distribution obtained from the analytical model with measurement and FEA results.

2.5.3 Magnetic Field Distribution in the Air Gap

The proposed analytical model is validated with 3D FEA and experiment. The distribution of B_z and B_x component above the primary coil at $z = 2$ cm, obtained from the analytical model, FEA, and experiment are compared in Figs. 2.11-2.12. Figs. 2.11(a) and 2.12(a) show the tangential component of magnetic field density along x and y direction, respectively, whereas Figs. 2.11(b) and 2.12(b) show the normal component of magnetic field density along x and y-direction, respectively. In Figs. 2.11 and 2.12 tangential components of magnetic field density (B_x and B_y) and normal component of magnetic field density (B_z) are symmetrical due to the rectangular shape of the coil.

In this sub-section, B_x, B_y and B_z obtained from the analytical model, measurements and FEA model has been compared. It observed that the magnetic field distribution obtained from the analytical model follows the results obtained from 3-D FEA and experimental, which confirm the accuracy of the proposed analytical model. The next sub-section compares the mutual inductance obtained from the analytical model with measurement and FEA results.

2.5.4 Mutual Inductance

The proposed analytical model is used to calculate the mutual inductance for different misalignments. The comparison of variations in mutual inductance obtained from analytical, FEA, and measurement are shown in Figs. 2.13-2.18. Fig. 2.13 shows the variation of mutual inductance when the secondary coil moves in the z-direction. Here, mutual inductance decreases as the secondary coil moves along the z-axis. This decrease in mutual inductance is because of the decrease in the magnitude of the magnetic field density with respect to the z-direction.

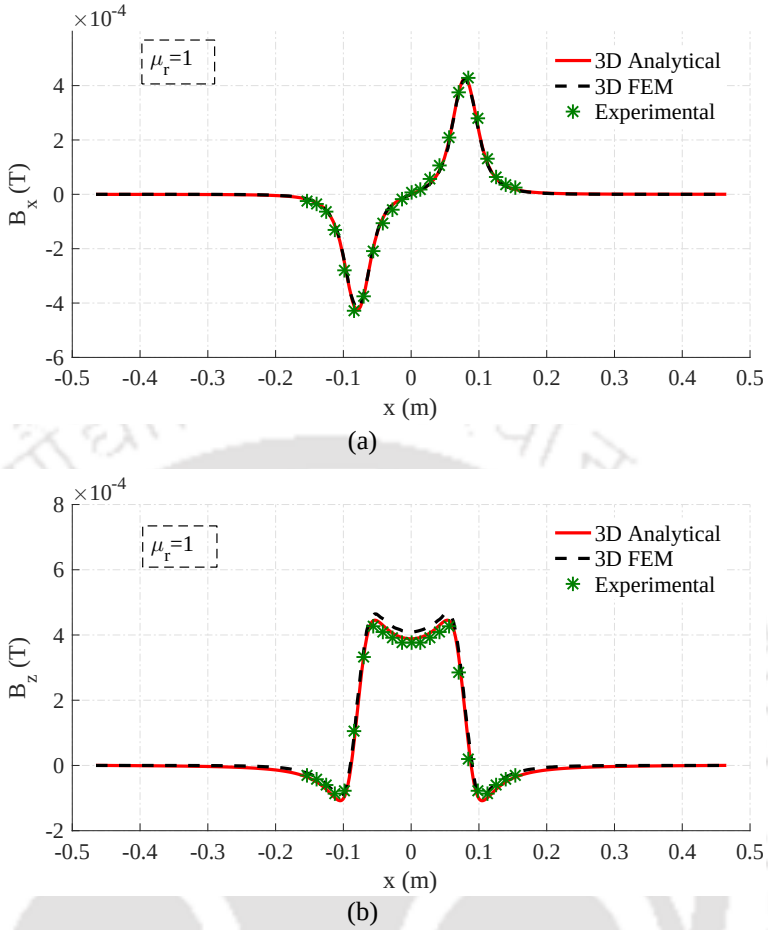

Figure 2.11: Distribution of (a) B_x and (b) B_z along x-direction at $y = 0$ and $z = 2$ cm.

The variation in mutual inductance due to angular misalignment is shown in Fig. 2.14. For the measurement, the centre position of the secondary coil is kept at $z = 10.25$ cm, and the coil is tilted around y-axis from 0° to 90° with an interval of 10°. Here, flux linkage through the secondary coil increases till 40°, which increases the mutual inductance and then flux linkage, mutual inductance start decreasing for ≥ 40°.

Fig. 2.15 shows the variation in mutual inductance for a planar misalignment. Here, it is observed that the mutual inductance decreases for 0° to 90° rotation of secondary coil and again increases for 90° to 180° rotation, and this is due to the decrease and increase in the overlapping area between coils, respectively.

The variation in mutual inductance for the case where the secondary coil moves along the x -direction is reported in Figs. 2.16-2.18. These figures show that mutual inductance decreases as the secondary coil moves away from the centre of the primary coil, because of the decrease in mutual

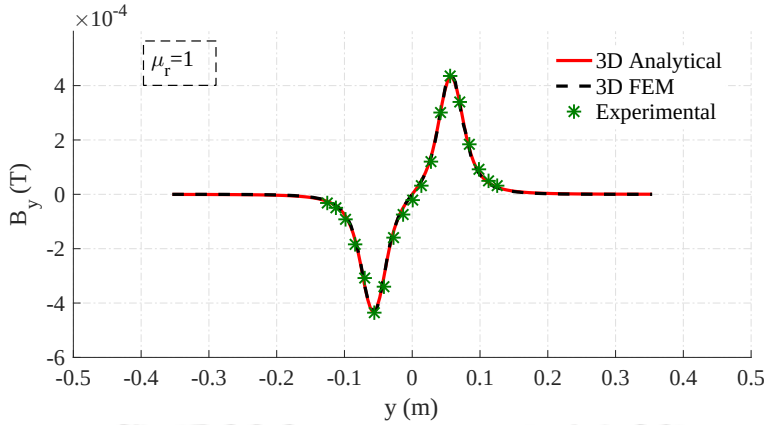

(a)

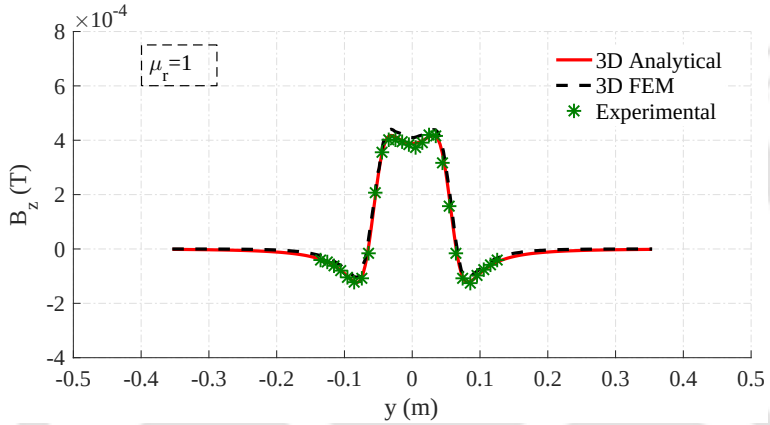

(b)

Figure 2.12: Distribution of (a) B_y and (b) B_z along y-direction at $x = 0$ and $z = 2$ cm.

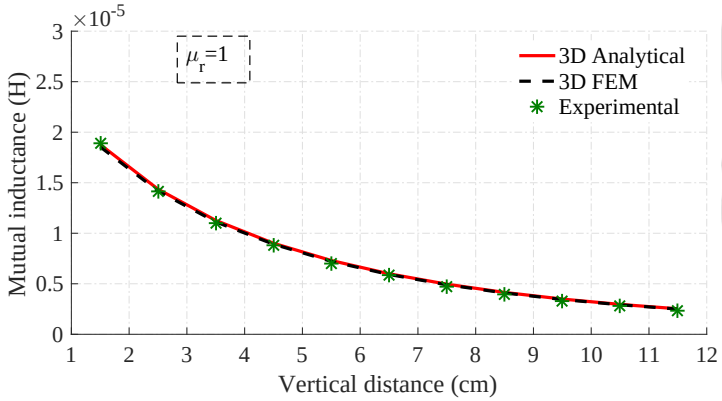

Figure 2.13: Mutual inductance variation in z-direction without shielding.

coupling. In Fig. 2.17, both angular and horizontal misalignment, is illustrated. Here, the secondary coil moves along the x-direction with an angular rotation of 10° and 20° around the y-axis, having its centre at $z = 3.2$ cm and 4.74 cm, respectively. For the measurement of variation in mutual inductance due to both planar and horizontal misalignment is shown in Fig. 2.18. Here, the secondary coil moves

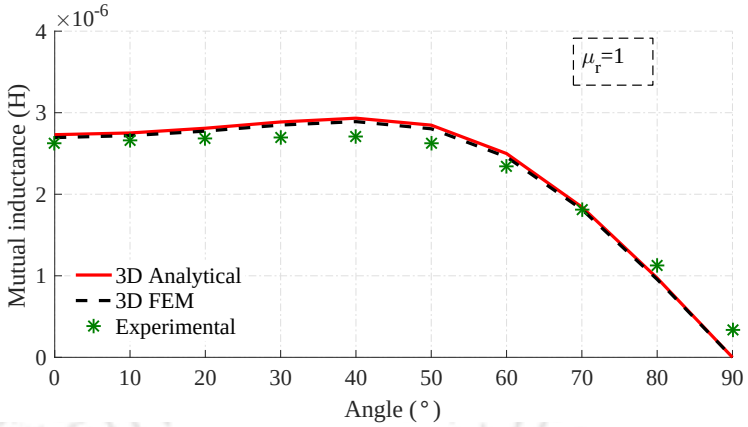

Figure 2.14: Mutual inductance variation for angular misalignment.

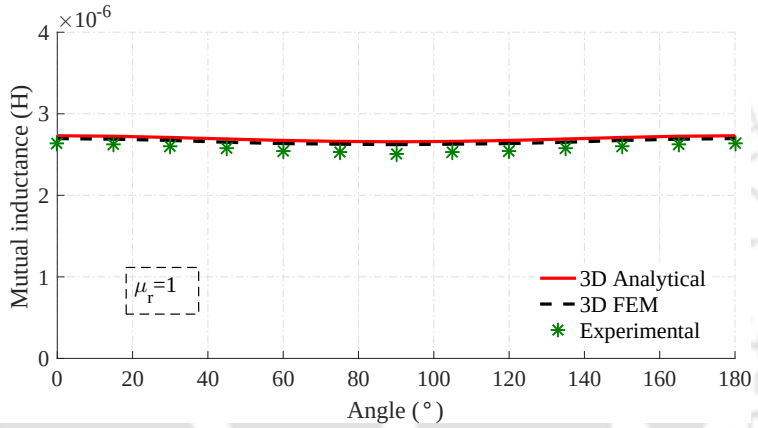

Figure 2.15: Mutual inductance variation for planar misalignment at z = 10.25 cm

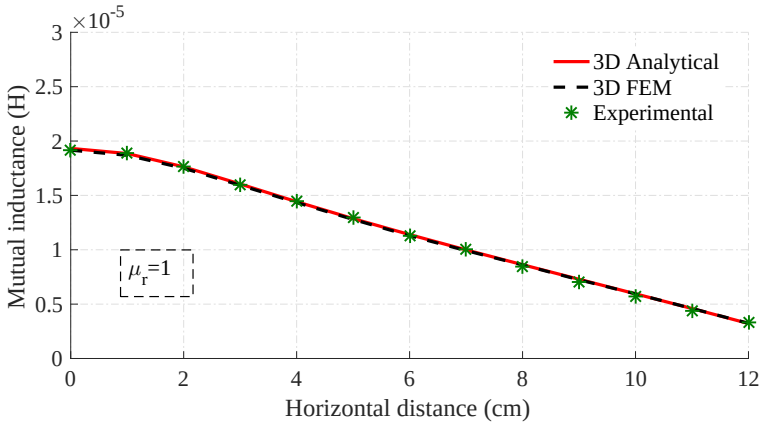

Figure 2.16: Mutual inductance variation for horizontal misalignment at z = 1.35 cm.

along the x-direction having z = 2.4 cm and planar rotation of 20° (around z-axis). From Figs. 2.13-2.18, it is observed that mutual inductance variation obtained from the analytical model, FEA, and experiment are following the same pattern.

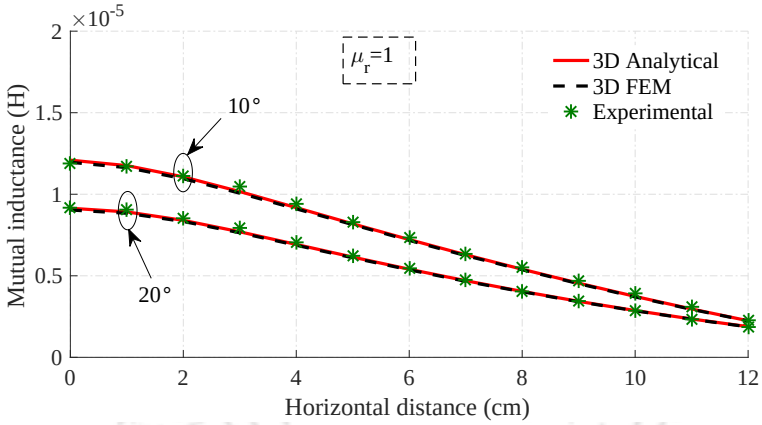

Figure 2.17: Mutual inductance variation for both angular and horizontal misalignment.

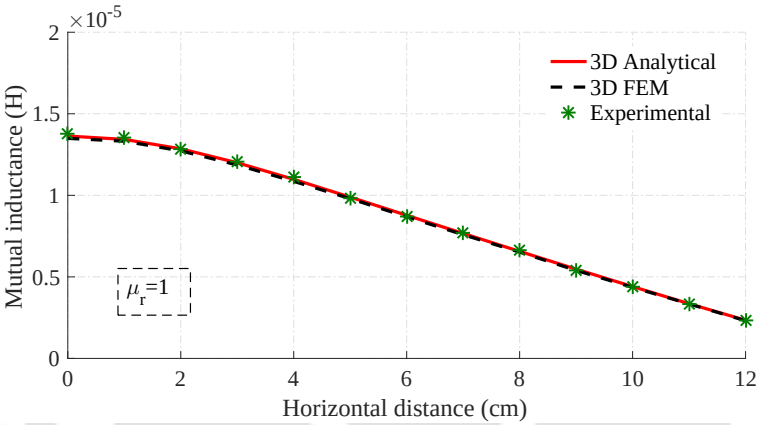

Figure 2.18: Mutual inductance variation for both planar and horizontal misalignment.

2.6 Summary

In this chapter, an analytical model is presented to compute the mutual inductance between the coils for different misalignments. Magnetic vector potential and magnetic scalar potential are used to develop the analytical model. Moreover, an experimental setup with different misalignments is developed in the laboratory to validate the efficacy of the model. The results of the analytical model are compared with the simulation and the measurement results, and a good agreement has been found. Therefore, the proposed model can be used in the initial designing of such a WPT system.

Generally, the ferromagnetic magnetic material is used to concentrate the magnetic flux, which increases the mutual inductance. The proposed model predicts the mutual inductance for a rectangular coil system where ferromagnetic material (magnetic shield) is absent, and the next chapter discusses the analytical modelling, which includes magnetic shielding in the coil system.

Note: The contribution of this chapter is published in:

B. K. Kushwaha, G. Rituraj and P. Kumar, "Mathematical model for the analysis of seriesparallel compensated wireless power transfer system for different misalignments," IET Circuits, Devices and Systems, *vol. 13, no. 7, pp. 970-978, 10 2019.*

3

3-D Analytical Model for Computation of Mutual Inductance for Different Misalignment with Shielding in WPT System

Contents

3.1 Introduction 44
3.2 Analytical modelling 45
3.3 Possible Misalignments 52
3.4 Verification of Analytical Model 54
3.5 Summary 62

3.1 Introduction

The previous chapter introduced a 3-D analytical model to calculate mutual inductance for an air-core coil system without a magnetic shield for the WPT system. The results obtained from the analytical model have been compared with FEA and experimental results, and they were found to be in good agreement. The harmonic modelling technique has been used in the analytical model. In the WPT system, with the air-core coils, large leakage flux results in reduced mutual coupling. Usually, a ferrite core (Magnetic shield) is used in the WPT system to increase the mutual coupling and minimize the exposure of other installations in the vicinity of the WPT system [49]. Hence, the WPT coils with the ferrite core (coil system) are preferred. The illustration of such a coil system is shown in Fig. 3.1.

The Magnetic Equivalent Circuit (MEC), finite element analysis (FEA), and harmonic modelling method (HM), which has been discussed in chapter 2 can be the possible modelling method to model coils with the ferrite core. Among these methods, the harmonic modelling technique is found suitable for the coils with ferrite. Some of the studies have presented an analytical model using a harmonic modelling method to calculate the mutual inductance and magnetic flux density distribution by considering an iron bar with a relative permeability of infinite value. [77,88,89,94]. The analytical model, which considers the permeability of used magnetic shield infinite gives a result that deviates from the actual result.

This chapter presents a 3-D analytical model to calculate the mutual inductance and magnetic flux density distribution in the air medium for a coil system, which includes the magnetic shielding of finite permeability. The harmonic modelling method is used for 3-D analytical modelling. Magnetic vector potential and scalar potential described in the three-dimensional Cartesian coordinate system are used in modelling. The mutual inductance for various misalignments is also described. To show the efficacy of the analytical model, results are compared with FEA and experimental results. The proposed analytical model is capable of taking into account the parameter of magnetic shieldings, such as permeability and width. In order to see the effect of the magnetic shield on the mutual inductance between the coils, the mutual inductance for the coil system without a magnetic shield (discussed in the previous chapter) is also presented in this chapter.

The chapter is organized as follows: Section 3.2 describes problem formulation and assumptions made for modelling. The various forms of considered misalignment are discussed in section 3.3. Section 3.4 verifies the proposed analytical model with FEA results and measurements. Finally, the summary of this chapter is given in section 3.5.

3.2 Analytical modelling

The harmonic modelling method has been used to model the coil system shown in Fig. 3.1. In the harmonic modelling method, the electromagnetic system is divided along the non-periodic direction(Here it is *z*-direction) [72]. Then the Poissons or Laplace equations are solved for each region. The solution of Poissons or Laplace equations provide magnetic potentials with the unknown coefficients. These unknown coefficients are calculated by applying boundary conditions at the boundaries of each region. This section presents these modelling steps in subsequent subsections. Subsection 3.2.1 gives an overview of the coil system with assigned regions and assumptions made during modelling. Subsection 3.2.2 presents the potential solution of each assigned regions. Finally, the boundary condition applied between each region has been discussed in Subsection 3.2.3.

3.2.1 Coil System Overview

The 3-D geometry of contactless coils with its regions is shown in Fig. 3.1. It consists of two rectangular coils and also a high permeable magnetic material below the primary coil. Figs. 3.3(a) and 3.3(b) show an actual coil of the WPT system and its equivalent circuit model.

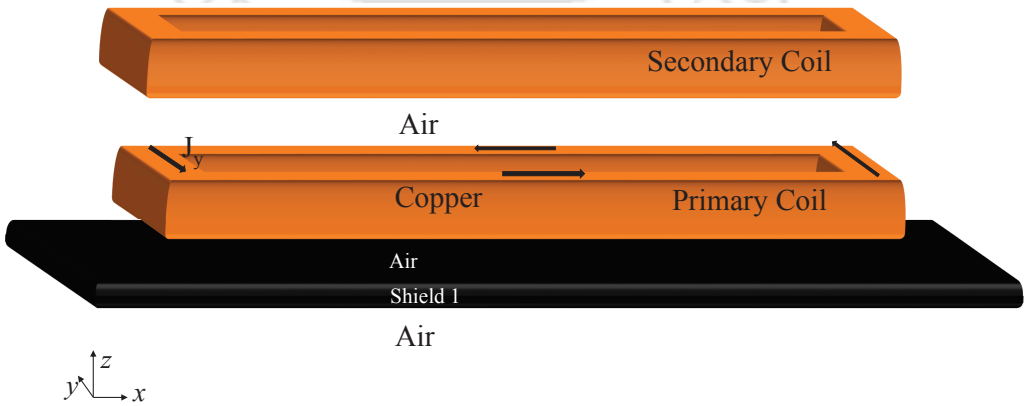

Figure 3.1: 3D illustration of contactless coils with its regions.

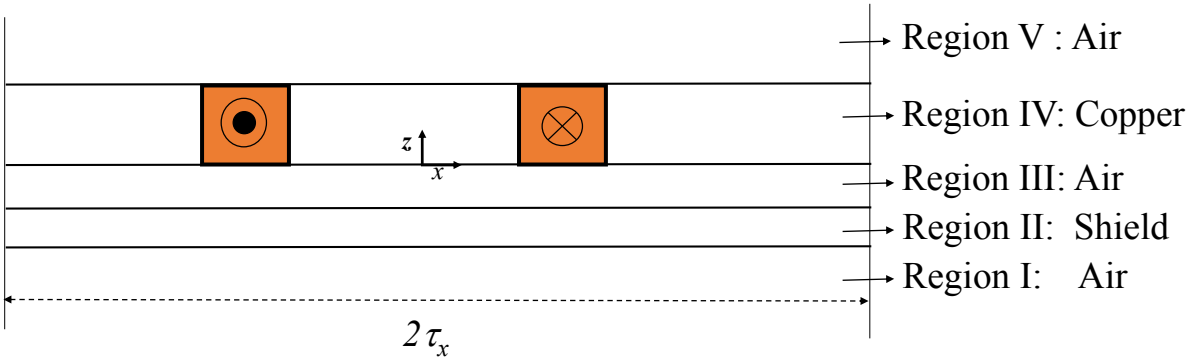

Figure 3.2: Schematic cross section of the coil system shown in Fig. 3.1

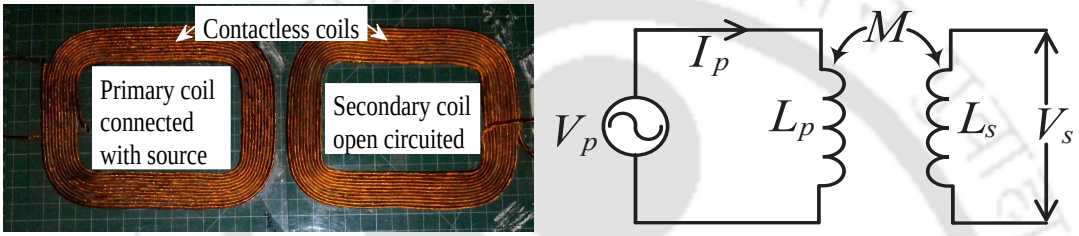

(a) (b)

Figure 3.3: WPT system having (a) an actual coils, and (b) equivalent circuit model of contactless coils (where V_p is the high frequency AC source, I_p is the primary current, L_s and L_s are the self-inductances of primary and secondary side respectively, V_s is the open circuit voltage of secondary side, and M is the mutual inductance).

The whole domain is divided into five regions, as shown in Fig. 3.1. The cross-section view of the coil system shown in Fig. 3.1, with the assigned region and their dimension, is shown in Fig. 3.2. Region I is an air medium which is below the shielding material, and the magnetic shielding material is presented as Region II. The base of the primary coil (region III) having relative permeability one ($\mu_r = 1$) is considered as air medium, and Region IV is a primary coil which carries source current. Region V is above the primary coil, which is an air medium, the secondary coil carries no current, and its relative permeability is one; hence, it is considered in region V. Each divided region is described by either magnetic vector potential or magnetic scalar potential. The magnetic vector potential is used in the region where the current source is present, and magnetic scalar potentials are used in other regions [94].

The magnetic field calculated from the proposed model considers the following assumptions:

- The eddy-current induced in coil and magnetic shields are neglected;
- The magnetic shields used in coil system are considered as isotropic;

- The quantities which are temperature-dependent such as resistance of the primary coil is neglected in magnetic modelling;
- No current exists in the z - direction.

Table 3.1: Design parameters for WPT system

Parameters	Description	Value	Unit
d_w	Difference in outer and inner width of a coil in x- and y-direction	27.5	mm
h_2	Diameter of coil	2.5	mm
h_1	Thickness of base of coil	3.16	mm
s_1	Thickness of magnetic shield	0.02	mm
τ_x	Coil pitch in x-direction	465	mm
τ_y	Coil pitch in y-direction	353.75	mm
J	Current density in the coil	0.713	A-mm^{-2}
N	Harmonics in x- direction	50	
M	Harmonics in y- direction	50	

Here, the considered coil system with the assigned regions has been discussed. Moreover, the assumption involved in modelling is also mentioned. For calculating the magnetic field in the assigned regions, the magnetic potential in each region should be known. The next subsection gives the solution of the magnetic vector potential and scalar potentials.

3.2.2 Magnetic Field Description

The magnetic field of the divided region of the coil system shown in Fig. 3.1 is calculated with magnetic potentials. The magnetic field in the current-carrying region (Region IV) is calculated by-

$$\mathbf{B} = \nabla \times \mathbf{A} \tag{3.1}$$

Here, **A** and **B** is the magnetic vector potential and magnetic field density in region IV, respectively. Whereas, the magnetic field of the regions representing air medium and magnetic shield region is calculated by-

$$\mathbf{H}_r = -\nabla (\varphi_r) \tag{3.2}$$

where φ_r is scalar magnetic potential, and r can be the region I, II, III, or V.

The solution of magnetic potentials used in (3.1) and (3.2) is given in the following sub-sub

section: The Sub-sub section 3.2.2.1 presents the solution of the magnetic vector potential, whereas the magnetic scalar potential is explained in sub-sub section 3.2.2.2.

3.2.2.1 Region IV

This region is described by the primary coil, which consists of the current source. Since the current is present in this region, the magnetic vector potential is used in describing the magnetic field. [77, 88, 94]. The direction of vector potential is in the direction of current density. The solution of the magnetic vector potential is given by following Poisson and Laplace equations-

$$\nabla^2 A_x = -\mu_0 J_x \tag{3.3}$$

$$\nabla^2 A_y = -\mu_0 J_y \tag{3.4}$$

$$\nabla^2 A_z = 0 \tag{3.5}$$

where A_x, A_y, and A_z are the components of the magnetic vector potential **A** in x, y, and z-directions, respectively. The expression of magnetic vector potential, by solving (3.3) - (3.5) using separation of variable method, is given as

$$\begin{aligned} A_x &= -\sum_{n=1,3,5}^{\infty}\sum_{m=1,3,5}^{\infty}\left(c_{IV_1}e^{k_z z} + d_{IV_1}e^{-k_z z}\right)\cos(k_x x)\sin(k_y y) + \frac{\mu_0 J_x}{k_z^2} \\ A_y &= \sum_{n=1,3,5}^{\infty}\sum_{m=1,3,5}^{\infty}\left(c_{IV_2}e^{k_z z} + d_{IV_2}e^{-k_z z}\right)\sin(k_x x)\cos(k_y y) + \frac{\mu_0 J_y}{k_z^2} \\ A_z &= 0 \end{aligned} \tag{3.6}$$

where $J_x(x, y)$ and $J_y(x, y)$ are current density distributions along the x, and y , respectively. It is similar to the current density distribution given in chapter 2. And A_x, A_y, and A_z are vector potentials in the direction of x, y, and z. Here, A_z is zero because current is absent in z-direction.

The unknown coefficients involve in the magnetic vector potential given in (3.6) depends on the boundary conditions. The boundary conditions in this chapter are different from the previous chapter due to the inclusion of the magnetic shield. Therefore, the magnetic vector potential of the primary coil region given in (3.6) is different from the magnetic vector potential given in chapter 2.

Here, The magnetic vector potential for the current-carrying region (Primary coil) has been dis-

cussed. The next sub-sub section gives the solution of magnetic scalar potential for the regions where current is absent (air medium).

3.2.2.2 Region I, II, III, and V

In these regions, the current source is absent. Hence, magnetic scalar potential is used in describing the magnetic field [88]. The magnetic scalar potential for these regions is given by (3.7) - (3.10). Region II and III represent the magnetic shield region and base of the primary coil, respectively, and these regions are bounded. Whereas the regions I and V that represent air medium are unbounded, as shown in Fig. 3.1. Therefore, the scalar potential equation in regions II and III has two exponential terms; on the other hand, the scalar potential equation in the region I and V have only one exponential term.

$$\varphi_I = \sum_{n=1,3,5}^{\infty} \sum_{m=1,3,5}^{\infty} c_I e^{k_z z} \cos(k_x x) \cos(k_y y) \tag{3.7}$$

$$\varphi_{II} = \sum_{n=1,3,5}^{\infty} \sum_{m=1,3,5}^{\infty} \left(c_{II} e^{k_z z} + d_{II} e^{-k_z z}\right) \cos(k_x x) \cos(k_y y) \tag{3.8}$$

$$\varphi_{III} = \sum_{n=1,3,5}^{\infty} \sum_{m=1,3,5}^{\infty} \left(c_{III} e^{k_z z} + d_{III} e^{-k_z z}\right) \cos(k_x x) \cos(k_y y) \tag{3.9}$$

$$\varphi_V = \sum_{n=1,3,5}^{\infty} \sum_{m=1,3,5}^{\infty} c_V e^{-k_z z} \cos(k_x x) \cos(k_y y) \tag{3.10}$$

where

$$k_z = \sqrt{k_x^2 + k_y^2} \tag{3.11}$$

The Magnetic flux density **B** is obtain by (3.12)

$$\mathbf{B}_r = \mu \mathbf{H}_r \tag{3.12}$$

where μ is the permeability of corresponding region and given by (3.13).

$$\mu = \mu_r \mu_0 \tag{3.13}$$

where μ_r is the relative permeability of the medium. The scalar potentials used here are different compared to the magnetic scalar potential used in chapter 2 due to different boundary conditions.

This subsection defined magnetic vector and scalar potential with unknown coefficients for each assigned region. These unknown coefficients are calculated by applying boundary conditions at the interface between regions. The applied boundary conditions are discussed in the next subsection.

3.2.3 Boundary Conditions

The unknown coefficients c_I - c_V of magnetic scalar potential and magnetic vector potential, as described in section 3.2, are obtained by applying boundary conditions. In this chapter, a magnetic shield is added as additional material as compared to a coil system given in the previous chapter. Therefore this chapter involves additional boundary conditions as due to the inclusion of magnetic shield as compare to boundary conditions given in the previous chapter. These additional boundary conditions are obtained by applying boundary conditions at the boundary of the magnetic shield. The additional boundary condition is obtained by the continuity of magnetic scalar potential at the boundary of the magnetic shield region in the z-direction.

The boundary conditions are defined by the continuity of tangential magnetic field intensity, vertical magnetic field density, and magnetic scalar potential. The boundary conditions are applied in z-direction at points where medium changes such as $z = -(h_1 + s_1)$, $z = -h_1$, $z = 0$, and $z = h_2$ shown in Fig. 3.4.

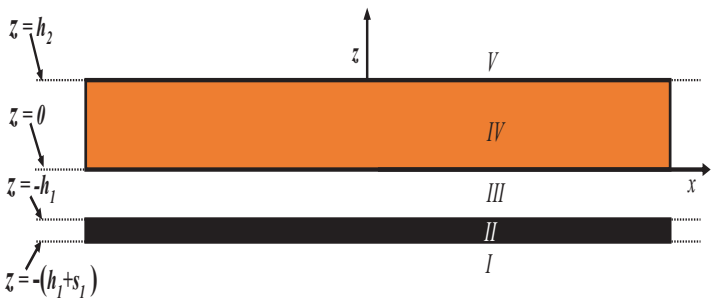

Figure 3.4: *xz* face of rectangular coil

The equations based on boundary conditions are listed in (3.14).

$$
\begin{aligned}
B_{zI}(x,y,-(h_1+s_1)) &= B_{zII}(x,y,-(h_1+s_1)) \\
\varphi_I(x,y,-(h_1+s_1)) &= \varphi_{II}(x,y,-(h_1+s_1)) \\
B_{zII}(x,y,-h_1) &= B_{zIII}(x,y,-h_1) \\
\varphi_{II}(x,y,-h_1) &= \varphi_{III}(x,y,-h_1) \\
H_{xIII}(x,y,0) &= H_{xIV}(x,y,0) \\
H_{yIII}(x,y,0) &= H_{yIV}(x,y,0) \\
B_{zIII}(x,y,0) &= B_{zIV}(x,y,0) \\
H_{xIV}(x,y,h_2) &= H_{xV}(x,y,h_2) \\
H_{yIV}(x,y,h_2) &= H_{yV}(x,y,h_2) \\
B_{zIV}(x,y,h_2) &= B_{zV}(x,y,h_2)
\end{aligned}
\tag{3.14}
$$

The development of (3.14) provides simultaneous linear equation. After solving linear equations, the

obtained unknown coefficient is given as-

$$c_I = -\frac{2\mu\mu_0\left(J_x k_y + J_y k_x\right)\left(1-e^{-k_z h_2}\right)}{k_z^3\left((\mu+\mu_0)^2-(\mu-\mu_0)^2 e^{-2k_z s_1}\right)} \tag{3.15}$$

$$c_{II} = -\frac{\mu_0\left(\mu+\mu_0\right)\left(J_x k_y + J_y k_x\right)\left(1-e^{-k_z h_2}\right)}{k_z^3\left((\mu+\mu_0)^2-(\mu-\mu_0)^2 e^{-2k_z s_1}\right)} \tag{3.16}$$

$$d_{II} = -\frac{\mu_0\left(\mu-\mu_0\right)\left(J_x k_y + J_y k_x\right)\left(1-e^{-k_z h_2}\right)e^{-2k_z h_1}}{k_z^3\left((\mu+\mu_0)^2 e^{2k_z s_1}-(\mu-\mu_0)^2\right)} \tag{3.17}$$

$$c_{III} = -\frac{\left(J_x k_y + J_y k_x\right)\left(1-e^{-k_z h_2}\right)}{2k_z^3} \tag{3.18}$$

$$d_{III} = -\frac{\left(J_x k_y + J_y k_x\right)\left(1-e^{-k_z h_2}\right)\left(e^{-2k_z(s_1+h_1)}-e^{-2k_z h_1}\right)}{2k_z^3\left((\mu+\mu_0)^2-(\mu-\mu_0)^2 e^{-2k_z s_1}\right)} \tag{3.19}$$

$$c_{IV_1} = -\frac{\mu_0 k_y\left(J_x k_y + J_y k_x\right)e^{-k_z h_2}}{2k_z^4} \tag{3.20}$$

$$d_{IV_1} = -\frac{\mu_0 k_y\left(J_x k_y + J_y k_x\right)}{2k_z^4}\left(1+\frac{\left(\mu^2-\mu_0^2\right)\left(1-e^{-k_z h_2}\right)\left(e^{2k_z(s_1-h_1)}-e^{-2k_z h_1}\right)}{\left((\mu-\mu_0)^2-(\mu+\mu_0)^2 e^{2k_z s_1}\right)}\right) \tag{3.21}$$

$$c_{IV_2} = -\frac{\mu_0 k_x\left(J_x k_y + J_y k_x\right)e^{-k_z h_2}}{2k_z^4} \tag{3.22}$$

$$d_{IV_2} = -\frac{\mu_0 k_x\left(J_x k_y + J_y k_x\right)}{2k_z^4}\left(1+\frac{\left(\mu^2-\mu_0^2\right)\left(1-e^{-k_z h_2}\right)\left(e^{2k_z(s_1-h_1)}-e^{-2k_z h_1}\right)}{\left((\mu-\mu_0)^2-(\mu+\mu_0)^2 e^{2k_z s_1}\right)}\right) \tag{3.23}$$

$$c_V = -\frac{\left(J_x k_y + J_y k_x\right)}{2k_z^3\left((\mu-\mu_0)^2-(\mu+\mu_0)^2\right)} \times \left(\left(\mu^2-\mu_0^2\right)\left(e^{-k_z(2h_1+h_2)}-e^{-k_z(2s_1+2h_1+h_2)}\right.\right. \tag{3.24}$$

$$\left.\left.-e^{-2k_z h_1}+e^{-2k_z(s_1+h_1)}\right)+(\mu+\mu_0)^2\left(1-e^{k_z h_2}\right)+(\mu-\mu_0)^2\left(e^{-k_z(2s_1-h_2)}-e^{-2k_z s_1}\right)\right) \tag{3.25}$$

After calculating unknown coefficients of the magnetic potentials, the magnetic potentials (3.6) and (3.10) can be used to calculate the self-inductance and mutual inductances for different misalignments, respectively. The next section discusses the possible misalignments that can happen.

3.3 Possible Misalignments

The possible misalignments that can happen between the coils are shown in Fig. 3.5. Here, the secondary coil is underneath of EV, whereas the primary coil with a magnetic shield is kept under the ground. Therefore, the secondary coil in the coil system is moving part, and the primary coil with the

shield is stationary. Depending on the different movements of the secondary coil with respect to the primary coil, the misalignments are considered. As compared to the coil system discussed in chapter 2, the only difference is that in chapter 2, the primary coil is surrounded by air, whereas here magnetic shield exists near the primary coil. The secondary coil is similar in both the coil system. Since the misalignment is decided with the movement of the secondary coil. Therefore the same misalignments are considered, which are:

(i) Vertical Variation (VV);

(ii) Planar Misalignment (PM);

(iii) Angular Misalignment (AM);

(iv) Horizontal Misalignment (HM);

(v) Planar with Horizontal Misalignment (PHM);

(vi) Angular with Horizontal Misalignment (AHM).

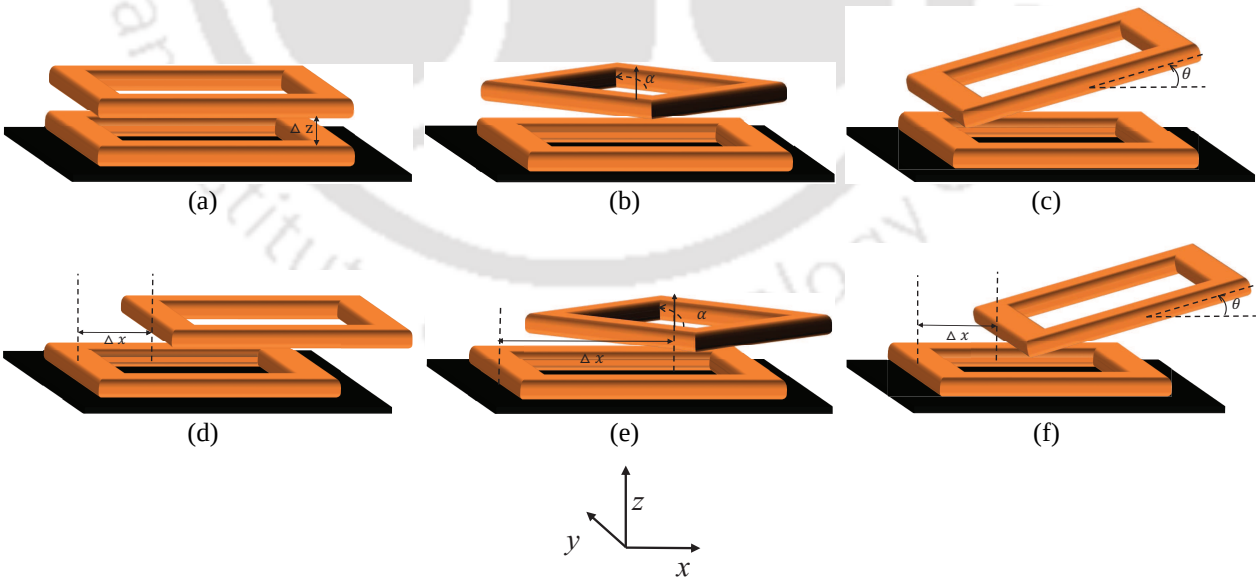

Figure 3.5: Schematic of studied variations (a) vertical variation (VV), (b) planar misalignment, (c) angular misalignment, (d) horizontal misalignment, (e) planar with horizontal misalignment and (f) angular with horizontal misalignment.

The detailed description of these misalignments is given in chapter 2.

The verification of proposed 3-D misalignment by considering these misalignments has been discussed in the next section.

3.4 Verification of Analytical Model

The proposed analytical model is verified with FEA simulation and hardware-setup in subsequent sub-sections. Subsection 3.4.1 describes the developed 3D FEA model. 3.4.2 explains the built hardware. The distribution of B_x, B_y, and B_z obtained from 3-D analytical and 3-D FEA with the measurements are given subsection 3.4.3. The verification of the mutual inductance for different misalignments and self-inductance has been discussed in subsection 3.4.4. Finally, subsection 3.4.5 compares the mutual inductance obtained from the proposed analytical model and model presented in [1].

3.4.1 FEA Simulation

The prepared 3-D FEA simulation model of rectangular coils is shown in Fig. 3.7. This model is based on the parameters given in Table 3.1. In the simulation, the size of the magnetic shield has been taken comparatively larger than the coil dimension, because of the assumption of the infinite size of the magnetic shield in the analytical model. The primary coil is made of four rectangular bars according to the assumption made in the analytical model. The other simulation specification is given in chapter 2.

To show the effect of magnetic shielding on leakage flux, 2D simulation (using ANSYS Maxwell 14.0.0) without and with shielding also has been done, shown in Fig.3.6. From Fig. 3.6(b), it is found that magnetic shielding decreases the leakage flux by concentrating flux lines around the primary coil.

3.4.2 Experimental Set-up

In order to verify the validity of the analytical model, a developed hardware-setup is shown in Fig. 3.8. The set-up consists of an H-bridge inverter, two rectangular coils, four pick-up coils, and a high permeability magnetic material. The designing of H-bridge inverter, rectangular coils, and pick-up has been described in chapter 1. To guide the magnetic flux, a high permeability magnetic material 3M Flux Field Directional Material (FFDM) EM80KM as a magnetic shield is used, shown in Fig.

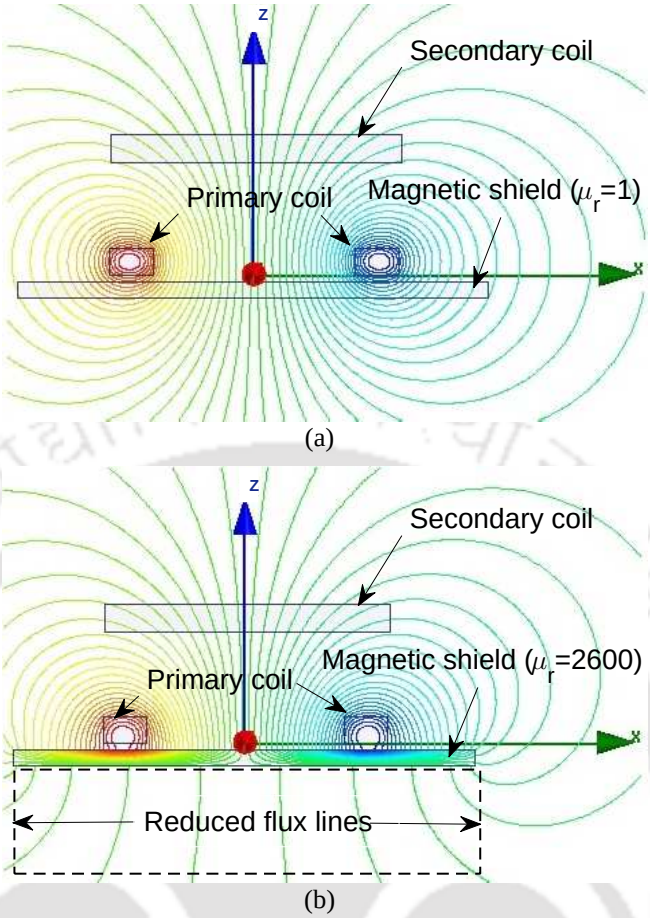

Figure 3.6: Magnetic flux lines (a) without shielding and (b) with shielding.

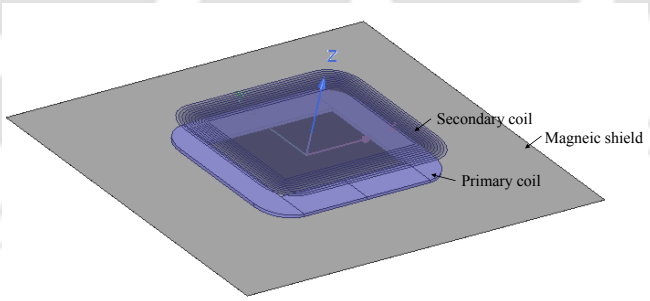

Figure 3.7: 3-D FEM model of rectangular coils.

3.8(c).

3.4.3 Magnetic Field Distribution in the Air Gap

To show the effect of magnetic shielding and accuracy of the analytical model, 2-D graphs of B_x, B_y, and B_z component in the air gap (z = 2 cm) for without shielding and with shielding, are compared in Figs. 3.9-3.12. From Figs. 3.9-3.12 it can be seen that the magnitude of the magnetic field (B_x,

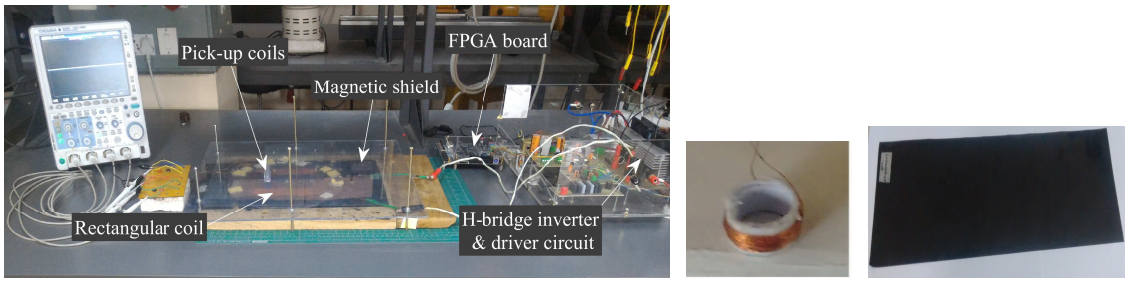

(a) (b) (c)

Figure 3.8: Experimental set-up (a) hardware prototype, (b) pick-up coil and (c) magnetic shield.

B_y, and B_z) for the coil system having a magnetic shield is higher than the magnitude of the magnetic field for the coil system without the shield.

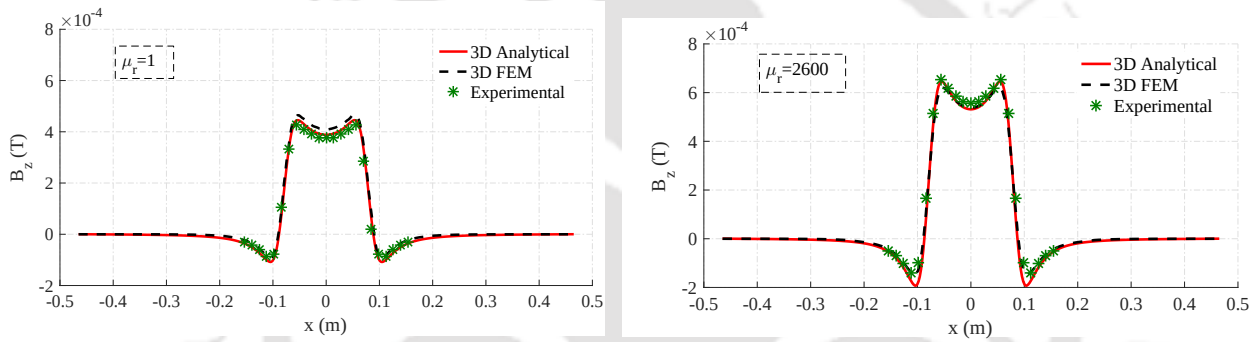

(a) (b)

Figure 3.9: Magnetic field distribution of B_z along x-direction at $y = 0$ and $z = 2$ cm (a) without shielding and (b) with shielding.

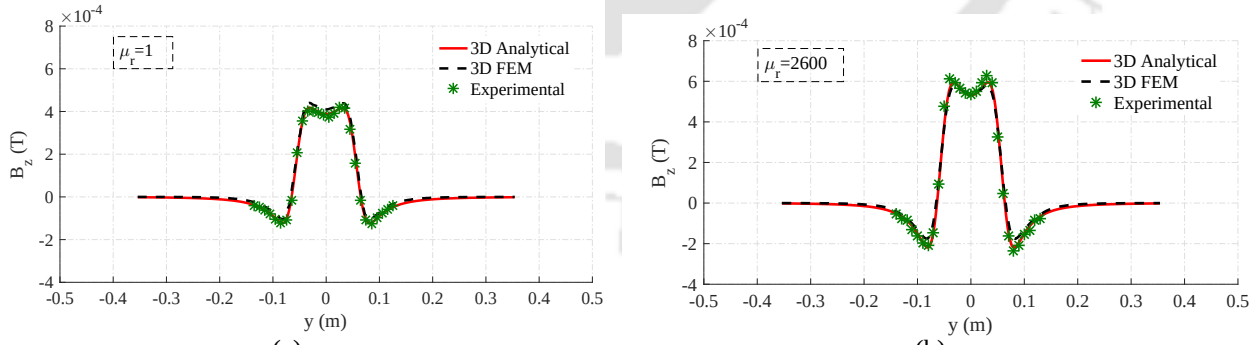

(a) (b)

Figure 3.10: Magnetic field distribution of B_z along y-direction at $x = 0$ and $z = 2$ cm (a) without shielding (b) with shielding and.

Here, the magnetic field distribution obtained from the analytical model has been compared with the results obtained from 3-D FEA and experimental. It is observed that the magnetic field distribution obtained from the analytical model matches with the results obtained from 3-D FEA and experimen-

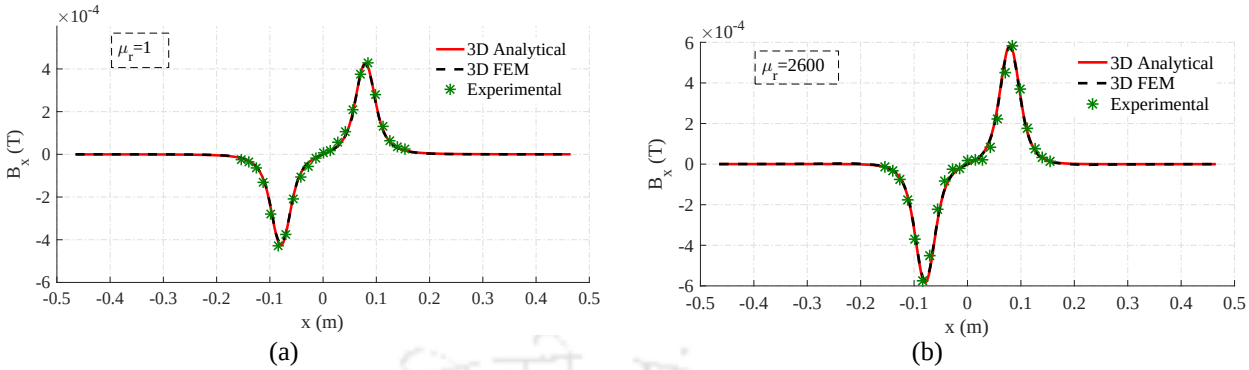

Figure 3.11: Magnetic field distribution of B_x along x-direction at $y = 0$ and $z = 2$ cm (a) without shielding and (b) with shielding.

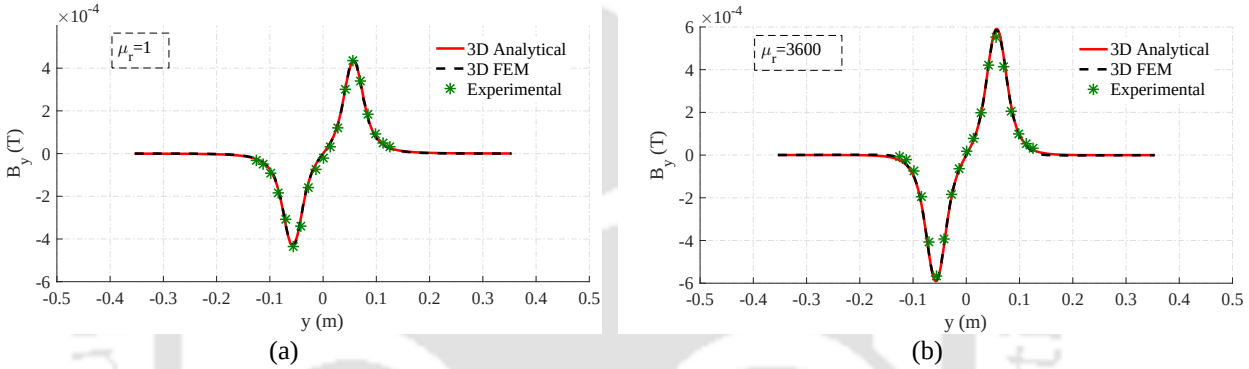

Figure 3.12: Magnetic field distribution of B_y along x-direction at $x = 0$ and $z = 2$ cm (a) without shielding and (b) with shielding.

tal, which confirm the accuracy of the proposed analytical model. The next subsection presents a comparison in mutual inductance for different misalignments obtained from the analytical model, 3-D FEA, and measurements.

3.4.4 Mutual Inductance

The proposed analytical model is used to calculate the mutual inductance for different misalignments. The mutual inductance from the analytical model is calculated by surface integration of the magnetic field in Region V obtained from (3.12), over the rectangular surface of dimension $2a_2$ and $2b_2$. The mutual inductance M is expressed as follows:

$$M = \frac{1}{I_p} \oiint B_V . dA \tag{3.26}$$

where I_p is the rms current flowing in primary coil.

The comparison of variations in mutual inductance without shielding and with shielding, obtained from analytical, FEA, and measurement are shown in Figs. 3.13-3.18. In the Figs. 3.13-3.18, for each misalignment, variation in mutual inductance with shielding shows the same pattern with a higher magnitude compared to without shielding. This is due to the reduction in leakage flux.

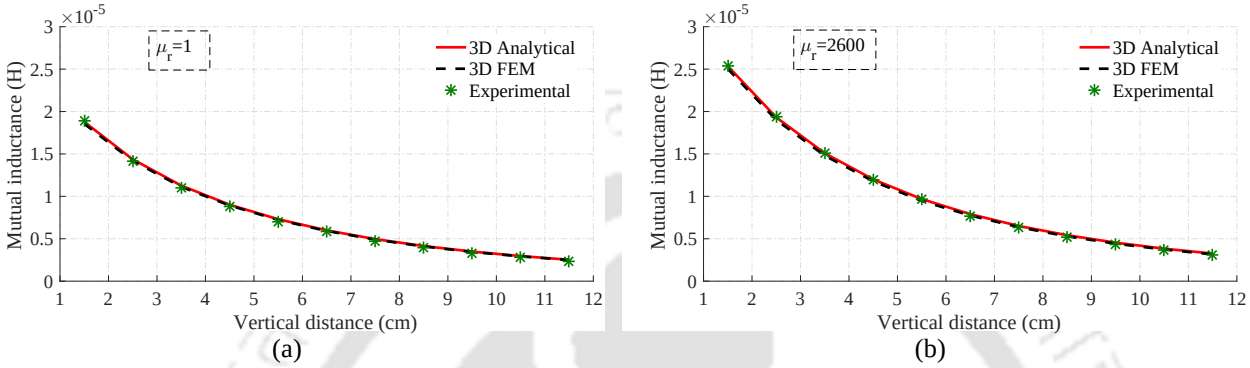

Figure 3.13: Mutual inductance variation in *z*-direction (a) without shielding and (b) with shielding.

Fig. 3.13 shows the variation of mutual inductance as the secondary coil moves along the *z*-direction. Here, mutual inductance decreases as the secondary coil moves along the *z*-axis because of the decrease in flux linkage.

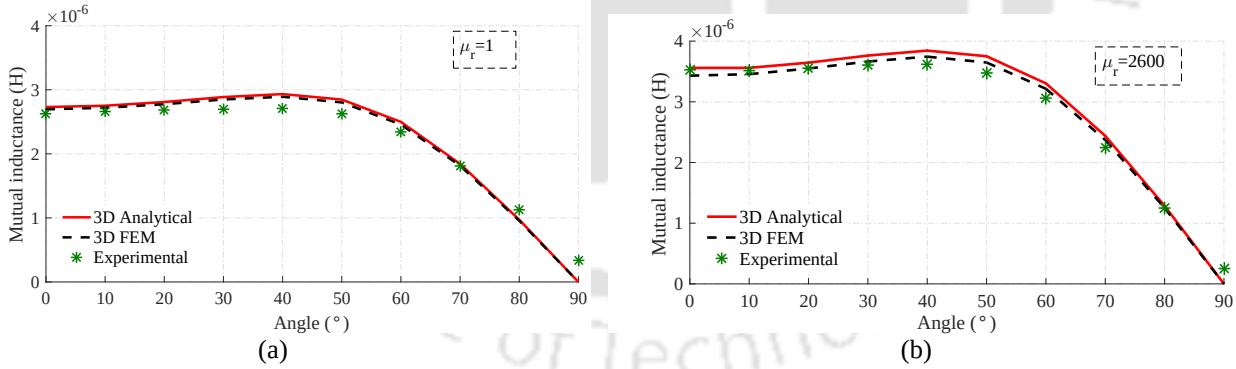

Figure 3.14: Mutual inductance variation for angular misalignment (a) without shielding and (b) with shielding.

The variation in mutual inductance due to angular misalignment is shown in Fig. 3.14. For the measurement, the centre position of the secondary coil is kept at $z = 10.25$ cm, and the coil is tilted around the *y*-axis from 0° to 90° with an interval of 10°. Here, until 40°, both the cease small variation in mutual inductance is observed, and after this, it decreases drastically. In this variation, B_x and B_z both contribute to mutual inductance as the coil tilt the contribution of B_z in mutual inductance

decreases.

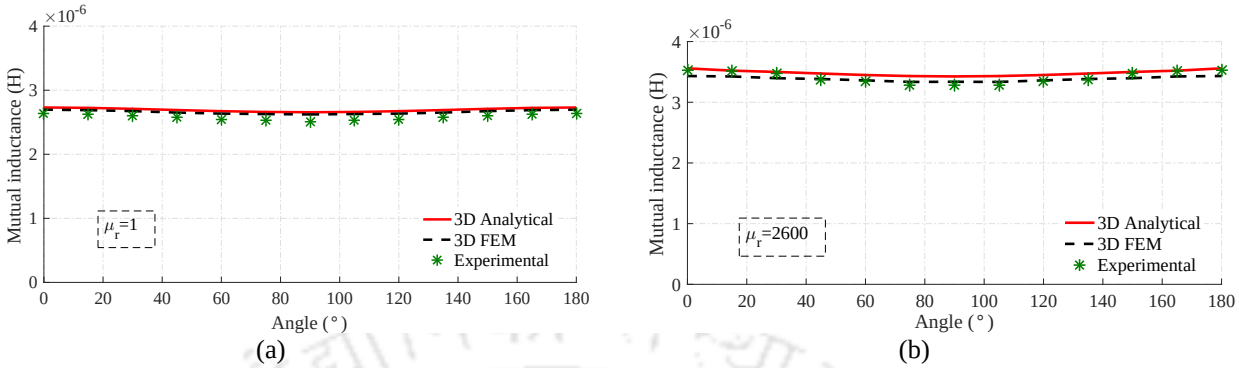

Figure 3.15: Mutual inductance variation for planar misalignment at z = 10.25 cm (a) without shielding and (b) with shielding.

Fig. 3.15 shows the variation in mutual inductance for a planar misalignment. Since in this variation, the plane of the secondary coil is in parallel with the plane of the primary coil. Therefore only B_z contributes to mutual inductance. Here, it is observed that mutual inductance decreases for 0° to 90° rotation of the secondary coil and again increases for 90° to 180° rotation. This is due to a decrease in the overlapping area between coils during the rotation of 0° to 90° and an increase in the overlapping area during the rotation of 90° to 180°.

The variation in mutual inductance for the case where secondary coil moves along the x -direction are reported in Figs. 3.16-3.18. It may be seen from Figs. 3.16-3.18, as the secondary coil moves away from the centre of the primary coil, there is a decrease in the overlapping area between the coils, and hence, the mutual inductance between the coils gets reduced.

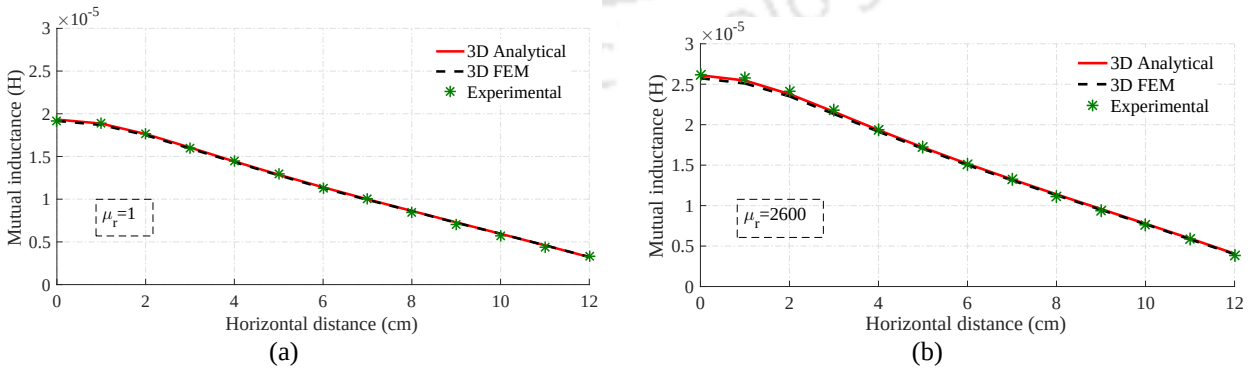

Figure 3.16: Mutual inductance variation for horizontal misalignment at z = 1.35 cm. (a) without shielding and (b) with shielding.

In Fig. 3.17 angular with horizontal misalignment (AHM) is illustrated. Here, the secondary coil moves along *x*-direction with the angular rotation of 10° and 20° around the *y*-axis, having its centre at z = 3.2 cm and 4.74 cm, respectively. From Fig. 3.17 it can be seen that horizontal misalignment for 10° rotation has a higher magnitude mutual inductance as compare to 10° rotation.

For the measurement of variation in mutual inductance due to planar with horizontal misalignment (PHM) is shown in Fig. 3.18. Here, the secondary coil moves along *x*-direction having z = 2.4 cm and planar rotation of 20° (around *z*-axis). Among all the misalignments shown in Figs. 3.13-3.18, it can be observed that planar misalignment shows the small variation in mutual inductance during the misalignment.

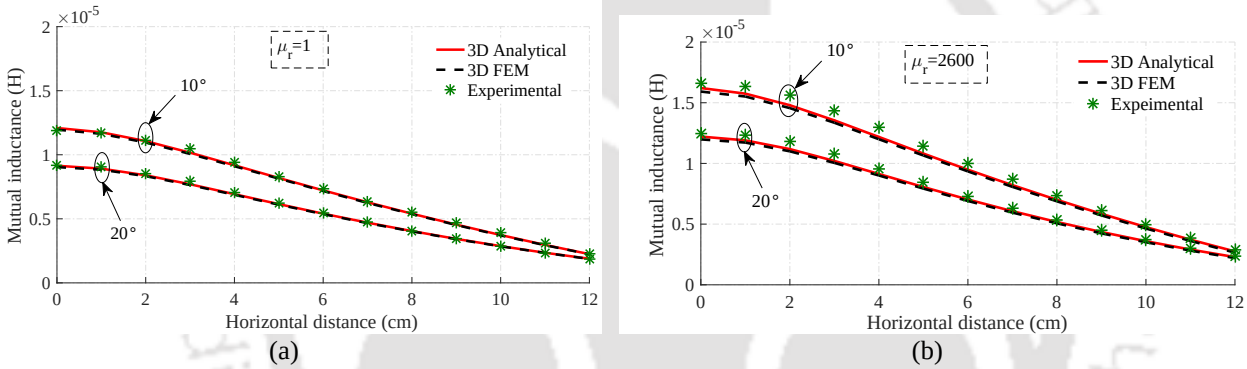

Figure 3.17: Mutual inductance variation for both angular and horizontal misalignment. (a) without shielding and (b) with shielding.

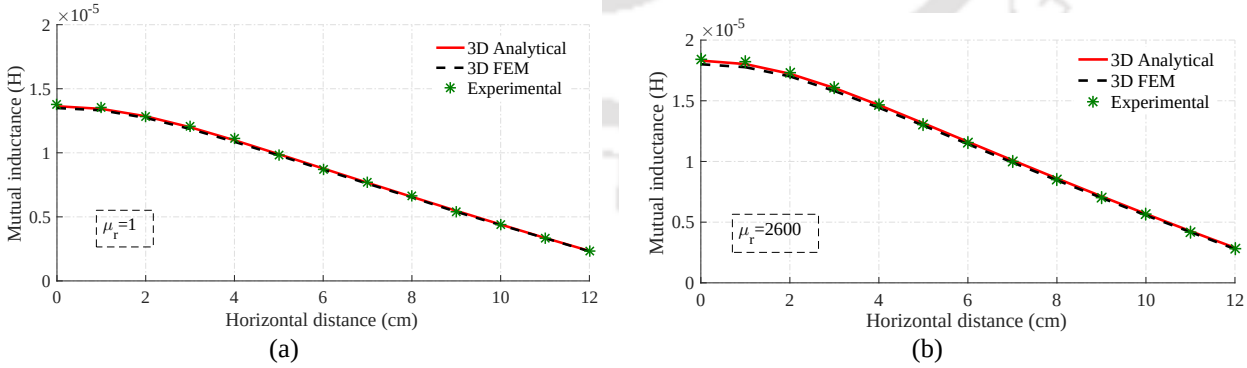

Figure 3.18: Mutual inductance variation for both planar and horizontal misalignment. (a) without shielding and (b) with shielding.

The magnetic field obtained in Region IV is used to calculate the self-inductance (L_p) of the

primary coil (with and without shielding). The expression for the self-inductance is given in (3.27)

$$L_p = \frac{1}{I_p} \oiint B_{IV}.dA \tag{3.27}$$

The obtained self-inductances (with and without shielding) from an analytical model are compared in Table 3.2 with measured values. The self-inductances are measured at 100 kHz with the help of LCR meter.

Table 3.2: Comparison of the primary self-inductance (L_p)

Coil	Analytical (μH)	Measured (μH)
Without shielding	28.41	28.74
With shielding	41.12	40.50

In this subsection, the variation in mutual inductance for different misalignments are shown in Figs. 3.13-3.18. It is observed that for the coil system shown in Fig. 3.1, mutual inductance variation obtained from the analytical model, FEA, and experiment are following the same pattern, which confirms the accuracy of the proposed analytical model. The next subsection compares proposed analytical results with the analytical model reported in [1].

3.4.5 Comparison with method given in [1]

The calculated mutual inductance by the proposed model has been compared with the model given in [1]. In [1], the mutual inductance is calculated based on the Biot-Savart principle. The integrals used in the Biot-Savart formula are computed numerically. The numerical calculation is done by dividing each turn area of the secondary coil into multiple small areas. Then, the flux linked with each small region is calculated. The flux linked to the single turn of the secondary coil has been calculated by summing all the flux linkage of small regions. The same procedure has been repeated for all the turns. The accuracy and computational time of mutual inductance calculation in this method depend on the number of small regions of the receiver coil. To calculate the mutual inductance from [1], the secondary coil is divided into 20 and 16 divisions in the *x*- and *y*-directions, respectively. For achieving high accuracy, the number of divided regions required, which increases computational time. Moreover, this method does not calculate mutual inductance for the coil system, which has magnetic shielding near the coils. However, the proposed model is able to calculate mutual

inductance for both the coil system (coil system surrounded by air and magnetic shield as well). Therefore, the coils that are surrounded by air have been selected for comparison.

The comparison for angular, planar, and horizontal misalignment without shielding is given in Table 3.3. At a vertical height of $z = 10.25$ cm, the mutual inductance for angular, planar, and horizontal misalignment are calculated. The values of mutual inductance obtained from the proposed model and [1] are given in Table 3.3. The difference obtained in Table 3.3 is due to the consideration

Table 3.3: Comparison of Angular, Planar, and Horizontal Misalignment Results with [1]

Angular misalignment				Planar misalignment				Horizontal misalignment			
Angle (°)	[1] (μH)	This work (μH)	Discrepancy (μH)	Angle (°)	[1] (μH)	This work (μH)	Discrepancy (μH)	Distance (cm)	[1] (μH)	This work (μH)	Discrepancy (μH)
0	2.883	2.810	0.073	0	2.883	2.810	0.073	0	2.883	2.810	0.073
10	2.913	2.841	0.072	10	2.879	2.807	0.072	1	2.863	2.790	0.073
20	2.993	2.928	0.071	20	2.867	2.796	0.071	2	2.803	2.732	0.071
30	3.121	3.056	0.065	30	2.851	2.781	0.070	3	2.707	2.637	0.070
40	3.214	3.165	0.049	40	2.833	2.764	0.069	4	2.579	2.511	0.068
50	3.126	3.106	0.02	50	2.816	2.747	0.069	5	2.424	2.359	0.065
60	2.690	2.689	0.001	60	2.800	2.732	0.068	6	2.248	2.185	0.063
70	1.932	1.932	0	70	2.788	2.721	0.067	7	2.056	1.997	0.059
80	1.001	1.009	0.008	80	2.781	2.713	0.068	8	1.854	1.798	0.056
90	0	0	0	90	2.778	2.710	0.068	9	1.646	1.594	0.052
								10	1.437	1.390	0.047

of small regions of the receiver coil. But in the proposed model, the mutual inductance is calculated by solving the equations in the required region.

3.5 Summary

A 3-D analytical model to calculate the distribution of magnetic flux density and mutual inductance for different misalignments for a coil system having a magnetic shield below the primary coil is proposed. This model has the flexibility to change the width and permeability of shielding material. A comparison in mutual inductance for coil system with shield and without shield has been made. It is observed that the coil system having a magnetic shield below the primary coil shows higher mutual inductance than the coil system without the shield. For the modelling, magnetic vector and scalar potential definitions in the Cartesian coordinate system is used. The magnetic flux density distribution and mutual inductance calculations obtained from the analytical model, FEA, and experiment results

are in close agreement.

In the proposed model, the length of the magnetic shield is infinite, which is impractical. The next chapter discusses the analytical modelling, which includes magnetic shielding of finite length.

Note: The contribution of this chapter is published in:

B. K. Kushwaha, G. Rituraj and P. Kumar, "3-D Analytical Model for Computation of Mutual Inductance for Different Misalignments With Shielding in Wireless Power Transfer System," IEEE Trans. Transp. Electrif., *vol. 3, no. 2, pp. 332-342, June 2017.*

4

A Subdomain Analytical Model of Coil System with Magnetic Shields of Finite Dimensions and Finite Permeability for WPT systems

Contents

4.1	Introduction	66
4.2	2-D Subdomain Model for the Coil System	67
4.3	Superposition of Two 2-D Subdomain Models	83
4.4	Verification of Analytical Model	88
4.5	Summary	90

4.1 Introduction

The previous chapter discussed a 3-D analytical model to calculate the mutual inductance for a coil system, which includes a magnetic shield below the primary coil using a harmonic modelling technique. Here, the permeability of the magnetic shield was finite, but the dimension of the magnetic shield was infinite, which is impractical. Hence, the analytical model for the coil system with magnetic shields of finite dimension, for both the primary and the secondary coil, is needed. Fig. 4.1(a) shows a coil system that is closer to the actual scenario.

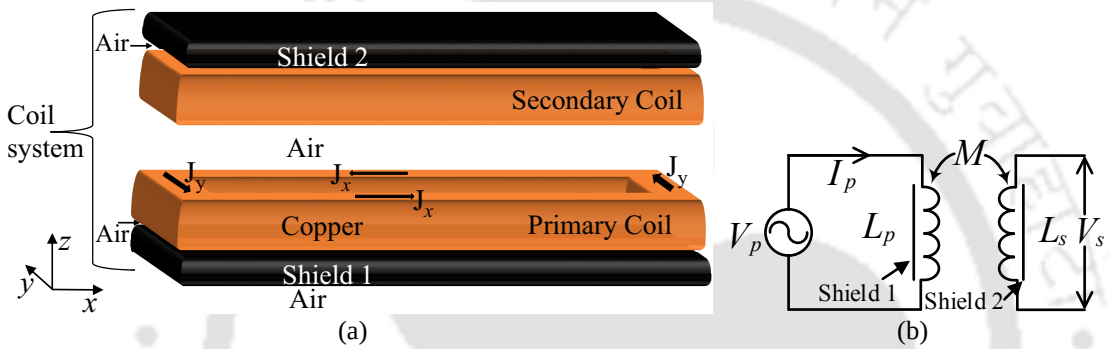

Figure 4.1: (a) 3-D illustration of the coil system (Shields 1 and 2 have finite dimensions and finite permeability). (b) An equivalent circuit model of the coil system (Here, V_p and I_p are the high-frequency voltage source and primary current, respectively. L_p and L_s are the self-inductances of the primary and secondary coils, and M is the mutual inductance between these coils. V_s is the open-circuit voltage of the secondary coil. The primary coil generates the high-frequency magnetic field through I_p, and the secondary coil receives these magnetic fields to generate the voltage V_s).

In the harmonic modelling technique, the coil system is divided only in non-periodic regions(i.e., in the z-direction). Therefore, in the previous chapter, the dimension of the magnetic shield was infinite. While in practice, the material in electromechanical system changes in periodic and non-periodic directions both. To include the different medium changes in both the direction, researcher have modified the harmonics modelling technique with the mode matching technique [72, 74–76]. With this technique [73] has presented an analytical model having the magnetic shielding of finite dimension but the infinite permeability. The analytical model with the assumption of infinite permeability does not give the effect of a finite permeable shield, which is practically used.

Further, to incorporate the magnetic shield of finite permeability and finite dimension in modelling, the author Pluk *et al.* [95] assume non-physical boundaries of infinite permeability at horizontal (x-direction)-edges of the magnetic shield. This assumption introduces error in the analytical

results [95], which depends on the thickness of the used magnetic shield.

Developing a 3-D analytical model for the system shown in Fig. 4.1(a) is difficult because it requires more equations in the mathematical formulation compared to the 2-D analytical model. Therefore, this chapter proposes a 2-D analytical model using the subdomain technique [96] to incorporate the finite dimension of the magnetic shields. This subdomain model incorporates magnetic shields of finite dimension and finite permeability, as shown in Fig. 4.1(a). A 3-D subdomain model is developed using the superposition of two 2-D subdomain models to get tangible results. These 2-D subdomain models are developed for *xz*- and *yz*-planes, which are invariant in their third direction (i.e., in the y-direction for *xz*-plane and the x-direction in *yz*-plane). In this context, a correction factor for 2-D subdomain models is introduced to make it variant in their third direction. The proposed 3-D subdomain model can incorporate any changes in the parameters of magnetic shielding such as length, width, and relative permeability. Moreover, with the proposed subdomain model, square and rectangular coil system of any dimensions can be designed and analyzed. The accuracy of the proposed 3-D subdomain model is verified by comparing the results, for the vertical and horizontal misalignments, of the 3-D subdomain model with results of 3-D FEA and measurements.

The organization of this chapter is as follows. Section 4.2 presents an overview of the considered coil system along with a 2-D subdomain model. Further, this section compares the results obtained from the proposed 2-D subdomain model with 2-D FEA to verify its accuracy. Section 4.3 provides a 3-D subdomain model using the superposition of two 2-D subdomain models along with the correction factors. Section 4.4 verifies the results obtained from the 3-D subdomain model with results obtained from 3-D FEA and measurements. Finally, section 4.5 surmises the presented work.

4.2 2-D Subdomain Model for the Coil System

This Section explains each step involved in developing the 2-D subdomain model of the coil system shown in Fig. 4.1(a). Section 4.2.1 describes the division of the coil system in different regions based on their material properties. In section 4.2.2 the differential equations for magnetic vector potential are solved for each region, which contains various unknown coefficients. These unknown coefficients are calculated by applying the interface conditions in each region, which is discussed in section 4.2.4. Finally, the obtained analytical results are compared with 2-D FEA results

in section 4.2.5. The steps involved in creating a 2-D subdomain model for the coil system shown in Fig. 4.1(a) are summarized in Fig. 4.2.

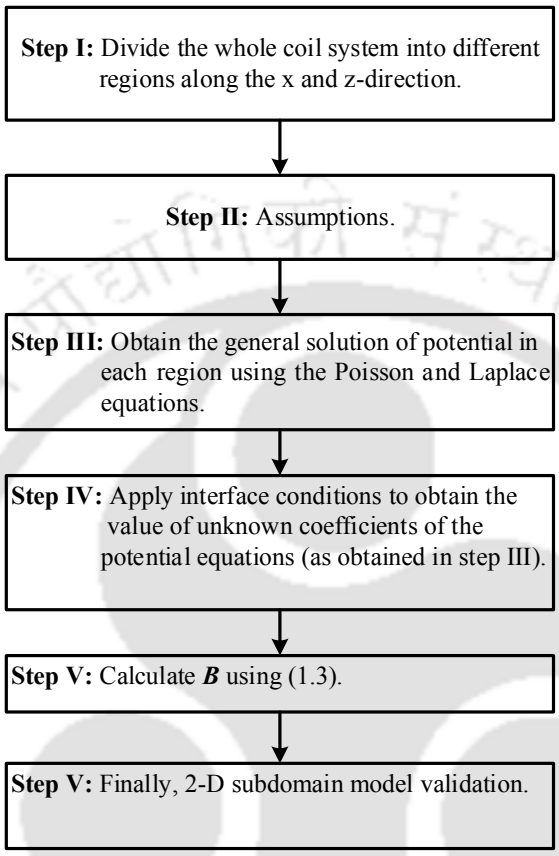

Figure 4.2: Steps involved in creating the 2-D subdomain model.

4.2.1 System Overview

Fig. 4.1(a) shows a 3-D illustration of the considered coil system. The rectangular coils in Fig. 4.1(a) are named as primary coil and secondary coil, and the magnetic shields below and above them are called Shield 1 and Shield 2, respectively. In this work, the primary coil together with Shield 1, is called the primary coil arrangement, whereas the secondary coil together with Shield 2 is called the secondary coil arrangement. Here, two geometrically identical rectangular coils and magnetic shields are taken. However, the presented model is general and can be used for different dimensions of magnetic shields and coils.

Fig. 4.3 shows the detailed cross-sectional view (*xz*-plane) of the coil system (Fig. 4.1(a)), used for formulating the 2-D subdomain model, and Table 4.1 gives the geometrical parameters for the coil

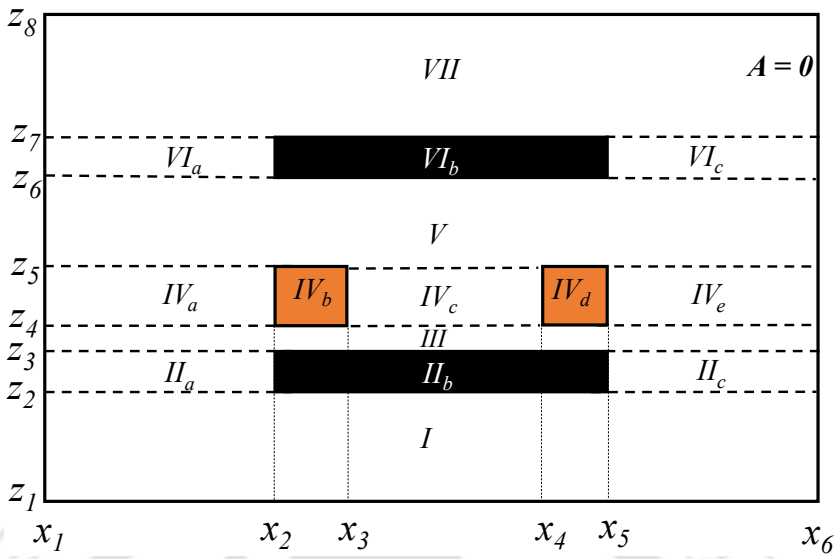

Figure 4.3: *xz*-face of the coil system.

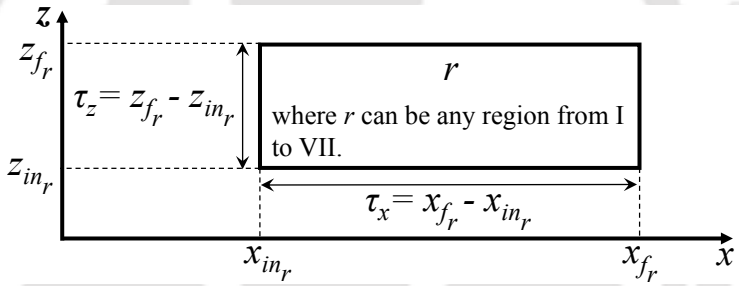

Figure 4.4: Co-ordinate representation of different regions demonstrated in Fig. 4.3.

system. These parameter has been chosen as an example to verify the subdomain model; however, one can use this subdomain model for different dimensions of the coil system shown in Fig. 4.1(a).

The whole coil system is divided into several regions in the horizontal (*x*-direction) as well as in the vertical (*z*-direction) directions, as shown in Fig. 4.3. These regions are divided based on the interaction of different material properties. Region *I* represents air medium below the Shield 1, whereas Region *VII* represents the air medium above the Shield 2. Regions II_b and VI_b represent Shield 1 and Shield 2, respectively. The air medium to the left of the Shield 1 is called Region II_a, whereas the one to the right, is called Region II_c. Similarly, the air medium to the left and right side of Shield 2 is represented as Regions VI_a and VI_c, respectively. Region *III* is the air gap between the primary coil and the Shield 1, and Region *V* represents the air gap between the primary coil and Shield 2. Since the secondary coil is open-circuited hence carries no current, it is included in the Region *V*. Regions IV_a and IV_e represent the air medium to the left and the right side of the primary

coil, respectively. Regions IV_b and IV_d, respectively, represent the two coil sides (carrying current inward and outward of the *xz*-plane , i.e., in the *y*-direction) of the primary coil. The Region IV_c represents the air medium between the two coil sides of the primary coil.

The proposed analytical model considers the following assumptions:

- The eddy-current induced in magnetic shields are neglected;
- The magnetic shields used in coil system are considered as isotropic;
- The coil system is surrounded by a vacuum through a rectangular box, as shown in Fig. 4.3. The magnetic vector potential to at the edge of this rectangular box is assumed zero;
- The temperature-dependent quantity such as resistance of the primary coil is neglected in magnetic modelling;
- No current exists in the z-direction.

Table 4.1: Parameters of the Coil System and Subdomain Model

Parameters, symbols	Value
Diameter of the primary and secondary coils (w)	2.4 mm
Number of turn in primary and secondary coils ($turn$)	11
Relative permeability of Shield 1 and Shield 2 (μ_{IIb}, μ_{VIb})	20000
Geometrical specification in the x-direction (x_1, x_2, x_3, x_4, x_5, x_6)	(0, 45, 47.75, 60.85, 63.60, 108.6) cm
Coil length in the x-direction x_5-x_2	18.6 cm
Coil length in the y-direction y_5-y_2	14.11 cm
Geometrical specification in the x-direction (z_1, z_2, z_3, z_4, z_5)	(-100.511, -0.511, -0.509, 0, 0.25) cm
Current density in the primary coil (at 3.5 A)	0.56 A-mm^{-2}
Number of Harmonics in x- direction for Big region (N_I, N_{III}, N_V, N_{VII})	210
Harmonics in x- direction for Regions II_a,II_b,II_c (N_{IIa}, N_{IIb}, N_{IIc})	100
Harmonics in z- direction for Regions II_a,II_b,II_c (L_{IIa}, L_{IIb}, L_{IIc})	30
Harmonics in x- direction for Regions IV_a,IV_c,IV_e (N_{IV_a}, N_{IVc}, N_{IVe})	50
Harmonics in z- direction for Regions IV_a,IV_c,IV_e (L_{IVa}, L_{IVc}, L_{IVe})	30
Harmonics in x- direction for Regions IV_b,IV_e (N_{IV_a}, N_{IVc}, N_{IVe})	60
Harmonics in z- direction for Regions IV_b,IV_e (L_{IVa}, L_{IVc}, L_{IVe})	60
Harmonics in x- direction for Regions VI_a, VI_b, VI_c (N_{IIa}, N_{IIb}, N_{IIc})	100
Harmonics in z- direction for Regions VI_a, VI_b, VI_c (L_{IIa}, L_{IIb}, L_{IIc})	30

The magnetic vector potential formulation has been used in subdomain modelling. A region r has been defined to represent the magnetic vector potential for each subdomain, as shown in Fig. 4.4. The inial and final co-ordinates in the x-direction of region r are denoted by x_{in_r} and x_{f_r}, whereas in the z-direction, they are denoted by z_{in_r} and z_{f_r}, respectively. The region r can be any of the regions, from I to VII, as shown in Fig. 4.3. The exact values of x_{in_r}, x_{f_r}, z_{in_r}, and z_{f_r} for a particular region can be taken from Fig. 4.3. For example, the values of x_{in_r}, x_{f_r}, z_{in_r}, and z_{f_r} for the region IV_c (r = IV_c) are x_3, x_4, z_4, and z_5, respectively.

The magnetic field for each described region is calculated by magnetic vector potential, which is obtained using the Poisson and Laplace equations, as discussed in the next subsection.

4.2.2 Magnetic Field Description

The magnetic vector potential in the region where the current density is present (i.e., regions IV_b and IV_d in Fig. 4.3), governed by the Poisson's equation [77], given by (4.1)

$$\frac{\partial^2 \mathbf{A}_r}{\partial x^2} + \frac{\partial^2 \mathbf{A}_r}{\partial z^2} = -\mu_0 \mathbf{J} \tag{4.1}$$

whereas, for all other regions (except IV_b and IV_d) where the current density is absent; it is governed by the Laplace's equation and is given as

$$\frac{\partial^2 \mathbf{A}_r}{\partial x^2} + \frac{\partial^2 \mathbf{A}_r}{\partial z^2} = 0 \tag{4.2}$$

The magnetic flux density is calculated using the magnetic vector potential by (4.3)

$$\mathbf{B}_r = \nabla \times \mathbf{A}_r \tag{4.3}$$

Here, $\mathbf{A}_r$ is the magnetic vector potential for rth region (the regions are shown in Fig. 4.3). The magnetic field intensity is calculated by

$$\mathbf{H}_r = \mathbf{B}_r / \mu_r \mu_0 \tag{4.4}$$

Here, μ_r is relative permeability of region r, and μ_0 is relative permeability of air medium.

From the (4.3), it can be seen that the calculation of the magnetic field requires magnetic vector

potential. The next subsection presents the expressions of vector potentials for each region discussed in section 4.2.1.

4.2.3 Magnetic Vector Potentials

For the *xz*- the plane has been considered for modelling, and the current density vector has only a component in the *y*-direction. Therefore, the magnetic vector potential has only one component in the *y*-direction. This subsection gives the magnetic vector potentials of each region. Sub-sub section 4.2.3.1 presents the solution of vector potential for the coil and shield region. The solution of the magnetic vector potential for the regions existing between the primary coil to shield 1 and shield 2 is given in sub-sub section 4.2.3.1. Finally, sub-sub section 4.2.3.3 and sub-sub section 4.2.3.4 give the solution of magnetic vector potential for the regions which have a boundary with zero potential regions.

4.2.3.1 Regions II_b, IV_b, IV_d, and VI_b

Region II_b and VI_b represent shield 1 and shield 2, respectively, whereas Region II_b and VI_b define the primary coil. The forward conductor is represented by Region IV_b, whereas Region IV_d represents the return conductor. The expression of magnetic vector potential for coil region (IV_b and IV_d) is obtained by solving (4.1), and given by (4.5). The expression of magnetic vector potential for shield regions (II_b and VI_b), is obtained by solving (4.2) and given by (B.66).

$$\mathbf{A}_r = (A_y^x + A_y^z + A_y^s)\,\vec{e_y} \tag{4.5}$$

$$\mathbf{A}_r = (A_y^x + A_y^z)\,\vec{e_y} \tag{4.6}$$

where A_y^x, A_y^z, and A_y^s are given as

$$\begin{aligned} A_y^x &= (z_{f_r} - z)c_{0_r} + (z - z_{in_r})d_{0_r} + \sum_{n_r=1}^{N_r} \cos(k_{x_r}(x - x_{in_r})) \cdot \\ &\quad \left(c_r \frac{\sinh(k_{x_r}(z_{f_r} - z))}{\sinh(k_{x_r}\tau_{z_r})} + d_r \frac{\sinh(k_{x_r}(z - z_{in_r}))}{\sinh(k_{x_r}\tau_{z_r})}\right) \end{aligned} \tag{4.7}$$

$$A_y^z = \sum_{l_r=1}^{L_r} \left(-\frac{e_r \cosh(k_{z_r}(x - x_{f_r}))}{k_{z_r}\sinh(k_{z_r}\tau_{x_r})} + \frac{f_r \cosh(k_{z_r}(x - x_{in_r}))}{k_{z_r}\sinh(k_{z_r}\tau_{x_r})}\right) \cdot \sin(k_{z_r}(z - z_{in_r}))$$

$$A_y^s = -0.5\mu_0 J_y y^2 \tag{4.8}$$

Here, for a region r, n_r and l_r are the spatial harmonic orders in the x-and z-directions, respectively, and c_{0_r}, d_{0_r}, c_r, d_r, e_r, and f_r are unknown coefficients. k_{x_r} and k_{z_r} are the spatial frequencies in the x and z-directions with the periods of $\tau_{x_r} = (x_{f_r} - x_{in_r})$ and $\tau_{z_r} = (z_{f_r} - z_{in_r})$, respectively, and are given by (4.9).

$$k_{x_r} = n_r\pi/\tau_{x_r},\ k_{z_r} = l_r\pi/\tau_{z_r}. \tag{4.9}$$

4.2.3.2 Regions *III* and *V*

Regions *III* and *V* both represent air medium. Region *III* exists between shield 1 and the primary coil, whereas region *V* is the region between the primary coil and shield 2. The two edges of these regions have zero potential at $x=x_1$ and $x=x_6$, respectively. The magnetic vector potential for the region *III* and region *V* is given as

$$\mathbf{A}_r = \sum_{n_r=1}^{N_r} \left(-\frac{c_r \cosh(k_{x_r}(z - z_{f_r}))}{k_{x_r} \sinh(k_{x_r}\tau_{z_r})} + \frac{d_r \cosh(k_{x_r}(z - z_{in_r}))}{k_{x_r} \sinh(k_{x_r}\tau_{z_r})} \right) \cdot \sin(k_{x_r}(x - x_{in_r}))\, \vec{e_y} \tag{4.10}$$

4.2.3.3 Regions *IIa*, *IIc*, *IVa*, *IVc*, *IVe*, *VIa*, and *VIc*

The magnetic vector potential for these regions is described by (4.11)

$$\mathbf{A}_r = (A_y^x + A_y^z)\, \vec{e_y} \tag{4.11}$$

where the expression of A_y^x and A_y^z is given by (4.12) and (4.13), respectively.

$$A_y^x = \sum_{n_r=1}^{N_r} \left(c_r \frac{\sinh(k_{x_r}(z_{f_r} - z))}{\sinh(k_{x_r}\tau_{z_r})} + d_r \frac{\sinh(k_{x_r}(z - z_{in_r}))}{\sinh(k_{x_r}\tau_{z_r})} \right) \cdot \sin(k_{x_r}(x - x_{in_r})) \tag{4.12}$$

$$A_y^z = \sum_{l_r=1}^{L_r} \left(e_r \frac{\sinh(k_{z_r}(x_{f_r} - x))}{\sinh(k_{z_r}\tau_{x_r})} + f_r \frac{\sinh(k_{z_r}(x - x_{in_r}))}{\sinh(k_{z_r}\tau_{x_r})} \right) \cdot \sin(k_z(z - z_{in_r})) \tag{4.13}$$

The magnetic vector potential for regions *IIa*, *IVa*, and *VIa* is obtained by putting $e_r = 0$ in (4.13), whereas for regions *IIc*, *IVe*, and *VIc*, the magnetic vector potentials are obtained by assigning $f_r = 0$ in (4.13).

4.2.3.4 Regions *I* and *VII*

Region *I* and *VII* represents air medium below the shield 1 and above the shield 2, respectively. The magnetic vector potential at the three sides of these regions is equal to zero, which leaves the interface condition to be applicable at only one side for the region. The expression of magnetic vector potential for regions *I* and *VII* are obtained by applying $c_r = 0$ and $d_r = 0$, respectively, in (4.14).

$$\mathbf{A}_r = \sum_{n_r=1}^{N_r} \left(-\frac{c_r \sinh(k_{x_r}(z_{f_r} - z))}{k_{x_r} \cosh(k_{x_r}\tau_{z_r})} + \frac{d_r \sinh(k_{x_r}(z - z_{in_r}))}{k_{x_r} \cosh(k_{x_r}\tau_{z_r})} \right) \cdot \sin(k_{x_r}(x - x_{in_r}))\, \vec{e_y} \tag{4.14}$$

The expression magnetic vector potential for each region is presented in Appendix C.

For the calculation of magnetic field density using (4.3), the unknown coefficients of magnetic vector potentials should be known for each region. These unknown coefficients are determined using the boundary condition, which is applied between each region, and it is explained in the next subsection.

4.2.4 Boundary Conditions

The boundary conditions are applied between the *x* and *z* edge of each region. Here, the divided regions are shown in Fig. 4.3, are classified as big and small regions based on the width of the region along the *x*-direction. The example is shown in Fig. 4.5 explains the application of boundary conditions. The big region is denoted by region *p*, where *p* can be the region *I*, *III*, *V*, or *VII*, as shown in Fig. 4.3. The small region is denoted by q_j, where *q* can be the region *II*, *IV*, *VI*, or *j* can be *a* to *e* (decided by Fig. 4.3). For example, if *q* is region *II*, then *j* is *a* to *c*, and if *q* is region *IV*, then *j* is *a* to *e*. The interaction of a big region with small regions occur at z', as shown in Figs. 4.5(a) and 4.5(b). Here, z' can be z_2 to z_7. The interface of subregions occurs at x', as shown in Figs. 4.5(c) and 4.5(d). Here, the interface between *a* and *b* is shown. Although, it can be between *b* and *c* or *c* and *d* or *d* and *e* depending on the value of x'. The value of x' can be x_2 to x_5.

The boundary conditions are defined by the continuity of tangential magnetic field intensity and magnetic vector potentials at *x* and *z* edge of each subregion. The tangential magnetic field strength H_{xp} must be equal to tangential magnetic field strength H_{xqj} of each subregion for respective width subregion at z', as shown in Fig. 4.5(a). The magnetic vector potential of each region q_j must be

equal to the magnetic vector potential of the region p at z', as shown in Fig. 4.5(b). Similarly, in Figs. 4.5(c) and 4.5(d), the continuity of tangential magnetic field strength and magnetic vector potential should be at x'. The boundary conditions can be written as

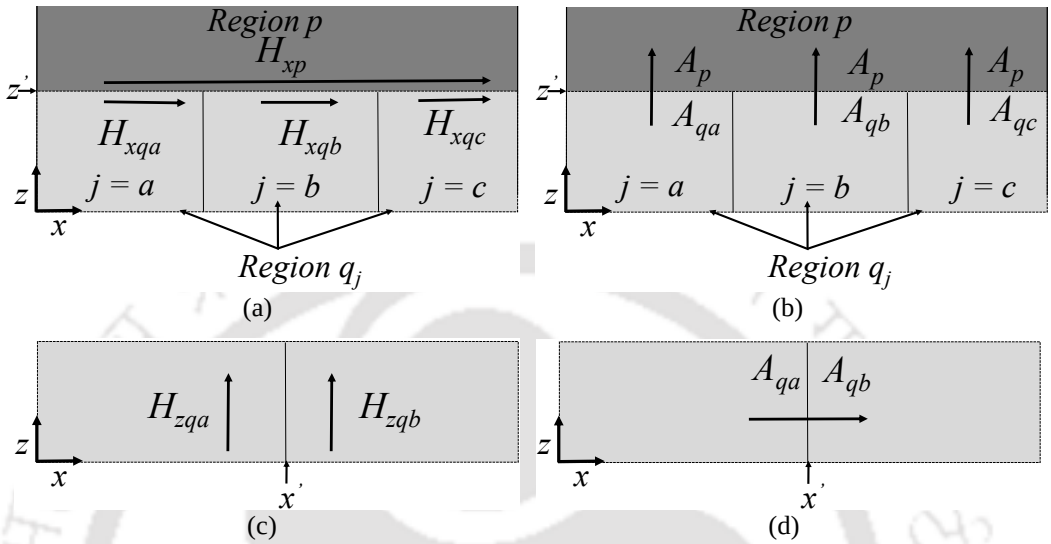

Figure 4.5: Illustration of the interface conditions by continuity of (a) magnetic field intensity and (b) magnetic vector potential at $z=z'$, and continuity of (c) magnetic field intensity and (d) magnetic vector potential at $x=x'$.

$$\mathbf{H}_{xp}(x,z') = \sum_j \mathbf{H}_{xqj}(x,z') \text{ where } x_{in_{qj}} \le x \le x_{in_{qj}} + \tau_{x_{qj}} \tag{4.15}$$

$$\mathbf{A}_{qj}(x,z') = \mathbf{A}_p(x,z') \text{ where } x_{in_{qj}} \le x \le x_{in_{qj}} + \tau_{x_{qj}} \tag{4.16}$$

$$\mathbf{H}_{zqb}(x',z) = \mathbf{H}_{zqa}(x',z) \text{ where } z_{in_{qb}} \le z \le z_{in_{qb}} + \tau_{z_{qb}} \tag{4.17}$$

$$\mathbf{A}_{qa}(x',z) = \mathbf{A}_{qb}(x',z) \text{ where } z_{in_{qa}} \le z \le z_{in_{qb}} + \tau_{z_{qb}}. \tag{4.18}$$

The boundary condition at the edge of each region is given in Appendix C. The boundary conditions, given in (4.15)-(4.18), are applied between the regions having unequal width. This unequal width implies that regions have different fundamental spatial frequencies. Equations (4.15)-(4.18) show that two waveforms of different fundamental spatial frequencies should be equal for a specific interval, and it is implemented by expressing a Fourier series of one's region waveform into a specific interval (width of another region). Therefore, equations (4.15)-(4.18) can be implemented by (4.19)-(4.22),

respectively.

$$uc_p^x = \frac{1}{\tau_{x_{qj}}} \sum_{n_p=1}^{N_p} \sum_{j} \int_{x_{in_{qj}}}^{x_{in_{qj}}+\tau_{x_{qj}}} H_{xqj}(x, z') \sin(k_{x_p}(x - x_{in_p}))dx \tag{4.19}$$

$$uc_{qj}^x = \frac{1}{\tau_{x_{qj}}} \sum_{n_{qj}=1}^{N_{qj}} \int_{x_{in_{qj}}}^{x_{inqj}+\tau_{xqj}} A_p(x, z') \sin(k_{x_{qj}}(x - x_{in_{qj}}))dx \tag{4.20}$$

$$uc_{qb}^z = \frac{1}{\tau_{zqb}} \sum_{l_{qb}=1}^{L_{qb}} \int_{z_{in_{qb}}}^{z_{in_{qb}}+\tau_{zqb}} H_{zqa}(x', z) \sin(k_{z_{qb}}(z - z_{in_{qb}}))dz \tag{4.21}$$

$$uc_{qa}^z = \frac{1}{\tau_{zqa}} \sum_{l_{qa}=1}^{L_{qa}} \int_{z_{in_{qa}}}^{z_{in_{qa}}+\tau_{zzqa}} A_{qb}(x', z) \sin(k_{z_{qa}}(z - z_{in_{qa}}))dz \tag{4.22}$$

where uc is an unknown coefficient of region r, and depending on z', it can be c_r or d_r, whereas depending on x', it can be e_r or f_r. By using (4.19)-(4.22), the developed simultaneous linear equations are solved by rewriting these equations into matrix form as [83, 96].

$$[UC] = [BC]^{-1}[SV] \tag{4.23}$$

Here, the matrix $[BC]$ and $[UC]$ contain elements of known and unknown coefficients, respectively. The matrix $[SV]$ contains the elements representing the source within the equations. The expanded form of [UC] is given by (4.41).

$$UC = \Big[\ [UC_I]\ \ [UC_{IIa}]\ \ [UC_{IIb}]\ \ [UC_{IIc}]\ \ [UC_{III}]\ \ [UC_{IVa}]\ \ [UC_{IVb}]\ \ [UC_{IVc}]\ \ [UC_{IVd}]\ \ [UC_{IVe}]$$
$$[UC_V]\ \ [UC_{VIa}]\ \ [UC_{VIb}]\ \ [UC_{VIc}]\ \ [UC_{VII}]\ \Big]^T \tag{4.24}$$

Each element of [UC] is sub-matrix, the element of this submatrix represents unknown coefficients

of magnetic vector potentials described in subsection 4.2.3, given by (4.25)-(4.39).

$$[UC_I] = \left[[d_1^x]_{N_1\times 1}\right] \tag{4.25}$$

$$[UC_{IIa}] = \left[\, [c_{IIa}^x]_{N_{IIa}\times 1} \;\; [d_{IIa}^x]_{N_{IIa}\times 1} \;\; [f_{IIa}^z]_{L_{IIa}\times 1} \,\right] \tag{4.26}$$

$$[UC_{IIb}] = \left[\, [c0_{IIb}^x]_{1\times 1} \;\; [c_{IIb}^x]_{N_{IIb}\times 1} \;\; [d0_{IIb}^x]_{1\times 1} \;\; [c_{IIb}^x]_{N_{IIb}\times 1} \;\; [e_{IIb}^z]_{L_{IIb}\times 1} \;\; [f_{IIb}^z]_{L_{IIb}\times 1} \,\right] \tag{4.27}$$

$$[UC_{IIc}] = \left[\, [c_{IIc}^x]_{N_{IIc}\times 1} \;\; [d_{IIc}^x]_{N_{IIc}\times 1} \;\; [e_{IIc}^z]_{L_{IIc}\times 1} \,\right] \tag{4.28}$$

$$[UC_{III}] = \left[\, [c_{III}^x]_{N_{III}\times 1} \;\; [d_{III}^x]_{N_{III}\times 1} \,\right] \tag{4.29}$$

$$[UC_{IVa}] = \left[\, [c_{IVa}^x]_{N_{IVa}\times 1} \;\; [d_{IVa}^x]_{N_{IVa}\times 1} \;\; [f_{IVa}^z]_{L_{IVa}\times 1} \,\right] \tag{4.30}$$

$$[UC_{IVb}] = \left[\, [c0_{IVb}^x]_{1\times 1} \;\; [c_{IVb}^x]_{N_{IVb}\times 1} \;\; [d0_{IVb}^x]_{1\times 1} \;\; [d_{IVb}^x]_{N_{IVb}\times 1} \;\; [e_{IVb}^z]_{L_{IVb}\times 1} \;\; [f_{IVb}^z]_{L_{IVb}\times 1} \,\right] \tag{4.31}$$

$$[UC_{IVc}] = \left[\, [c_{IVc}^x]_{N_{IVc}\times 1} \;\; [d_{IVc}^x]_{N_{IVc}\times 1} \;\; [e_{IVc}^z]_{L_{IVc}\times 1} \;\; [f_{IVc}^z]_{L_{IVc}\times 1} \,\right] \tag{4.32}$$

$$[UC_{IVd}] = \left[\, [c0_{IVd}^x]_{1\times 1} \;\; [c_{IVd}^x]_{N_{IVd}\times 1} \;\; [d0_{IVd}^x]_{1\times 1} \;\; [d_{IVd}^x]_{N_{IVd}\times 1} \;\; [e_{IVd}^z]_{L_{IVd}\times 1} \;\; [f_{IVd}^z]_{L_{IVd}\times 1} \,\right] \tag{4.33}$$

$$[UC_{IVe}] = \left[\, [c_{IVe}^x]_{N_{IVe}\times 1} \;\; [d_{IVe}^x]_{N_{IVe}\times 1} \;\; [e_{IVe}^z]_{L_{IVe}\times 1} \,\right] \tag{4.34}$$

$$[UC_V] = \left[\, [c_V^x]_{N_V\times 1} \;\; [d_V^x]_{N_V\times 1} \,\right] \tag{4.35}$$

$$[UC_{VIa}] = \left[\, [c_{VIa}^x]_{N_{VIa}\times 1} \;\; [d_{VIa}^x]_{N_{VIa}\times 1} \;\; [f_{VIa}^z]_{L_{VIa}\times 1} \,\right] \tag{4.36}$$

$$[UC_{VIb}] = \left[\, [c0_{VIb}^x]_{1\times 1} \;\; [c_{VIb}^x]_{N_{VIb}\times 1} \;\; [d0_{VIb}^x]_{1\times 1} \;\; [d_{VIb}^x]_{N_{VIb}\times 1} \;\; [e_{VIb}^z]_{L_{VIb}\times 1} \;\; [f_{VIb}^z]_{L_{VIb}\times 1} \,\right] \tag{4.37}$$

$$[UC_{VIc}] = \left[\, [c_{VIc}^x]_{N_{VIc}\times 1} \;\; [d_{VIc}^x]_{N_{VIc}\times 1} \;\; [e_{VIc}^z]_{L_{VIc}\times 1} \,\right] \tag{4.38}$$

$$[UC_{VII}] = \left[[d_{VII}^x]_{N_{VII}\times 1}\right] \tag{4.39}$$

The matrix [BC] with its element is expressed as

$$
[BC] = \begin{bmatrix}
[I] & \left[K_{I}^{IIa}\right] & \left[K_{I}^{IIb}\right] & \left[K_{I}^{IIc}\right] & [0] & [0] & [0] & [0] & [0] & [0] & [0] & [0] & [0] & [0] & [0] \\
\left[K_{IIa}^{I}\right] & [I] & \left[K_{IIa}^{IIb}\right] & [0] & \left[K_{IIa}^{III}\right] & [0] & [0] & [0] & [0] & [0] & [0] & [0] & [0] & [0] & [0] \\
\left[K_{IIb}^{I}\right] & \left[K_{IIb}^{IIa}\right] & [I] & \left[K_{IIb}^{IIc}\right] & \left[K_{IIb}^{III}\right] & [0] & [0] & [0] & [0] & [0] & [0] & [0] & [0] & [0] & [0] \\
\left[K_{IIc}^{I}\right] & [0] & \left[K_{IIc}^{IIb}\right] & [I] & \left[K_{IIc}^{III}\right] & [0] & [0] & [0] & [0] & [0] & [0] & [0] & [0] & [0] & [0] \\
[0] & \left[K_{III}^{IIa}\right] & \left[K_{III}^{IIb}\right] & \left[K_{III}^{IIc}\right] & [I] & \left[K_{III}^{IVa}\right] & \left[K_{III}^{IVb}\right] & \left[K_{III}^{IVc}\right] & \left[K_{III}^{IVd}\right] & \left[K_{III}^{IVe}\right] & [0] & [0] & [0] & [0] & [0] \\
[0] & [0] & [0] & [0] & \left[K_{IVa}^{III}\right] & [I] & \left[K_{IVa}^{IVb}\right] & [0] & [0] & [0] & \left[K_{IVa}^{V}\right] & [0] & [0] & [0] & [0] \\
[0] & [0] & [0] & [0] & \left[K_{IVb}^{III}\right] & \left[K_{IVb}^{IVa}\right] & [I] & \left[K_{IVb}^{IVc}\right] & [0] & [0] & \left[K_{IVb}^{V}\right] & [0] & [0] & [0] & [0] \\
[0] & [0] & [0] & [0] & \left[K_{IVc}^{III}\right] & [0] & \left[K_{IVc}^{IVb}\right] & [I] & \left[K_{IVc}^{IVd}\right] & [0] & \left[K_{IVc}^{V}\right] & [0] & [0] & [0] & [0] \\
[0] & [0] & [0] & [0] & \left[K_{IVd}^{III}\right] & [0] & [0] & \left[K_{IVd}^{IVc}\right] & [I] & \left[k_{IVd}^{IVe}\right] & \left[K_{IVd}^{V}\right] & [0] & [0] & [0] & [0] \\
[0] & [0] & [0] & [0] & \left[K_{IVe}^{III}\right] & [0] & [0] & [0] & \left[K_{IVe}^{IVd}\right] & [I] & \left[K_{IVe}^{V}\right] & [0] & [0] & [0] & [0] \\
[0] & [0] & [0] & [0] & [0] & \left[K_{V}^{IVa}\right] & \left[K_{V}^{IVb}\right] & \left[K_{V}^{IVc}\right] & \left[K_{V}^{IVd}\right] & \left[K_{V}^{IVe}\right] & [I] & \left[K_{V}^{VIa}\right] & \left[K_{V}^{VIb}\right] & \left[K_{V}^{VIc}\right] & [0] \\
[0] & [0] & [0] & [0] & [0] & [0] & [0] & [0] & [0] & [0] & \left[K_{VIa}^{V}\right] & [I] & \left[K_{IVa}^{VIb}\right] & [0] & \left[K_{VIa}^{VII}\right] \\
[0] & [0] & [0] & [0] & [0] & [0] & [0] & [0] & [0] & [0] & \left[K_{VIb}^{V}\right] & \left[K_{VIb}^{VIa}\right] & [I] & \left[K_{VIb}^{VIc}\right] & \left[K_{VIb}^{VII}\right] \\
[0] & [0] & [0] & [0] & [0] & [0] & [0] & [0] & [0] & [0] & \left[K_{VIc}^{V}\right] & [0] & \left[K_{IVc}^{VIb}\right] & [I] & \left[K_{VIc}^{VII}\right] \\
[0] & [0] & [0] & [0] & [0] & [0] & [0] & [0] & [0] & [0] & [0] & \left[K_{VII}^{VIa}\right] & \left[K_{VII}^{VIb}\right] & \left[K_{VII}^{VIc}\right] & [I]
\end{bmatrix}
\tag{4.40}
$$

The matrix [SV] is given in (4.41).

$$[SV] = \Big[\ [SV_I]\ \ [SV_{IIa}]\ \ [SV_{IIb}]\ \ [SV_{IIc}]\ \ [SV_{III}]\ \ [SV_{IVa}]\ \ [SV_{IVb}]\ \ [SV_{IVc}]\ \ [SV_{IVd}]\ \ [SV_{IVe}]$$
$$[SV_V]\ \ [SV_{VIa}]\ \ [SV_{VIb}]\ \ [SV_{VIc}]\ \ [SV_{VII}]\ \Big]^T \tag{4.41}$$

Each element of vector [SV] is given in (S21)-(4.55).

$$[SV_I] = \left[[0]_{N_1\times 1}\right] \tag{4.42}$$

$$[SV_{IIa}] = \left[\ [0]_{N_{IIa}\times 1}\ \ [0]_{N_{IIa}\times 1}\ \ [0]_{L_{IIa}\times 1}\ \right] \tag{4.43}$$

$$[SV_{IIb}] = \left[\ [0]_{1\times 1}\ \ [0]_{N_{IIb}\times 1}\ \ [0]_{1\times 1}\ \ [0]_{N_{IIb}\times 1}\ \ [0]_{L_{IIb}\times 1}\ \ [0]_{L_{IIb}\times 1}\ \right] \tag{4.44}$$

$$[SV_{IIc}] = \left[\ [0]_{N_{VIc}\times 1}\ \ [0]_{N_{VIc}\times 1}\ \ [0]_{L_{VIc}\times 1}\ \right] \tag{4.45}$$

$$[SV_{III}] = \left[\ [0]_{N_{III}\times 1}\ \ [SV_{III}]_{N_{III}\times 1}\ \right] \tag{4.46}$$

$$[SV_{IVa}] = \left[\ [0]_{N_{IVa}\times 1}\ \ [0]_{N_{IVa}\times 1}\ \ [SV_{IVa}]_{L_{IVa}\times 1}\ \right] \tag{4.47}$$

$$[SV_{IVb}] = \left[\ [SV_{IVb\_c0}]_{1\times 1}\ \ [0]_{N_{IVb}\times 1}\ \ [SV_{IVb\_d0}]_{1\times 1}\ \ [0]_{N_{IVb}\times 1}\ \ [0]_{L_{IVb}\times 1}\ \ [0]_{L_{IVb}\times 1}\ \right] \tag{4.48}$$

$$[SV_{IVc}] = \left[\ [0]_{N_{IVc}\times 1}\ \ [0]_{N_{IVc}\times 1}\ \ [SV_{eIVc}]_{L_{IVc}\times 1}\ \ [SV_{fIVc}]_{L_{IVc}\times 1}\ \right] \tag{4.49}$$

$$[SV_{IVd}] = \left[\ [ES_{IVd\_c0}]_{1\times 1}\ \ [0]_{N_{IVd}\times 1}\ \ SV_{IVd\_d0}]_{1\times 1}\ \ [0]_{N_{IVd}\times 1}\ \ [0]_{L_{IVd}\times 1}\ \ [0]_{L_{IVd}\times 1}\ \right] \tag{4.50}$$

$$[SV_{IVe}] = \left[\ [0]_{N_{IVe}\times 1}\ \ [0]_{N_{IVa}\times 1}\ \ [SV_{IVa}]_{L_{IVa}\times 1}\ \right] \tag{4.51}$$

$$[SV_{VIa}] = \left[\ [0]_{N_{VIa}\times 1}\ \ [0]_{N_{VIa}\times 1}\ \ [0]_{L_{VIa}\times 1}\ \right] \tag{4.52}$$

$$[SV_{IVb}] = \left[\ [0]_{1\times 1}\ \ [0]_{N_{VIb}\times 1}\ \ [0]_{1\times 1}\ \ [0]_{N_{VIb}\times 1}\ \ [0]_{L_{VIb}\times 1}\ \ [0]_{L_{VIb}\times 1}\ \right] \tag{4.53}$$

$$[SV_{VIc}] = \left[\ [0]_{N_{VIc}\times 1}\ \ [0]_{N_{VIc}\times 1}\ \ [0]_{L_{VIc}\times 1}\ \right] \tag{4.54}$$

$$[SV_{VII}] = \left[[0]_{N_{VII}\times 1}\right] \tag{4.55}$$

The element of matrix [BC] and [SV] is given in appendix C. The elements of matrix [BC] and [SV] can be obtained from the simultaneous equations developed from (4.19)-(4.22). The dimension of matrix [BC] is $D_{max}\times D_{max}$, and the dimension of matrix [IC] and [SV] is $D_{max}\times 1$. The value of D_{max}

is given by

$$\begin{aligned} D_{\max} &= \mathrm{N}_1 + 2\cdot\mathrm{N}_{\mathrm{IIa}} + L_{\mathrm{IIa}} + 2\cdot(\mathrm{N}_{\mathrm{IIb}} + L_{\mathrm{IIb}} + 1) + 2\cdot\mathrm{N}_{\mathrm{IIc}} + L_{\mathrm{IIc}} + 2\cdot\mathrm{N}_{\mathrm{III}} + 2\cdot\mathrm{N}_{\mathrm{IVa}} + L_{\mathrm{IVa}} \\ &+2\cdot(\mathrm{N}_{\mathrm{IVb}} + L_{\mathrm{IVb}} + 1) + 2\cdot(\mathrm{N}_{\mathrm{IVc}} + L_{\mathrm{IVc}}) + 2\cdot(\mathrm{N}_{\mathrm{IVd}} + L_{\mathrm{IVd}} + 1) + 2\cdot\mathrm{N}_{\mathrm{IVe}} + L_{\mathrm{IVe}} + 2\cdot\mathrm{N}_{V} \\ &+2\cdot\mathrm{N}_{\mathrm{VIa}} + L_{\mathrm{VIa}} + 2\cdot(\mathrm{N}_{\mathrm{VIb}} + L_{\mathrm{VIb}} + 1) \\ &+2\cdot\mathrm{N}_{\mathrm{VIc}} + L_{\mathrm{VIc}} + \mathrm{N}_{\mathrm{VI1}}. \end{aligned} \tag{4.56}$$

The accuracy and computational time of the subdomain model depend on the maximum number of harmonics taken into account in the solution. The maximum number of harmonics depends on the available memory of the computer [96]. After a certain number of harmonics, the linear system becomes ill-conditioned and gives inaccurate results [75]. The less number of harmonics gives inaccurate field solutions at discontinuous points in the geometry, especially at the edge of the magnetic shields. This is due to the dominance of the Gibbs phenomenon at the interface of regions. However, having different sizes of regions, the magnetic potentials series can be truncated at different points. Here, the different number of harmonics (given in Table 4.1) for different regions has been selected to obtain a correctly converged solution. A detailed discussion on the number of the harmonic taken into account is given in [96]. The finite number of harmonics N_I-N_{VII} (x-edge) and L_{IIa}-L_{VIa} (z-edge), given in Table 4.1, have been used for calculating the analytical results. With the obtained value of unknown coefficients, the magnetic field density can be calculated using (4.3). Further, the analytical results of the magnetic field are compared with 2-D FEA results in the next subsection.

4.2.5 2-D Subdomain Model Verification

For a fair comparison, the magnetic field densities obtained from subdomain model and 2-D FEA are plotted on Path 1, as shown in Fig. 4.6. Path 1 is located between the coils at z_m, which is the distance from the bottom of the primary coil to Path 1 ,and it is 15 mm. The distance between the Shield 1 and the top of the primary coil (represented as air in Fig. 4.1(a)) is 5.09 mm due to the presence of base material (acrylic) and adhesive. The same is true for the secondary coil arrangement. The Shield 2 is at (z_6) 20.09 mm.

Fig. 4.7 depicts the magnetic field distribution for the perfect alignment of the coils. In this case, the magnetic field distribution is symmetric to the centre of the coil. Fig. 4.8 illustrates the magnetic

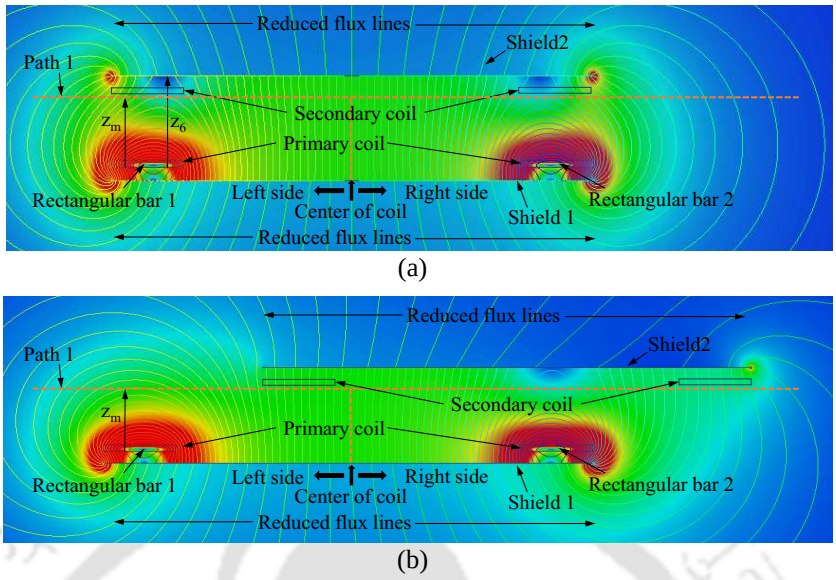

Figure 4.6: 2-D flux distribution of the practical coil system in *xz*-plane (a) without shift and (b) with 40mm horizontal shift of the secondary coil arrangement.

field distribution for 40 mm horizontal displacement of the secondary coil arrangement. Here, the asymmetrical pattern in the distribution of B_x and B_z is observed because the flux distribution between the coils becomes unsymmetrical, as shown in Fig. 4.6(b). This asymmetry in flux distribution is due to an increase in flux concentration in the direction of the movement of Shield 2. Similarly, the magnetic field distribution inside the Shield 1 and Shield 2 for perfect alignment and misalignment cases is shown in Figs. 4.9-4.10. From Figs. 4.7-4.10, it can be seen that the results from the 2-D subdomain model, for the aligned as well as the misaligned cases, show an excellent agreement with 2-D FEA results. Fig. 4.11 shows the comparison in B_z obtained from the 2-D subdomain model

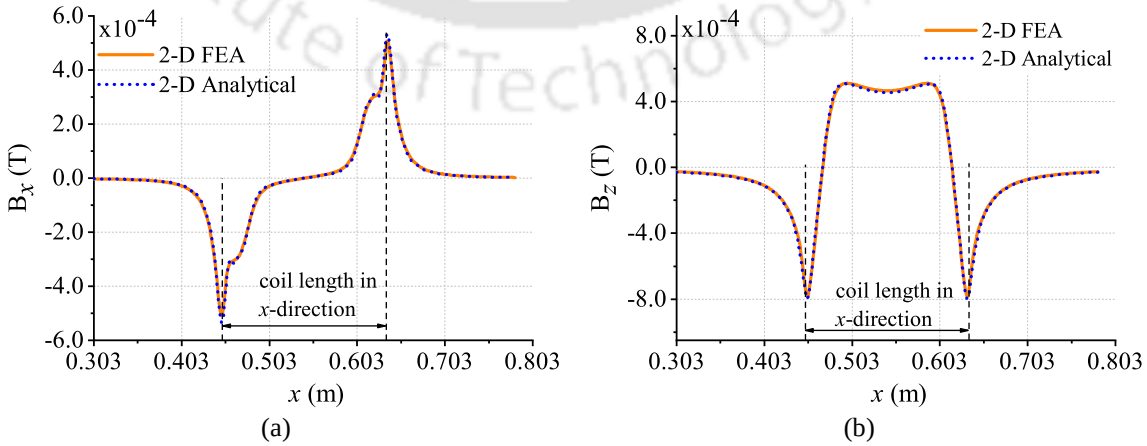

Figure 4.7: Distribution of (a) B_x and (b) B_z along Path 1.

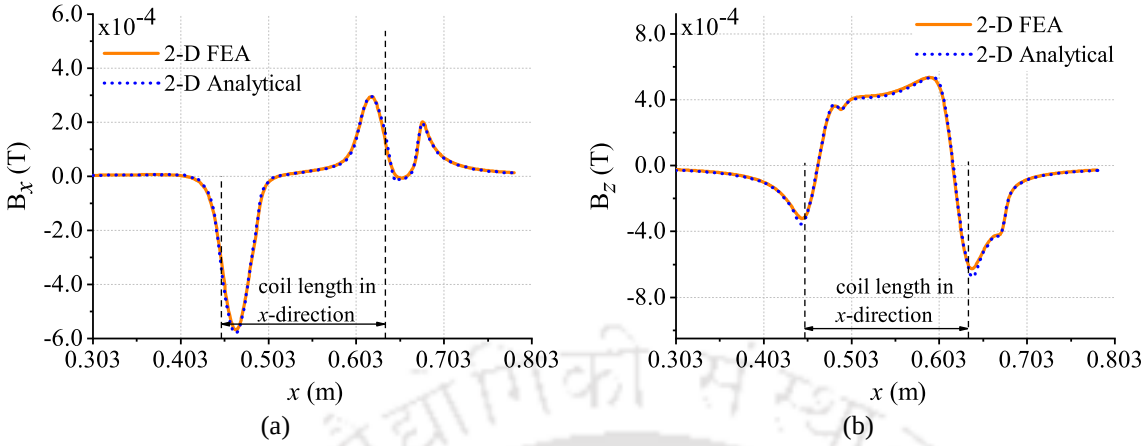

Figure 4.8: Distribution of (a) B_x and (b) B_z along Path 1 with 40mm horizontal shift of the secondary coil arrangement.

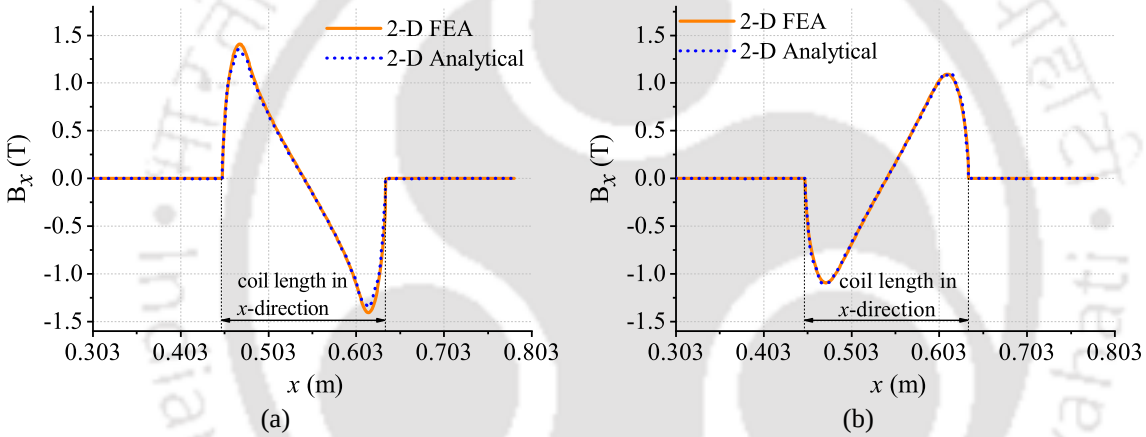

Figure 4.9: B_x distribution, along the x-direction, on the center of (a) Shield 1 and (b) Shield 2.

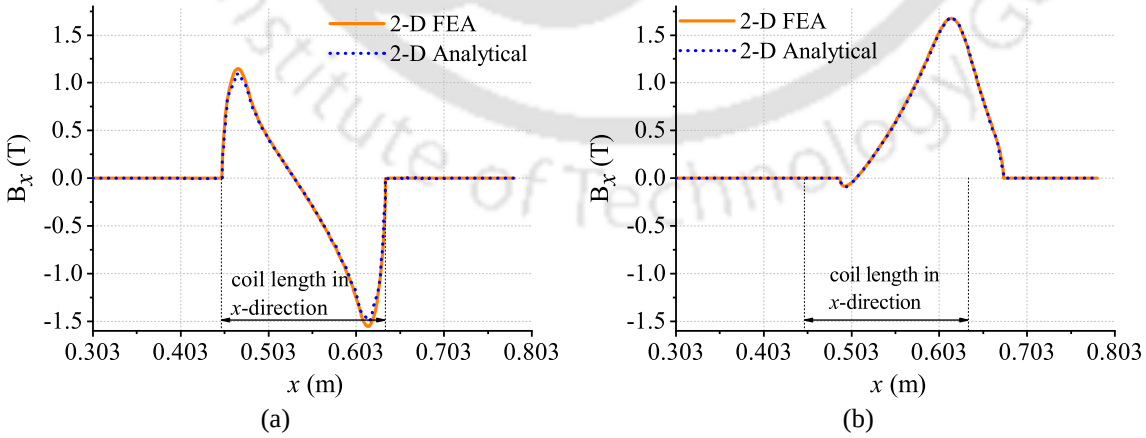

Figure 4.10: B_x distribution, along the x-direction with 40mm horizontal shift of the secondary coil arrangement, on the center of (a) Shield 1 and (b) Shield 2.

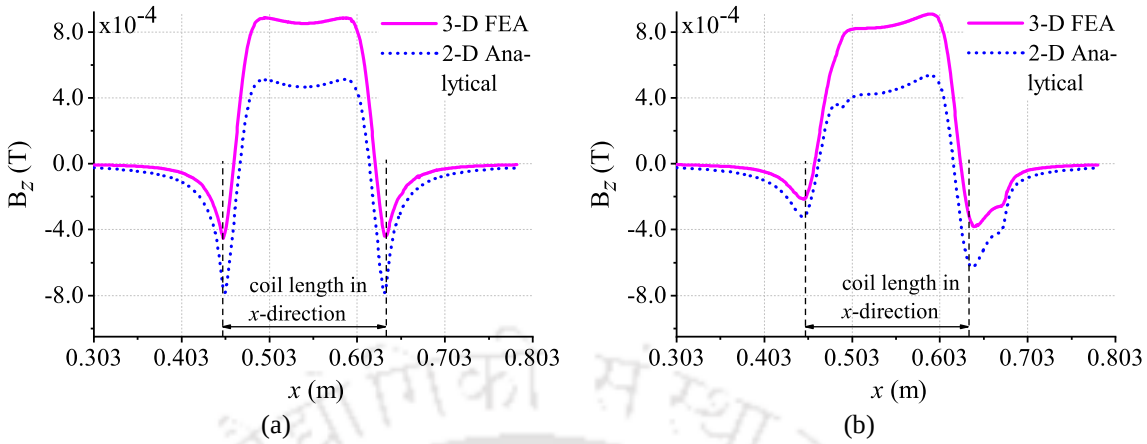

Figure 4.11: Magnetic field density distribution of B_z on Path 1, obtained from 2-D subdomain model and 3-D FEA (a) without shift and (b) with 40 mm shift of the secondary coil arrangement.

and 3-D FEA model (shown in Fig. 4.12) on Path 1 and Path 2, respectively, where Path 2 is the line along the x-axis at z_m = 15 mm and y = 0, as shown in Fig. 4.12. From Fig. 4.11, a clear difference in B_z obtained from the 2-D subdomain model and 3-D FEA model can be seen. This difference is due to the contribution of four-bars (having current in both x- and y-directions) in the magnetic field obtained from the 3-D FEA model, as shown in Fig. 4.12, whereas in a 2-D subdomain model, it is of two rectangular bars (current is only in one (y-) direction). Similarly, a 2-D subdomain model for yz-plane can be developed. Two 2-D subdomain models are superimposed to include the effect of four rectangular bars, and it is discussed in the next section.

4.3 Superposition of Two 2-D Subdomain Models

The superposition of two 2-D subdomain models is performed in this section to get the 3-D analytical results. Here, 2-D subdomain models for the xz-plane (invariant in the y-direction) and yz-plane (invariant in the x-direction) are added according to (4.57).

$$B_r^{\mathrm{s}} = B_r(x,z)|_{\text{for } xz\text{-plane}} + B_r(y,z)|_{\text{for } xz\text{-plane}} \tag{4.57}$$

By using (4.57), B_z on Path 2 is calculated and compared again with the 3-D FEA result, as shown in Fig. 4.13. From Fig. 4.13, it is observed that the superimposed result still does not follow the 3-D FEA result. This mismatch is because of the 2-D subdomain model considers infinite length in the third direction [79]. Therefore, a correction factor is necessary to take into account the finite length in the third direction for a 2-D subdomain model [97, 98].

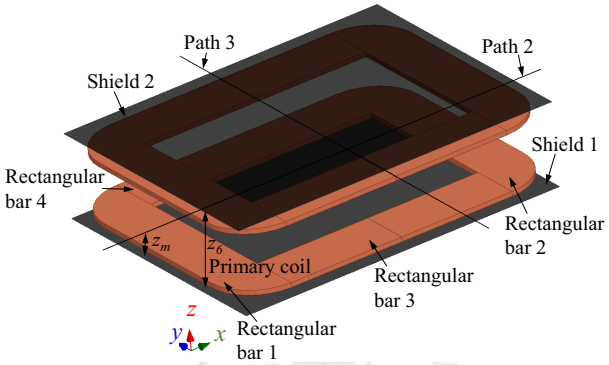

Figure 4.12: 3-D FEA model of coil system.

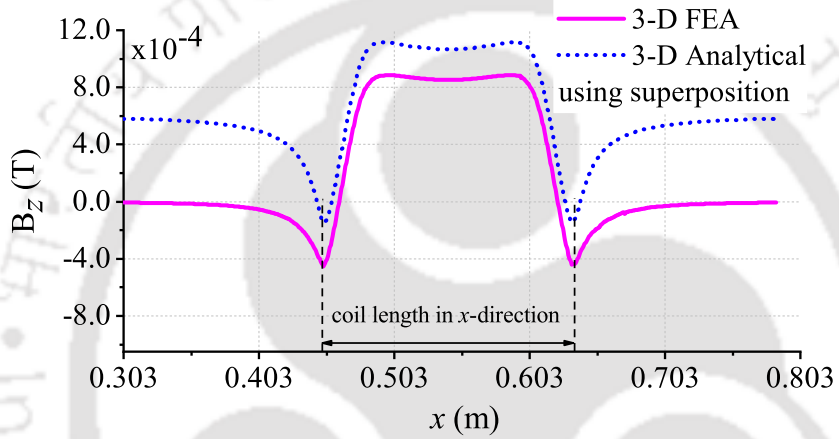

Figure 4.13: Distribution of B_z on Path 3 using (25) and 3-D FEA.

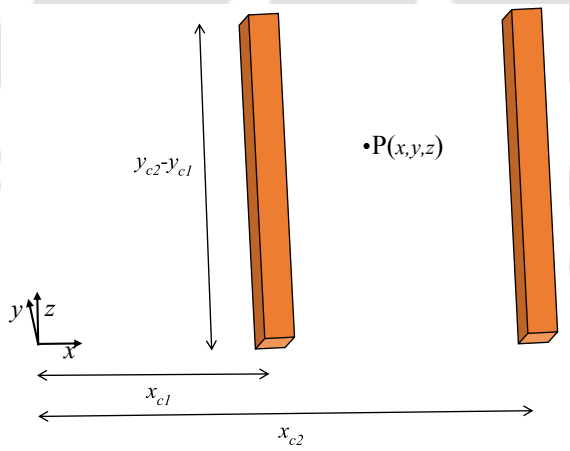

Figure 4.14: Top view of coil.

The 2D subdomain model has been developed for two conductors and two magnetic shields. Therefore, the correction has been derived in two-part. In one, it derived for two parallel conductors, which is based on Biot-Savart law [63] and the other is for a magnetic shield with the help of curve fitting. The magnetic field density at an arbitrary point P(x,y,z) due to two parallel conductors

surrounded by air shown in Fig. 4.14, is given by (4.58)

$$f_1(x,y,z) = \frac{\mu_0 I_p}{2\pi \cdot g_1}\left(\frac{g_4}{\sqrt{{g_1}^2+{g_4}^2}} - \frac{g_3}{\sqrt{{g_1}^2+{g_3}^2}}\right) + \frac{\mu_0 I_p}{2\pi \cdot g_2}\left(\frac{g_4}{\sqrt{{g_2}^2+{g_4}^2}} - \frac{g_3}{\sqrt{{g_2}^2+{g_3}^2}}\right), \quad (4.58)$$

and the magnetic field density due to two parallel conductor of infinite length in the y-direction is given as-

$$f_2(x,y,z) = \frac{\mu_0 I_p}{4\pi \cdot g_1} + \frac{\mu_0 I_p}{4\pi \cdot g_2} \quad (4.59)$$

where $g_1 = \sqrt{(x-x_{c1})^2+(z-r)^2}$, $g_2 = \sqrt{(x-x_{c2})^2+(z-r)^2}$, $g_3 = (y_{c1}-y)$, and $g_4 = (y_{c2}-y)$ with $x_{c1} = 0.5\,(x_2+x_3)$, $x_{c2} = 0.5\,(x_4+x_5)$, $y_{c1} = 0.5\,(y_2+y_3)$, and $y_{c1} = 0.5\,(y_2+y_3)$, $y_{c2} = 0.5\,(y_4+y_5)$. The ratio of ratio of (4.58)/(4.59), given as

$$f_3(x,y,z) = f_1(x,y,z)/f_2(x,y,z), \quad (4.60)$$

provide a factor which can be used to make 2D analytical model variant in third direction having two conductor surrounded by air. Here, the magnetic shield is not included in the factor, and an additional factor is required. This factor is determined by curve fitting, and the points for curve fitting are calculated at different values of μ_r using (4.61). The obtained curves with its expression are shown in Fig. 4.15. The factor $G_{\mu r}$, is valid only for the rectangular and square shape of the coil.

$$f(\mu_r) = \frac{B_{z,rms}^{\text{3-D FEA}}(\mu_r)}{B_{z,rms}^{\text{2-D FEA}}(\mu_r)} \Bigg/ \frac{B_{z,rms}^{\text{3-D FEA}}(\mu_r = 1)}{B_{z,rms}^{\text{2-D FEA}}(\mu_r = 1)} \quad (4.61)$$

The correction factor for coil system shown in Fig. 4.14 is given as-

$$f_{xz}(x,y,z) = 0.5 G_{\mu_r} f_3(x,y,z) \quad (4.62)$$

Figs. 4.16(a) and (b) show the plot of (4.62) along the x- and y-directions, respectively. Since $f_{xz}(x,y,z)$ varies with the y-direction, as shown in Fig 4.16(b), its multiplication with a 2-D subdomain model (xz-plane) facilitates to calculate the magnetic field in third (y-) direction. Similarly, the multiplication of $f_{yz}(x,y,z)$ in subdomain model for yz- plane enables to calculate the magnetic field in the third (x-) direction. Thus, to obtain the tangible results for the coil system shown in Fig. 1(a),

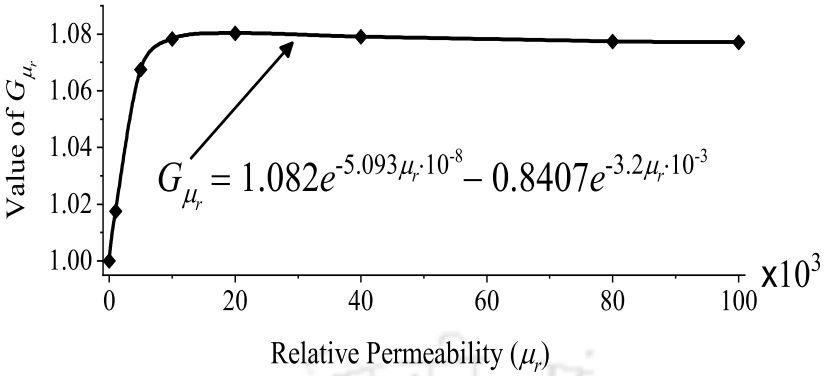

Figure 4.15: Result of G_{μ_r} at different μ_r.

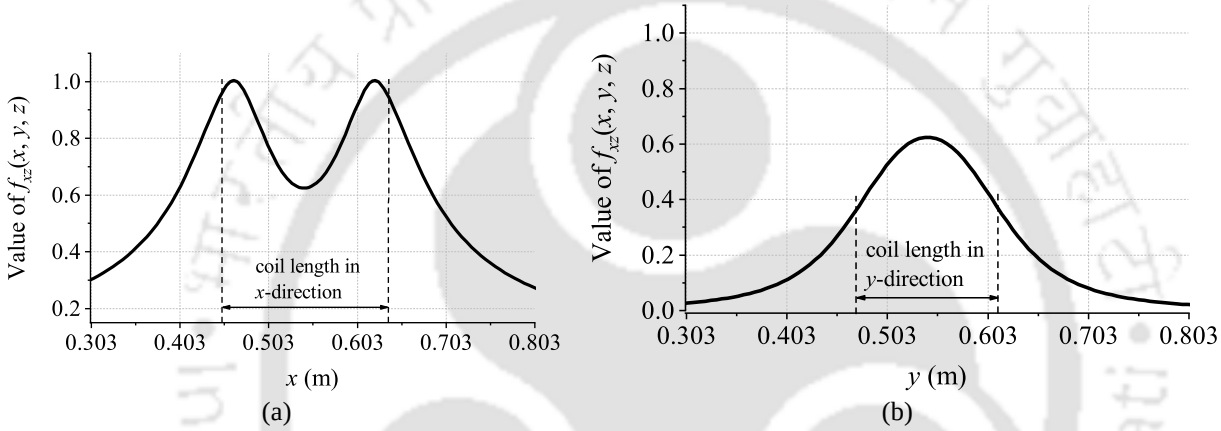

Figure 4.16: Results of $f_{xz}(x, y, z)$ along (a) Path 2 and (b) Path 3.

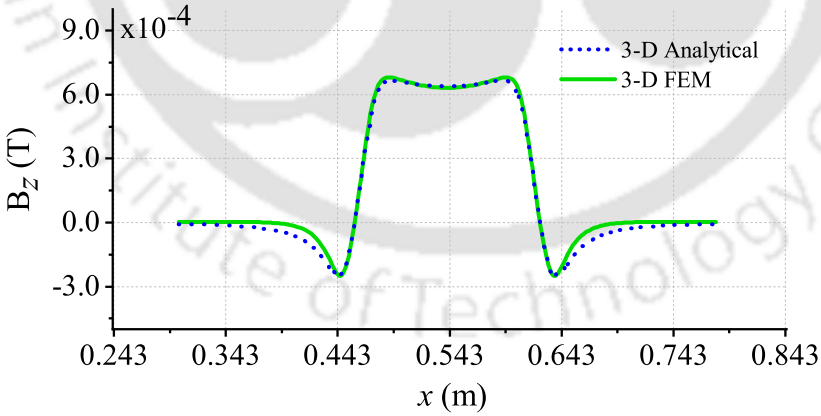

Figure 4.17: Prediction of B_z distribution (on Path 2) for the considered coil system using (4.63) and 3-D FEA.

the magnetic field in region r can be expressed as

$$B_r^{\text{cf}}(x, y, z) = (B_r(x, z)|_{\text{for } xz\text{-plane}}) \cdot f_{xz}(x, y, z) + (B_r(y, z)|_{\text{for } yz\text{-plane}}) \cdot f_{yz}(x, y, z) \tag{4.63}$$

where $f_{yz}(x, y, z)$ is the correction factor for the yz-plane subdomain model. Now, the question arises;

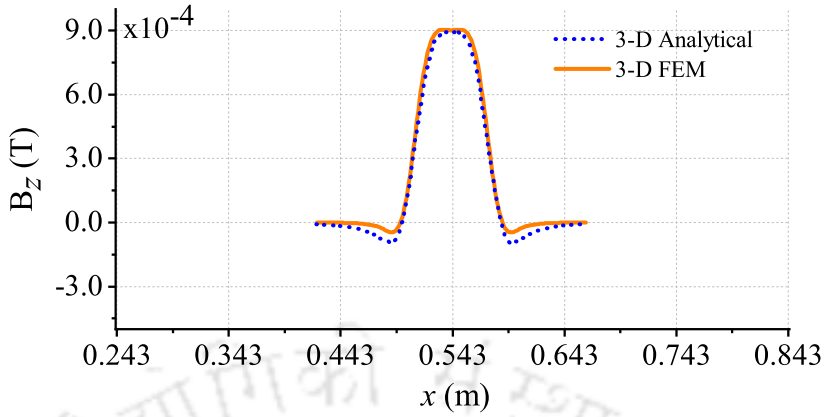

Figure 4.18: Prediction of B_z distribution (on Path 2) for the coil system whose dimension is half of the considered coil system using (4.63) and 3-D FEA.

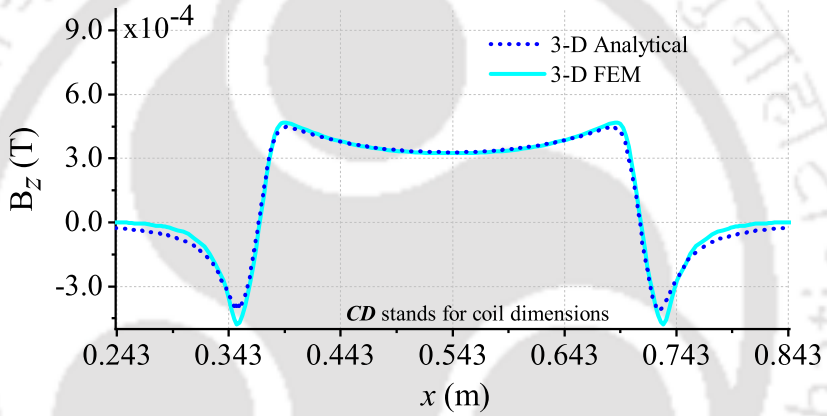

Figure 4.19: Prediction of B_z distribution (on Path 2) for the coil system whose dimension is two times of the considered coil system using (4.63) and 3-D FEA.

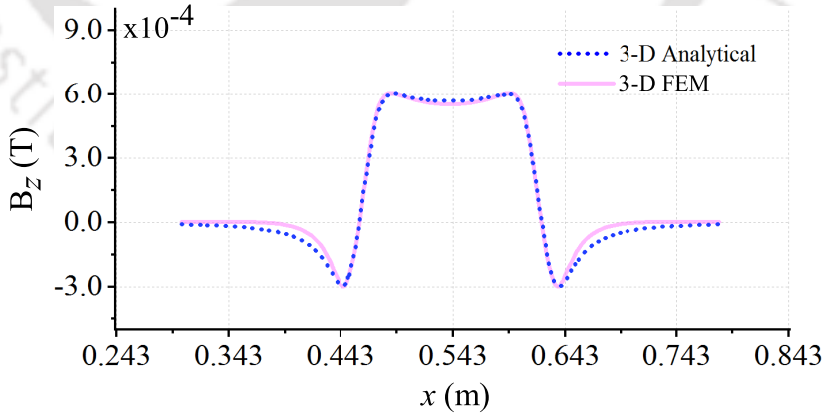

Figure 4.20: Prediction of B_z distribution (on Path 2) for the square coil system whose length is x5-x2 using (4.63) and 3-D FEA.

is the obtained expression (4.62) applicable for different dimensions of the coils? In this context, expression (4.63) is used to confirm the same. Figs. 4.17-4.20 shows the distributions of B_z (on Path 2) obtained from (4.63) and 3-D FEA for different dimensions of the coils. Here, the magnetic field

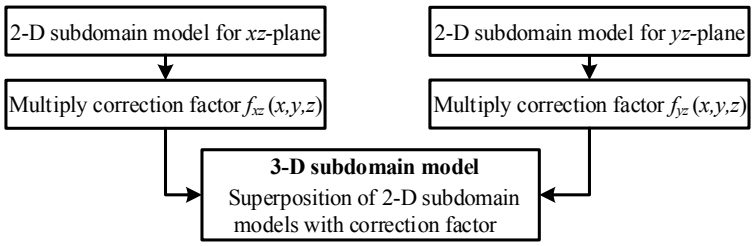

Figure 4.21: Development of 3-D subdomain model form 2-D subdomain models.

distributions obtained from (4.63) are matching well with the 3-D FEA results, which confirm the applicability of the correction factor (4.62) for the coil system shown in Fig. 4.1(a) of different dimensions. Therefore, expression (4.63) can be used for different dimensions of rectangular (including square) coil systems.

The mutual inductance from the proposed subdomain model is calculated by

$$M = \frac{\lambda}{I_p} = \frac{1}{I_p}\sum_{t=1}^{turn}\left(\int_{(x_2+t\cdot w)}^{(x_5-t\cdot w)}\int_{(x_2+t\cdot w)}^{(x_5-t\cdot w)} B_V^{cf}(x,y,z)dxdy\right) \tag{4.64}$$

where λ is the flux linkage to the secondary coil, and $B_V^{cf}(x,y,z)$ is the magnetic field in region V with the correction factor. The steps involved in developing the 3-D subdomain model are summarized in Fig 5.4. The magnetic field distributions obtained from (4.63) and 3-D FEA are compared with measurements in the next section.

4.4 Verification of Analytical Model

This section verifies the analytical model by comparing analytical results with measurements and FEA simulation results. Section 4.4.1 presents a description of the developed experimental setup. Section 4.4.1 compares magnetic field density and mutual inductance obtained from analytical, measurements, and 3D FEA simulation.

4.4.1 Experimental Setup

The proposed subdomain model is validated with experimental results. For this, an experimental setup shown in Fig. 4.22 is built in the laboratory. Here, two rectangular coils are made of American wire gauge (AWG)#32 copper wire. 3M high permeability magnetic shielding sheet 1380 is used as a Shield 1 and Shield 2, which are glued on the other side of the base (acrylic sheet) of the coils. The specifications of coils and magnetic shields are mentioned in Table I. Further, a pick-up coil of

a 2 mm radius and 200 turns is used to measure the magnetic field density in the air gap, which is made of AWG#40 copper wire. An H-bridge inverter is used to supply a 100-kHz current of 3.5 A to the primary coil. Cyclone-II FPGA board is used to generate the pulses to drive the MOSFETs (IRFP450) of H-bridge inverter. The mutual inductance between the coils is measured with Hewlett Packard 4263B LCR meter.

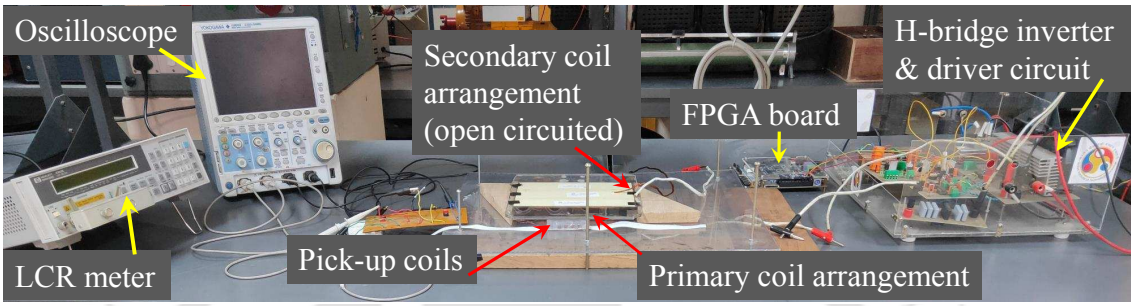

(a)

(b)

(c)

Figure 4.22: (a) Experimental setup. (b) Pick-up coil. (c) Magnetic shield.

4.4.2 Results Description

This section compares the results of the magnetic field and mutual inductance for different misalignments between the coils obtained from (4.63) and (4.64), respectively, with the 3-D FEA and experimental results. The comparison of the magnetic field is performed on Path 2 and Path 3, as shown in Fig. 4.12, where Path 3 is the line along the y-axis at z_m and $x = 0$. For the measurement ease, $z_6 = 34.98$ mm and $z_m = 13.89$ mm. For the perfect aligned coils, the magnetic field distributions are given in Fig. 4.23. The waveforms of B_x and B_z in Fig. 4.23 are in good agreement with 3-D FEA and measurement results, which confirm the accuracy of (4.63).

The variation in mutual inductance for different misalignments between coils is shown in Fig. 4.24. Figs. 4.24(a) and (b) show the mutual inductance variation for the horizontal misalignment in the x- and y-directions, respectively, at $z_6 = 20.09$ mm. For the horizontal misalignment in the x-direction, the secondary coil arrangement is moved at a step of 10 mm in the positive x-direction, whereas in the y-direction, secondary coil arrangement is moved in the positive y-direction with the

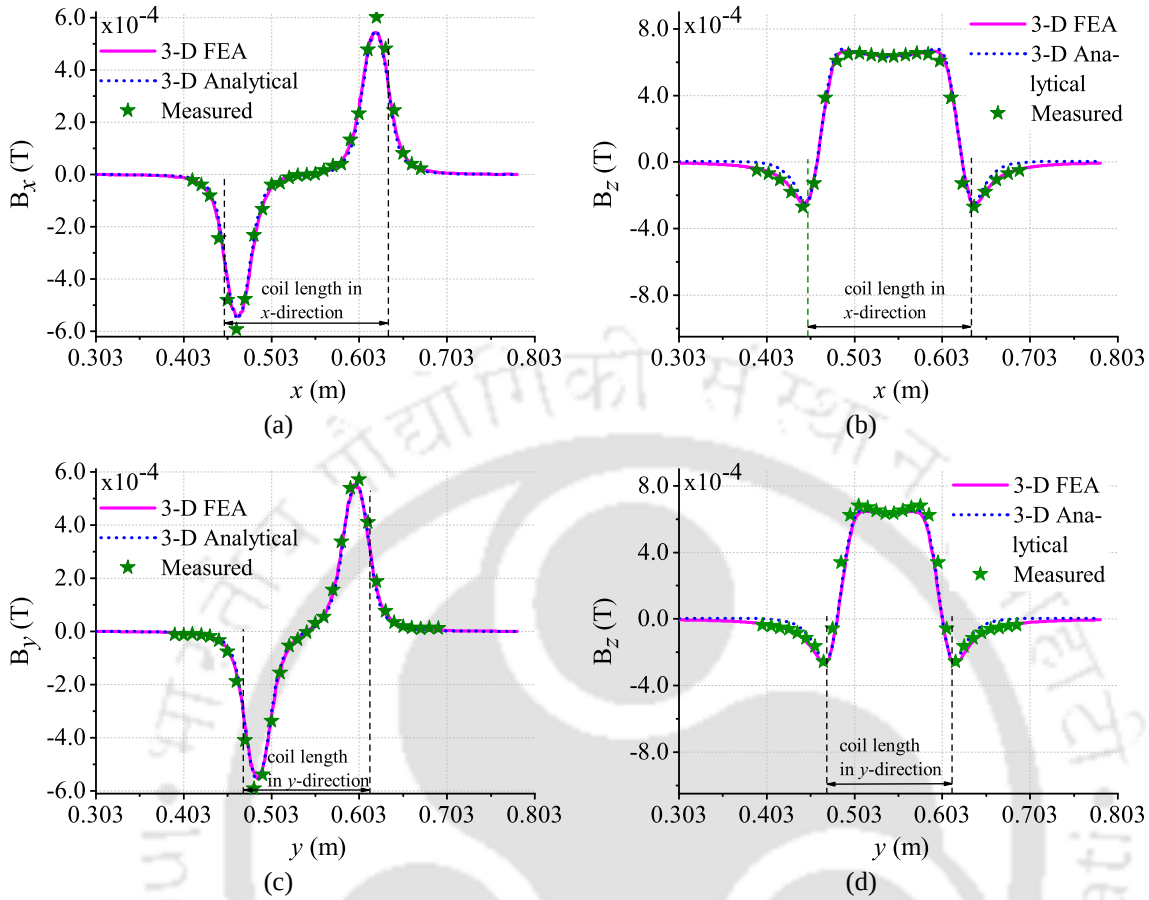

Figure 4.23: Distributions of B_x and B_z shown in (a) and (b), respectively, along Path 2. Distributions of B_x and B_z shown in (c) and (d), respectively, along Path 3. The coils are perfectly aligned at z_m = 13.89 mm.

same step. From Figs. 4.24(a) and (b), it is observed that as misalignment increases, the value of mutual inductance decreases because of decrement in the flux linkage in the secondary coil.

Fig. 4.24(c) shows the variation in mutual inductance for vertical misalignment. Here, the secondary arrangement is moved towards a positive *z*-direction with a step of 10 mm from an initial position of z_6 = 24.09 mm. From Fig. 4.24(c), it can be seen that as the separation between the primary and secondary coil arrangements increases, the value of mutual inductance decreases due to decrement in the magnitude of the magnetic field density. The calculated mutual inductance in Fig. 4.24 is in a good agreement with 3-D FEA and measurement results, which confirm the accuracy of the proposed 3-D subdomain model.

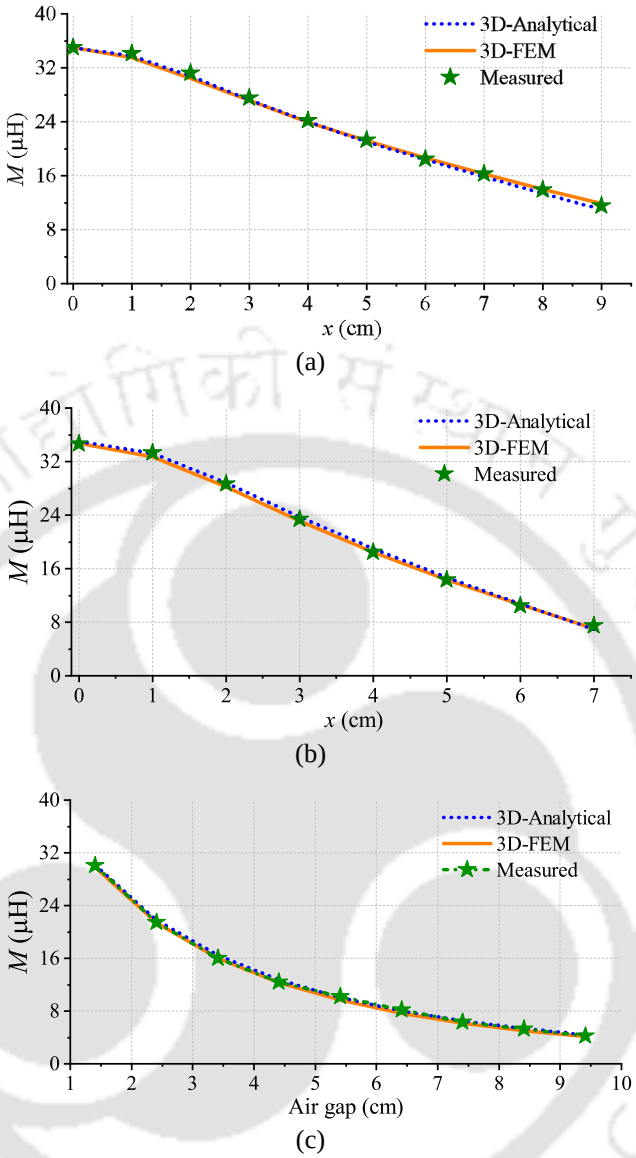

Figure 4.24: Mutual inductance variation in the (a) *x*-direction , (b) *y*-direction, and (c) *z*-direction.

4.5 Summary

This chapter presents an analytical model based on the subdomain technique to calculate the magnetic field distribution and mutual inductance between the coils in the WPT system having magnetic shields of finite dimension and finite permeability. The magnetic vector potential formulation in the cartesian coordinate system has been used in subdomain modelling. For the subdomain modelling, the continuity of magnetic vector potential and magnetic field intensity is applied in two directions (i.e., *x*- and *y*-edges). The comparison in magnetic field distribution obtained from the subdomain model and 2-D FEA has been made. The magnetic field distributions obtained from the 2-D subdo-

main model coincide with the magnetic field obtained from 2-D FEA, which confirms the accuracy of the 2-D subdomain model. A 3-D subdomain model has been formulated by the superposition of two 2-D subdomain models to obtain the result close to measurement results. For limiting the 2-D subdomain model in the third direction, a correction factor has been introduced. The proposed subdomain model is validated by the computation of magnetic field density distribution in the air gap and compared with FEA and experiment. It shows a good agreement. The mutual inductance from the 3-D subdomain model has been compared with FEA results and measurement. The proposed subdomain model facilitates to change the parameters (length, width, and permeability) of magnetic shields. The results from the proposed subdomain model are acceptably accurate for initial designing and optimization of the WPT system having magnetic shielding of finite dimension and permeability.

The change in mutual inductance affects the power transfer capability and the efficiency of the entire WPT system. The impact of misalignments on these parameters for the series-parallel (SP) compensated WPT system is discussed in the next chapter.

5

Mathematical Model for Analysis of Series Parallel Compensated Wireless Power Transfer System for Different Misalignments

Contents

5.1 Introduction 94
5.2 System Description and Mathematical Model 95
5.3 Experimental Setup Description 100
5.4 Results and Discussion 102
5.5 Summary 113

5.1 Introduction

The previous chapters discussed the analytical models to calculate mutual inductance for different coil system without and with shielding. These chapters also discussed the variation in mutual inductance for different misalignments. The change in the mutual inductance impacts the power transfer capability, and the efficiency of the entire system [47, 48], and in this chapter, the focus is on developing a comprehensive analytical model for WPT system for charging of EV batteries.

Generally, constant current (CC) and constant voltage (CV) modes are used to charge the battery. Series-series (SS) and series-parallel (SP) topologies, which are capable of operating in CC and CV modes [99, 100], are mostly used. In case of misalignment between the coils, the current in the primary coil, for SS topology, can increase to a very high value [101]. However, in the case of SP topology, the current does not increase to a very high value [101]. Hence, in this chapter, SP topology is chosen for charging of EV batteries and a detailed analytical model for it is developed.

The impact of change in the mutual inductance on system parameters has been presented in [102–104]. In these works, the circular coil geometry, with multiple transmitters and receivers, is used. In [105], the authors have presented a model to evaluate the performance of WPT systems for linear actuators. However, the limitation of this work is that it is valid for only horizontal misalignment. Thus, it is evident from the previous research that a detailed mathematical model that considers the effect of different misalignments on the electrical parameters for SP compensated WPT system has not been reported.

In this chapter, an analytical model to predict the variation in the electrical parameter of the SP compensated WPT system during misalignments has been presented. For determining the variation in the electrical parameter of the SP compensated WPT system, the mutual inductance for different misalignments has been used as direct input for the steady-state model. The variation in electrical parameters has been considered for the two coil systems, one without shield (discussed in chapter 2) and the other with shield (discussed in chapter 4). This makes the proposed model a suitable tool for use in the initial design process of the SP compensated WPT system.

5.2 System Description and Mathematical Model

Two coils with air gaps are the primary subsystem of the wireless power transfer system, which can be model by the electrical equivalent circuit. This section describes the component of SP compensated WPT system and its steady-state modelling. This section is organized as follows: Section 5.2.2 describes the series-parallel compensated WPT system. The mathematical model based on the equivalent circuit is given in section 5.2.2.

5.2.1 System Description

The block diagram of the SP compensated WPT system is shown in Fig. 5.1. It consists of high-frequency (HF) H-Bridge inverter, HF rectifier, primary and secondary coils, and compensation capacitors. One compensation capacitor is connected in series with the primary coil, and the other is connected in parallel to the secondary coil, which is denoted as C_p and C_s, respectively. The values of C_p and C_s are determined at the resonance frequency of ω_0 (discussed in subsection 5.2.2) for a case when the coils are perfectly aligned and have a separation of 20.15 mm. These values (ω_0, C_p, and C_s) are kept constant for all the misalignments analysis.

The H-bridge inverter used in the system (Fig. 5.1) converts the input DC voltage to HF square wave voltage. The square wave voltage has harmonics, and the proposed model takes these harmonics into account.

5.2.2 Steady-State Model

The steady-state model of the SP compensated WPT system is developed using the equivalent circuit model, as shown in Fig. 5.2. The C_p and C_s are calculated by (5.1) and (5.2), respectively [46, 47, 104].

$$C_p = \frac{1}{\omega_0^2 \left(L_p - \frac{M^2}{L_s}\right)} \tag{5.1}$$

$$C_s = \frac{1}{\omega_0^2 L_s} \tag{5.2}$$

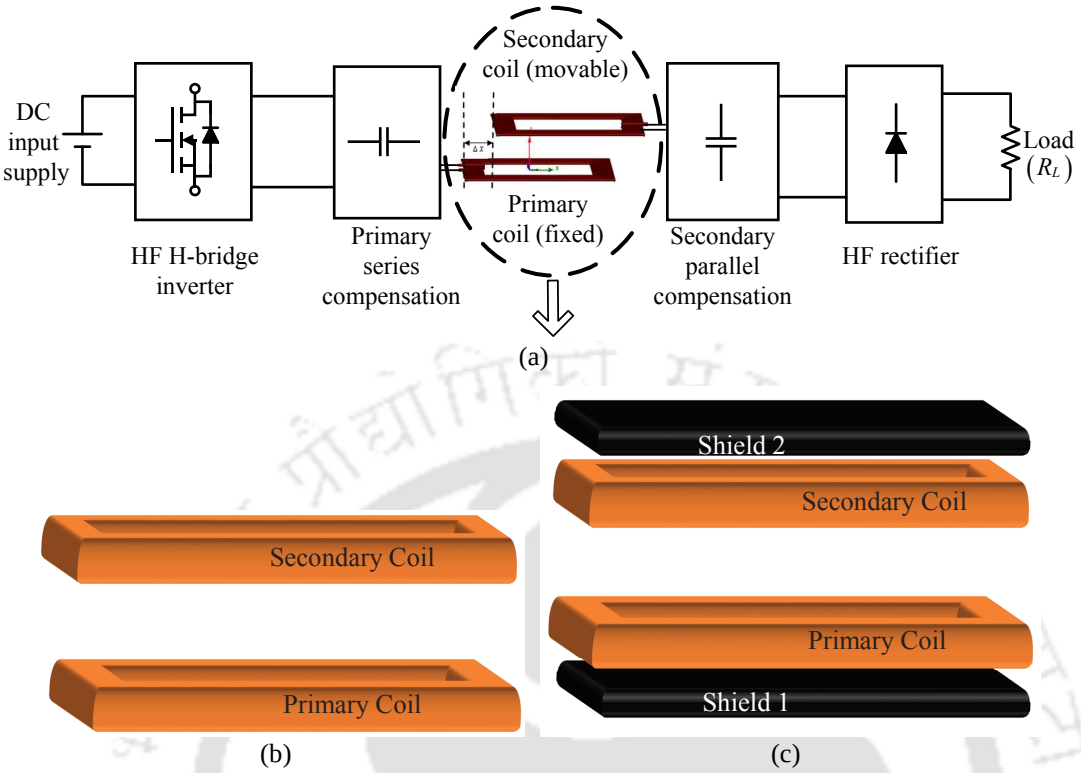

Figure 5.1: (a) Block diagram of the SP compensated WPT system for the coil system (b) without a magnetic shield, and (c) with magnetic shields.

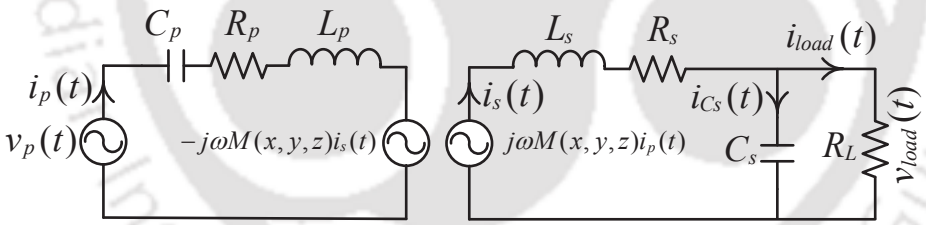

Figure 5.2: Equivalent circuit model of the SP compensated WPT system.

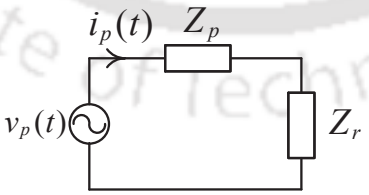

Figure 5.3: Impedance of the SP compensated WPT system seen by the source.

where the self-inductance of the primary and secondary coils are represented as L_p and L_s, respectively and the mutual inductance between the coils as M. From (5.1), it can be seen that the value of C_p is dependent on M. Due to the misalignment between the coils, the value of M changes and the primary side is no more in resonance (it gets mistuned). The impact of mistuning on the electri-

cal parameters of the SP compensated WPT system is investigated using the proposed mathematical model.

The impedance of primary side Z_p, as seen from the input source, and the impedance of secondary side Z_s (as seen from the induced voltage source), as shown in Fig. 5.2, for h^{th} harmonic, are given in (5.3) and (5.4), respectively.

$$Z_p = R_p + j\left(h\omega L_p - \frac{1}{h\omega C_p}\right) \tag{5.3}$$

$$Z_s = R_s + jh\omega L_s + \left(\frac{R_L}{1 + jh\omega C_s R_L}\right) \tag{5.4}$$

The secondary side impedance referred to the primary side, is given by

$$Z_r = \frac{(h\omega M(x,y,z))^2}{R_s + jh\omega L_s + \left(\frac{R_L}{1+jh\omega C_s R_L}\right)}. \tag{5.5}$$

The total impedance Z_t of the SP compensated WPT system (Fig. 5.3), as seen by the source, is given by

$$Z_t = Z_p + Z_r \tag{5.6}$$

5.2.2.1 Modelling of the Primary Side

The Fourier series expression of the instantaneous output voltage $v_p(t)$ for the H-bridge inverter is given by (5.7)

$$v_p(t) = \frac{4V_{dc}}{\pi} \sum_{h=1,3,5..}^{\infty} \frac{1}{h} \sin h\omega t \tag{5.7}$$

The instantaneous primary current $i_p(t)$, using (5.6) and (5.7) is given as

$$i_p(t) = \sum_{h=1,3,5..}^{\infty} I_{pm} \sin(h\omega t - \varphi_t) \tag{5.8}$$

where I_{pm} is the maximum value of $i_p(t)$ and φ_t is the impedance angle of Z_t for the h^{th} harmonic, and are expressed by (5.9) and (5.10), respectively.

$$I_{pm} = \frac{4V_{in}}{\pi h|Z_t|} \tag{5.9}$$

$$\varphi_t = \tan^{-1}(Z_t) \tag{5.10}$$

The instantaneous voltage across the primary capacitor $v_{C_p}(t)$ is obtained by

$$v_{C_p}(t) = \sum_{h=1,3,5..}^{\infty} \left|X_{C_p}\right| I_{pm} \sin\left(h\omega t - \varphi_t + \varphi_{C_p}\right) \tag{5.11}$$

where

$$X_{C_p} = \frac{1}{j\omega h C_p} \tag{5.12}$$

$$\varphi_{C_p} = \tan^{-1}(X_{C_p}). \tag{5.13}$$

and the instantaneous voltage across the primary coil $v_{L_p}(t)$ is obtained by

$$v_{L_p}(t) = \sum_{h=1,3,5..}^{\infty} \left(\frac{4V_{dc}}{\pi h} \sin h\omega t - \left|X_{C_p}\right| \left|I_{pm}\right| \sin\left(h\omega t + \varphi_{L_p}\right)\right) \tag{5.14}$$

where

$$\varphi_{L_p} = \varphi_{C_p} - \varphi_t. \tag{5.15}$$

The instantaneous input power of the compensated primary coil $p_p(t)$ and the active power P_P are calculated using (5.16) and (5.17), respectively.

$$p_p(t) = v_p(t)\, i_p(t) \tag{5.16}$$

$$P_P = \frac{1}{T} \int_0^T p_p(t)\, dt \tag{5.17}$$

5.2.2.2 Modelling of the Secondary Side

For the secondary side modelling, the induced voltage on the secondary coil is considered as a voltage source. The instantaneous induced voltage $v_{ind}(t)$ is expressed as

$$v_{ind}(t) = jh\omega M(x, y, z)\, i_p(t). \tag{5.18}$$

The instantaneous secondary current $i_s(t)$ is calculated by (5.4) and (5.18) and is expressed as

$$i_s(t) = \sum_{h=1,3,5..}^{\infty} I_{sm} \sin\left(h\omega t + \frac{\pi}{2} - \varphi_t - \varphi_s\right) \tag{5.19}$$

where I_{sm} is the maximum value of $i_s(t)$ and φ_s is the impedance angle of Z_s for h^{th} harmonic and are expressed by (5.20) and (5.21), respectively:

$$I_{sm} = \frac{h\omega M(x,y,z)\, I_{pm}}{|Z_s|} \tag{5.20}$$

$$\varphi_s = \tan^{-1}(Z_s) \tag{5.21}$$

The instantaneous current flowing through secondary capacitor $i_{C_s}(t)$ is given by

$$i_{C_s}(t) = \sum_{h=1,3,5..}^{\infty} |\mathrm{Z_{d1}}|\,|I_{sm}| \sin\left(h\omega t + \frac{\pi}{2} - \varphi_t - \varphi_s + \varphi_{\mathrm{d1}}\right) \tag{5.22}$$

where

$$\mathrm{Z_{d1}} = \left(\frac{R_L}{R_L + \frac{1}{j\omega h C_s}}\right) \tag{5.23}$$

$$\varphi_{\mathrm{d1}} = \tan^{-1}(\mathrm{Z_{d1}}). \tag{5.24}$$

and the instantaneous current flowing through the load $i_{load}(t)$ is given by

$$i_{load}(t) = \sum_{h=1,3,5..}^{\infty} \left|\mathrm{Z_{d_2}}\right| |I_{sm}| \sin\left(h\omega t + \frac{\pi}{2} - \varphi_t - \varphi_s + \varphi_{\mathrm{d_2}}\right) \tag{5.25}$$

where

$$\mathrm{Z_{d_2}} = \left(\frac{\frac{1}{j\omega h C_s}}{R_L + \frac{1}{j\omega h C_s}}\right) \tag{5.26}$$

$$\varphi_{\mathrm{d_2}} = \tan^{-1}(\mathrm{Z_{d_2}}). \tag{5.27}$$

The instantaneous voltage across the load $v_{load}(t)$ is given by

$$v_{load}(t) = \sum_{h=1,3,5..}^{\infty} R_L \left|\mathrm{Z_{d_2}}\right| |I_{sm}| \sin\left(h\omega t + \frac{\pi}{2} - \varphi_t - \varphi_s + \varphi_{\mathrm{d2}}\right). \tag{5.28}$$

The instantaneous power of the load $p_{load}(t)$ and the active power P_{load} at the secondary side are obtained by (5.29) and (5.30), respectively.

$$p_{load}(t) = v_{load}(t)\, i_{load}(t) \tag{5.29}$$

$$P_{load} = \frac{1}{T}\int_0^T p_{load}(t)\, dt \tag{5.30}$$

Furthermore, the efficiency of the compensated coils η_{cc} is given by

$$\eta_{cc} = \frac{P_{load}}{P_P}. \tag{5.31}$$

The rms value of $x(t)$ is calculated using (5.32) and $x(t)$ can be $v_p(t)$, $v_{C_p}(t)$, $v_{L_p}(t)$, $v_{load}(t)$, $i_p(t)$, $i_s(t)$, $i_{C_s}(t)$, and $i_{load}(t)$.

$$X = \left[\frac{1}{T}\int_0^T x^2(t)\,dt\right]^{1/2}. \tag{5.32}$$

where the calculated rms value X of $x(t)$ is represented as V_P, V_{C_p}, V_{L_p}, V_{load}, I_P, I_S, I_{C_s}, and I_{load}, respectively. The procedure for initial designing of SP compensated system is given in flowchart 5.4

Table 5.1: Experimental parameters of the SP compensated WPT system

Parameter	Term	Value
N_p	Number of turn in primary coil	11
N_s	Number of turn in secondary coil	11
L_p	Self-inductance of primary coil	29.97 μH
L_s	Self-inductance of secondary coil	30.59 μH
R_p	Primary coil AC resistance at 200kHz	0.138 Ω
R_s	Secondary coil AC resistance at 200kHz	0.141 Ω
C_p	Primary side compensation capacitor at M = 15.38 μH	30.65 nF
C_s	Secondary side compensation capacitor	21.70 nF
C'_p	Primary side compensation capacitor for coil system having magnetic shield at M = 35 μH	31.33 nF
C'_s	Secondary side compensation capacitor for coil system having magnetic shield	13.87 nF
f_0	Resonance frequency	197.50 kHz
V_{dc}	Input dc voltage	60 V
R_L	Load resistance	88.10 Ω

5.3 Experimental Setup Description

To validate the efficacy of the proposed mathematical model, an experimental implementation of the SP compensated WPT system with different misalignments is conducted on a scaled-down prototype of 300 W, as shown in Fig. 5.5(a). The specification related to HF H-bridge inverter and coil design has been given in chapter 2. The secondary side HF rectifier is built with Hyperfast diodes RHRP30120. A wooden frame is used to create different misalignments in real-time. With this frame, the secondary coil can be adjusted in the positive x- and z-directions up to 14 cm and 12 cm, respectively. The distance in the z-direction is measured from the bottom of the primary coil to the mid of secondary coil. A digital vernier calliper is used to measure the distances in x- and z-directions. Other specifications related to design parameters are given in Table 5.1.

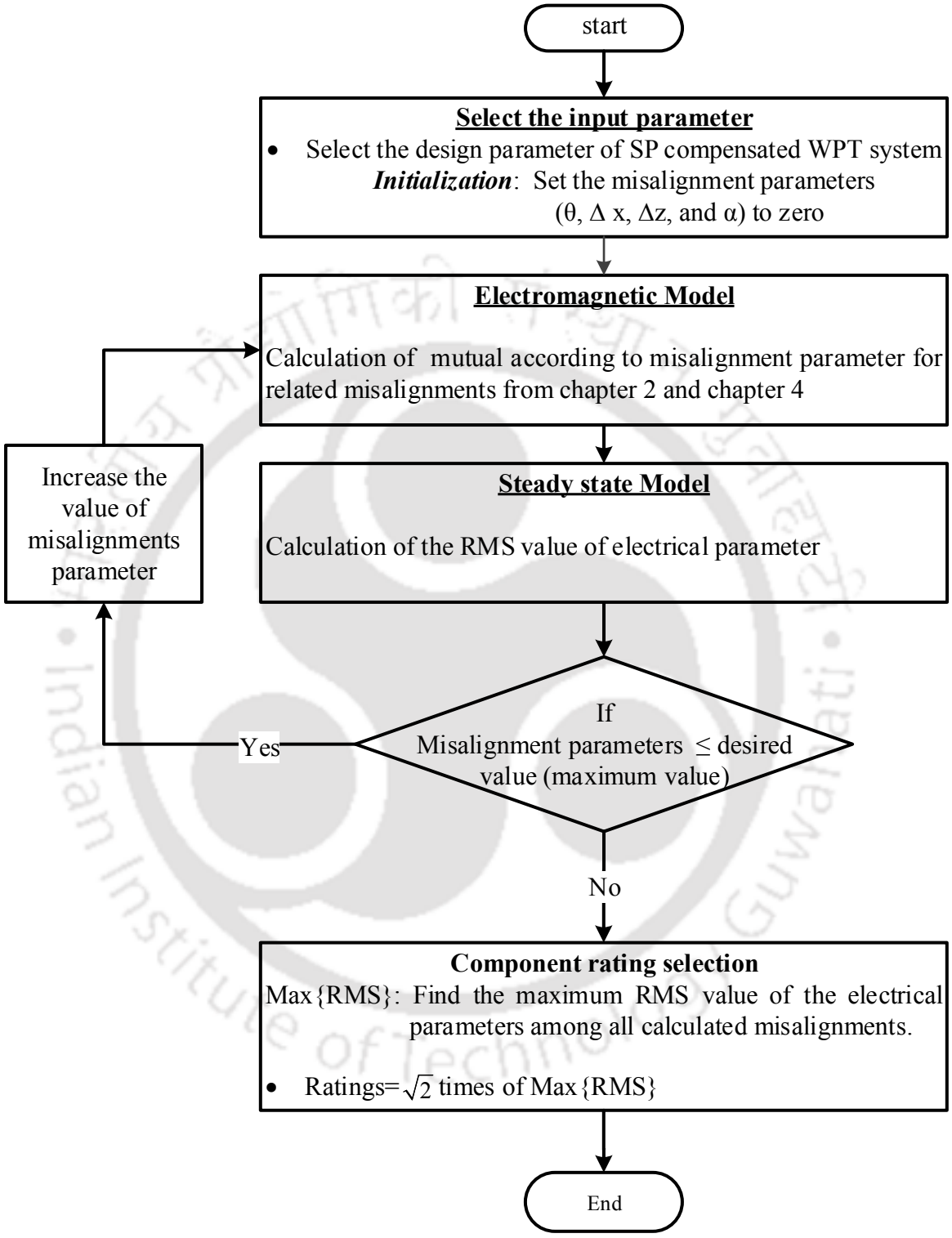

Figure 5.4: Flowchart presenting procedure of proposed analytical model.

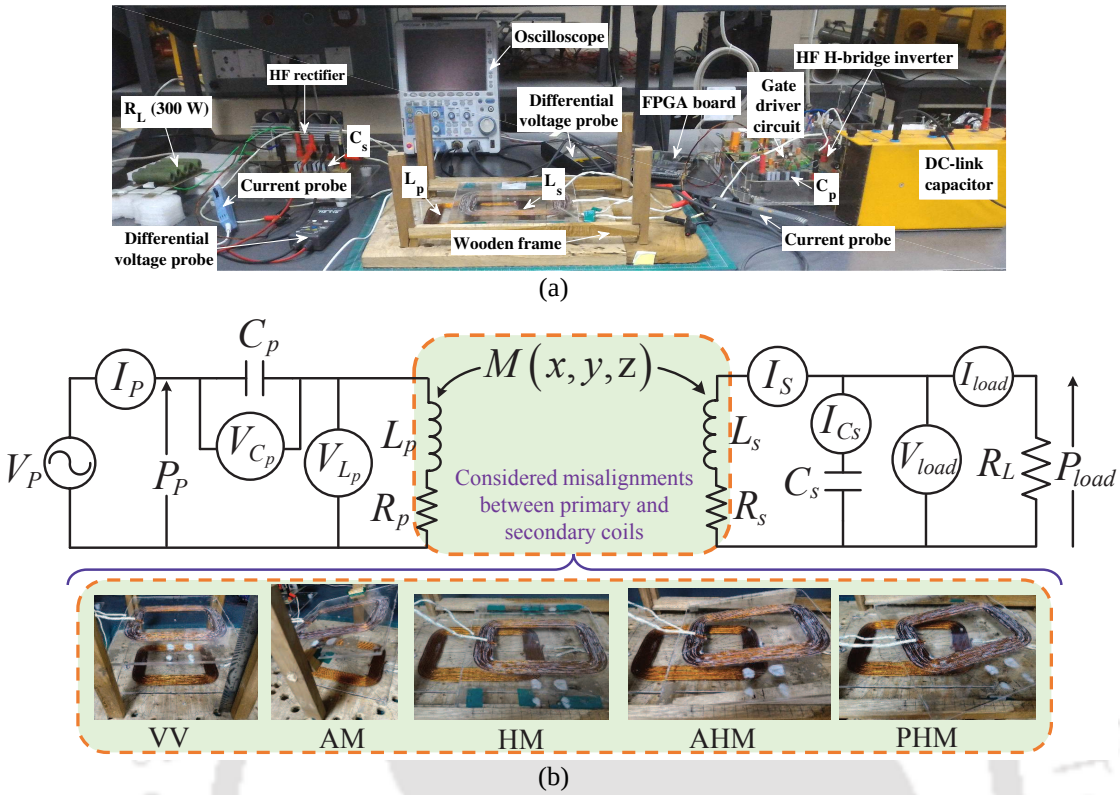

Figure 5.5: (a) Experimental setup and (b) Measurement connections of the electrical parameters with considered misalignments.

5.4 Results and Discussion

The results of the steady-state model are determined by considering 50 harmonics. The system parameters are given in Table 5.1, are used in the steady-state model and simulation. At V_{dc} = 60 V, the V_P from (5.32) is calculated to 59.76 V, which was maintained constant throughout the experiment.

The steady-state waveforms are calculated from the mathematical model, the simulation model based on MATLAB/Simulink, and the experiment when the secondary coil was perfectly aligned with the primary coil at z = 20.15 mm. The steady-state waveforms of $v_p(t)$, $i_p(t)$, $v_{load}(t)$, and $i_{load}(t)$ are computed from (5.7), (5.14), (5.28), and (5.25), respectively, and are shown in Fig. 5.6.

The proposed analytical model takes into account the harmonics of the voltages and currents, and this enables the model to capture the instantaneous waveforms. Fig. 5.6(b) shows the primary current waveform, which is close to a sine wave because the switching frequency has been selected lower than the resonance frequency. The switching frequency has been selected lower than resonance frequency to achieve zero voltage switching (ZVS). In Fig. 5.6, the waveforms calculated from the mathematical

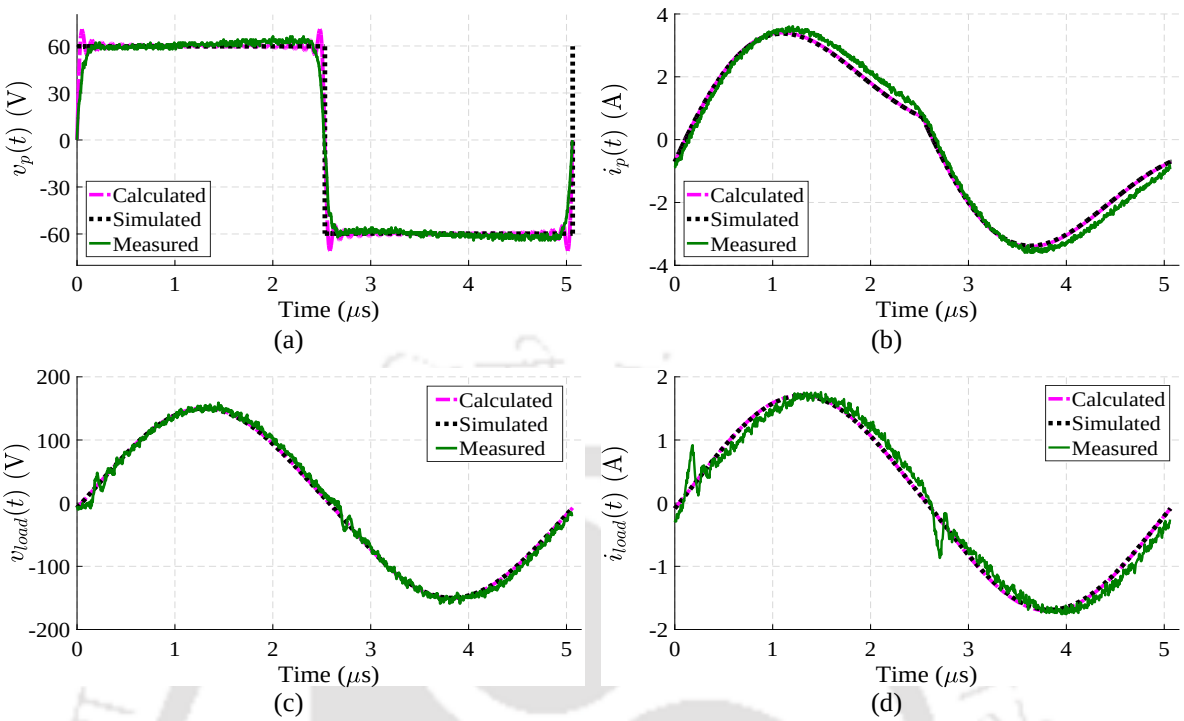

Figure 5.6: Waveforms at $z = 20.15$ mm for (a) primary voltage, (b) primary current, (c) load voltage, and (d) load current.

model match with the simulated waveforms. However, the waveforms from the measurement show a small difference with the waveforms from the mathematical model. This difference is due to a small variation in the mutual inductance, obtained from the experiment and the electromagnetic model.

5.4.1 Results with Different Misalignments

In this subsection, the variation in Z_t, P_{rp}, P_P, P_{load}, η_{cc}, I_P, I_S, I_{C_s}, I_{load}, V_{C_p}, V_{L_p}, and V_{load} for different types of misalignments are discussed. The detailed discussion about different types of misalignment, such as VV, AM, HM, AHM, and PHM, are discussed in chapter 2. First, the parameter variation for the coil system without a magnetic shield for misalignments, shown in Fig. 5.5(b), is investigated then parameter variation for coil system with the magnetic shield for vertical and horizontal misalignments is investigated.

Fig. 5.7 shows the variation in total impedance (Z_t) for different misalignments for the coil system surrounded by air. The variation in total impedance is calculated by (5.6). Here, it can be seen that as misalignment occurs, total impedance starts decreasing sharply, and after some misaligned, it again increases except for planar variation (shown in Fig. 5.7(b)) where it remains almost constant.

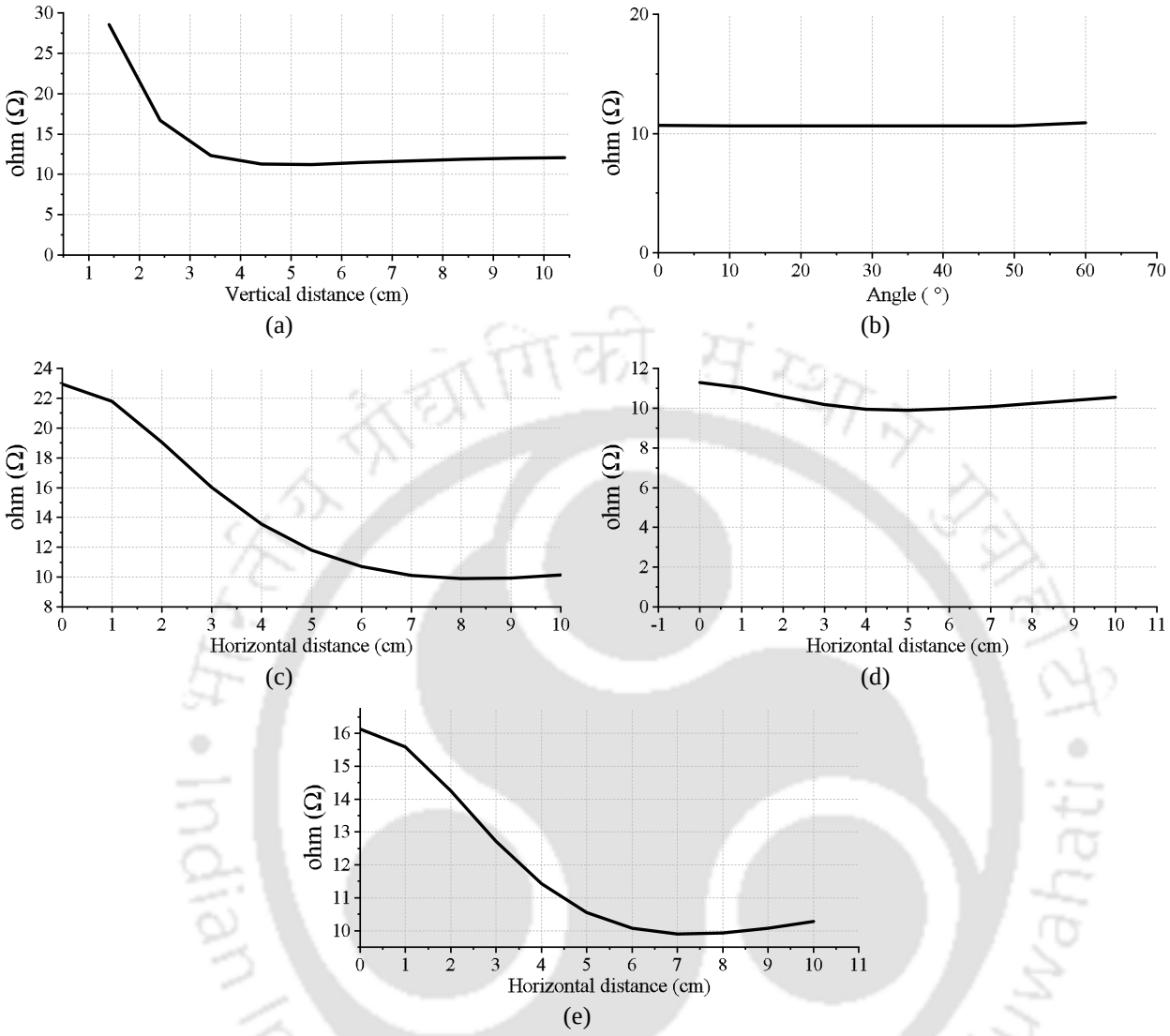

Figure 5.7: The variation in total impedance during (a) VV, (b) AM, (c) HM, (d) AHM (e) PHM.

Figs. 5.8-5.19 show the variation in P_P, P_{load}, η_{cc}, I_P, I_S, I_{C_s}, I_{load}, V_{C_p}, V_{L_p}, and V_{load} for the misalignments. The P_P, P_{load}, and η_{cc} are calculated from (5.17), (5.30), and (5.31) for the different misalignments, are given in Figs. 5.11-5.19, and compared with the experimental results. I_P, I_S, I_{C_s}, I_{load}, V_{C_p}, V_{L_p}, and V_{load} are evaluated for the different misalignments by using (5.32), respectively, are plotted in Figs. 5.8-5.10 with the experimental results.

The primary current for all considered misalignments is calculated by the ratio of the inverter output voltage to the total impedance of the SP compensated WPT system, given by (5.8). Since total impedance, Z_t for different variations is decreasing and increasing nature. Therefore, the primary current variation in different variations is increasing and decreasing nature. The V_{C_p}, V_{L_p} and induced

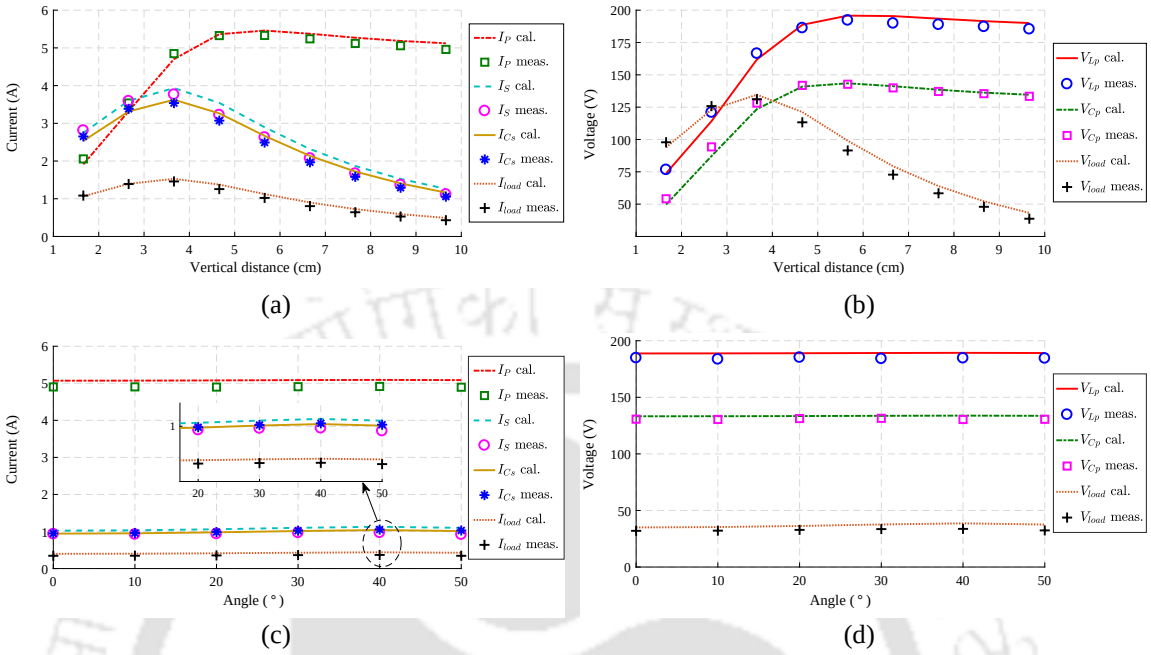

Figure 5.8: (a)-(b) and (c)-(d) are the current and voltage variation w.r.t. VV and AM, respectively.

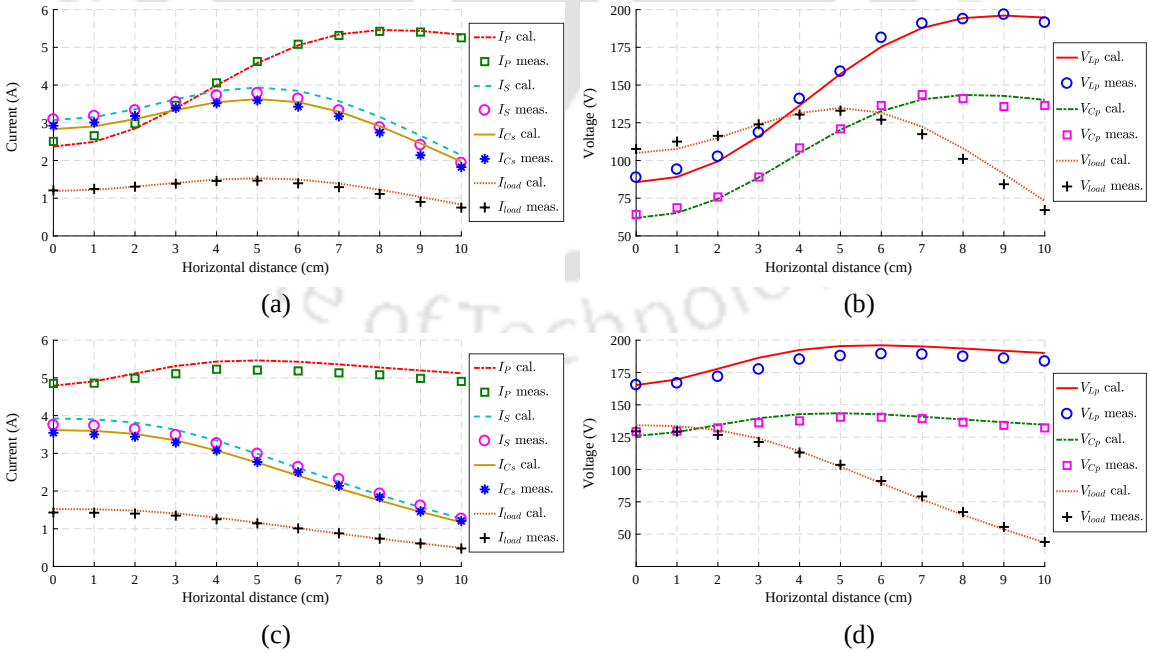

Figure 5.9: (a)-(b) and (c)-(d) are the current and voltage variation w.r.t. HM and AHM, respectively.

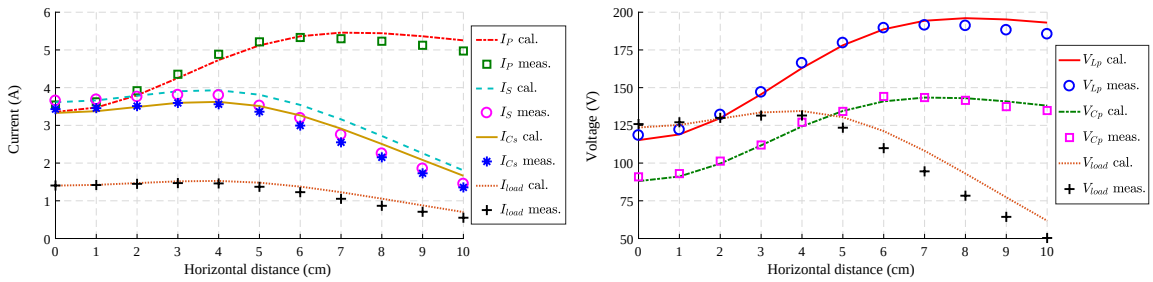

(a) (b)

Figure 5.10: (a) Current and (b) voltage variation for PHM.

voltage and its derive quantities such as I_S, I_{C_s}, I_{load} is proportional to I_P. Therefore, variation in these quantities follows a similar pattern for different misalignment as I_P.

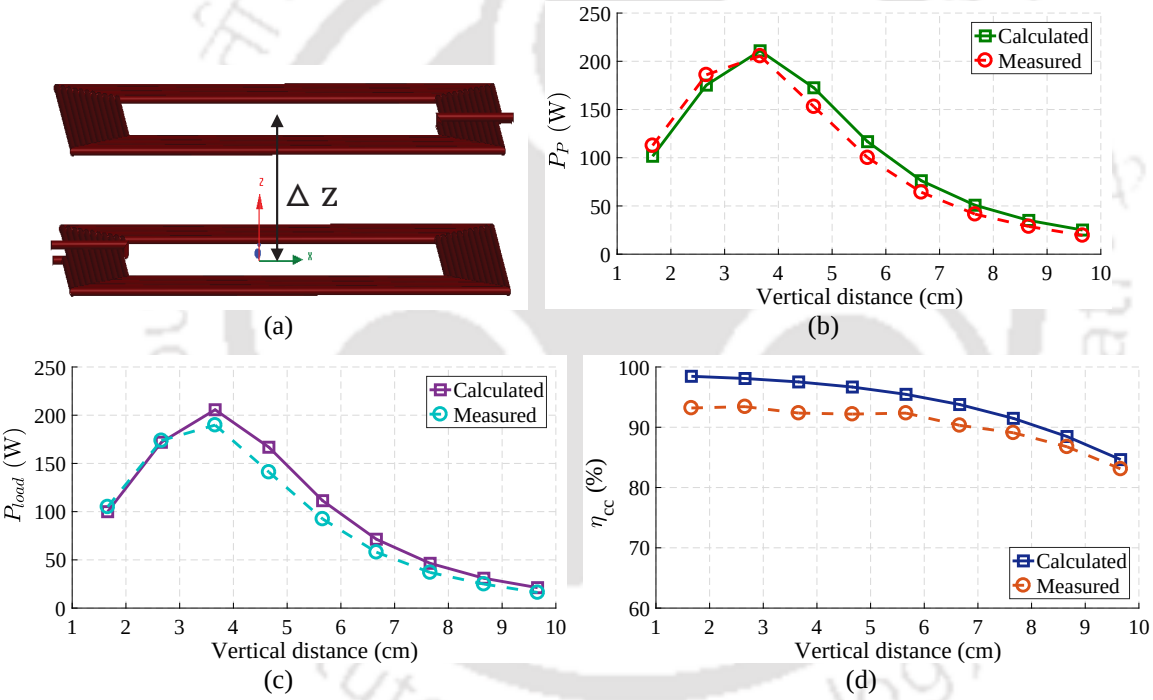

(a) (b) (c) (d)

Figure 5.11: (a) Representation of VV, (b) primary power, (c) output power and, (d) compensated coil efficiency.

For VV, the secondary coil is moved along the *z*-axis from 1.66 to 9.66 cm in a step of 1 cm, as shown in Fig. 5.11(a). The electrical parameter variations w.r.t. VV are shown in Figs. 5.11(b)-(d), 5.8(a) and (b). It can be seen from Fig.5.8(a), as the vertical distance between the primary and secondary coils increases, the reflected impedance Z_r decreases, which results in an increase in the primary current I_P. It is observed that the maximum value of I_P, V_{C_p}, and V_{L_p} occurs at $4cm$ displacement from the starting point and it approximately 2.6 times the initial value whereas the

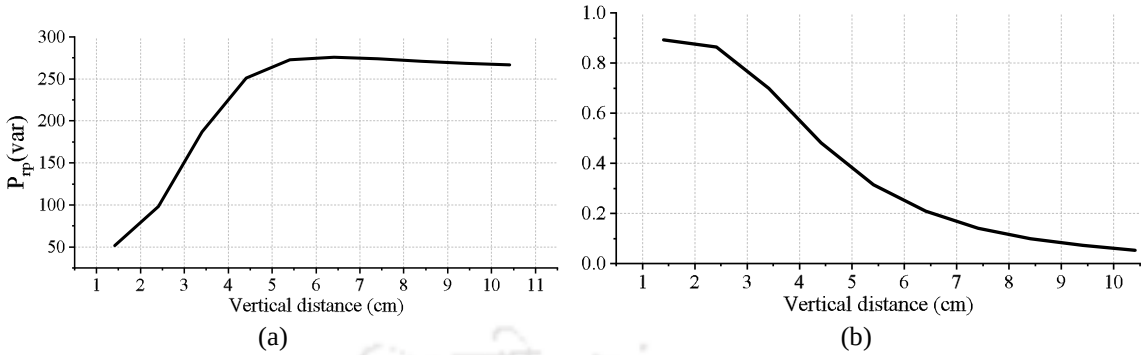

Figure 5.12: Variation in, (a) input reactive power and, (b) power factor for vertical variation.

maximum value of I_S, I_{C_s}, I_{load}, and V_{load} observed at 3cm displacement, and it is approximately 1.4 times the initial value. Therefore, the ratings of secondary side elements (such as MOSFET, Diode, inductor, and capacitor) can be lower than ratings of primary side elements. The variations in primary side reactive power and power factor w.r.t. VV are shown in Figs. 5.12(a) and 5.12(b). Here, it can be seen that as the secondary coil moves away from the primary coil, reactive power increases, whereas the power factor decreases.

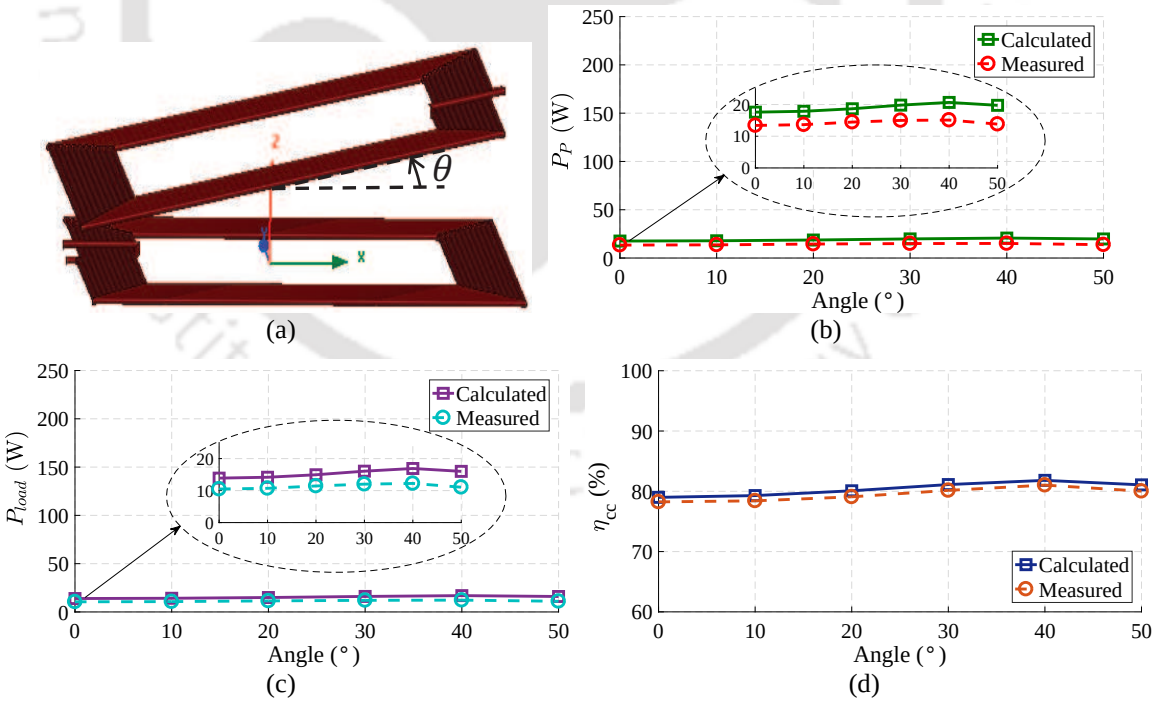

Figure 5.13: At z = 108.40 mm (a) Representation of AM, (b) primary power, (c) output power and, (d) compensated coil efficiency.

Fig. 5.13(a) shows the representation of AM. Here, the secondary coil is tilted around the y-axis

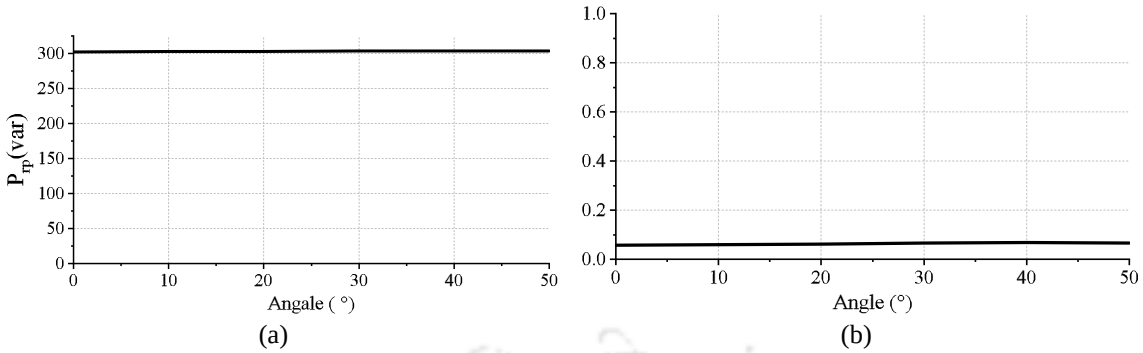

Figure 5.14: Variation in, (a) primary reactive power and (b) power factor for angular misalignments.

from 0° to 50° in the step of 10° at z = 108.40 mm. In this variation, as the secondary coil tilts, the effective area for the flux linkage decreases; this results in a decrease of reflective impedance. The variation in electrical parameters w.r.t. AM are shown in Figs. 5.13(b)-(d), 5.8(c), and (d) and it is observed that variation remains unchanged. The variations in primary side reactive power and power factor w.r.t. AM are shown in Figs. 5.14(a) and 5.14(a). Here, it is observed that during this misalignment, reactive power and power factor remains constant.

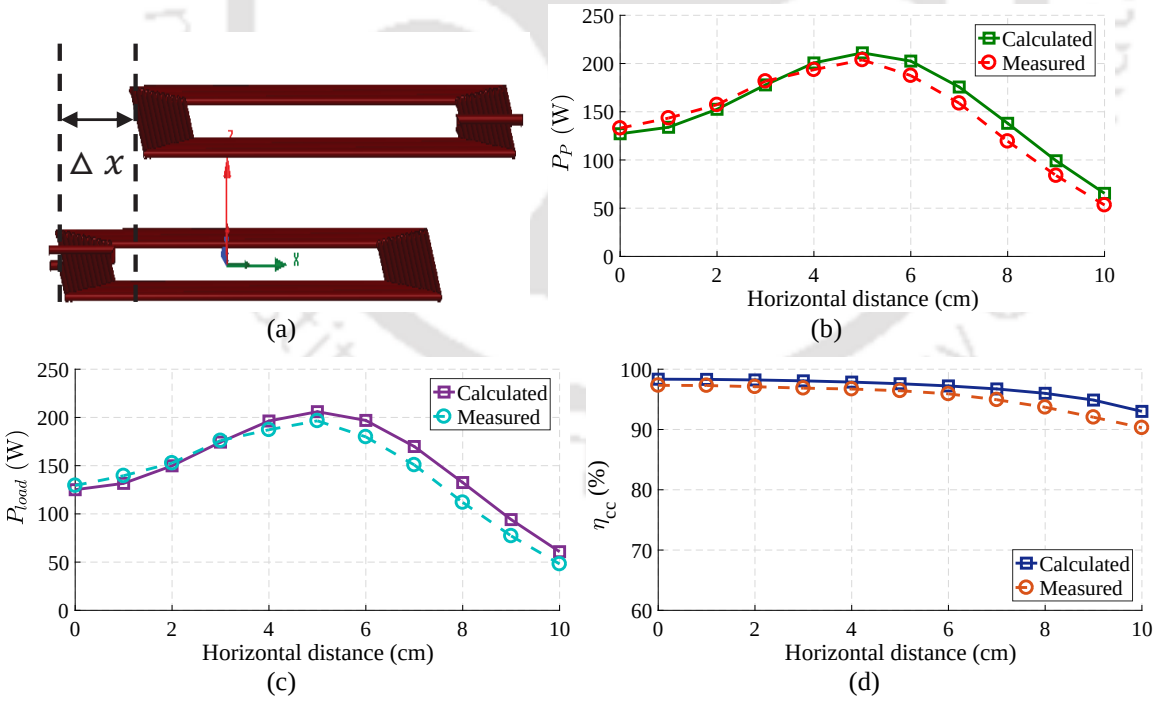

Figure 5.15: At z = 20.15 mm (a) Representation of HM, (b) primary power, (c) output power and, (d) compensated coil efficiency.

For HM, the secondary coil is moved along the x-axis from 0 to 10 cm at a step 1 cm at z = 20.15

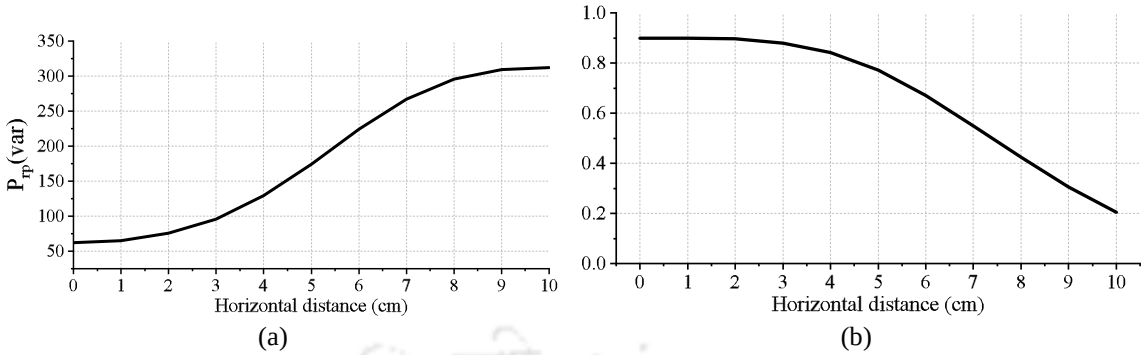

Figure 5.16: Variation in (a) primary reactive power, (b) power factor for horizontal misalignments.

mm, as shown in Fig. 5.15(a). As the secondary coil moves, the overlapping area between the coils decreases, which reduces the mutual inductance. The decrease in mutual inductance affects the magnitude of electrical parameters, as shown in Figs. 5.15(b)-(d), 5.9(a), and (b). It can be seen that the max RMS values of I_P, V_{C_p}, and V_{L_p} are approximately 2.3 times the initial value when the displacement between the two coils is 8*cm* in positive the *x*-direction from the initial position (x=0), whereas the maximum value of I_S, I_{C_s}, I_{load} and V_{load} are observed at 5*cm* displacement, and it is approximately 1.2 times the initial value. Figs. 5.12(a) and 5.12(b) shows the variations in primary side reactive power and power factor w.r.t. HM. Here, as the misalignment between primary and secondary coil increases, primary coil reactive power increases, whereas the power factor decreases.

In AHM, as shown in Fig. 5.17(a), the secondary coil is kept at an angle of 10.17° (around the *y*-axis) and moved along the *x*-axis from 0 to 10 cm at a step 1 cm at z = 39.06 mm. Figs. 5.17(b)-(d), 5.9(c), (d), and 5.18 show the variation in electrical parameters w.r.t. this misalignment. It is observed that the maximum rms value of I_P, V_{C_p}, and V_{L_p} is approximately 1.2 times of the initial value at the horizontal displacement of 6*cm*, whereas the secondary parameters are decreases from intimal values during misalignment.

Fig. 5.19(a) represents the PHM variation. Here, the secondary coil is kept at an angle of 8° (around the *z*-axis) at z = 26.40 mm and moved along the *x*-axis from 0 to 10 cm at a step of 1 cm. The variation in electrical parameters w.r.t. PHM are shown in Figs. 5.19(b)-(d), 5.10(a), (b) and 5.20. It is observed that the primary electrical parameters are approximately 1.7 times of the initial value at the horizontal displacement of 7*cm*, whereas the value of the secondary side electrical parameter remains almost the same.

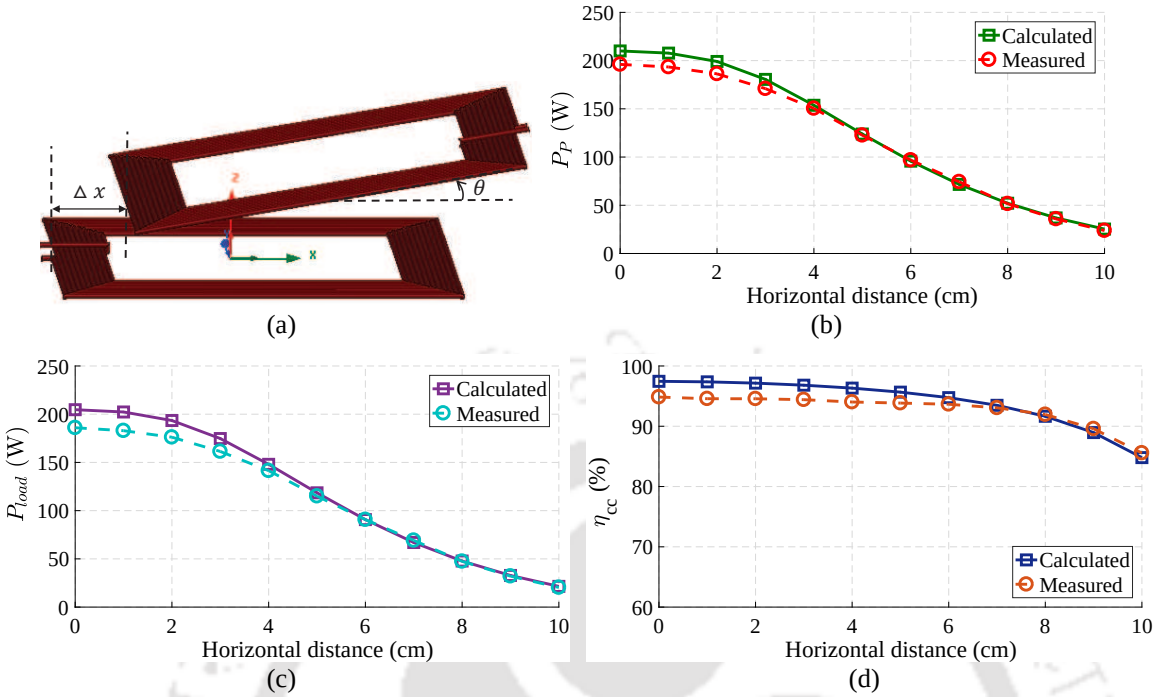

Figure 5.17: At an angle of 10.17° and z = 39.06 mm (a) Representation of AHM, (b) primary power, (c) output power and, (d) compensated coil efficiency.

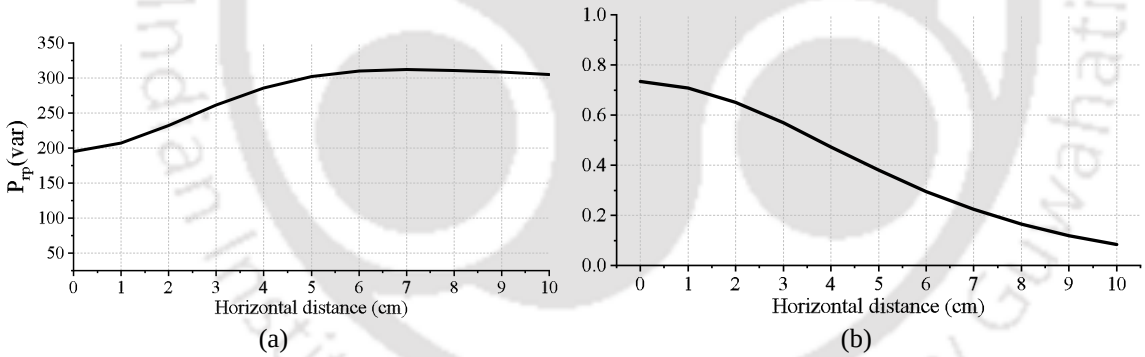

Figure 5.18: Variation in (a) input reactive power and (b) power factor for AHM variation.

From the above discussion, it is concluded that The VV shows the maximum deviation in electrical parameters among all the six misalignments.

5.4.2 Variation in electrical parameter for coil system having magnetic shields

The variation in parameters of the sp compensated system with the magnetic shield for vertical and horizontal misalignment is shown in Figs. 5.21-5.23. Fig. 5.21 shows the variation in the self-inductance of vertical and horizontal misalignments. The variation in electrical parameter for vertical misalignment is shown in Fig. 5.22, whereas the variation in the electrical parameter for horizontal

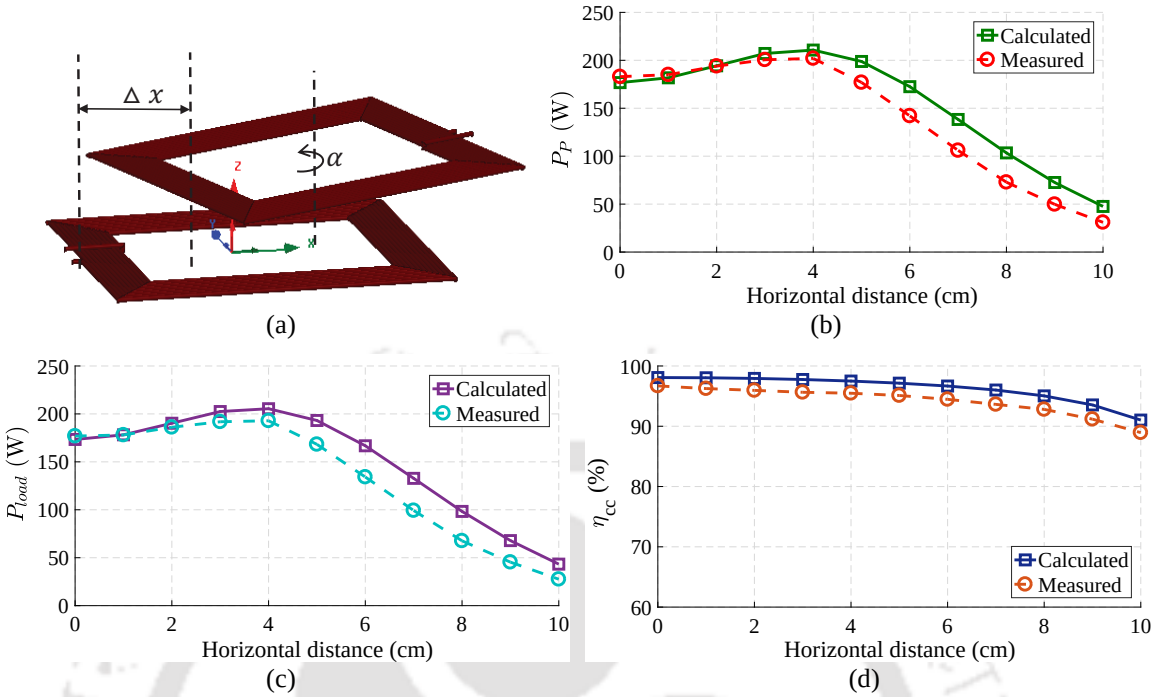

Figure 5.19: At an angle of 8° and z = 26.40 mm (a) Representation of PHM, (b) primary power, (c) output power and, (d) compensated coil efficiency.

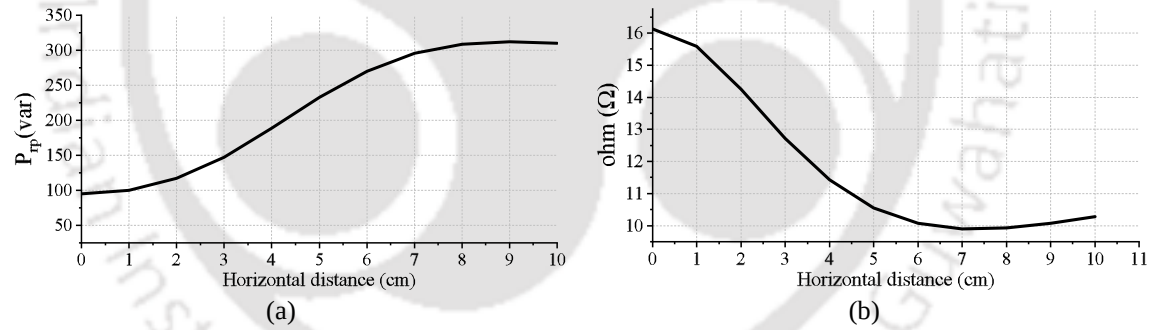

Figure 5.20: Variation in (a) primary reactive primary power and (b) power factor for PHM variation.

misalignment is shown in Fig. 5.23.

From Fig. 5.22 it is observed that the maximum RMS value of I_P, V_{C_p}, and V_{L_p} occurs at 6cm displacement from the starting point, and it approximately 2.15 times the initial value, whereas the maximum value of I_S, I_{C_s}, I_{load}, and V_{load} observed at 2cm displacement, and it is approximately 1.18 times the initial value.

From Figs. 5.22(a)-5.22(b) it can be seen that the max RMS values of I_P, V_{C_p}, and V_{L_p} are approximately 1.72 times the initial value when the displacement between the two coils is 7cm in positive the x-direction from the initial position (x=0), whereas the maximum value of I_S, I_{C_s}, I_{load},

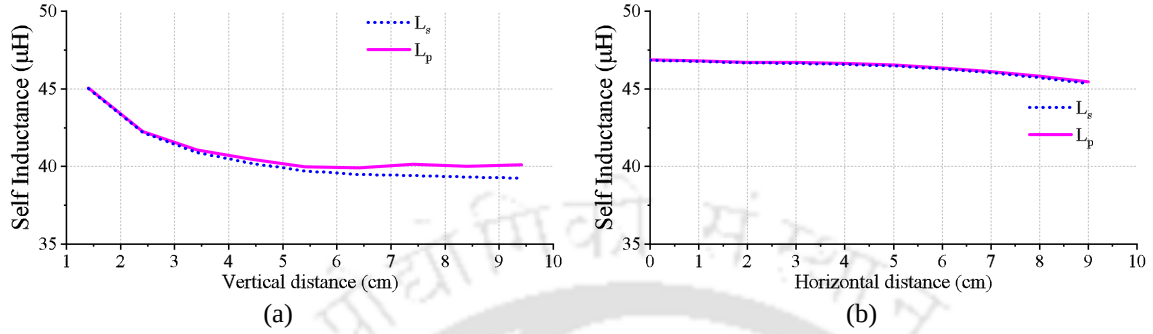

Figure 5.21: Self-inductance variation w.r.t. VV and HM.

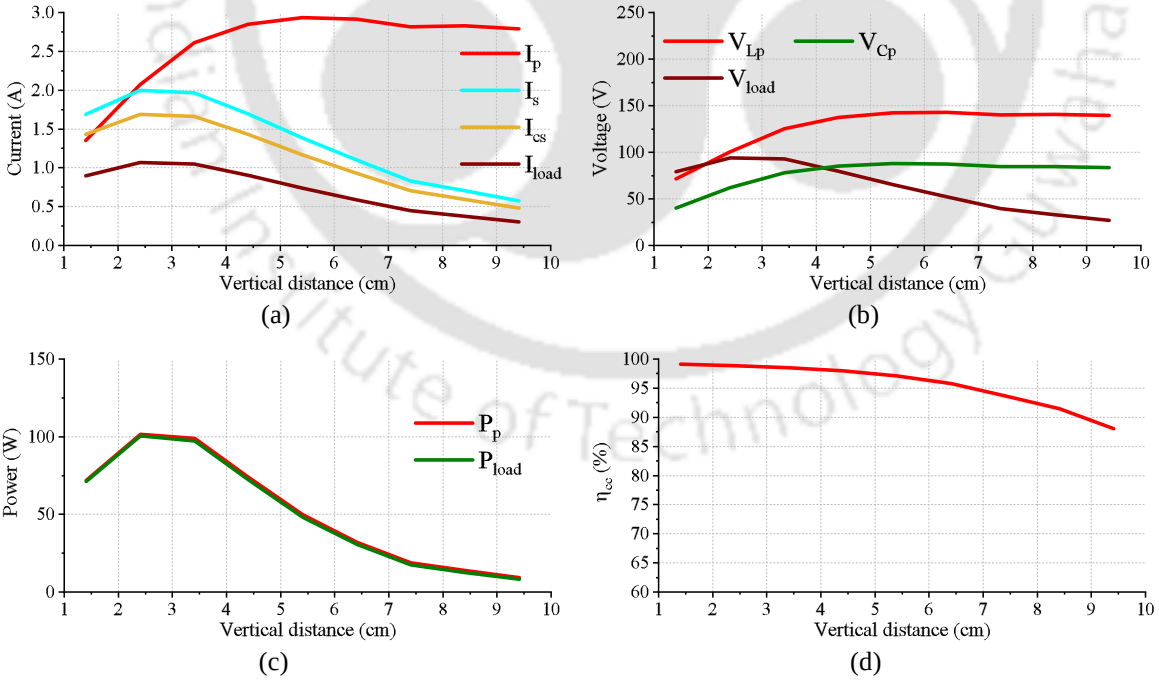

Figure 5.22: Variation in electrical parameter w.r.t. VV.

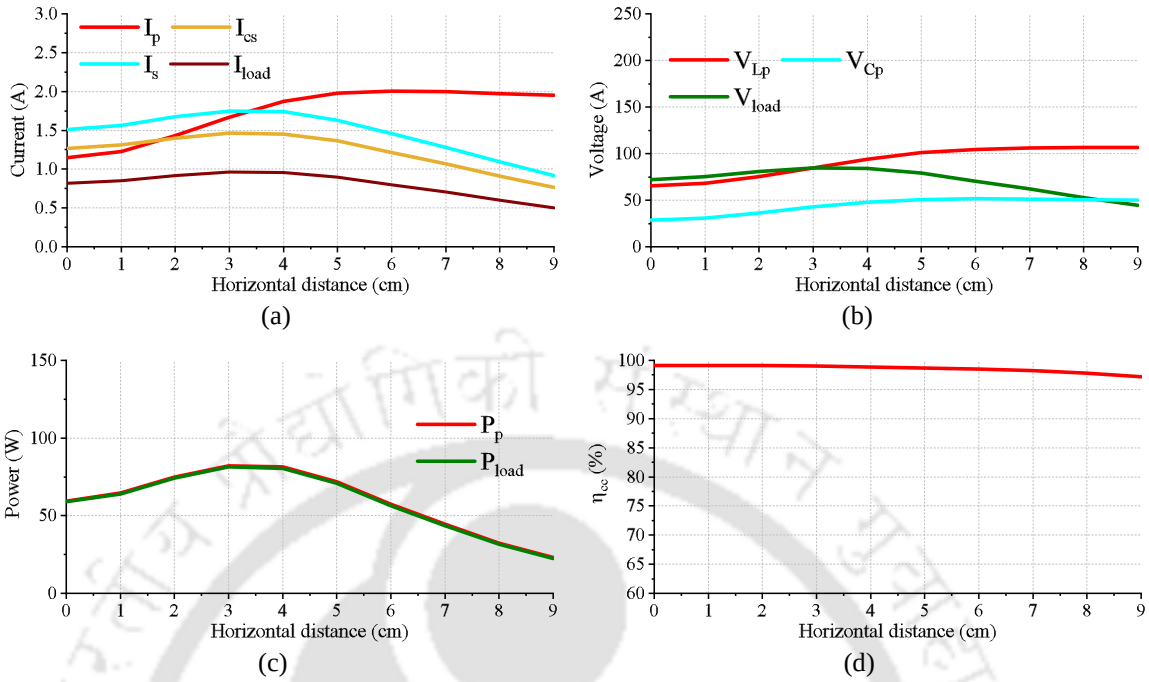

Figure 5.23: Variation in electrical parameter w.r.t. horizontal misalignments.

and V_{load} are observed at 3*cm* displacement, and it is approximately 1.17 times the initial value.

From comparing the variation in the electrical parameter of SP compensated WPT system for coil system without shield and with shield, it is obtained that parameter variation in sp compensated WPT system with shields has lesser variation than sp compensated WPT system without the shield.

5.5 Summary

In this chapter, the variation in voltage, current, power, and efficiency of the SP compensated WPT system for different misalignments, such as horizontal, angular, planar, etc, has been discussed. The steady-state model is used to calculates the electrical parameter variation of the SP compensated WPT system. In order to get an accurate result, the effect of the harmonics is considered in the steady-state model. Moreover, an experimental setup of 300 W for SP compensated WPT system with different misalignments is developed in the laboratory to validate the efficacy of the model. The analytical results are compared with the simulation and the measurement results, and a good agreement has been found. Therefore, the proposed model can be used for analyzing the component stress of the SP compensated WPT system for different misalignments, which helps in the initial design process of such a WPT system.

6

Conclusion and Future Works

Contents

6.1 Summary of the Work 116
6.2 Limitations of the Work 118
6.3 Scope for Future Research 119

6.1 Summary of the Work

For the designing WPT system, an accurate modelling of the magnetic field is required. The 3-D finite element analysis (FEA) is used to design a coil system because of its high accuracy. However, high mesh-density in the 3-D FEA model requires high computational power. An iterative design process, to achieve the desired coil system, requires numerous modifications in the 3-D FEA model, which is a tedious process. Moreover, many FEA packages do not provide a straight relationship between the performance and the parameter of the WPT system.

To address this issue, the objective of this thesis is to present an alternative FEA modelling for the designing of the WPT system. For this, an accurate, comprehensive analytical model to predict parameter variation during misalignment for the WPT system has been given. The analytical model consists of electromagnetic and steady-state models. The electromagnetic model is used to compute the mutual inductance between the coils for different misalignments. On the other hand, the steady-state model calculates the voltage, current, power, and efficiency of the SP compensated WPT system (by using the mutual inductance information from the electromagnetic model). This model can be used to analyze the component stress of the SP compensated WPT system. The results of the mathematical model are verified experimentally. Thus, the proposed method can be adopted in the initial design process of the SP compensated WPT system.

The electromagnetic model has been developed for different coil systems. First, the modelling has been done for the coil system without a magnetic shield. For the modelling, various modelling method has been discussed, and it is found that harmonic model found suitable to describe the magnetic field distribution and mutual inductance between the coils of the coil system of WPT system. The harmonic model divides the three-dimensional coil system into different regions in the non-periodic direction (Here, z-direction) according to the material property. For each region, either three-dimensional magnetic vector potential or magnetic scalar potential, by solving Poisson or Laplace equation using the method separation of variables, has been formulated in the cartesian coordinates system. These magnetic potentials contain unknown coefficients, which is solved by applying boundary conditions between the regions. The boundary conditions are defined by the continuity of tangential magnetic field intensity and normal component of the magnetic flux density at the edge of each region in the

z-direction. Applying the various boundary conditions gives a set of linear equations, which is solved to obtain the value of unknown coefficients of magnetic potentials. The number of linear equations is equal to the number of unknowns. These magnetic potentials have been used to calculate the magnetic flux density distribution in the air-gap and mutual inductance between the coils. The coil is modelled by four current overlapping bars and mathematically represented in similar for magnetic vector potential. The mutual inductance from the proposed analytical model has been calculated for different misalignments and validated with a 3-D FEA model and measurements. Moreover, the variation in mutual inductance for different misalignments (such as horizontal, angular, planar, etc.), which are the practical case of wireless charging for EVs, are also discussed. The results of the analytical model are compared with the 3-D FEA model and the measurements, and a good agreement has been found.

Furthermore, the analytical model for the coil system having magnetic below the primary coil has been developed. The developed analytical model for the coil system without a shield with some modification has been successfully applied to the coil system having magnetic below the primary coil. With the addition of a magnetic shield underneath of primary coil, as compared to the previous model, a region representing a magnetic shield has been added in the modelling. The magnetic scalar potential is used to describes the magnetic field in this region. This magnetic potential contains unknown coefficients, which is calculated by applying boundary conditions at the boundary of the magnetic shield region. The boundary conditions have been defined by the continuity of magnetic scalar potential and normal component of the magnetic flux density at the edge of the magnetic shield region. This model has the flexibility to change the width and permeability of shielding material. The presented analytical model is verified for different misalignments with FEA results and measurements.

The proposed analytical model considers the length of the magnetic shield is infinite, which is impractical. In practice, the magnetic shielding of finite permeability and finite dimensions is practically used with the primary and secondary coils. Therefore, a 3-D analytical model that considers the magnetic shields of finite permeability and finite dimension has been developed. The magnetic vector potential formulation in the cartesian coordinate system has been used in subdomain modelling. For the subdomain modelling, the continuity of magnetic vector potential and magnetic field intensity is applied in two directions (i.e., x- and y-edges). The comparison in magnetic field distribution obtained

from the subdomain model and 2-D FEA has been made. The magnetic field distributions obtained from the 2-D subdomain model coincide with the magnetic field obtained from 2-D FEA, which confirms the accuracy of the 2-D subdomain model. A 3-D subdomain model has been formulated by the superposition of two 2-D subdomain models to obtain the result close to measurement results. For limiting the 2-D subdomain model in the third direction, a correction factor has been introduced. The proposed subdomain model is validated by the computation of magnetic field density distribution in the air gap and compared with FEA and experiment. It shows a good agreement. The mutual inductance from the 3-D subdomain model has been compared with FEA results and measurement. The proposed subdomain model facilitates to change the parameters (length, width, and permeability) of magnetic shields. The results from the proposed subdomain model are acceptably accurate for initial designing and optimization of the WPT system having magnetic shielding of finite dimension and permeability.

The change in the mutual inductance impacts the power transfer capability and the efficiency of the entire WPT system. To investigate the variation in voltage, current, power, and efficiency of the SP compensated WPT system for different misalignments, such as horizontal, angular, planar, etc. , a steady-state model of SP compensated WPT system has been developed. The mutual inductance calculated by electromagnetic model is used as direct input to the steady-state model. In order to get an accurate result, harmonics effect is considered in the steady-state model. Moreover, an experimental setup of 300 W for SP compensated WPT system with different misalignments is developed in the laboratory to validate the efficacy of the model. The results of the mathematical model are compared with the simulation and the measurement results, and a good agreement has been found. Therefore, the proposed model can be used for analyzing the component stress of the SP compensated WPT system for different misalignments, which helps in the initial design process of such a WPT system.

6.2 Limitations of the Work

This thesis developed 3-D analytical models to analyze the magnetic field distribution in the WPT system. Different coil system has been considered in the modelling. In developing the analytical models, harmonic and subdomain technique has been used. During the development of analytical models, several assumptions such as current in the z-direction, eddy current, temperature-dependent

quantity, non-linearity and hysteretic property of magnetic shield have been neglected to simplify the analytical model. These assumptions limit the applicability of proposed models. Moreover, The presented subdomain model in chapter 4 calculates mutual inductance only for horizontal and vertical misalignments.

6.3 Scope for Future Research

The following recommendations are made to improve the range of applicability of the proposed model:

- Much research has been carried out to improve the coupling between the coils in the WPT system. For this, different coil structures such as DD, DDQ, multiple coil couplers, etc. [106–108], have been designed. By changing the definition of the current density in the proposed analytical models, one can develop the analytical model for the WPT system having these coils.
- Include the current in the *z*-direction.
- By re-defining magnetic potential in the proposed 3-D analytical model, the eddy currents can be included in the modelling. .
- The analytical model using the subdomain technique discussed in chapter 4 predicts mutual inductance does not consider angular and planar misalignments. The magnetic vector potentials can be further modified to include these misalignments.
- The applicability of the proposed electromagnetic model can be increased with the inclusion of non-linear magnetic property of the applied magnetic shield.
- The transferred power in the WPT system depends on the resistance of the coils. The resistance of coils varies with the temperature of the coils. A thermal model can be included in the proposed models to predict the parameter variation with temperature in the WPT system.
- The research has been focussed on the magnetic design of the WPT system. Moreover, the variation in the electrical parameter for the SP compensated WPT system also has been studied. For the SP compensated WPT system, resonance frequency depends on the mutual inductance and

the self inductances of the coils. Due to the misalignment between the coils, the value of M, L_p, and L_s changes, and the WPT system is no more in resonance (it gets mistuned), this mistuning impacts the electrical parameters of the SP compensated WPT. The dc-ac converter with the ability of self-tuning can overcome the variation in electrical parameters during misalignments.

A

Calculation of Expression of Mutual Inductance

A.1 Calculation of Expression

To get a generalized expression a case is considered where the coil is shifted and tilted by angle θ and shifted in Δx in x-direction as shown in Fig. A.1, a generalized expression can be derived as follows:

In (3.26), the integration has been done from the coordinate point $P(x_i, y_i)$ to $Q(x_f, y_i)$ and $P(x_i, y_i)$ to $Q(x_f, y_i)$ indicated in Fig.(A.1).

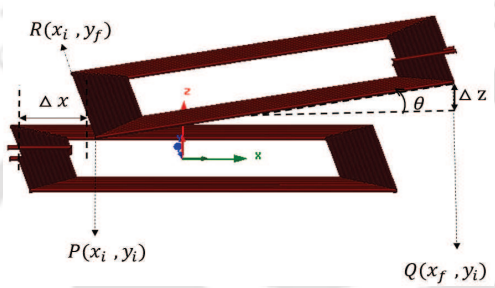

Figure A.1: Generalized coil position.

The value of x_i,x_f,y_i and y_f can be written in terms of θ and Δx as-

$$x_i = (\mathrm{n_s} \times \mathrm{w} - \mathrm{a_{2s}}) \times \cos(\theta) + \Delta \mathrm{x} \tag{A.1}$$

$$x_f = (\mathrm{n_s} \times \mathrm{w} - \mathrm{a_{2s}}) \times \cos(\theta) + \Delta \mathrm{x} \tag{A.2}$$

$$y_i = \mathrm{n_s} \times \mathrm{sw} - \mathrm{b_{2s}} \tag{A.3}$$

$$y_f = \mathrm{n_s} \times \mathrm{sw} - \mathrm{b_{2s}} \tag{A.4}$$

The coil parameters such as a_{2s}, b_{2s}, etc. are given in Table 2.1. Since the integration limit is taken in x and y coordinate, writing z in terms of x as-

$$z = -\tan(\theta) \times (x - \Delta \mathrm{x}) + \Delta z \tag{A.5}$$

Now From (3.26)

$$M(x,y,z) = \int_{y_i}^{y_f} \int_{x_i}^{x_f} \left(\frac{(B_{III}) \cdot \left(\sin(\theta)\,\hat{i} + \cos(\theta)\,\hat{k} \right)}{\cos(\theta)} \right) dxdy \qquad \text{(A.6)}$$

B

Magnetic Vector Potential of Different Regions

B.1 Applied Boundary Conditions Between Different Regions

In this section the boundary condition between each regions of coil system shown in Fig. 4.3 is presented. The boundary condition is applied at the interface between the each regions.// At z_3

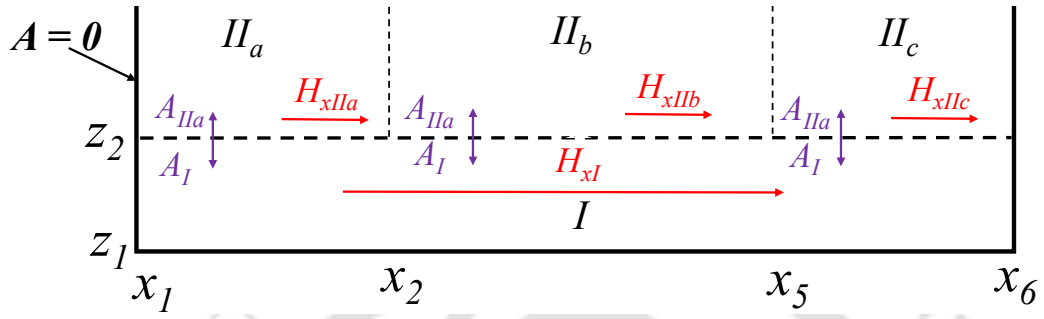

Figure B.1: Illustration of boundary condition at $z=z_2$.

$$\mathbf{H}_{xI}(x,z_2) = \mathbf{H}_{xIIa}(x,z_2)|_{x_1\le x\le x_2} + \mathbf{H}_{xIIb}(x,z_2)|_{x_2\le x\le x_5} + \mathbf{H}_{xIIc}(x,z_2)|_{x_5\le x\le x_6} \quad \text{(B.1)}$$

$$\mathbf{A}_{IIa}(x,z_2) = \mathbf{A}_I(x,z_2) \text{ where } x_1 \le x \le x_2 \quad \text{(B.2)}$$

$$\mathbf{A}_{IIb}(x,z_2) = \mathbf{A}_I(x,z_2) \text{ where } x_2 \le x \le x_5 \quad \text{(B.3)}$$

$$\mathbf{A}_{IIc}(x,z_2) = \mathbf{A}_I(x,z_2) \text{ where } x_5 \le x \le x_6 \quad \text{(B.4)}$$

At z_3

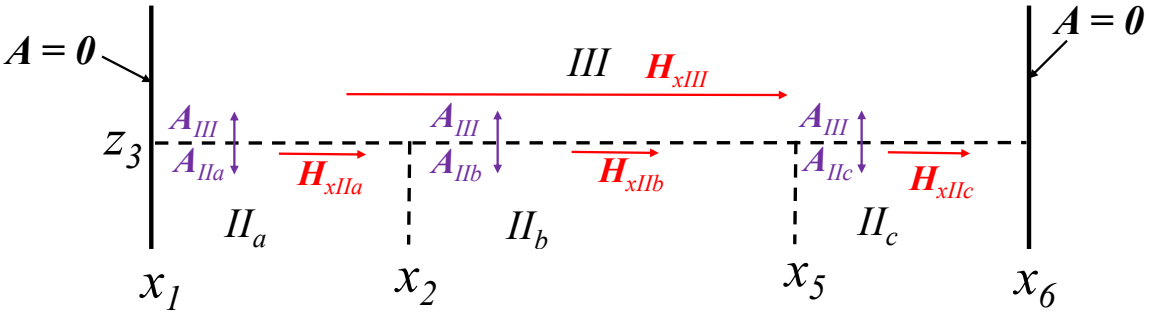

Figure B.2: Illustration of boundary condition at $z=z_3$.

$$H_{x_{III}}(x,z_3) = H_{x_{IIa}}(x,z_3)\big|_{x_1\le x\le x_2} + H_{x_{IIb}}(x,z_3)\big|_{x_2\le x\le x_5} + H_{x_{IIc}}(x,z_3)\big|_{x_5\le x\le x_6} \quad \text{(B.5)}$$

$$A_{IIa}(x,z_3) = A_{III}(x,z_3) \text{ where } x_1 \le x \le x_2 \quad \text{(B.6)}$$

$$A_{IIb}(x,z_3) = A_{III}(x,z_3) \text{ where } x_2 \le x \le x_5 \quad \text{(B.7)}$$

$$A_{IIc}(x,z_3) = A_{III}(x,z_3) \text{ where } x_5 \le x \le x_6 \quad \text{(B.8)}$$

At z_4

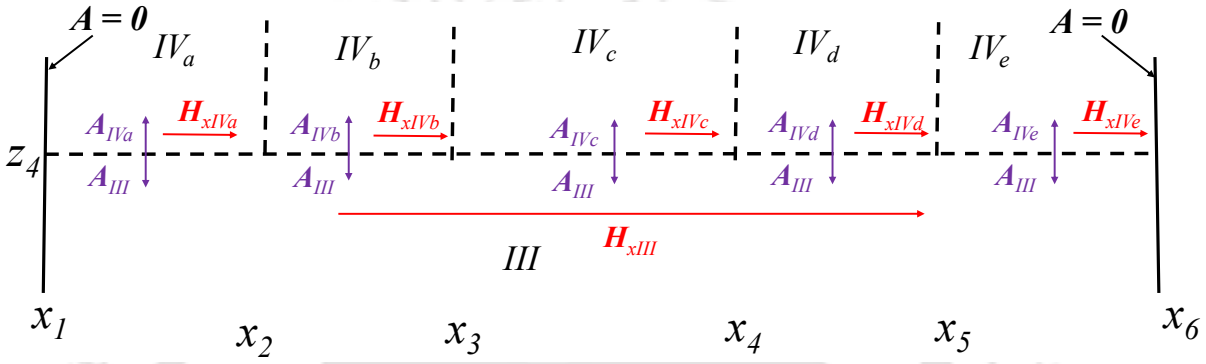

Figure B.3: Illustration of boundary condition at $z=z_4$.

$$H_{x_{III}}(x,z_4) = H_{x_{IVa}}(x,z_4)\big|_{x_1\le x\le x_2} + H_{x_{IVb}}(x,z_4)\big|_{x_2\le x\le x_3} + H_{x_{IVc}}(x,z_4)\big|_{x_3\le x\le x_4} \quad \text{(B.9)}$$

$$+ H_{x_{IVd}}(x,z_4)\big|_{x_4\le x\le x_5} + H_{x_{IVe}}(x,z_4)\big|_{x_5\le x\le x_6} \quad \text{(B.10)}$$

$$A_{IV_a}(x,z_4) = A_{III}(x,z_4) \text{ where } x_1 \le x \le x_2 \quad \text{(B.11)}$$

$$A_{IV_b}(x,z_4) = A_{III}(x,z_4) \text{ where } x_2 \le x \le x_3 \quad \text{(B.12)}$$

$$A_{IV_c}(x,z_4) = A_{III}(x,z_4) \text{ where } x_3 \le x \le x_4 \quad \text{(B.13)}$$

$$A_{IV_d}(x,z_4) = A_{III}(x,z_4) \text{ where } x_4 \le x \le x_5 \quad \text{(B.14)}$$

$$A_{IV_e}(x,z_4) = A_{III}(x,z_4) \text{ where } x_5 \le x \le x_6 \quad \text{(B.15)}$$

Region z_5

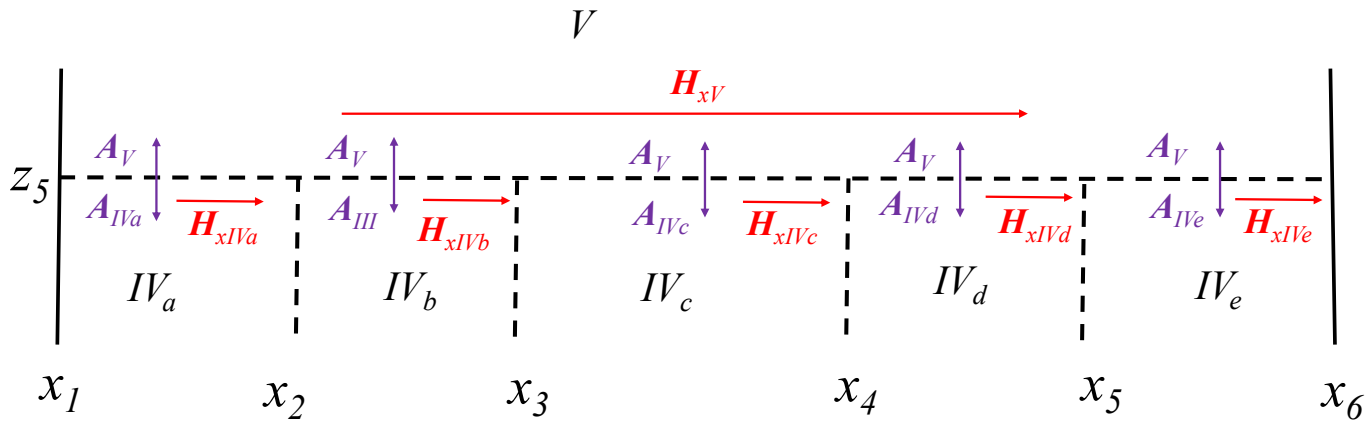

Figure B.4: Illustration of boundary condition at $z=z_5$.

$$H_{x_V}(x,z_5) = H_{x_{IVa}}(x,z_5)\big|_{x_1\le x\le x_2} + H_{x_{IVb}}(x,z_5)\big|_{x_2\le x\le x_3} + H_{x_{IVc}}(x,z_5)\big|_{x_3\le x\le x_4} \quad \text{(B.16)}$$

$$+ H_{x_{IVd}}(x,z_5)\big|_{x_4\le x\le x_5} + H_{x_{IVe}}(x,z_5)\big|_{x_5\le x\le x_6} \quad \text{(B.17)}$$

$$A_{IV_a}(x,z_5) = A_V(x,z_5)\,;\text{where } x_1 \le x \le x_2 \quad \text{(B.18)}$$

$$A_{IV_b}(x,z_5) = A_V(x,z_5)\,;\text{where } x_2 \le x \le x_3 \quad \text{(B.19)}$$

$$A_{IV_c}(x,z_5) = A_V(x,z_5)\,;\text{where } x_3 \le x \le x_4 \quad \text{(B.20)}$$

$$A_{IV_d}(x,z_5) = A_{III}(x,z_5)\,;\text{where } x_4 \le x \le x_5 \quad \text{(B.21)}$$

$$A_{IV_e}(x,z_5) = A_V(x,z_5)\,;\text{where } x_5 \le x \le x_6 \quad \text{(B.22)}$$

At z_6

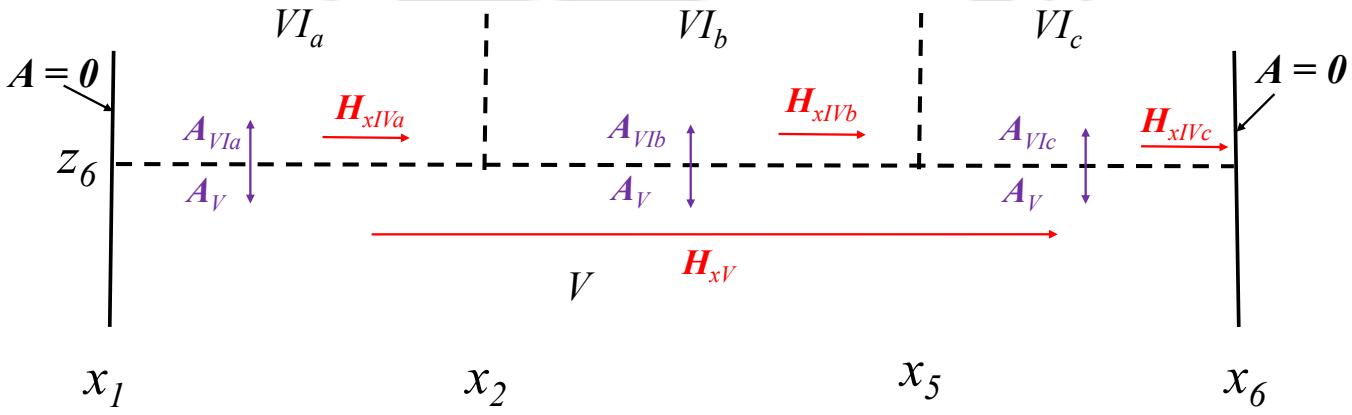

Figure B.5: Illustration of boundary condition at $z=z_6$.

$$H_{x_V}(x, z_6) = H_{x_{VIa}}(x, z_6)\big|_{x_1 \le x \le x_2} + H_{x_{VIb}}(x, z_6)\big|_{x_2 \le x \le x_5} + H_{x_{VIc}}(x, z_6)\big|_{x_5 \le x \le x_6} \quad \text{(B.23)}$$

$$A_{VI_a}(x, z_6) = A_V(x, z_6); \text{where } x_1 \le x \le x_2 \quad \text{(B.24)}$$

$$A_{VI_b}(x, z_6) = A_V(x, z_6); \text{where } x_2 \le x \le x_5 \quad \text{(B.25)}$$

$$A_{VI_c}(x, z_6) = A_{III}(x, z_6); \text{where } x_5 \le x \le x_6 \quad \text{(B.26)}$$

At z_7

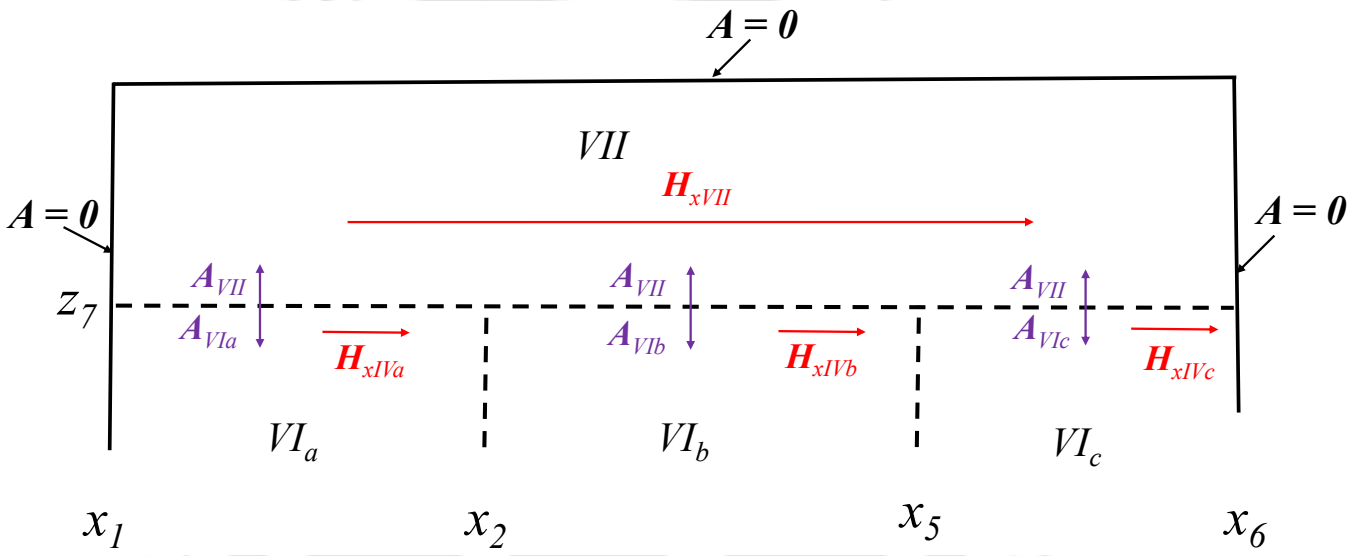

Figure B.6: Illustration of boundary condition at $z=z_7$.

$$H_{x_{VII}}(x, z_7) = H_{xVIa}(x, z_7)|_{x_1 \le x \le x_2} + H_{xVIb}(x, z_7)|_{x_2 \le x \le x_5} + H_{xVIc}(x, z_7)|_{x_5 \le x \le x_6} \quad \text{(B.27)}$$

$$A_{VIa}(x, z_7) = A_{VII}(x, z_7); \text{where } x_1 \le x \le x_2 \quad \text{(B.28)}$$

$$A_{VIb}(x, z_7) = A_{VII}(x, z_7); \text{where } x_2 \le x \le x_5 \quad \text{(B.29)}$$

$$A_{VIc}(x, z_7) = A_{VII}(x, z_7); \text{where } x_5 \le x \le x_6 \quad \text{(B.30)}$$

At x_2

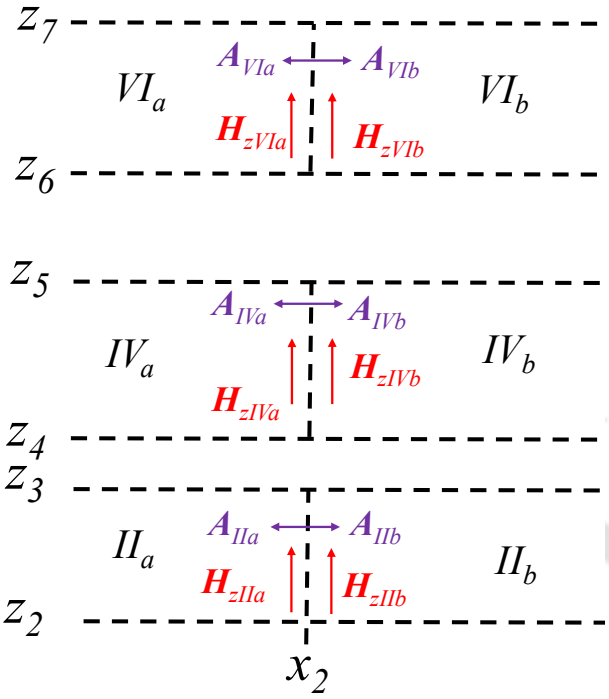

Figure B.7: Illustration of boundary condition at $x=x_2$.

$$A_{IIa}(x_2, z) = A_{IIb}(x_2, z)\,; \text{where } z_2 \le z \le z_3 \quad \text{(B.31)}$$

$$H_{zIIb}(x_2, z) = H_{zIIa}(x_2, z)\,; \text{where } z_2 \le z \le z_3 \quad \text{(B.32)}$$

$$A_{IVa}(x_2, z) = A_{IVb}(x_2, z)\,; \text{where } z_4 \le z \le z_5 \quad \text{(B.33)}$$

$$H_{z_{IVb}}(x_2, z) = H_{z_{IVa}}(x_2, z)\,; \text{where } z_4 \le z \le z_5 \quad \text{(B.34)}$$

$$A_{VIa}(x_2, z) = A_{IVb}(x_2, z)\,; \text{where } z_6 \le z \le z_7 \quad \text{(B.35)}$$

$$H_{zVIb}(x_5, z) = H_{zVIa}(x_5, z)\,; \text{where } z_6 \le z \le z_7 \quad \text{(B.36)}$$

At x_3

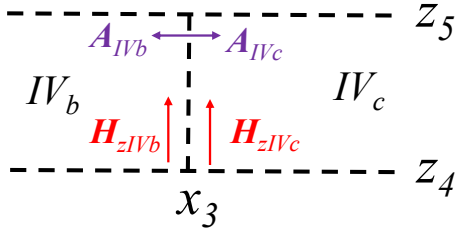

Figure B.8: Illustration of boundary condition at $x=x_3$.

$$H_{z_{IVb}}(x_3, z) = H_{z_{IVc}}(x_3, z)\,; \text{where } z_4 \le z \le z_5 \quad \text{(B.37)}$$

$$A_{IVc}(x_3, z) = A_{IVb}(x_3, z)\,; \text{where } z_4 \le z \le z_5 \quad \text{(B.38)}$$

At x_4

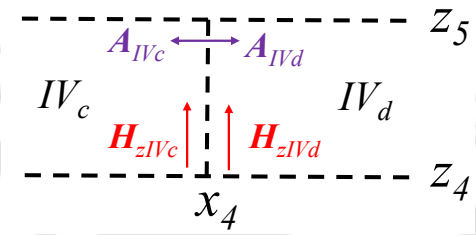

Figure B.9: Illustration of boundary condition at $x=x_4$.

$$A_{IV_c}(x_4, z) = A_{IV_d}(x_4, z)\,; \text{where } z_4 \le z \le z_5 \quad \text{(B.39)}$$

$$H_{zIVd}(x_4, z) = H_{zIVc}(x_4, z)\,; \text{where } z_4 \le z \le z_5 \quad \text{(B.40)}$$

At x_5

$$H_{zII_b}(x_5, z) = H_{zII_c}(x_5, z)\,; \text{where } z_2 \le z \le z_3 \quad \text{(B.41)}$$

$$A_{II_c}(x_5, z) = A_{II_b}(x_5, z)\,; \text{where } z_2 \le z \le z_3 \quad \text{(B.42)}$$

$$H_{zIVd}(x_5, z) = H_{zIVe}(x_5, z)\,; \text{where } z_4 \le z \le z_5 \quad \text{(B.43)}$$

$$A_{IV_e}(x_5, z) = A_{IV_d}(x_5, z)\,; \text{where } z_4 \le z \le z_5 \quad \text{(B.44)}$$

$$H_{zVI_b}(x_5, z) = H_{zVI_c}(x_5, z)\,; \text{where } z_6 \le z \le z_7 \quad \text{(B.45)}$$

$$A_{VI_c}(x_5, z) = A_{IV_d}(x_5, z)\,; \text{where } z_6 \le z \le z_7 \quad \text{(B.46)}$$

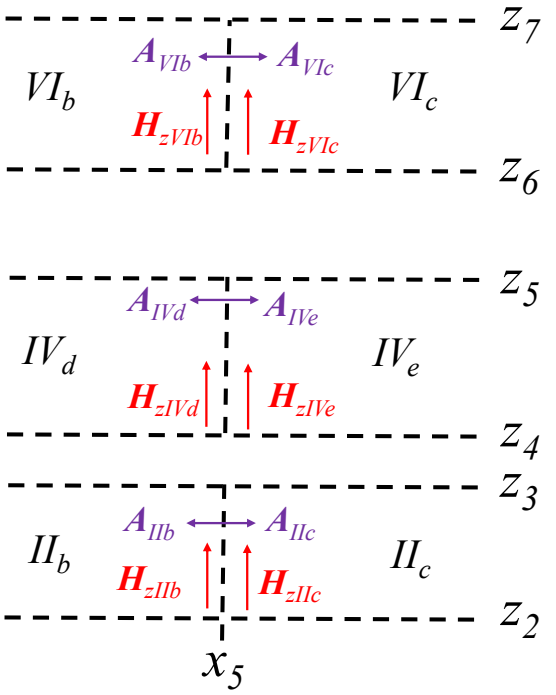

Figure B.10: Illustration of boundary condition at $x=x_5$.

B.2 Regions with Applied Boundary Conditions

The divided region of the coil system for which magnetic vector potential needs to be derived is shown in Fig. 4.3. Based on the applied boundary conditions at the interface of each region, the divided regions are classified into different cases, as shown in Fig. B.11.

B.3 Magnetic Vector Potential of Different Regions

The regions with applied boundary conditions are shown in Fig. B.11. In this section, the detailed derivation for only case 1 shown Fig. B.11(a) is explained. The magnetic vector potentials of regions with other cases are derived with the same steps.

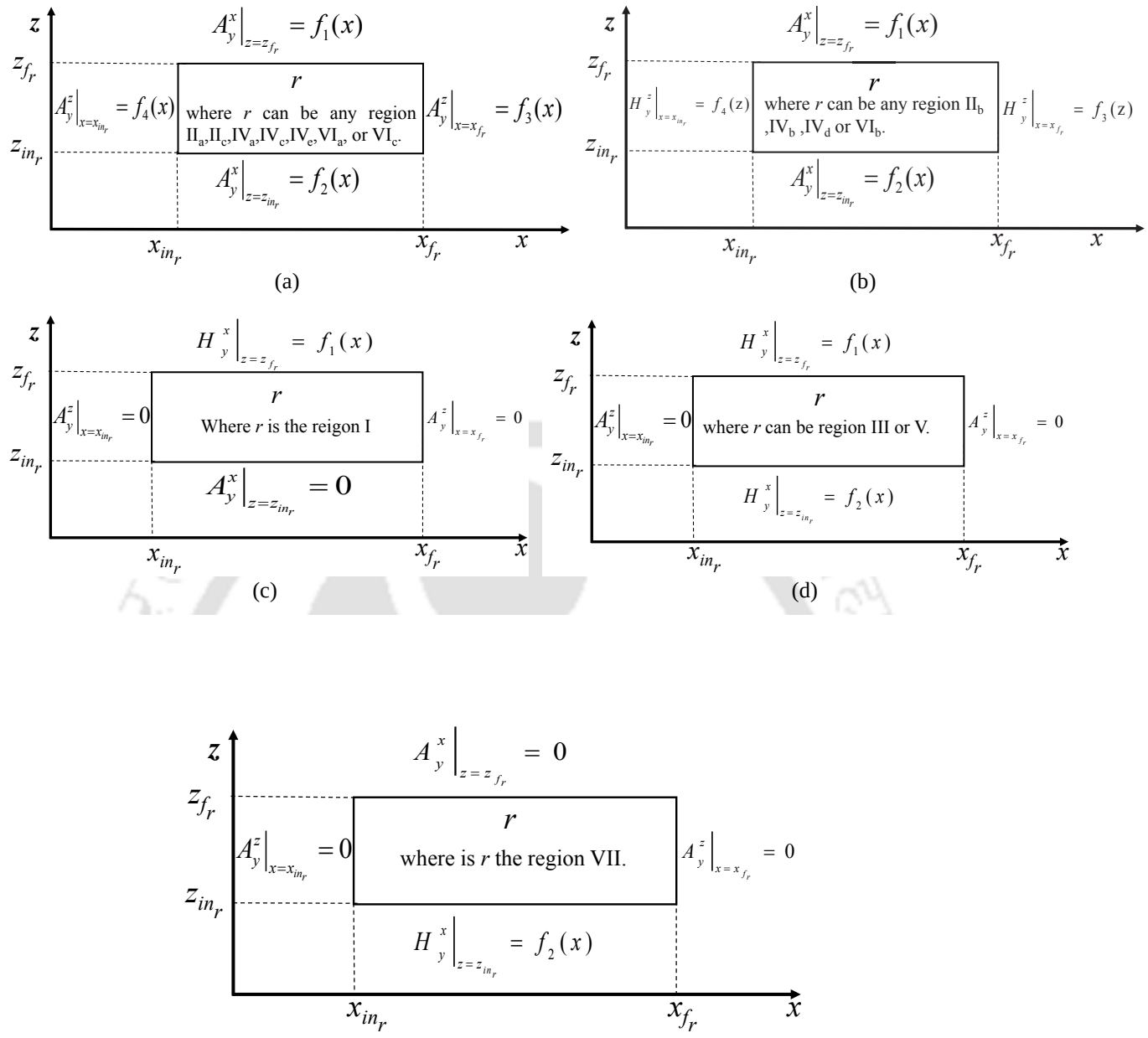

Figure B.11: Illustration of divided regions with applied boundary condition (a) case 1, (c) case 2, (d) case 3, (b) cse 4, and (e) case 5.

B.3.1 General Solution of Magnetic Vector Potential

The magnetic vector potential of regions of the coil system is governed by the Laplace equation given in (B.47)

$$\frac{\partial^2 \mathbf{A}_y}{\partial x^2} + \frac{\partial^2 \mathbf{A}_y}{\partial z^2} = 0 \tag{B.47}$$

Solving (B.47) by the method of separation of variables, the solution of Ay in the Cartesian coordinates (x,z) can be written as

$$\mathbf{A}_y = (A_y^x + A_y^z)\,\vec{e_y} \tag{B.48}$$

$$\begin{aligned} A_y^x &= (c_{0_{r1}} + d_{0_{r1}} x)\,(c_{0_{r2}} + d_{0_{r2}} z) \\ &+ \sum_{n_r=1,2,3}^{\infty} (c_{r1}\cosh(k_{x_r} z) + d_{r1}\sinh(k_{x_r} z))\,(c_{r2}\cos(k_{x_r} x) + d_{r2}\sin(k_{x_r} x)) \end{aligned} \tag{B.49}$$

$$\begin{aligned} A_y^z &= (e_{0_{r1}} + f_{0_{r1}} x)\,(e_{0_{r2}} + f_{0_{r2}} z) \\ &+ \sum_{l_r=1,2,3}^{\infty} (e_{r1}\cosh(k_{x_r} x) + f_{r1}\sinh(k_{x_r} x))\,(e_{r2}\cos(k_{x_r} z) + f_{r2}\sin(k_{x_r} z)) \end{aligned} \tag{B.50}$$

Here, for a region r, n_r and l_r are the spatial harmonic orders in the x-and z-directions, respectively, and $c_{0_{r1}}$, $d_{0_{r1}}$, c_{r1}, d_{r1},$c_{0_{r2}}$, $d_{0_{r2}}$, c_{r2}, d_{r2}, $e_{0_{r1}}$, $f_{0_{r1}}$,e_{r1}, f_{r1},$e_{0_{r2}}$, $f_{0_{r2}}$,e_{r2}, and f_{r2} are unknown coefficients. k_{x_r} and k_{z_r} are the spatial frequencies in the x and z-directions with the periods of $\tau_{x_r} = (x_{f_r} - x_{in_r})$ and $\tau_{z_r} = (z_{f_r} - z_{in_r})$.

B.3.2 Derivation of magnetic vector potential according to imposed boundary conditions

Fig. B.11(a) show regions whose magnetic vector potentials are applied as a boundary condition on all edges. For applying the boundary conditions, the principle of superposition is used, illustrated in Fig. B.12(a). With the principle of superposition, the solution of A_y for the regions in case 1 can be obtained by-

$$\mathbf{A}_y = (A_1 + A_2 + A_3 + A_4.)\,\vec{e_y} \tag{B.51}$$

For obtaining the solution of A_1 and A_2 the boundary condition shown in Fig. B.12(b) and Fig. B.12(c) are applied to (B.49). Therefore,

$$A_y^x = A_1 + A_2 \tag{B.52}$$

Whereas, the solution of A_3 and A_4 are obtained by applying solution boundary conditions shown

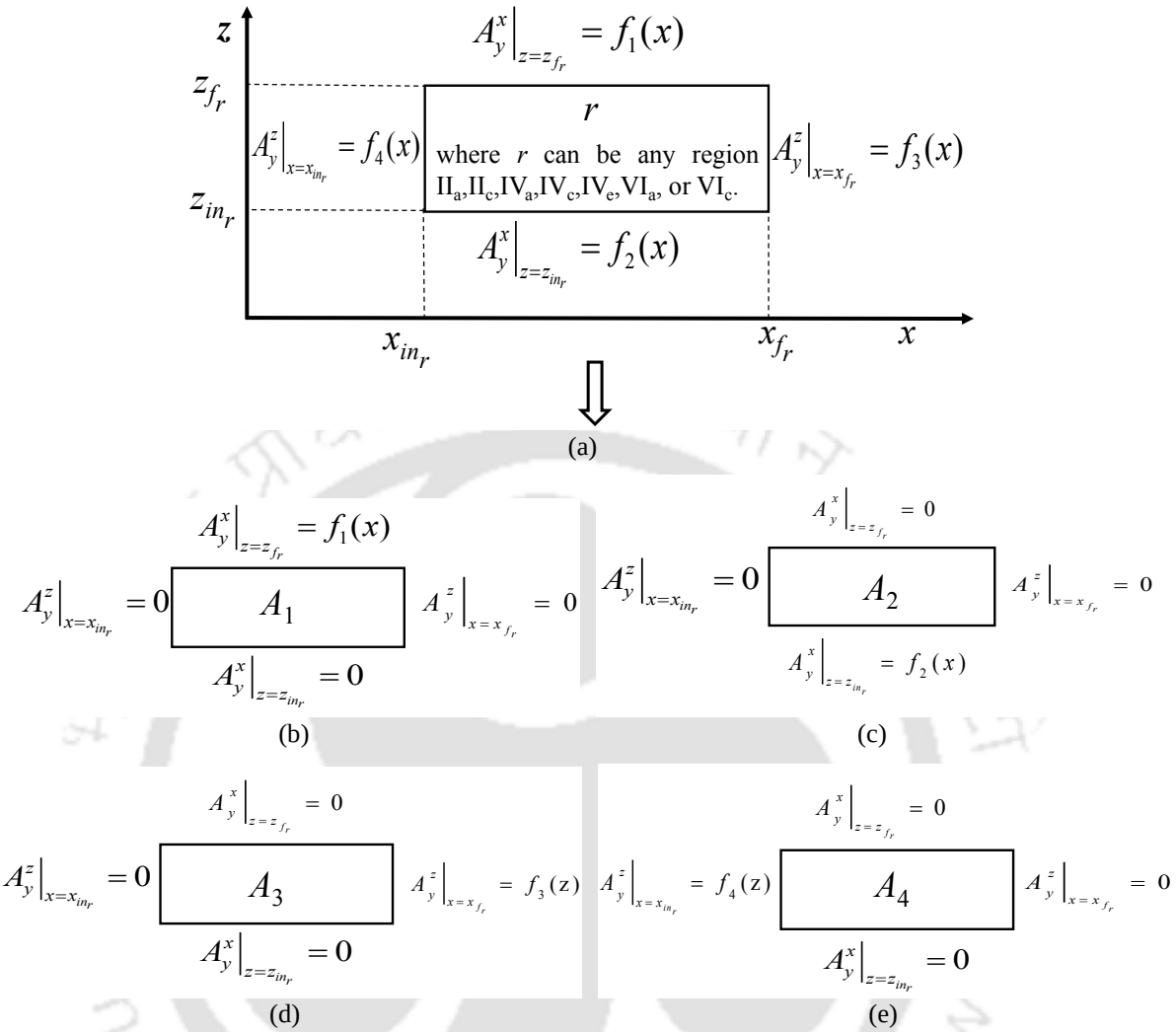

Figure B.12: case 1 where Az is applied at all edge a region and principle of superposition. (a) (b) (c) (d) (e)

in Fig. B.12(b) and Fig. B.12(c) in (B.50). Therefore,

$$A_y^z = A_3 + A_4 \tag{B.53}$$

Solution of A_1:Applying $A_y^z\big|_{x=x_{in_r}} = 0$ in (B.49), we get $c_{0_{r1}} = 0; d_{0_{r1}} = 0; c_{0_{r2}} = 0; d_{0_{r2}} = 0; c_{r2} = 0$. Therefore, (B.49) becomes

$$A_1 = \sum_{n_r=1,2,3}^{\infty} (c_{r1}\cosh(k_{x_r}z) + d_{r1}\sinh(k_{x_r}z))\,(\sin(k_{x_r}(x - x_{in_r}))). \tag{B.54}$$

Applying $A_y^x\big|_{z=z_{in_r}} = 0$, we get

$$c_{r1} = -\frac{d_{r1}\sinh(k_{x_r}z_{in_r})}{\sinh(k_{x_r}z_{in_r})} \tag{B.55}$$

putting the value of c_{r1} in (B.54) and rearranging we get-

$$A_1 = \sum_{n_r=1,2,3}^{\infty} (d_{r1} \sinh(k_{x_r}(z - z_{in_r}))) (\sin(k_{x_r}(x - x_{in_r}))) \tag{B.56}$$

Applying $A_y^x\big|_{z=z_{fr}} = f_1(x)$ in (B.56), we get

$$d_{r1} = \int_{x_{in_r}}^{x_{in_r}+\tau_{x_r}} \frac{f_1(x)}{\sinh(k_{x_r}(z_{f_r} - z_{in_r}))} \sinh(k_{x_r}(z - z_{in_r}))dx \tag{B.57}$$

Therefore (B.56) can be rewritten as-

$$A_1 = \sum_{n_r=1,2,3}^{\infty} \left(d_{r1} \frac{\sinh(k_{x_r}(z - z_{in_r}))}{\sinh(k_{x_r}\tau_{z_r})}\right) (\sin(k_{x_r}(x - x_{in_r}))) \tag{B.58}$$

Solution of A_2: To get the solution of A_2 the boundary condition shown in Fig. B.12(c) are applied in (B.49). Since, boundary conditions shown in Fig. B.12(b) and Fig. B.12(c) at $x = x_{in_r}$ and $x = x_{f_r}$ are same. Therefore, (B.54) is used to apply vertical boundary conditions. Applying $A_y^x\big|_{z=z_{fr}} = 0$ in (B.54) we get

$$d_{r1} = -\frac{c_{r1} \cosh(k_{x_r} z_{f_r})}{\sinh(k_{x_r} z_{f_r})}. \tag{B.59}$$

putting the value of d_{r1} in (B.54) and rearranging we get-

$$A_2 = \sum_{n_r=1,2,3}^{\infty} \left(c_{r1} \sinh(k_{x_r}(z_{f_r} - z))\right) (d_{r2} \sin(k_{x_r}(x - x_{in_r}))) \tag{B.60}$$

Applying $A_y^x\big|_{z=z_{in_r}} = f_1(x)$ in (B.60), we get

$$c_{r1} = \int_{x_{in_r}}^{x_{in_r}+\tau_{x_r}} \frac{f_2(x)}{\sinh(k_{x_r}\tau_{z_r})} \sinh(k_{x_r}(z - z_{in_r}))dx \tag{B.61}$$

Therefore (B.60) can be rewritten as-

$$A_y^x = \sum_{n_r=1,2,3}^{\infty} \left(c_{r1} \frac{\sinh(k_{x_r}(z_{f_r} - z))}{\sinh(k_{x_r}\tau_{z_r})}\right) (\sin(k_{x_r}(x - x_{in_r}))) \tag{B.62}$$

With (B.52) we can write-

$$A_y^x = \sum_{n_r=1,2,3}^{\infty} \left(c_{r1} \frac{\sinh(k_{x_r}(z_{f_r} - z))}{\sinh(k_{x_r}\tau_{z_r})} + d_{r1} \frac{\sinh(k_{x_r}(z - z_{in_r}))}{\sinh(k_{x_r}\tau_{z_r})}\right) (\sin(k_{x_r}(x - x_{in_r}))) \tag{B.63}$$

The same procedure can be applied for the boundary condition shown in Fig. B.12(d) and Fig. B.12(e) in (B.50). The obtained A_y^z with boundary condition is given as-

$$A_y^z = \sum_{l_r=1,2,3}^{\infty} \left(e_r \frac{\sinh(k_{z_r}(x_{f_r} - x))}{\sinh(k_{z_r}\tau_{x_r})} + f_r \frac{\sinh(k_{z_r}(x - x_{in_r}))}{\sinh(k_{z_r}\tau_{x_r})} \right) \sin(k_z(z - z_{in_r})) \tag{B.64}$$

The magnetic vector potentials are given by (B.65)-(B.96).

- Region I

$$A_I = \sum_{n_r=1}^{N_I} \left(\frac{d_I}{k_{x_I}} \frac{\sinh(k_{x_I}(z - z_1))}{\cosh(k_{x_I}\tau_{z_I})} \right) \sin(k_{x_I}(x - x_I))\, \vec{e_y} \tag{B.65}$$

- Region II_a

$$A_{II_a} = (A_y^x + A_y^z)\, \vec{e_y} \tag{B.66}$$

where, A_y^x, A_y^z, and A_y^s is given as

$$\begin{aligned} A_y^x &= \sum_{n_{IIa}=1}^{N_{IIa}} \left(c_{IIa} \frac{\sinh(k_{x_{IIa}}(z_3 - z))}{\sinh(k_{x_{IIa}}\tau_{z_{IIa}})} + d_{_{IIa}} \frac{\sinh(k_{x_{IIa}}(z - z_2))}{\sinh(k_{x_{IIa}}\tau_{z_{IIa}})} \right) \sin(k_{x_{IIa}}(x - x_5)) \\ A_y^z &= \sum_{l_r=1}^{L_{IIa}} \left(e_{IIa} \frac{\sinh(k_{z_{IIa}}(x - x_1))}{\sinh(k_{z_{IIa}}\tau_{x_{IIa}})} \right) \sin(k_{z_{IIa}}(z - z_2)) \end{aligned}$$

and

$$k_{x_{IIa}} = \frac{n_{IIa}\pi}{\tau_{x_{IIa}}}; \quad k_{z_{IIa}} = \frac{n_{IIa}\pi}{\tau_{z_{IIa}}}; \quad \tau_{x_{IIa}} = x_2 - x_1; \quad \tau_{z_{IIa}} = z_3 - z_2. \tag{B.67}$$

- Region II_b

$$A_{II_b} = (A_y^x + A_y^z)\, \vec{e_y} \tag{B.68}$$

where, A_y^x, A_y^z, and A_y^s is given as

$$\begin{aligned} A_y^x &= (z_3 - z)c_{0_{IIb}} + (z - z_2)d_{0_{IIb}} \\ &+ \sum_{n_{IIa}=1}^{N_{IIa}} \left(c_{IIb} \frac{\sinh(k_{x_{IIb}}(z_3 - z))}{\sinh(k_{x_{IIb}}\tau_{z_{IIb}})} + d_{IIb} \frac{\sinh(k_{x_{IIb}}(z - z_2))}{\sinh(k_{x_{IIb}}\tau_{z_{IIb}})} \right) \cos(k_{x_{IIb}}(x - x_2)) \qquad \text{(B.69)} \\ A_y^z &= \sum_{l_{IIb}=1}^{L_{IIb}} \left(-\frac{e_{IIb}}{k_{z_{IIb}}} \frac{\cosh(k_{z_{IIb}}(x - x_5))}{\sinh(k_{z_{IIb}}\tau_{x_{IIb}})} + \frac{f_{IIb}}{k_{z_{IIb}}} \frac{\cosh(k_{z_{IIb}}(x - x_2))}{\sinh(k_{z_{IIb}}\tau_{x_{IIb}})} \right) \sin(k_{z_{IIb}}(z - z_2)) \text{and} \end{aligned}$$

$$k_{x_{IIb}} = \frac{n_{IIb}\pi}{\tau_{x_{IIb}}}; \quad k_{z_{IIb}} = \frac{n_{IIb}\pi}{\tau_{z_{IIb}}}; \quad \tau_{x_{IIb}} = x_5 - x_2; \quad \tau_{z_{IIb}} = z_3 - z_2 \tag{B.70}$$

- Region II_c

$$A_{II_c} = (A_y^x + A_y^z)\,\vec{e}_y \tag{B.71}$$

where, A_y^x, A_y^z, and A_y^s is given as

$$A_y^x = \sum_{n_{IIc}=1}^{N_{IIc}} \left(c_{IIc} \frac{\sinh(k_{x_{IIc}}(z_3 - z))}{\sinh(k_{x_{IIc}}\tau_{z_{IIc}})} + d_{_{IIc}} \frac{\sinh(k_{x_{IIc}}(z - z_2))}{\sinh(k_{x_{IIc}}\tau_{z_{IIc}})} \right) \sin(k_{x_{IIc}}(x - x_5))$$

$$A_y^z = \sum_{l_r=1}^{L_{IIc}} \left(e_{IIc} \frac{\sinh(k_{z_{IIc}}(x_6 - x))}{\sinh(k_{z_{IIc}}\tau_{x_{IIc}})} \right) \sin(k_{z_{IIc}}(z - z_2))$$

and

$$k_{x_{IIc}} = \frac{n_{IIc}\pi}{\tau_{x_{IIc}}}; \quad k_{z_{IIc}} = \frac{n_{IIc}\pi}{\tau_{z_{IIc}}}; \quad \tau_{x_{IIc}} = x_6 - x_5; \quad \tau_{z_{IIc}} = z_3 - z_2. \tag{B.72}$$

- Region III

$$A_y = \sum_{n_{III}=1}^{N_{III}} \left(-\frac{c_{III}}{k_{x_{III}}} \frac{\cosh(k_{x_{III}}(z - z_4))}{\sinh(k_{x_{III}}\tau_{z_{III}})} + \frac{d_{III}}{k_{x_{III}}} \frac{\cosh(k_{x_r}(z - z_3))}{\sinh(k_{x_{III}}\tau_{z_{III}})} \right) \sin(k_{x_{III}}(x - x_1))\,\vec{e}_y \tag{B.73}$$

and

$$k_{x_{III}} = \frac{n_{III}\pi}{\tau_{x_{III}}}; \quad \tau_{x_{III}} = x_6 - x_1 \tag{B.74}$$

- Region IV_a

$$A_{IV_a} = (A_y^x + A_y^z)\,\vec{e}_y \tag{B.75}$$

where, A_y^x, A_y^z, and A_y^s is given as

$$A_y^x = \sum_{n_{IIa}=1}^{N_{IIa}} \left(c_{IVa} \frac{\sinh(k_{x_{IVa}}(z_5 - z))}{\sinh(k_{x_{IVa}}\tau_{z_{IIa}})} + d_{IVa} \frac{\sinh(k_{x_{IVa}}(z - z_3))}{\sinh(k_{x_{IVa}}\tau_{z_r})} \right) \sin(k_{x_{IVa}}(x - x_1))$$

$$A_y^z = \sum_{l_{IIa}=1}^{L_{IIa}} \left(f_{IVa} \frac{\sinh(k_{z_{IVa}}(x - x_1))}{\sinh(k_{z_{IVa}}\tau_{x_{IIa}})} \right) \sin(k_{z_{IVa}}(z - z_4))$$

and

$$k_{x_{IVa}} = \frac{n_{IVa}\pi}{\tau_{x_{IVa}}}; \quad k_{z_{IVa}} = \frac{n_{IVa}\pi}{\tau_{z_{IVa}}}; \quad \tau_{x_{IVa}} = x_2 - x_1; \quad \tau_{z_{IVa}} = z_5 - z_4 \tag{B.76}$$

- Region IV_b

$$A_{IV_b} = (A_y^x + A_y^z)\,\vec{e}_y \tag{B.77}$$

where, A_y^x, A_y^z, and A_y^s is given as

$$\begin{aligned} A_y^x &= (z_5 - z)c_{0_{IVb}} + (z - z_4)d_{0_{IVb}} \\ &+ \sum_{n_{IVb}=1}^{N_{IVb}} \left(c_{IVb} \frac{\sinh(k_{x_{IVb}}(z_5 - z))}{\sinh(k_{x_{IVb}}\tau_{z_{IVb}})} + d_{IVb} \frac{\sinh(k_{x_{IVb}}(z - z_4))}{\sinh(k_{x_{IVb}}\tau_{z_{IVb}})} \right) \cos(k_{x_{IVb}}(x - x_2)) \end{aligned} \quad \text{(B.78)}$$

$$A_y^z = \sum_{l_{IVb}=1}^{L_{IVb}} \left(-\frac{e_{IVb}}{k_{z_{IVb}}} \frac{\cosh(k_{z_{IVb}}(x - x_3))}{\sinh(k_{z_{IVb}}\tau_{x_{IVb}})} + \frac{f_{IVb}}{k_{z_{IVb}}} \frac{\cosh(k_{z_{IVb}}(x - x_2))}{\sinh(k_{z_{IVb}}\tau_{x_{IVb}})} \right) \sin(k_{z_{IVb}}(z - z_4))$$

and

$$k_{x_{IVb}} = \frac{n_{IVb}\pi}{\tau_{x_{IVb}}}; \quad k_{z_{IVb}} = \frac{n_{IVb}\pi}{\tau_{z_{IVb}}}; \quad \tau_{x_{IVb}} = x_3 - x_2; \quad \tau_{z_{IVb}} = z_5 - z_4 \quad \text{(B.79)}$$

- Region IV_c

$$A_{IV_c} = (A_y^x + A_y^z)\vec{e}_y \quad \text{(B.80)}$$

where, A_y^x, A_y^z, and A_y^s is given as

$$A_y^x = \sum_{n_{IVc}=1}^{N_{IVc}} \left(c_{IVc} \frac{\sinh(k_{x_{IVc}}(z_5 - z))}{\sinh(k_{x_{IVc}}\tau_{z_{IVc}})} + d_{IVc} \frac{\sinh(k_{x_{IVc}}(z - z_4))}{\sinh(k_{x_{IVc}}\tau_{z_{IVc}})} \right) \sin(k_{x_{IVc}}(x - x_3))$$

$$A_y^z = \sum_{l_r=1,2,3}^{\infty} \left(e_{IVc} \frac{\sinh(k_{z_{IVc}}(x_4 - x))}{\sinh(k_{z_{IVc}}\tau_{x_{IVc}})} + f_{IVc} \frac{\sinh(k_{z_{IVc}}(x - x_3))}{\sinh(\tau_{z_{IVc}}\tau_{x_{IVc}})} \right) \sin(\tau_{z_{IVc}}(z - z_4))$$

and

$$k_{x_{IVc}} = \frac{n_{IVc}\pi}{\tau_{x_{IVc}}}; \quad k_{z_{IVc}} = \frac{n_{IVc}\pi}{\tau_{z_{IVc}}} \quad \tau_{x_{IVc}} = x_4 - x_3 \quad \tau_{z_{IVc}} = z_5 - z_4 \quad \text{(B.81)}$$

- Region IV_d

$$A_{IV_d} = (A_y^x + A_y^z)\vec{e}_y \quad \text{(B.82)}$$

where, A_y^x, A_y^z, and A_y^s is given as

$$\begin{aligned} A_y^x &= (z_5 - z)c_{0_{IVd}} + (z - z_4)d_{0_{IVd}} \\ &+ \sum_{n_{IVd}=1}^{N_{IVd}} \left(c_{IVd} \frac{\sinh(k_{x_{IVd}}(z_5 - z))}{\sinh(k_{x_{IVd}}\tau_{z_{IVd}})} + d_{IVd} \frac{\sinh(k_{x_{IVd}}(z - z_4))}{\sinh(k_{x_{IVd}}\tau_{z_{IVd}})} \right) \cos(k_{x_{IVd}}(x - x_4)) \end{aligned} \quad \text{(B.83)}$$

$$A_y^z = \sum_{l_{IVd}=1}^{L_{IVd}} \left(-\frac{e_{IVd}}{k_{z_{IVd}}} \frac{\cosh(k_{z_{IVd}}(x - x_5))}{\sinh(k_{z_{IVd}}\tau_{x_{IVd}})} + \frac{f_{IVd}}{k_{z_{IVd}}} \frac{\cosh(k_{z_{IVd}}(x - x_4))}{\sinh(k_{z_{IVd}}\tau_{x_{IVd}})} \right) \sin(k_{z_{IVd}}(z - z_4))$$

and

$$k_{x_{IVd}} = \frac{n_{IVd}\pi}{\tau_{x_{IVd}}}; \quad k_{z_{IVd}} = \frac{n_{IVd}\pi}{\tau_{z_{IVd}}}; \quad \tau_{x_{IVd}} = x_5 - x_4; \quad \tau_{z_{IVd}} = z_5 - z_4 \quad \text{(B.84)}$$

- Region IV_e

$$A_{IV_e} = (A_y^x + A_y^z)\,\vec{e_y} \tag{B.85}$$

where, A_y^x, A_y^z, and A_y^s is given as

$$A_y^x = \sum_{n_{IVe}=1}^{N_{IVe}} \left(c_{IVe} \frac{\sinh(k_{x_{IVe}}(z_5 - z))}{\sinh(k_{x_{IVe}}\tau_{z_{IVe}})} + d_{IVe} \frac{\sinh(k_{x_{IVe}}(z - z_4))}{\sinh(k_{x_{IVe}}\tau_{z_{IVe}})} \right) \sin(k_{x_{IVe}}(x - x_5))$$

$$A_y^z = \sum_{l_{IVe}=1}^{L_{IVe}} \left(e_{IIc} \frac{\sinh(k_{z_{IVe}}(x_6 - x))}{\sinh(k_{z_{IVe}}\tau_{x_{IVe}})} \right) \sin(k_{z_{IVe}}(z - z_2))$$

and

$$k_{x_{IVe}} = \frac{n_{IVe}\pi}{\tau_{x_{IVe}}}; \quad k_{z_{IVe}} = \frac{n_{IVe}\pi}{\tau_{z_{IVe}}}; \quad \tau_{x_{IVe}} = x_6 - x_5; \quad \tau_{z_{IVe}} = z_3 - z_2 \tag{B.86}$$

- Region V

$$A_V = \sum_{n_V=1}^{N_V} \left(-\frac{c_V}{k_{x_V}} \frac{\cosh(k_{x_V}(z - z_6))}{\sinh(k_{x_V}\tau_{z_V})} + \frac{d_V}{k_{x_V}} \frac{\cosh(k_{x_V}(z - z_5))}{\sinh(k_{x_V}\tau_{z_V})} \right) \sin(k_{x_V}(x - x_1))\,\vec{e_y} \tag{B.87}$$

and

$$k_{x_V} = \frac{n_V\pi}{\tau_{x_V}}; \quad \tau_{x_V} = x_6 - x_1 \tag{B.88}$$

- Region VI_a

$$A_{VI_a} = (A_y^x + A_y^z)\,\vec{e_y} \tag{B.89}$$

where, A_y^x, A_y^z, and A_y^s is given as

$$A_y^x = \sum_{n_{VIa}=1}^{N_{VIa}} \left(c_{VIa} \frac{\sinh(k_{x_{VIa}}(z_7 - z))}{\sinh(k_{x_{VIa}}\tau_{z_{VIa}})} + d_{VIa} \frac{\sinh(k_{x_{VIa}}(z - z_6))}{\sinh(k_{x_{VIa}}\tau_{z_{VIa}})} \right) \sin(k_{x_{VIa}}(x - x_1))$$

$$A_y^z = \sum_{l_{VIa}=1}^{L_{VIa}} \left(f_{VIa} \frac{\sinh(k_{z_{VIa}}(x - x_1))}{\sinh(k_{z_{VIa}}\tau_{x_{VIa}})} \right) \sin(k_{z_{VIa}}(z - z_6))$$

and

$$k_{x_{VIa}} = \frac{n_{VIa}\pi}{\tau_{x_{IIa}}}; \quad k_{z_{VIa}} = \frac{n_{VIa}\pi}{\tau_{z_{VIa}}}; \quad \tau_{x_{IIa}} = x_2 - x_1; \quad \tau_{z_{VIa}} = z_7 - z_6 \tag{B.90}$$

- Region VI_b

$$A_{VI_a} = (A_y^x + A_y^z)\,\vec{e_y} \tag{B.91}$$

where, A_y^x, A_y^z, and A_y^s is given as

$$\begin{aligned} A_y^x &= (z_7 - z)c_{0_{VIb}} + (z - z_6)d_{0_{VIb}} \\ &+ \sum_{n_{IIa}=1}^{N_{IIa}} \left(c_{VIb} \frac{\sinh(k_{x_{VIb}}(z_7 - z))}{\sinh(k_{x_{VIb}}\tau_{z_{VIb}})} + d_{VIb} \frac{\sinh(k_{x_{VIb}}(z - z_6))}{\sinh(k_{x_{VIb}}\tau_{z_{VIb}})} \right) \cos(k_{x_{VIb}}(x - x_2)) \end{aligned} \quad \text{(B.92)}$$

$$A_y^z = \sum_{l_{IIb}=1}^{L_{IIb}} \left(-\frac{e_{VIb}}{k_{z_{VIb}}} \frac{\cosh(k_{z_{VIb}}(x - x_5))}{\sinh(k_{z_{VIb}}\tau_{x_{VIb}})} + \frac{f_{VIb}}{k_{z_{VIb}}} \frac{\cosh(k_{z_{VIb}}(x - x_2))}{\sinh(k_{z_{VIb}}\tau_{x_{VIb}})} \right) \sin(k_{z_{VIb}}(z - z_2))$$

and

$$k_{x_{VIb}} = \frac{n_{VIb}\pi}{\tau_{x_{VIb}}}; \quad k_{z_{VIb}} = \frac{n_{VIb}\pi}{\tau_{z_{VIb}}}; \quad \tau_{x_{VIb}} = x_5 - x_2; \quad \tau_{z_{VIb}} = z_7 - z_6 \quad \text{(B.93)}$$

- Region VI_c

$$A_{VI_a} = (A_y^x + A_y^z)\,\vec{e_y} \quad \text{(B.94)}$$

where, A_y^x, A_y^z, and A_y^s is given as

$$A_y^x = \sum_{n_{VIc}=1}^{N_{VIc}} \left(c_{VIc} \frac{\sinh(k_{x_{VIc}}(z_7 - z))}{\sinh(k_{x_{VIc}}\tau_{z_{VIc}})} + d_{VIc} \frac{\sinh(k_{x_{VIc}}(z - z_6))}{\sinh(k_{x_{VIc}}\tau_{z_{VIc}})} \right) \sin(k_{x_{VIc}}(x - x_5))$$

$$A_y^z = \sum_{l_{VIc}=1}^{L_{IIc}} \left(e_{VIc} \frac{\sinh(k_{z_{VIc}}(x_6 - x))}{\sinh(k_{z_{VIc}}\tau_{x_{VIc}})} \right) \sin(k_{z_{VIc}}(z - z_6))$$

and

$$k_{x_{VIc}} = \frac{n_{VIc}\pi}{\tau_{x_{VIc}}}; \quad k_{z_{VIc}} = \frac{n_{VIc}\pi}{\tau_{z_{VIc}}}; \quad \tau_{x_{VIc}} = x_6 - x_5; \quad \tau_{z_{VIc}} = z_7 - z_6 \quad \text{(B.95)}$$

- Region VII

$$A_{VII} = \sum_{n_{VII}=1}^{N_{VII}} \left(-\frac{c_{VII}}{k_{x_{VII}}} \frac{\sinh(k_{x_r}(z_8 - z))}{\cosh(k_{x_{VII}}\tau_{z_{VII}})} \right) \sin(k_{x_{VII}}(x - x_1))\,\vec{e_y} \quad \text{(B.96)}$$

$$k_{x_{VII}} = \frac{n_{VII}\pi}{\tau_{x_{VII}}}; \quad \tau_{x_{VII}} = x_6 - x_1; \quad \tau_{z_{VII}} = z_8 - z_7 \quad \text{(B.97)}$$

Bibliography

[1] E. R. Joy, A. Dalal, and P. Kumar, "Accurate computation of mutual inductance of two air core square coils with lateral and angular misalignments in a flat planar surface," *IEEE Trans. Magn.*, vol. 50, no. 1, pp. 1–9, Jan 2014.

[2] Z. Zhang, H. Pang, A. Georgiadis, and C. Cecati, "Wireless power transferan overview," *IEEE Trans. Ind. Electron.*, vol. 66, no. 2, pp. 1044–1058, 2019.

[3] C. T. Rim and C. Mi, *Mobile Applications for Phones and Robots*. IEEE, 2017. [Online]. Available: https://ieeexplore.ieee.org/document/7953981

[4] Y. M. Roshan and E. J. Park, "Design approach for a wireless power transfer system for wristband wearable devices," *IET Power Electron.*, vol. 10, no. 8, pp. 931–937, 2017.

[5] J. Yin, D. Lin, T. Parisini, and S. Y. . Hui, "Front-end monitoring of the mutual inductance and load resistance in a series-series compensated wireless power transfer system," *IEEE Trans. Power Electron.*, vol. 31, no. 10, pp. 7339–7352, Oct 2016.

[6] G. Guidi and J. A. Suul, "Minimizing converter requirements of inductive power transfer systems with constant voltage load and variable coupling conditions," *IEEE Trans. Ind. Electron.*, vol. 63, no. 11, pp. 6835–6844, Nov 2016.

[7] C. Y. Huang, J. E. James, and G. A. Covic, "Design considerations for variable coupling lumped coil systems," *IEEE Trans. Power Electron.*, vol. 30, no. 2, pp. 680–689, Feb 2015.

[8] S. R. Cove and M. Ordonez, "Wireless-power-transfer planar spiral winding design applying track width ratio," *IEEE Trans. Ind. Appl.*, vol. 51, no. 3, pp. 2423–2433, May 2015.

[9] V. Jiwariyavej, T. Imura, and Y. Hori, "Coupling coefficients estimation of wireless power transfer system via magnetic resonance coupling using information from either side of the system," *IEEE J. Emerg. Sel. Topics Power Electron.*, vol. 3, no. 1, pp. 191–200, March 2015.

[10] S. Samanta and A. K. Rathore, "A new current-fed clc transmitter and lc receiver topology for inductive wireless power transfer application: Analysis, design, and experimental results," *IEEE Trans. Transport. Electrific.*, vol. 1, no. 4, pp. 357–368, Dec 2015.

[11] S. A. Mirbozorgi, H. Bahrami, M. Sawan, and B. Gosselin, "A smart multicoil inductively coupled array for wireless power transmission," *IEEE Trans. Ind. Electron.*, vol. 61, no. 11, pp. 6061–6070, Nov 2014.

[12] K. Lee, Z. Pantic, and S. M. Lukic, "Reflexive field containment in dynamic inductive power transfer systems," *IEEE Trans. Power Electron.*, vol. 29, no. 9, pp. 4592–4602, Sept 2014.

[13] A. Abdolkhani, A. P. Hu, G. A. Covic, and M. Moridnejad, "Through-hole contactless slipring system based on rotating magnetic field for rotary applications," *IEEE Trans. Ind. Appl.*, vol. 50, no. 6, pp. 3644–3655, Nov. 2014.

[14] Chang-Gyun Kim, Dong-Hyun Seo, Jung-Sik You, Jong-Hu Park, and B. H. Cho, "Design of a contactless battery charger for cellular phone," *IEEE Trans. Ind. Electron.*, vol. 48, no. 6, pp. 1238–1247, Dec 2001.

[15] Yungtaek Jang and M. M. Jovanovic, "A contactless electrical energy transmission system for portable-telephone battery chargers," *IEEE Trans. Ind. Electron.*, vol. 50, no. 3, pp. 520–527, June 2003.

[16] X. Liu, C. Liu, and P. W. T. Pong, "Tmr-sensor-array-based misalignment-tolerant wireless charging technique for roadway electric vehicles," *IEEE Trans. Magn.*, vol. 55, no. 7, pp. 1–7, July 2019.

[17] A. A. S. Mohamed, A. Meintz, and L. Zhu, "System design and optimization of in-route wireless charging infrastructure for shared automated electric vehicles," *IEEE Access*, vol. 7, pp. 79 968–79 979, 2019.

[18] X. Mou, D. T. Gladwin, R. Zhao, and H. Sun, "Survey on magnetic resonant coupling wireless power transfer technology for electric vehicle charging," *IET Power Electron.*, vol. 12, no. 12, pp. 3005–3020, 2019.

[19] A. F. A. Aziz, M. F. Romlie, and Z. Baharudin, "Review of inductively coupled power transfer for electric vehicle charging," *IET Power Electron.*, vol. 12, no. 14, pp. 3611–3623, 2019.

[20] V. Vu, V. Phan, M. Dahidah, and V. Pickert, "Multiple output inductive charger for electric vehicles," *IEEE Trans. Power Electron.*, vol. 34, no. 8, pp. 7350–7368, Aug 2019.

[21] J. K. Nama, M. Srivastava, and A. K. Verma, "Modified inductive power transfer topology for electrical vehicle battery charging using auxiliary network to achieve zero-voltage switching for full load variations," *IET Power Electronics*, vol. 12, no. 10, pp. 2513–2522, 2019.

[22] M. Kim, D. Joo, and B. K. Lee, "Design and control of inductive power transfer system for electric vehicles considering wide variation of output voltage and coupling coefficient," *IEEE Trans. Power Electron.*, vol. 34, no. 2, pp. 1197–1208, Feb 2019.

[23] S. Y. Jeong, J. H. Park, G. P. Hong, and C. T. Rim, "Autotuning control system by variation of self-inductance for dynamic wireless ev charging with small air gap," *IEEE Trans. Power Electron.*, vol. 34, no. 6, pp. 5165–5174, June 2019.

[24] L. Zhao, D. J. Thrimawithana, U. K. Madawala, A. P. Hu, and C. C. Mi, "A misalignment-tolerant series-hybrid wireless ev charging system with integrated magnetics," *IEEE Trans. Power Electron.*, vol. 34, no. 2, pp. 1276–1285, Feb 2019.

[25] V. Cirimele, M. Diana, F. Freschi, and M. Mitolo, "Inductive power transfer for automotive applications: State-of-the-art and future trends," *IEEE Trans. Ind. Appl.*, vol. 54, no. 5, pp. 4069–4079, Sep. 2018.

[26] Y. D. Chung, E. Y. Park, W. S. lee, and J. Y. lee, "Impact investigations and characteristics by strong electromagnetic field of wireless power charging system for electric vehicle under air and water exposure indexes," *IEEE Trans. Appl. Supercond.*, vol. 28, no. 3, pp. 1–5, April 2018.

[27] A. Ahmad, M. S. Alam, and R. Chabaan, "A comprehensive review of wireless charging technologies for electric vehicles," *IEEE Trans. Transport. Electrific.*, vol. 4, no. 1, pp. 38–63, March 2018.

[28] W. Liu, K. T. Chau, C. H. T. Lee, C. Jiang, and W. Han, "A switched-capacitorless energy-encrypted transmitter for roadway-charging electric vehicles," *IEEE Trans. Magn.*, vol. 54, no. 11, pp. 1–6, Nov 2018.

[29] C. Cai, J. Wang, Z. Fang, P. Zhang, M. Hu, J. Zhang, L. Li, and Z. Lin, "Design and optimization of load-independent magnetic resonant wireless charging system for electric vehicles," *IEEE Access*, vol. 6, pp. 17 264–17 274, 2018.

[30] Y. Hsieh, Z. Lin, M. Chen, H. Hsieh, Y. Liu, and H. Chiu, "High-efficiency wireless power transfer system for electric vehicle applications," *IEEE Trans. Circuits Syst. II, Exp. Briefs*, vol. 64, no. 8, pp. 942–946, Aug 2017.

[31] Q. Zhu, Y. Zhang, C. Liao, Y. Guo, L. Wang, and F. Li, "Experimental study on asymmetric wireless power transfer system for electric vehicle considering ferrous chassis," *IEEE Trans. Transport. Electrific.*, vol. 3, no. 2, pp. 427–433, June 2017.

[32] A. Hariri, A. Elsayed, and O. A. Mohammed, "An integrated characterization model and multiobjective optimization for the design of an ev chargers circular wireless power transfer pads," *IEEE Trans. Magn.*, vol. 53, no. 6, pp. 1–4, June 2017.

[33] Y. Gao, C. Duan, A. A. Oliveira, A. Ginart, K. B. Farley, and Z. T. H. Tse, "3-d coil positioning based on magnetic sensing for wireless ev charging," *IEEE Trans. Transport. Electrific.*, vol. 3, no. 3, pp. 578–588, Sep. 2017.

[34] D. Patil, M. K. McDonough, J. M. Miller, B. Fahimi, and P. T. Balsara, "Wireless power transfer for vehicular applications: Overview and challenges," *IEEE Trans. Transport. Electrific.*, vol. 4, no. 1, pp. 3–37, March 2018.

[35] Y. Li, T. Lin, R. Mai, L. Huang, and Z. He, "Compact double-sided decoupled coils-based wpt systems for high-power applications: Analysis, design, and experimental verification," *IEEE Trans. Transport. Electrific.*, vol. 4, no. 1, pp. 64–75, March 2018.

[36] G. Rituraj, B. K. Kushwaha, and P. Kumar, "Contactless power transfer system for sealed lead acid battery charging," *Wireless Power Transfer*, vol. 5, no. 1, pp. 20–26, Mar. 2018.

[37] S. Y. R. Hui, W. Zhong, and C. K. Lee, "A critical review of recent progress in mid-range wireless power transfer," *IEEE Trans. Power Electron.*, vol. 29, no. 9, pp. 4500–4511, Sep. 2014.

[38] U. K. Madawala and D. J. Thrimawithana, "Modular-based inductive power transfer system for high-power applications," *IET Power Electron.*, vol. 5, no. 7, pp. 1119–1126, August 2012.

[39] W. Zhang, S. C. Wong, C. K. Tse, and Q. Chen, "Design for efficiency optimization and voltage controllability of series-series compensated inductive power transfer systems," *IEEE Trans. Power Electron.*, vol. 29, no. 1, pp. 191–200, Jan 2014.

[40] B. X. Nguyen, D. M. Vilathgamuwa, G. H. B. Foo, P. Wang, A. Ong, U. K. Madawala, and T. D. Nguyen, "An efficiency optimization scheme for bidirectional inductive power transfer systems," *IEEE Trans. Power Electron.*, vol. 30, no. 11, pp. 6310–6319, Nov 2015.

[41] S. Li and C. C. Mi, "Wireless power transfer for electric vehicle applications," *IEEE J. Emerg. Sel. Topics Power Electron.*, vol. 3, no. 1, pp. 4–17, March 2015.

[42] S. Li, W. Li, J. Deng, T. D. Nguyen, and C. C. Mi, "A double-sided lcc compensation network and its tuning method for wireless power transfer," *IEEE Trans. Veh. Technol.*, vol. 64, no. 6, pp. 2261–2273, June 2015.

[43] U. K. Madawala, M. Neath, and D. J. Thrimawithana, "A power-frequency controller for bidirectional inductive power transfer systems," *IEEE Trans. Ind. Electron.*, vol. 60, no. 1, pp. 310–317, Jan 2013.

[44] J. Nadakuduti, M. Douglas, L. Lu, A. Christ, P. Guckian, and N. Kuster, "Compliance testing methodology for wireless power transfer systems," *IEEE Trans. Power Electron.*, vol. 30, no. 11, pp. 6264–6273, Nov 2015.

[45] S. Y. Choi, J. Huh, W. Y. Lee, and C. T. Rim, "Asymmetric coil sets for wireless stationary ev chargers with large lateral tolerance by dominant field analysis," *IEEE Trans. Power Electron.*, vol. 29, no. 12, pp. 6406–6420, Dec 2014.

[46] L. Zhao, D. J. Thrimawithana, and U. K. Madawala, "Hybrid bidirectional wireless ev charging system tolerant to pad misalignment," *IEEE Trans. Ind. Electron.*, vol. 64, no. 9, pp. 7079–7086, Sept 2017.

[47] D. Baros, D. Voglitsis, N. P. Papanikolaou, A. Kyritsis, and N. Rigogiannis, "Wireless power transfer for distributed energy sources exploitation in dc microgrids," *IEEE Trans. Sustain.Energy*, pp. 1–1, 2018.

[48] G. Rituraj, E. R. Joy, B. K. Kushwaha, and P. Kumar, "Analysis and comparison of series-series and series-parallel topology of contactless power transfer systems," in *IEEE Reg. 10 Conf. (TENCON)*, Oct. 2014, pp. 1–6.

[49] C. C. Mi, G. Buja, S. Y. Choi, and C. T. Rim, "Modern advances in wireless power transfer systems for roadway powered electric vehicles," *IEEE Trans. Ind. Electron.*, vol. 63, no. 10, pp. 6533–6545, Oct 2016.

[50] R. F. S. Caldeirinha, T. R. Fernandes, J. Richter, and M. O. Al-Nuaimi, "Simplified ret model derived from path loss and directional spectrum measurements in vegetation media at 11.2 and 20 ghz," *IET Microwaves, Antennas Propagation*, vol. 11, no. 1, pp. 136–143, 2017.

[51] M. Nariman, F. Shirinfar, A. Papi Toda, S. Pamarti, A. Rofougaran, and F. De Flaviis, "A compact 60-ghz wireless power transfer system," *IEEE Trans. Microw. Theory Tech.*, vol. 64, no. 8, pp. 2664–2677, Aug 2016.

[52] X. Li, J. Zhou, B. Duan, Y. Yang, Y. Zhang, and J. Fan, "Performance of planar arrays for microwave power transmission with position errors," *IEEE Antennas and Wirel. Propag. Lett.*, vol. 14, pp. 1794–1797, 2015.

[53] W. C. Brown, "The history of power transmission by radio waves," *IEEE Trans. Microw. Theory Techn.*, vol. 32, no. 9, pp. 1230–1242, Sep. 1984.

[54] C. R. Valenta and G. D. Durgin, "Harvesting wireless power: Survey of energy-harvester conversion efficiency in far-field, wireless power transfer systems," *IEEE Microw. Mag.*, vol. 15, no. 4, pp. 108–120, June 2014.

[55] W. Zhou and K. Jin, "Optimal photovoltaic array configuration under gaussian laser beam condition for wireless power transmission," *IEEE Trans. Power Electron.*, vol. 32, no. 5, pp. 3662–3672, May 2017.

[56] W. Zhou and K. Jin, "Efficiency evaluation of laser diode in different driving modes for wireless power transmission," *IEEE Trans. Power Electron.*, vol. 30, no. 11, pp. 6237–6244, Nov 2015.

[57] K. Jin and W. Zhou, "Wireless laser power transmission: A review of recent progress," *IEEE Trans. Power Electron.*, vol. 34, no. 4, pp. 3842–3859, April 2019.

[58] F. Lu, H. Zhang, H. Hofmann, and C. Mi, "A double-sidedlclc-compensated capacitive power transfer system for electric vehicle charging," *IEEE Trans. Power Electron.*, vol. 30, no. 11, pp. 6011–6014, Nov 2015.

[59] F. Lu, H. Zhang, H. Hofmann, and C. C. Mi, "An inductive and capacitive combined wireless power transfer system withlc-compensated topology," *IEEE Trans. Power Electron.*, vol. 31, no. 12, pp. 8471–8482, Dec 2016.

[60] J. Smeets, "Contactless transfer of energy : 3d modeling and design of a position-independent inductive coupling integrated in a planar motor," Ph.D. dissertation, Eindhoven University of Technology, 2015.

[61] J. Dai and D. C. Ludois, "A survey of wireless power transfer and a critical comparison of inductive and capacitive coupling for small gap applications," *IEEE Trans. Power Electron.*, vol. 30, no. 11, pp. 6017–6029, Nov 2015.

[62] J. Feng, Q. Li, F. C. Lee, and M. Fu, "Transmitter coils design for free-positioning omnidirectional wireless power transfer system," *IEEE Trans. Ind. Informal.*, vol. 15, no. 8, pp. 4656–4664, Aug 2019.

[63] M. N. O. Sadiku, *Principles of Electromagnetics*, 4th ed. Oxford University Press, 2009.

[64] L. Urankar, "Vector potential and magnetic field of current-carrying finite arc segment in analytical form, part i: Filament approximation," *IEEE Trans. Magn.*, vol. 16, no. 5, pp. 1283–1288, Sep. 1980.

[65] L. Urankar, "Vector potential and magnetic field of current-carrying finite arc segment in analytical form, part iii: Exact computation for rectangular cross section," *IEEE Trans. Magn.*, vol. 18, no. 6, pp. 1860–1867, November 1982.

[66] K. J. W. Pluk, "Hybrid 3-d electromagnetic modeling : the challenge of magnetic shielding of a planar actuator," Ph.D. dissertation, Eindhoven University of Technology, 2011.

[67] K. Binns and P.J.Lawrenson, *Analysis and Computation of Electric and Magnetic Field Problems*, 2nd ed. Oxford University Press, 2009.

[68] M. Yilmaz and P. T. Krein, "Capabilities of finite element analysis and magnetic equivalent circuits for electrical machine analysis and design," in *2008 IEEE Power Electronics Specialists Conference*, June 2008, pp. 4027–4033.

[69] M. Curti, J. J. H. Paulides, and E. A. Lomonova, "An overview of analytical methods for magnetic field computation," in *2015 Tenth International Conference on Ecological Vehicles and Renewable Energies (EVER)*, March 2015, pp. 1–7.

[70] M. Amrhein and P. T. Krein, "3-d magnetic equivalent circuit framework for modeling electromechanical devices," *IEEE Trans. Energy Convers.*, vol. 24, no. 2, pp. 397–405, June 2009.

[71] H. W. Derbas, J. M. Williams, A. C. Koenig, and S. D. Pekarek, "A comparison of nodal- and mesh-based magnetic equivalent circuit models," *IEEE Trans. Energy Convers.*, vol. 24, no. 2, pp. 388–396, June 2009.

[72] G. B. L. J., "Generalized harmonic modeling technique for 2d electromagnetic problems, applied to the design of a direct-drive active suspension system," Ph.D. dissertation, Eindhoven University of Technology, 2011.

[73] K. J. W. Pluk, G. D. Gersem, J. W. Jansen, and E. A. Lomonova, "Field calculations for magnetic shielding: Fourier modeling extended with mode-matching technique applied on a shield with finite dimensions," *IEEE Trans. Magn.*, vol. 49, no. 5, pp. 1593–1596, May 2013.

[74] C. H. H. M. Custers, T. T. Overboom, J. W. Jansen, and E. A. Lomonova, "2-d semianalytical modeling of eddy currents in segmented structures," *IEEE Trans. Magn.*, vol. 51, no. 11, pp. 1–4, Nov 2015.

[75] B. L. J. Gysen, K. J. Meessen, J. J. H. Paulides, and E. A. Lomonova, "General formulation of the electromagnetic field distribution in machines and devices using fourier analysis," *IEEE Trans. Magn.*, vol. 46, no. 1, pp. 39–52, Jan 2010.

[76] R. L. J. Sprangers, J. J. H. Paulides, K. O. Boynov, E. A. Lomonova, and J. Waarma, "Comparison of two anisotropic layer models applied to induction motors," *IEEE Trans. Ind. Applica.*, vol. 50, no. 4, pp. 2533–2543, July 2014.

[77] J. P. C. Smeets, T. T. Overboom, J. W. Jansen, and E. A. Lomonova, "Three-dimensional analytical modeling technique of electromagnetic fields of air-cored coils surrounded by different ferromagnetic boundaries," *IEEE Trans. Magn.*, vol. 49, no. 12, pp. 5698–5708, Dec 2013.

[78] L. Urankar, "Vector potential and magnetic field of current-carrying finite arc segment in analytical form, part iii: Exact computation for rectangular cross section," *IEEE Trans. Magn.*, vol. 18, no. 6, pp. 1860–1867, November 1982.

[79] K. J. W. Pluk, J. W. Jansen, and E. A. Lomonova, "Three-dimensional modeling of shielding of magnetic stray fields based on superposition of 2-d models," *IEEE Trans. Ind. Appl.*, vol. 51, no. 5, pp. 3656–3665, Sept 2015.

[80] A. Rokopf, E. Br, C. Joffe, and C. Bonse, "Calculation of power losses in litz wire systems by coupling fem and peec method," *IEEE Trans. Power Electron.*, vol. 31, no. 9, pp. 6442–6449, Sep. 2016.

[81] Z. Q. Zhu, L. J. Wu, and Z. P. Xia, "An accurate subdomain model for magnetic field computation in slotted surface-mounted permanent-magnet machines," *IEEE Trans. Magn.*, vol. 46, no. 4, pp. 1100–1115, April 2010.

[82] F. J. Lpez-Alcolea, J. Vzquez, P. Roncero-Snchez, and A. Parreno Torres, "Modeling of a magnetic coupler based on single and double-layered rectangular planar coils with in-plane misalignment for wireless power transfer," *IEEE Trans. Power Electron.*, pp. 1–1, 2019.

[83] L. Roubache, K. Boughrara, F. Dubas, and R. Ibtiouen, "New subdomain technique for electromagnetic performances calculation in radial-flux electrical machines considering finite soft-magnetic material permeability," *IEEE Trans. Mag.*, vol. 54, no. 4, pp. 1–15, April 2018.

[84] Y. Cheng and Y. Shu, "A new analytical calculation of the mutual inductance of the coaxial spiral rectangular coils," *IEEE Trans. Magn.*, vol. 50, no. 4, pp. 1–6, April 2014.

[85] M. Aissaoui, H. Allag, and J. P. Yonnet, "Mutual inductance and interaction calculation between conductor or coil of rectangular cross section and parallelepiped permanent magnet," *IEEE Trans. Magn.*, vol. 50, no. 11, pp. 1–4, Nov 2014.

[86] J. Wang, S. L. Ho, W. N. Fu, and M. Sun, "Analytical design study of a novel witricity charger with lateral and angular misalignments for efficient wireless energy transmission," *IEEE Trans. Magn.*, vol. 47, no. 10, pp. 2616–2619, Oct 2011.

[87] K. Fotopoulou and B. W. Flynn, "Wireless power transfer in loosely coupled links: Coil misalignment model," *IEEE Trans. Magn.*, vol. 47, no. 2, pp. 416–430, Feb 2011.

[88] J. P. C. Smeets, T. T. Overboom, J. W. Jansen, and E. A. Lomonova, "Mode-matching technique applied to three-dimensional magnetic field modeling," *IEEE Trans. Magn.*, vol. 48, no. 11, pp. 3383–3386, Nov 2012.

[89] J. P. C. Smeets, T. T. Overboom, J. W. Jansen, and E. A. Lomonova, "Inductance calculation nearby conducting material," *IEEE Trans. Magn.*, vol. 50, no. 11, pp. 1–4, Nov 2014.

[90] R. Alipour-Sarabi, Z. Nasiri-Gheidari, and H. Oraee, "Development of a 3-d magnetic equivalent circuit model for axial flux machines," *IEEE Trans. Ind. Electron.*, pp. 1–1, 2019.

[91] K. J. Meessen, B. L. J. Gysen, J. J. H. Paulides, and E. A. Lomonova, "General formulation of fringing fields in 3-d cylindrical structures using fourier analysis," *IEEE Trans. Magn.*, vol. 48, no. 8, pp. 2307–2323, Aug 2012.

[92] B. K. Kushwaha, G. Rituraj, and P. Kumar, "3-d analytical model for computation of mutual inductance for different misalignments with shielding in wireless power transfer system," *IEEE Trans. Transport. Electrific.*, vol. 3, no. 2, pp. 332–342, Jun. 2017.

[93] G. Rituraj, B. K. Kushwaha, and P. Kumar, "3-d analytical modeling of magnetic field for air core rectangular coil in contactless power transfer system," in *IECON 2016 - 42nd Annual Conference of the IEEE Industrial Electronics Society*, Oct 2016, pp. 4459–4464.

[94] J. P. C. Smeets, T. T. Overboom, J. W. Jansen, and E. A. Lomonova, "Three-dimensional magnetic field modeling for coupling calculation between air-cored rectangular coils," *IEEE Trans. Magn.*, vol. 47, no. 10, pp. 2935–2938, Oct 2011.

[95] K. J. W. Pluk, G. D. Gersem, J. W. Jansen, and E. A. Lomonova, "Fourier modeling of magnetic shields with linear permeable material and finite dimensions," *IEEE Trans. Magn.*, vol. 49, no. 7, pp. 4160–4163, July 2013.

[96] F. Dubas and K. Boughrara, "New scientific contribution on the 2-d subdomain technique in cartesian coordinates: Taking into account of iron parts," *Math. Computat. Appl.*, vol. 22, no. 1, 2017.

[97] A. Demenko, R. M. Wojciechowski, and J. K. Sykulski, "2-d versus 3-d electromagnetic field modeling in electromechanical energy converters," *IEEE Trans. Magn.*, vol. 50, no. 2, pp. 897–900, Feb 2014.

[98] T. Bang, K. Shin, M. Koo, C. Han, H. Cho, and J. Choi, "Measurement and torque calculation of magnetic spur gear based on quasi 3-d analytical method," *IEEE Trans. Appl. Supercond.*, vol. 28, no. 3, pp. 1–5, April 2018.

[99] K. Aditya and S. S. Williamson, "Comparative study of series-series and series-parallel topology for long track ev charging application," in *IEEE Transport. Electrific. Conf. Expo. (ITEC)*, Jun. 2014, pp. 1–5.

[100] K. Aditya and S. S. Williamson, "Comparative study of series-series and series-parallel compensation topologies for electric vehicle charging," in *IEEE 23rd Int. Symp. Ind. Electron. (ISIE)*, Jun. 2014, pp. 426–430.

[101] C.-S. Wang, G. A. Covic, and O. H. Stielau, "Power transfer capability and bifurcation phenomena of loosely coupled inductive power transfer systems," *IEEE Trans. Ind. Electron.*, vol. 51, no. 1, pp. 148–157, Feb. 2004.

[102] J. P. K. Sampath, A. Alphones, and D. M. Vilathgamuwa, "Figure of merit for the optimization of wireless power transfer system against misalignment tolerance," *IEEE Trans. Power Electron.*, vol. 32, no. 6, pp. 4359–4369, Jun. 2017.

[103] D. Liu, H. Hu, and S. V. Georgakopoulos, "Misalignment sensitivity of strongly coupled wireless power transfer systems," *IEEE Trans. Power Electron.*, vol. 32, no. 7, pp. 5509–5519, Jul. 2017.

[104] M. Q. Nguyen, Y. Chou, D. Plesa, S. Rao, and J. C. Chiao, "Multiple-inputs and multiple-outputs wireless power combining and delivering systems," *IEEE Trans. Power Electron.*, vol. 30, no. 11, pp. 6254–6263, Nov. 2015.

[105] J. P. C. Smeets, T. T. Overboom, J. W. Jansen, and E. A. Lomonova, "Modeling framework for contactless energy transfer systems for linear actuators," *IEEE Trans. Ind. Electron.*, vol. 60, no. 1, pp. 391–399, Jan 2013.

[106] A. Zaheer, G. A. Covic, and D. Kacprzak, "A bipolar pad in a 10-khz 300-w distributed ipt system for agv applications," *IEEE Trans. Ind. Electron.*, vol. 61, no. 7, pp. 3288–3301, July 2014.

[107] G. A. Covic, M. L. G. Kissin, D. Kacprzak, N. Clausen, and H. Hao, "A bipolar primary pad topology for ev stationary charging and highway power by inductive coupling," in *2011 IEEE Energy Conversion Congress and Exposition*, Sep. 2011, pp. 1832–1838.

[108] S. Moon and G. Moon, "Wireless power transfer system with an asymmetric four-coil resonator for electric vehicle battery chargers," *IEEE Trans. Power Electron.*, vol. 31, no. 10, pp. 6844–6854, Oct 2016.

List of Publications

Journal Publications

1. **Brijesh Kumar Kushwaha**, Gautam Rituraj, Praveen Kumar, "**A Subdomain Analytical Model of Coil System with Magnetic Shields of Finite Dimensions and Finite Permeability for WPT Systems**," in *IEEE Transactions on Magnetics*, vol. 56, no. 12, pp. 1-11, Dec. 2020

2. **Brijesh Kumar Kushwaha**, Gautam Rituraj, Praveen Kumar "**3-D Analytical Model for Computation of Mutual Inductance for Different Misalignments With Shielding in Wireless Power Transfer System**," in *IEEE Transactions on Transportation Electrification*, vol. 3, no. 2, pp. 332-342, June 2017

3. **Brijesh Kumar Kushwaha**, Gautam Rituraj, Praveen Kumar and P. Bauer, "**Mathematical model for the analysis of seriesparallel compensated wireless power transfer system for different misalignments**," in *IET Circuits, Devices and Systems*, vol. 13, no. 7, pp. 970-978, 10 2019.

4. Gautam Rituraj, **Brijesh Kumar Kushwaha**, Praveen Kumar, "**A Unipolar Coil Arrangement Method for Improving the Coupling Coefficient without Ferrite Material in Wireless Power Transfer Systems**," in *IEEE Transactions on Transportation Electrification*, vol. 6, no. 2, pp. 497-509, June 2020

5. Gautam Rituraj, **Brijesh Kumar Kushwaha**, Praveen Kumar "**Contactless power transfer system for sealed lead acid battery charging**," in *Wireless Power Transfer, Cambridge University Press* 2018, 5, (1), pp.2026.

Conference Publications

1. **Brijesh Kumar Kushwaha**, Gautam Rituraj, Praveen Kumar and P. Bauer, "**Mathematical model of series-parallel compensation for contactless power transfer system**," *IEEE International Power Electronics and Motion Control Conference (PEMC)*, Varna, Bulgaria, 2016, pp. 1020-1025.

2. **Brijesh Kumar Kushwaha**, Gautam Rituraj and Praveen Kumar, "**Mathematical model of series-series compensation for contactless power transfer system**," *IECON 2015 - 41st Annual Conference of the IEEE Industrial Electronics Society*, Yokohama, 2015, pp. 001321-001326.

3. **Brijesh Kumar Kushwaha**, Gautam Rituraj and Praveen Kumar, "**Modeling and analysis of inductively coupled power transfer system**," *IEEE International Transportation Electrification Conference (ITEC)*,Chennai,2015,pp.1-4.

4. Gautam Rituraj, **Brijesh Kumar Kushwaha**, and Praveen Kumar, "**3-D analytical modeling of magnetic field for air core rectangular coil in contactless power transfer system**," *IECON 2016 - 42nd Annual Conference of the IEEE Industrial Electronics Society*, Florence, Italy, 2016, pp. 4459-4464.

5. Ezhil Reena Joy, **Brijesh Kumar Kushwaha**, Gautam Rituraj and Praveen Kumar, "**Analysis and comparison of four compensation topologies of contactless power transfer system**," *2015 4th International Conference on Electric Power and Energy Conversion Systems (EPECS)*, Sharjah, 2015, pp. 1-6.

6. Ezhil Reena Joy, **Brijesh Kumar Kushwaha**, Gautam Rituraj and Praveen Kumar, "**Impact of circuit parameters in contactless power transfer system**," *IEEE International Conference on Power Electronics, Drives and Energy Systems (PEDES)*, Mumbai, 2014, pp. 1-6.

7. Gautam Rituraj, Ezhil Reena Joy, **Brijesh Kumar Kushwaha** and Praveen Kumar, "**Analysis and comparison of series-series and series-parallel topology of contactless power transfer systems**," *TENCON 2014 - 2014 IEEE Region 10 Conference*, Bangkok, 2014, pp. 1-6.